NOVEL *BOTTOM-UP* SUB-MICRON ARCHITECTURES FOR ADVANCED FUNCTIONAL DEVICES

by

CHIARA BUSA'

A thesis submitted to

the University of Birmingham

for the degree of

DOCTOR OF PHILOSOPHY

Supervisor: Dr Pola Goldberg-Oppenheimer

Department of Chemical Engineering

College of Engineering and Physical Sciences

University of Birmingham

May 2017

UNIVERSITY OF BIRMINGHAM

University of Birmingham Research Archive

e-theses repository

Abstract

This thesis illustrates two novel routes for fabricating hierarchical micro-to-nano structures with interesting optical and wetting properties. The co-presence of asperities spanning the two length scales enables the fabrication of miniaturised, tuneable surfaces exhibiting a high potential for applications in for instance, waterproof coatings and nanophotonic devices, while exploiting the intrinsic properties of the structuring materials.

Firstly, scalable, superhydrophobic surfaces were produced *via* carbon nanotubes (CNT)-based electrohydrodynamic lithography, fabricating multiscale polymeric cones and nanohair-like architectures with various periodicities. CNT forests were used for manufacturing essential components for the electrohydrodynamic setup and producing controlled micro-to-nano features on a millimetre scale. The achieved high contact angles introduced switchable *Rose*-to-*Lotus* wetting regimes.

Secondly, a cost-effective method was introduced as a route towards plasmonic bandgap metamaterials *via* electrochemical replication of three-dimensional (3D) DNA nanostructures as sacrificial templates. A range of sub-30nm 3D DNA polyhedrons, immobilised onto conductive and insulating surfaces, were replicated with gold *via* electrochemical deposition and sputtering. Microscopic characterisation revealed detailed gold replicas preserving both edges and cavities of the DNA nanostructures. Accurate tuning of both polyhedrons' dimensions and gold plating conditions finally enabled sub-100nm structures which show promising optical properties such as, birefringence for potential applications in photonics, metamaterials and sensing.

Dedication

To my family, and in particular, to my father.

Acknoledgments

My first and deepest thanks go to my supervisor, Dr. *Pola Goldberg-Oppenheimer*, who supported my journey during these three years. My growth as a fully aware scientist and also as a person, is due to this extraordinary woman who provided valuable guidance and support during the deepest moments in both my professional and personal life. Your help was fundamental for keeping me on track, for stopping me from following some of my one too many ideas, while donating time for stimulating me to pursue my paths. For all these reasons I am honestly grateful for your inspiration as a scientist and a woman.

I'd like to thank my colleagues and in particular *JJ Rickard* for enduring my company, my crazy ideas and my slight obsession with having everything in order in the laboratories. Our different backgrounds and the consequential discussions helped me in broadening my research perspectives and attempting a lot of new experiments, and for that I sincerely thank you. Special thanks go to *Georgios Gotsis*, for the human support and friendship since our very first meeting. Life in the lab would have been way more solitary and tiresome without you to cheer me up. Moreover, professionally speaking, I don't have enough words for expressing my gratitude for all your help while building new setups and arranging microscopes and cameras. I'd also like to thank all the colleagues from the Advanced Nano-Materials, Structures and Applications (ANMSA) group, *Paolo, Carl*, *Emma*, and *Rachel*. Our different perspectives are the real strength of the group, and I'm profoundly grateful to you all for the help given to me in our time spent together.

The studies in these last three years brought me into contact with many brilliant scientists, every one of them enriching my knowledge and providing deep insights

Contents

List of Figures

List of Tables

List of Equations

List of Chemicals and Materials

	GRADE/ PURITY	SUPPLIER	FORM/ STATE	CAS
Silicon wafer	Single-polished	Si-Mat	Solid	n/a
Indium-Tin Oxide	n/a	Sigma-Aldrich	Solid	50926-11-9
Carbon film coated TEM grid	n/a	Fisher Scientific	Solid	AGS160
Mica disk	V1	Ted Pella	Solid	n/a
Water	HPLC	Sigma-Aldrich	Liquid	7732-18-5
Toluene	HPLC	Sigma-Aldrich	Liquid	108-88-3
Chloroform (CHCl₃)	HPLC	Sigma-Aldrich	Liquid	67-66-3
Magnesium acetate	≥99%	Sigma-Aldrich	Solid	16674-78-5
Polystyrene (PS)	n/a	Sigma-Aldrich	Solid	9003-53-6
Poly methyl methacrylate (PMMA)	Analytical standard	Sigma-Aldrich	Solid	9011-14-7
Poly (9-vinyl carbazole) (PVK)	n/a	Sigma-Aldrich	Solid	25067-59-8
Polychlorotri-fluoroethylene (PCTFE)	n/a	Sigma-Aldrich	Solid	9002-83-9
Tridecafluoro-1,1,2,2-tetrahydrooctyl-1-66 Trichloro- silane (FTS)	n/a	Gelest Inc.	Solid	78560-45-9
Octadecyl trichlorosilane (OTS)	≥90%	Sigma-Aldrich	Solid	3069-42-9
Bis(trimethylsilyl)amine (HMDS)	≥99%	Sigma-Aldrich	Solid	999-97-3

DNA strand S1 (tetrahedron)	Appendix 1	Eurofins Genomics	Solid	n/a
DNA strand S2 (tetrahedron)	Appendix 1	Eurofins Genomics	Solid	n/a
DNA strand S3 (tetrahedron)	Appendix 1	Eurofins Genomics	Solid	n/a
DNA strand S4 (tetrahedron)	Appendix 1	Eurofins Genomics	Solid	n/a
DNA strand Long (tetrahedron)	Appendix 1	Eurofins Genomics	Solid	n/a
DNA strand Medium (tetrahedron)	Appendix 1	Eurofins Genomics	Solid	n/a
DNA strand Short (tetrahedron)	Appendix 1	Eurofins Genomics	Solid	n/a
DNA strand Long (octahedron)	Appendix 1	Eurofins Genomics	Solid	n/a
DNA strand Medium (octahedron)	Appendix 1	Eurofins Genomics	Solid	n/a
DNA strand Short (octahedron)	Appendix 1	Eurofins Genomics	Solid	n/a

List of Symbols

N_A	Numerical aperture
A	Cross-section
d	Inter-electrode distance
f_s	Solid fraction underneath the liquid drop
f_v	Solid fraction that corresponds to the vapour gaps
f_r	Filling ratio
H	Structure height
h_0	Polymeric layer thickness
h	Initial film thickness
M	General metal
n	Refractive index
Ox	Oxidation product
p	Pressure
p_{el}	Electrostatic pressure
p_{ex}	Excess surface pressure
pK_a	Equilibrium constant
p_l	Laplace pressure
p_o	Ambient air pressure
p_{vdW}	Van der Waals
R	Upper dimensional limit
r	Lower dimensional limit
Red	Reducing agent

r_f	Roughness of the fraction of the surface in contact with the liquid
R_p	AFM sample size
R_s	Surface roughness factor and heterogeneity parameters ratio
S	Surface area ratio of the topography
T_r	Room temperature
T_g	Glass transition point
V	Voltage
$\Delta G°$	Free energy
ε	Permittivity
μ	Magnetic permeability
γ	Surface tension
φ	Fraction of the area of the solid surface that is wetted by liquid
φ_s	Fraction of surface available at the top of protrusions
θ	Contact angle (CA)
θ_0	Static CA for a smooth substrate
θ_{adv}	Advanced CA
θ_{rec}	Receding CA
θ_X	Contact angle with the vapour in the gaps
η	Viscosity
λ	Wavelength
λ_i	Intrinsic wavelength
Λ_m	Lateral periodicity
θ_r	Apparent contact angle
ρ	Roughness factor

ρ_f	Density
τ_f	Patterning termination times
ω_{tf}	Triple line length
λ	Wavelength

List of Abbreviations and Acronyms

A	Adenine
AFM	Atomic Force Microscopy
ALD	Atomic layer deposition
APTES	3-Aminopropyl triethoxysilane
BSE	Back-scattered electrons
BCP	Block-copolymer
C	Cytosine
CA	Contact Angle
CaDNAno	3D DNA origami nanostructures design software
CCD	Charge-coupled device
CE	Counter electrode
CNH	Curly nano-hair
CNT	Carbon nanotube
CVD	Chemical vapour deposition
CV	Cyclic voltammetry
DNA	Deoxyribonucleic acid
DLS	Dynamic light scattering
EBL	Electron-beam lithography
EDTA	Ethylenediaminetetraacetic Acid
EHL	Electrohydrodynamic lithography
EHD	Electrohydrodynamic
EM	Electromagnetic

ESI-MS	Electrospray ionisation-mass spectroscopy
FETMS	(2-(perfluorooctyl) ethyl)trimethoxysilane
G	Guanine
Hys	Hysteresis
HP	Hexagonal pillars
HPLC	High-pressure liquid chromatography
HPSF	High Purity Salt-Free purification
IR	Infrared
LbL	*Layer-by-layer* deposition
LSV	Linear sweep voltammetry
MM	Metamaterial
MWNT	Multi-walled CNT
NANEV	Nanosystems design software
NIR	Near-infrared
NIM	Negative refractive index material
NP	Nanoparticle
NS	Navier-Stokes
NSP	Nanosphere photolithography
OCP	Open-circuit potential
OM	Optical microscopy
PBG	Plasmonic bandgap
PCR	Thermal cycler machine
PDMS	Poly(dimethylsiloxane)
PED	Pulse electrodeposition

RE	Reference electrode
RIE	Reactive ion etching
ROI	Region of interest
RPM	Revolution per minute
SAM	Self-assembled monolayer
SEM	Scanning Electron Microscopy
SHE	Standard hydrogen electrode
SNH	Straight nano-hairs
SPM	Scanning probe microscopy
ssDNA	Single-stranded DNA
STEM	Scanning transmission electron microscope
SWCNT	Single-walled CNT
S1L	Single-level spikes with rounded edges
S2L	Two-levelled spiky cones
S2L2	Two-tiered hierarchical spiky cones
T	Thymine
TAE	Tris base, Acetic acid and EDTA buffer
TEM	Transmission Electron Microscopy
TPP	Two-photon polymerisation
UV	Ultraviolet
WE	Working electrode
vdW	Van der Waals
VACNT	Vertically-aligned CNT
VTMS	Vinyltrimethoxysilane

3D	Three-dimensional
2D	Two-dimensional
1D	One-dimensional

1 Introduction

1.1. Thesis Overview

The research developed in this thesis aims to explore and establish novel methods for producing a range of micro-to-nano morphologies for a broad variety of applications, focusing on **superhydrophobic** and **photonic three-dimensional (3D) nanostructured metallic surfaces**. Beyond the manufacturing of such structures, involving various elaborate techniques to enable the pre-designed nanostructures, this research work focused on highly controlled 3D material nano-structuring as the pivotal point, which has been developed towards the two distinctive applications discussed in detail in this thesis.

Initially, a viable procedure for fabricating a wide range of hierarchical structures for superhydrophobic applications, characterised by tuneable dimensions, pitch, aspect ratio and roughness, was developed and investigated.

Subsequently, a novel, cost-effective process for progressing toward the alternative structuring of gold nano-scaffolds was developed, by using specifically-arranged 3D DNA molecules as sacrificial templates, with the ultimate, long-term goal of manufacturing unique optically-active materials.

1.2. From Macro to Nano Patterns

Natural patterns have a cumbersome part to play in the world we, as human beings, experience every day. Nature exhibits infinite possibilities of spectacular colours and shapes, from large galaxies to tree leaves and colourful butterflies. It is common to observe highly organised patterns, such as the honeycomb or the disposition of the spines in cactus. In fact, recurring schemes are also easily perceived by the human brain (as explained by Mark P. Mattson in ''Superior pattern processing is the essence of the evolved human brain'' [1]), which is instinctively designed to recognise different sort of patterns, spanning from facial features, through the music notes to symbols, using all of our five senses. Order and repetition are fundamental aspects of natural features and are, therefore, of a unique appeal.

Since the times of ancient Greeks, mankind has tried to classify nature's patterns, which led Plato (427–347 BC) to define five regular polyhedrons, commonly known as *Platonic solids*, each associated with natural elements such as air, water, wind and fire [2]. In the XII century, Fibonacci (Fig. 1.1.) developed the '*Fibonacci* Sequence' which, not only is used in mathematics but also appears to be directly related to the natural world, which is exemplified by the *Phyllotaxis,* the spiral arrangement of leaves or stems around a pivotal point [3].
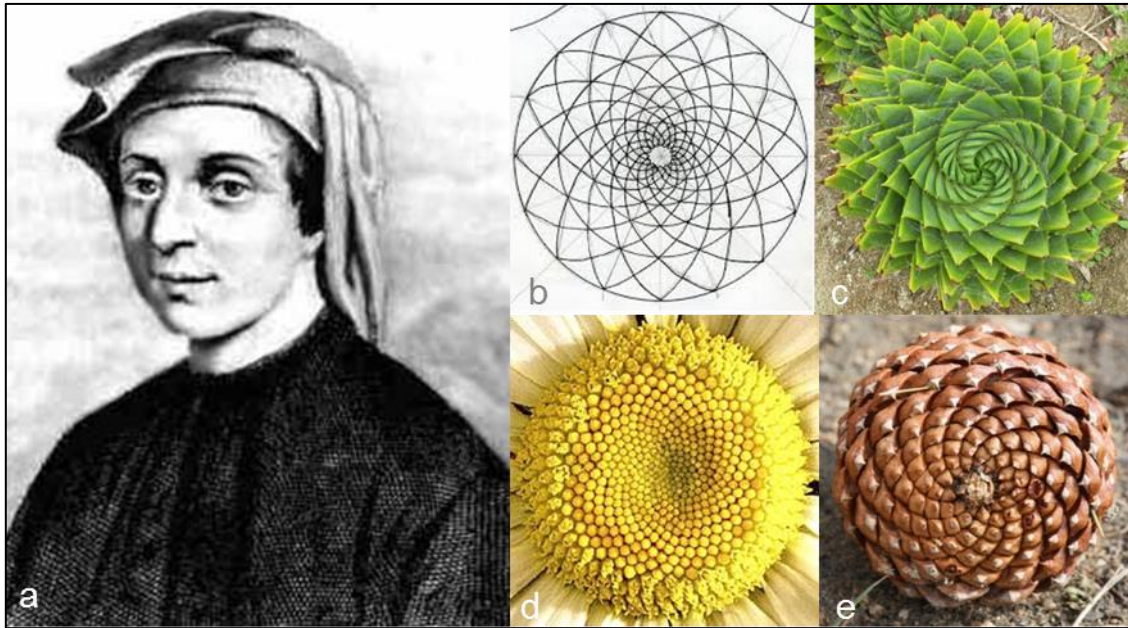
Figure 1.1. Natural systems mirroring the golden spiral. a) Portrait of Leonardo Fibonacci (1175 – 1250), who introduced the modern Hindu-Arabic numerals in his work, *Liber Abaci*, and introduced the *Fibonacci sequence*, formed by integer number which, after the first two, are the sum of the two preceding ones. The *golden spiral*, in **b)** can be formed by the progressive juxtaposition of squares with increasing side, following the sequence. The numbers are also common in various biological systems such as **c)** the phyllotaxis arrangement, **d)** the flower head disposition, and the **e)** pine cone bracts.

In the years to follow, pattern studies found fertile ground in Mathematics although, it was a biologist and botanist, Lindenmayer, who in 1968, introduced the concept of *fractals* for formalising the plant cell behaviour [4]. A fractal is defined as "*a curve or geometrical figure, each part of which has the same statistical character as the whole. They are useful in modelling structures (such as snowflakes) in which similar patterns recur at progressively smaller scales, and in describing partly random or chaotic phenomena such as crystal growth and galaxy formation*" [5]. Similarly, fractals are self-similar shapes, which repeat the same pattern while expanding in space. For example, the branch of a tree resembles the whole tree, following the fractal definition of expanding symmetry, similarly to mountains shapes, ferns or river basins [6–8].

3

Patterns in nature are especially intriguing because of the properties derived from such periodic arrays. In fact, many species of either the animal or the vegetal world possess ordered nanofeatures, responsible for all the unique properties we can observe such as water-repellent leaves or iridescent colours [9]. For example, the gerridae's or water strider's unique ability to walk on water without sinking (Fig.1.2.a-b) is due to a combination of factors, including the weight distribution and the legs' structures that are formed by ordered, nanoscaled hair, which trap air bubbles and allow them to float [10–12]. Moreover, a whole range of unique properties can be found in insects. For example, butterflies (Fig. 1.2.c-e) derive the wing iridescent colours from arrays of overlaying, protruded cells, which following the interaction with light, generate a range of changing hues when viewed at different angles [10,12–14]. Similarly, jewel beetles exhibit the astounding colour of the iridescent cover and wings from the conical shape of hexagonal cells on the outer shells [14,15].
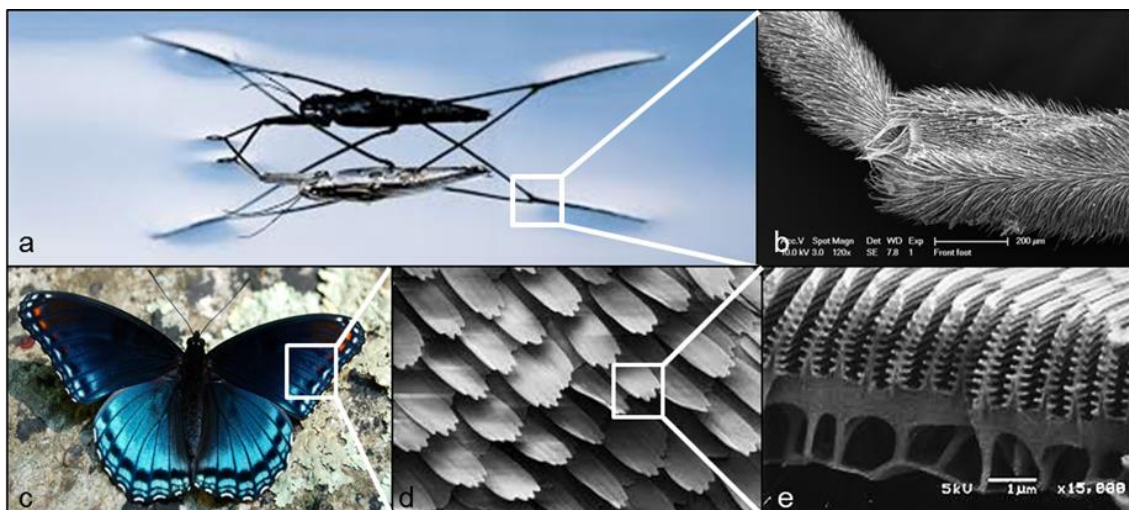
Figure 1.2. Water striders's legs and butterflies' wings nanoarchitectures. a) Water Strider are known for their ability to walk on water, which is given by the **b)** hydrophobic nanohair-like structures of their legs, which trap air bubbles within, and allow the Striders to float. **c)** Similarly, butterfly wings are comprised of thousands of **d)** micron *scales* which are in turn formed by **e)** nanoscaled *setae*, which reflect the light and letting the iridescent wings shades to arise.

In the modern era, another wide range of fascinating properties started to gain attention following the evolving scientific and commercial demands. For instance, research attempts at replicating the gecko's ability to walk on vertical surfaces have triggered a large number of studies of the fine structures of its feet [12,16–19]. The hierarchical structure of the gecko's feet with nanoscopic protrusions called *spatulae* acts as minute suction cups, ordered in grid-like arrays and capable of sustaining up to six times the gecko weight while sticking and walking on walls or ceilings (Fig. 1.3).
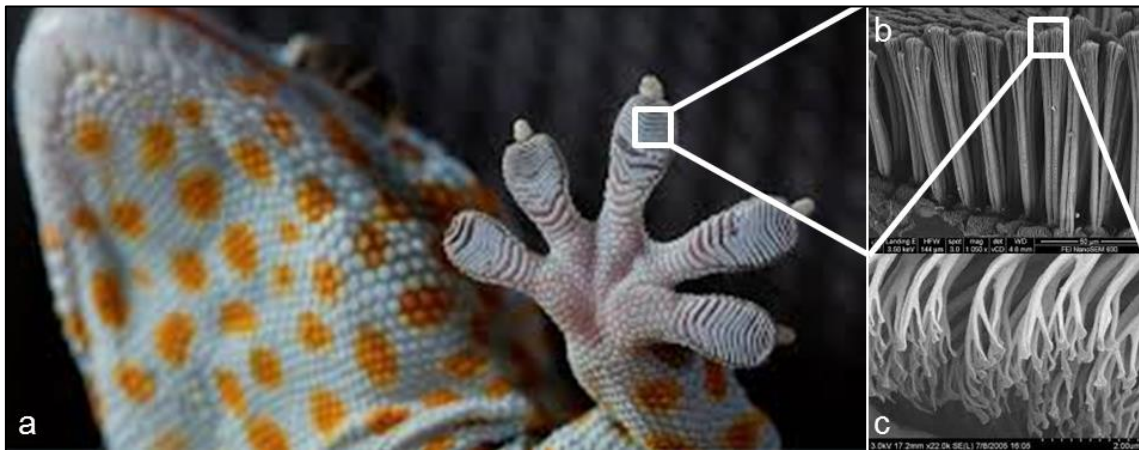
Figure 1.3. Gecko's feet nanostructure. a) The gecko is a type of lizard which possesses the unique ability to walk vertically. More than 60% of gecko species have multiscale toes, **b)** which are comprised of thousands and thousands of lamellar-arranged *spatulaes*. **c)** The final extremity ends in minute *setae*, provoking the adhesion on surfaces because of the Van der Waals forces [20,21] that bridge the surface with each one of them.

The term *biomimetics* has been established during the 1950s, defining the approach to study and reproduce natural systems and elements. The research toward this has proliferated introducing novel fields such as the bionics or robotics [22–24]. Thus, aiming at mimicking the natural properties and the fine intricate structures triggered the first step in characterising and replicating the multi-level

natural patterns. This inevitably led to significant difficulties and hurdles. After all, the evolution took more than thousands of years to achieve the natural structure, and develop physical, chemical [25,26] and structural ways to overcome the surrounding hostilities such as, for instance, "merging" with the environs like the chameleon does or eluding potential predators with iridescent and eye-mimicking wings, like moths do [26,27]. Thus, reproducing high-complexity, fine structures and also precisely maintaining the properties found in the natural world initiated many innovative fabrication routes [28].

Nowadays, two dominant approaches drive the manufacturing of sub-micron architectures. The *top-down* approach [29–32] is widely known as the miniaturisation process of material patches, which are traditionally cut and modelled into sub-micrometric designs by using mechanical or chemical tools. On the other hand, the *bottom-up* approach [33–35] enables the desired material to arrange in a pre-ordered manner, relying on the capability of the material itself to self-assemble throughout the accurate molecular design [34]. Most common examples of both strategies include soft lithography imprinting, photolithography, electron beam (e-beam) lithography, moulding, 3D printing or polymers self-assembly [36,37]. Despite the achieved results in micropatterning, these techniques are limited by several factors which reduce the reproducibility of structures for commercial devices [38–40]. For all the methods which require the presence of a mould, the scaling-up to the final device desired dimensions represents the possible bottleneck in generating large functional devices, mostly due to the likelihood of defects from the use of larger frameworks [41,42]. For

example, optical patterning techniques such as photolithography, are limited by the light diffraction limit, while depending upon the incident wavelength [43]. Thus, the dimension threshold for optically patterned surfaces is limited to $\lambda/4n$, where λ is the wavelength and n is the refractive index of the media.

Smaller nanoscale patterns can be achieved by both electron-beam and ion-beam lithography [44–46], although these are limited by the secondary electron scattering for the first technique and the high cost for producing the required short-range ion emission beam for the latter one, restricting their uses on a large scale. During the last decade, self-assembly methods, based on exploiting various polymers which can arrange on the micro-to-nanoscale length have revealed their potential when used in combination with traditional lithography techniques [47,48]. Nevertheless, the physical segregation of the polymers, coupled with elevated steric hindrance, have set additional limitations when the substrate's dimensions decrease to the nanometre scale features [48–51].

1.3.   Superhydrophobic Surfaces

The concept of superhydrophobic surfaces was first introduced in the 1960s, by observing the lotus leaf behaviour upon wetting. Although, the wettability theories for hydrophobic surfaces were already fully developed since the 1930s, with Wenzel and Cassie-Baxter Theories (please see Chapter 4.2), and a natural material, such as the plant named *Triticum* [52], with a contact angle (CA) > 150° firstly observed only in the 1940s. Thereafter, the proper formalisation of the

7

superhydrophobic state was finalised, almost 40 years later by Barthlott and Nehius in 1997, which explained how the wetting modes arise from the combination of surface roughness at a micro-to-nanoscale combined with a low surface energy (Figure 1.4). Moreover, the presence of hierarchical structures and overall surface roughness was demonstrated to induce self-cleaning properties, arising from the presence of air bubbles trapped between the solid asperities and the liquid droplet. A deep insight and discussion of the established wetting regimes will be given in Chapter 4.

The importance of mimicking and moving these properties towards modern world applications and device technologies is evidenced by the considerable efforts of research in this field, which, in particular, have focused on developing highly controlled, periodic micro- and nano-structures. Recently, novel formulations for super-apolar and low surface energy coatings were developed to address the market demand in a more immediate way, especially for anti-fouling and anti-icing coatings [53–57].

So far, a wide range of techniques and procedures have been established and will be discussed further in this thesis (see section 2.1), while pointing-out and discussing the advantages and disadvantages of each.
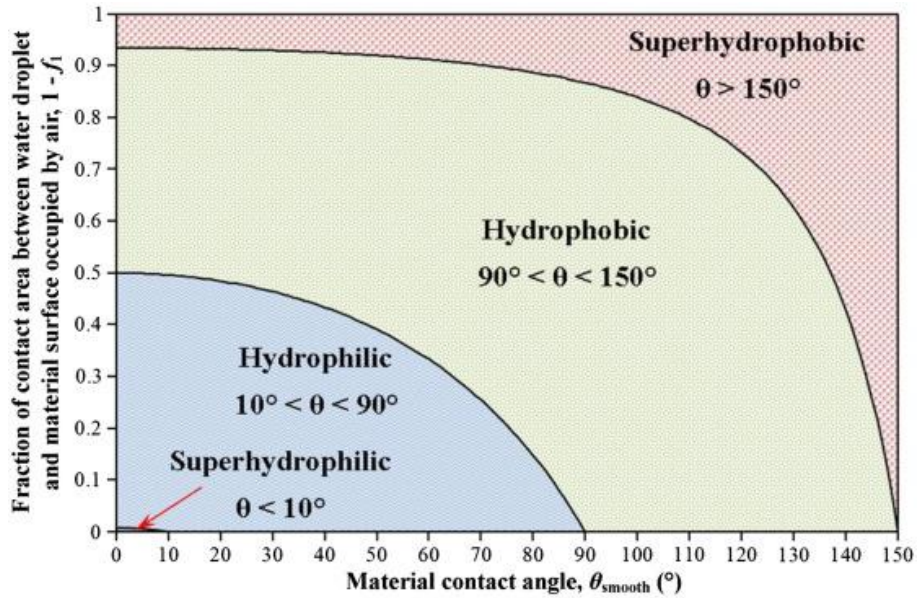
Figure 1.4. Material wettability (θ_smooth) and the proportion of air trapped within a rough surface diagram ratio. Reproduced from [58]

1.4. 3D Photonic Band Gap and Negative Refractive Index Metamaterials

The Oxford Dictionary defines a *metamaterial* as "*a synthetic composite material engineered to display properties not usually found in natural materials*", based on the accurate manipulation of the electromagnetic wave-material interaction. Unique and unnatural properties can arise from an electromagnetic (EM) wave when guided and controlled into artificially-oriented (meta)materials hence, introducing negative, near-zero or high values for parameters such as refractive index, permittivity or permeability, to list a few [40,59–65]. According to their properties, metamaterials (MM) can be divided into three main groups, electromagnetic, acoustic and mechanical although, unambiguous prerequisites

9

are yet to be decided [66–70]. Nowadays, MM are predominantly *man-made* although, the extent of this statement is discussion matter of debate since they are comprised of parent materials which are found in nature. The *properties* of MM are totally different from the original constituents in bulk or in the naturally-found arrangement. In particular, the optical metamaterials' properties are related to the permittivity (ε), which determines the extent and the way a forming electric field is affected by a material (especially a dielectric), and the magnetic permeability (μ), which measures the ability of a material to sustain an intrinsic magnetic field, as shown in Fig. 1.5 [71–74].
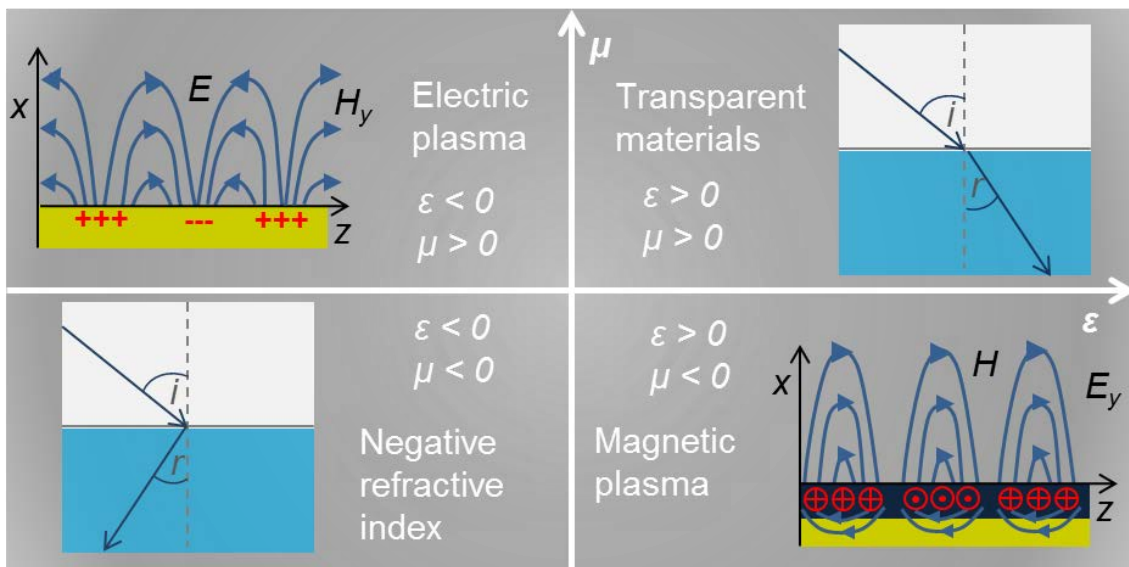
Figure 1.5. The medium permittivity (ε) and magnetic permeability (μ) quadrant and related different behaviour. The first quadrant explains the common behaviour of transparent or semi-transparent materials such as glass or water. The second quadrant shows the interaction of transverse-electric light with materials with $\varepsilon < 0$, Fundamental in *electric plasmonic* materials. The third quadrant is the more interesting for optical metamaterials since the coexistence of both ε and $\mu < 0$ determines properties such as the *negative refractive index*, which enables the technology behind the smart materials, "invisibility cloaks" and environment-mimicking devices. The fourth quadrant is representative of materials interacting with a transverse-magnetic polarised radiation, producing a magnetic plasma oscillation. Such phenomenon does not usually occur at optically visible wavelengths.

The term metamaterial (*meta-* derived from "beyond" in Greek) was coined merely a decade ago [40,75–77], and in a few short years the field has attracted inter-disciplinary interest and has nourished research fields such as physics, chemistry and engineering. Despite the fact that the term *metamaterials* is yet to be fully defined, such structures can be described as man-made materials, which exhibit unusual properties due to the unique fine structure arrangement [78,79]. In fact, the metamaterials' fundamental components, called *meta-atoms*, are not comparable with the length scales of the interacting wavelengths and neither is the distance between two proximal basic components [78,80]. It has been demonstrated that a periodic geometrical disposition of such structured materials is not a fundamental requirement since unnatural properties can arise from randomised (not periodical) distributions of the building blocks [77,81,82]. These artificial properties are also independent of the constituents' chemistry since a variety of materials such as gold, silver, aluminium and copper have been demonstrated to alter their conductivity properties due to the size of meta-atoms [77,80]. Indeed, phenomena occur when two meta-atoms are in proximity and this neighbouring between them can be achieved by using various yet expensive, techniques [76,83,84]. So far, MM fabrication has been focused on obtaining high-precision, subwavelength structured 2D materials which are also highly reproducible, flexible and robust. Nowadays, since the interest has widened to 3D metamaterials, "traditional" techniques such as nanoimprinting, electron-beam lithography and photolithography are getting replaced or enhanced by novel procedures for structuring proximal meta-atoms [77,80,85,86]. For instance, by multilayer deposition, block copolymers used as sacrificial scaffolds

or for large-scale substrates, by two-photon photopolymerization (TPP) or by direct laser writing [75,86,87]. The combination of these techniques with additional deposition techniques such as chemical vapour deposition (CVD) allows the scaling-up to larger areas, despite the limitations arising from the resolution and the materials [75,85,86,88].

1.5. 3D Nanofabrication

Since 2011, the miniaturisation and the reduction in dimensions of modern device components have reached a steady state from the nanoscale perspective [89–91]. Industrial processes working on such a scale refer to *nanoelectronics* and the production of such parts relies on the use of nanotechnologies for proceeding towards even smaller dimensions. Thus, novel techniques for nanofabrication are increasingly required, primarily focusing on fast, cost-effective and eco-friendly processes. Metals and semiconductor represent the basis of modern manufacturing due to the electrical and thermal properties and the high-efficiency performances [92,93].

Nowadays, fabrication processes strongly rely on a *top-down* approaches [29,33,42,94,95]. Nevertheless, the unmet need for continuously smaller devices has been shifting towards miniaturised *bottom-up* techniques, despite the higher costs and the need for highly specialised operators [96]. Therefore, the science and technology have constantly been developing, introducing innovative pathways, with a particular focus on polymers and biological structures such as

DNA and viruses, which after being metallised, have been demonstrated as efficient electrical conductors [97]. On the other hand, these types of structures are also easily bound to the substrates, and with an accurate design of the samples surface, beautiful, intrictae and functional features can be reproduced. For instance, DNA origami has been used by a Caltech group for precisely positioning fluorescent nanoparticles within a grid of over 60,000 resonant photonic crystal cavities, thus forming a replica of Van Gogh's famous painting 'The Starry Night' (Fig. 1.6.) [98]. Therefore, nanophotonics represents the next step for potential applications of the novel, versatile and tunable structures being developed.
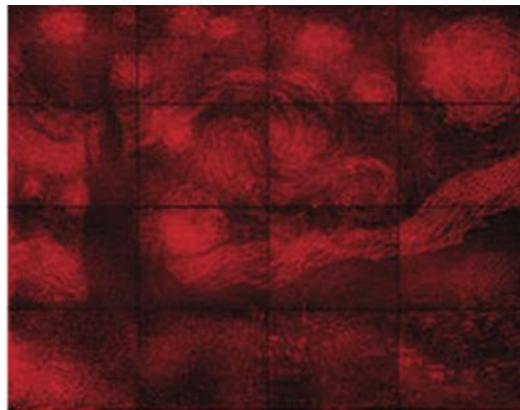
Figure 1.6. Starry Night reproduction from fluorescence nanocavities DNA origami.
Adapted and reproduced from [98]**.**

Additionally, nanofabrication has addressed the increasing demand for large-scale water-repellent surfaces, advancing the manufacturing processes with regard to superhydrophobic coatings. As described in Section 1.3, the manufacturing of such low surface energy areas is fundamental for novel technology, minimising the risks of short circuits and prolonging the devices' lifespan in case of unwanted contact with water.

Therefore, in this thesis, the issues related to 3D nano-manufacturing were identified, studied and further optimised to pursue two major applications described above. In parallel, although with different techniques, superhydrophobic and optically-active surfaces were manufactured with relatively inexpensive, eco-friendly materials and procedures.

1.6.   Aims and Objectives

Currently, the production of reproducible hierarchical surfaces with asperities spanning the micro-to-nanoscale involves, as introduced in this chapter, a conjunction of non-trivial procedures largely using unhealthy solvents and expensive technologies.

The environmental impact of this research had a fundamental importance in the materials and techniques selection, with the aspiration to establish further steps on the path of "green" surface technology for future everyday-applications.

In line with this eco-sustainable approach, the research described in this thesis aimed to explore and establish novel methodologies for producing a range of micro-to-nano morphologies for a broad range of applications particularly, focusing on superhydrophobic surfaces and photonic three-dimensional metal nanostructures.

The first part of this thesis is focused on the production of a vast range of superhydrophobic surfaces characterised by a range of hierarchical patterns using highly apolar materials and Electrohydrodynamic Lithography (EHL) [99–101] as the optimal, reasonable choice of technique for cost and simplicity. Since

the importance of anti-fouling and water repellent materials in the modern world, it is among the aims of this work to demonstrate the feasibility of EHL for superhydrophobic surface manufacturing.

The second section of this thesis focuses on developing an innovative approach for structuring 3D nanomaterials, targeting optical responses such as negative refractive index and plasmonic effects arising from the nano-structured material. Moreover, the work in this section aims to investigate the feasibility of optically-active materials production route involving sacrificial sub-50nm DNA-based templates for gold replication by plating techniques.

Below is an outline of the chapters and their contents.

The overall thesis is comprised of five chapters. Following the Introduction (**Chapter 1**), **Chapter 2** will provide a thorough overview of the state-of-the-art techniques for nanofabrication and related fabrication procedures, such as, for instance, the importance of substrates' cleaning, DNA self-assembly and the characterisation techniques utilised in this work.

Chapter 3 will provide a general overview of the experimental procedures used during the PhD. The description of the materials is followed by sample preparations, cleaning strategies, preliminary investigations and finally, the characterisation techniques. The corresponding theoretical background for the characterisation methods and procedures is outlined in **Chapter 2**.

Chapter 4 focuses on novel fabrication methods for tuneable superhydrophobic sub-micron architectures.

The main hypothesis (H_{1-EHD}) of this part of the work is that carbon nanotubes (CNTs), in the form of either forests or arrays, provide suitable and robust

electrodes for electrohydrodynamic (EHD) lithography for producing controllable and reproducible cone-like structures with asperities on the nanoscale, using superhydrophobic polymers as substrates. Water-repellent properties are to be tested from the produced patterned surfaces.

On the contrary, H_{0-EHD} states that CNTs as the top electrode in the EHD process do not enable an improved and well-controlled patterning of the polymers and particularly, sharp nano-cones, and introducing errors in the replication process.

This chapter provides additional theoretical background specific for the application targeted, experimental details and results of the fabrication of superhydrophobic thin polymer films, using vertically-aligned carbon nanotubes (VACNTs). This study demonstrates an unconventional route to manufacture nanohair-like surfaces as well as hierarchical cone-structure arrays with various curvatures, patterned from vertically aligned carbon nanotube-based master electrodes *via* advanced electrohydrodynamic lithography (CNT-EHL).

Prior to fabricating hierarchical nanohair-like structure and micron-sized conical pillar from plain polymer thin films, carbon nanotube forests are shown to be grown onto silicon substrates and etched into periodical arrays and then, used as a top electrode for the CNT-EHL fabrication. Morphological comparison of different stages of the pillars' growth is finally shown to relate to variations in the wetting properties.

Chapter 5 describes the background, synthetic strategies and experimental results for the fabrication of plasmonic band-gap (PBG) and metamaterials using the 3D DNA-templated gold nanomaterials.

The principal hypothesis ($H_{1\text{-OPT}}$) of this work is that self-assembled DNA polyhedrons, in the shape of cages, can be exploited as scaffolds for reproduction with inorganic materials which, in turn, can enable novel optical properties. $H_{0\text{-OPT}}$, on the contrary, affirms that either DNA polyhedrons are not suitable for inorganic replication, or that the patterned surfaces do not enable unique or unconventional optical properties.

This chapter comprises two distinctive parts: firstly, the exploitation of the novel 3D DNA designs and assembly and secondly, the replication of the novel nanostructures *via* gold electrodeposition. The work itself combines both the *top-down* and *bottom-up* approaches for optimising the consistency and repeatability of the fabricated nanostructured architectures. It is important to note, that unlike the 'traditional' biological role of the DNA as a carrier of genetic information, the molecules were considered as building blocks exploiting a more physical-chemical approach, fundamental in self-assembly methodologies.

The introduction part of chapter 5 provides background on the self-assembly and synthesis of 3D DNA nanostructures and emphasises their tunability into complex and more extensive architectures. This is followed by the description of the experimental details for identifying and establishing the assembly parameters such as concentration, annealing temperatures, salt strength strand length and the required solvents. Additional experimental procedures for the immobilisation of the 3D structures on the substrates and their replication by the homogenous deposition of noble metals around the hollow 3D DNA framework are followed by the description and discussion of the experimental results particularly, focusing

on the characterisation techniques for the sub-micron morphologies and the accomplished photonic properties.

Finally, this thesis concludes in **Chapter 6**, where the overview of the research and the results are summarised, and the hypothesis presented are discussed. Potential applications and future project directions are introduced, with an outlook towards alternative, complementary nanofabrication pathways and potential directions of nanoscale patterning exploiting the novel and unique approaches developed during this work.

2 From Conventional Fabrication Techniques towards Novel *Bottom-Up* Functional Nanoarchitectures

2.1.   Nanofabrication Techniques

Micro-to-nano scale manufacturing techniques utilise both *bottom-up* and *top-down* approaches depending on the final device assembly and functions required, while the ultimate shapes and overall morphological characteristics are usually pre-designed.

The *top-down* approach in nanofabrication widely utilises tools controlled by sets of experimental parameters, determined by the operator, for producing nano-scaled, functionalised materials starting from large dimension surfaces, to reduce them to the desired shapes and dimensions [30].

Alternatively, *bottom-up* approaches aim to build-up complex architectures from molecular, sometimes even atomic constituents, after careful calculation of the self-assembly mechanisms, based on intricate materials and techniques [1].

Representative *bottom-up* and *top-down* techniques used in both laboratory and on a larger, commercial scale are overviewed below.

2.1.1. Top-Down Techniques

2.1.1.1. Templating and Casting

Template-aided techniques involve the replication of an initial template, shaped according to the final features required. Used mainly for water-repellent surfaces, scaling-up and manufacturing, templating is a cost-effective and highly-reproducible method which allows replicating the minute details of plants and other natural features with a facile and quick procedure. The replicas are usually comprised of a polymeric cast-on material, which has native superhydrophobic properties. Therefore, the resulting bio-mimicked structures result in highly hydrophobic surfaces with asperities on the mesoscale.

For instance, a lotus-leaf is a common example of the often being replicated in poly(dimethylsiloxane) (PDMS) *via* polymer casting and using a nickel mould [102] as shown in Fig 2.1.a, as well as in poly(methyl methacrylate) (PMMA) [103] from spin-coated films using PDMS moulds (Fig 2.1.b).
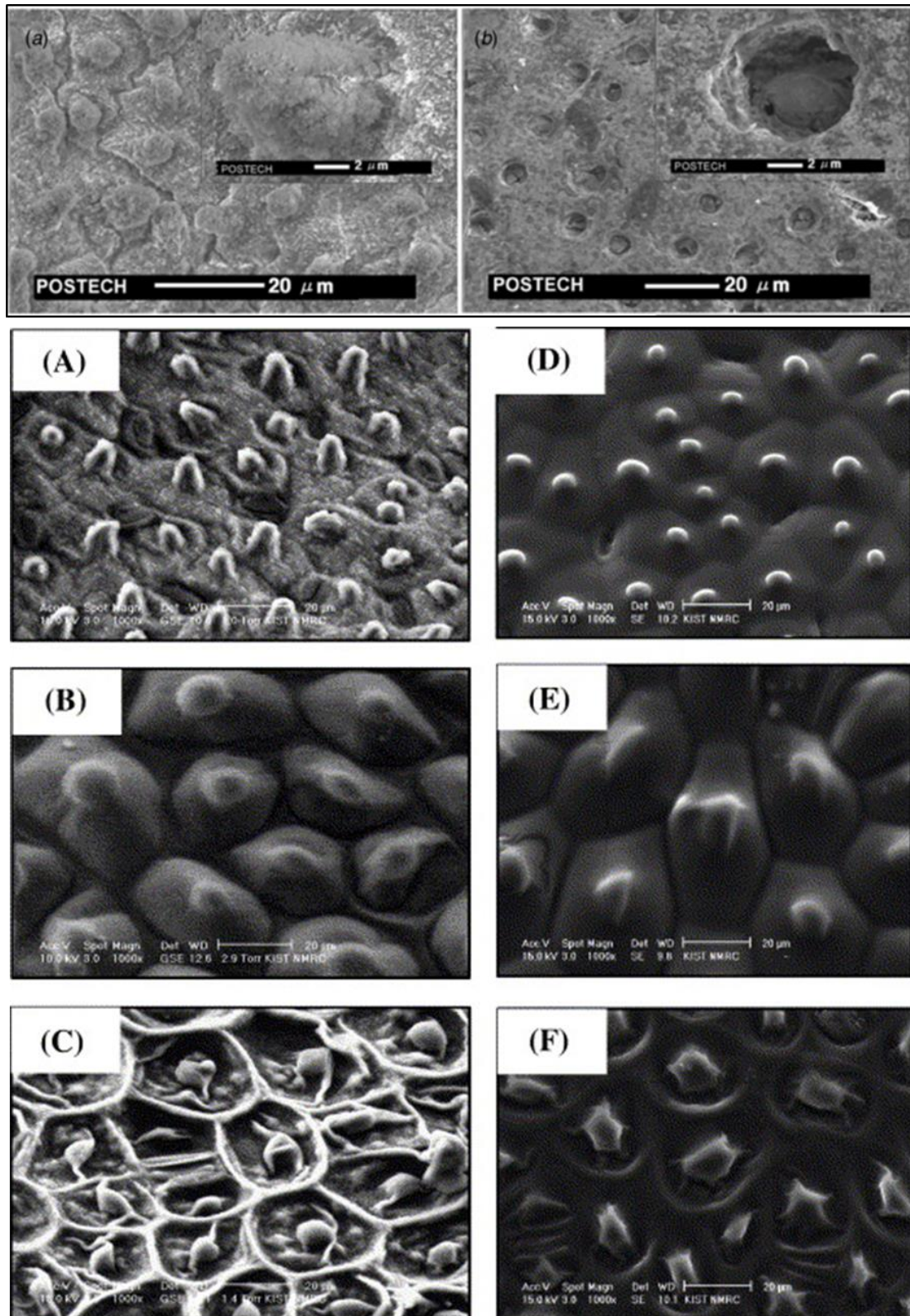
Figure 2.1. Templating techniques. Top) SEM images of (a) Lotus leaf. (b) Nickel-mould replica of (a). **Bottom)** SEM images of: (A) Lotus leaf (fresh), (B) Colocasia leaf (fresh) and (C) Colocasia leaf (dry), (D) Lotus-leaf replica (fresh), (E) Colocasia- leaf replica (fresh) and (F) Colocasia-leaf replica (dry) surfaces. Replicated from [99].

Lithography is a general, well-established method for producing superhydrophobic surfaces with improved control and accuracy to generate the micro-to-nano surface topography. In general terms, lithography based on the interaction between a beam and a mask to transfer a predesigned pattern onto a light-sensitive material, the *resist* [93].

Historically, **photolithography** [30,105,106] represents one of the first methods for fabricating microelectronics components and, nowadays, is still one of the most commonly used technologies due to its resolution and efficiency. In the photolithographic approach, the beam emitter is a light source, commonly a mercury lamp or UV laser emitting ultra violet light, hitting a mask coupled with an optical assembly to reduce the image onto the *photoresist*, an optically-sensitive chemical layer. The interaction of the guided light onto the photoresist allows the replication of a specific pattern onto the resist enabling a resolution well below 50 nm. Considerable studies have allowed the resolution limit, given by the Rayleigh equation (Eq. 2.1), to be further improved.

Equation 2.1. Rayleigh equation.

$$r \approx \frac{0.61\,\lambda}{N_A}$$

Where, *r* indicates the resolution, λ the incident wavelength, and N_A the numerical aperture.

As a general trend in modern commercial manufacturing and research, decreasing the incident wavelength while increasing the numerical aperture (N_A) was demonstrated as an effective solution to increase the resolution. Although, the typical limit of visible light diffraction pointed out the need for alternative light

sources, in particular focusing on excimer laser nowadays, manufacturers commonly use a 193 nm wavelength beam [105].

Further it is important to mention the "immersion lithography" [107] as an efficient method for reaching a 37 nm resolution, by filling the volume between the lens and focal plane with a medium, usually water, characterised by a refractive index higher than air.

At the state-of-the-art, photolithography is considered as an established technique which enables the production of high-fidelity replicas with details at the micro-to-nanoscale, typically using silicon wafers as substrates. For instance, the hierarchical micro-and nanostructure of the mosquito eye [103,108,109] was replicated by this lithographic method, preserving the anti-fogging properties of the hexagonally packed structures at the mesoscale, as shown in Figure 2.2.
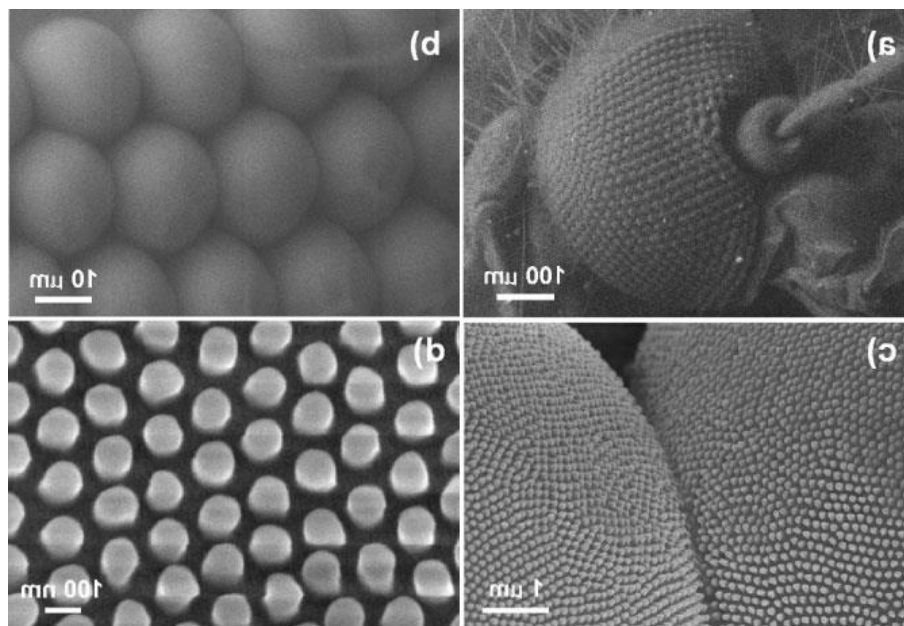
Figure 2.2. SEM images of the mosquito compound eyes at different magnification. Reproduced from [110].

Electron-beam lithography (EBL), developed in the late 60s, is also a well-established method for patterning in the sub-micron range. Electron beam lithography is an alternative approach that uses a scanning beam of electrons to write sub-micrometre structures into a resist that can subsequently be transferred to the substrate material, often by etching. The preparation of such patterns not only requires sequential writing steps, but is also vulnerable to beam drift or instability which may occur during the long exposure times. During the 70s, similar to the photolithography, EBL's higher resolution did not make up for the amount of time required for producing the final pattern and the cost of the manufacturing line and thus, limiting the EBL's commercial spread to niche uses. Nowadays however, EBL offers higher flexibility in dimensions and shapes [13,30,111] compared to "traditional" optical lithography, while maintaining the high precision requirements on the micron-to-nano scale. Moreover, it allows complex patterns to be printed directly on wafers, and to eliminate diffraction interference, typical of optical lithography, reaching below 50 nm in resolution. Although a high-resolution technique, EBL is not fast, poses various problems such as for instance, scattering, backscattering and secondary electrons emissions, which ultimately affect the quality of the final object [13,30,111,112]. Generally, EBL is comprised of a beam emitter which can be, alternatively, a thermionic, a photo or a field emitter, which produces the electron-beam focused by deflection coils and lenses onto the substrate, held under vacuum conditions for minimising the interferences in the electron beam.

Alternatively, **colloidal lithography** [105,113,114] is an additional patterning technique which uses colloidal particles assembled in a monolayer to

systematically replicate large areas. The high level of control can be achieved by accurate settings of the particle dimensions and spacings involved. For instance, polystyrene (PS) standardised nanoparticles carrying a negative charge, were electrostatically deposited into random arrays onto positively charged surfaces such as, *p*-doped silicon. Coupled with other types of lithography or etching, this technique enables good-resolution and fast patterning. Optical characterisation of these colloidal lithography fabricated substrates has shown the loss of reflectance properties especially, in the near-infrared (NIR) range of the manufactured surfaces [115,116] thus, paving the way for both antireflective and antifogging coatings, as shown in Figure 2.3. This technique is also known as Nanosphere Photolithography (NSP).
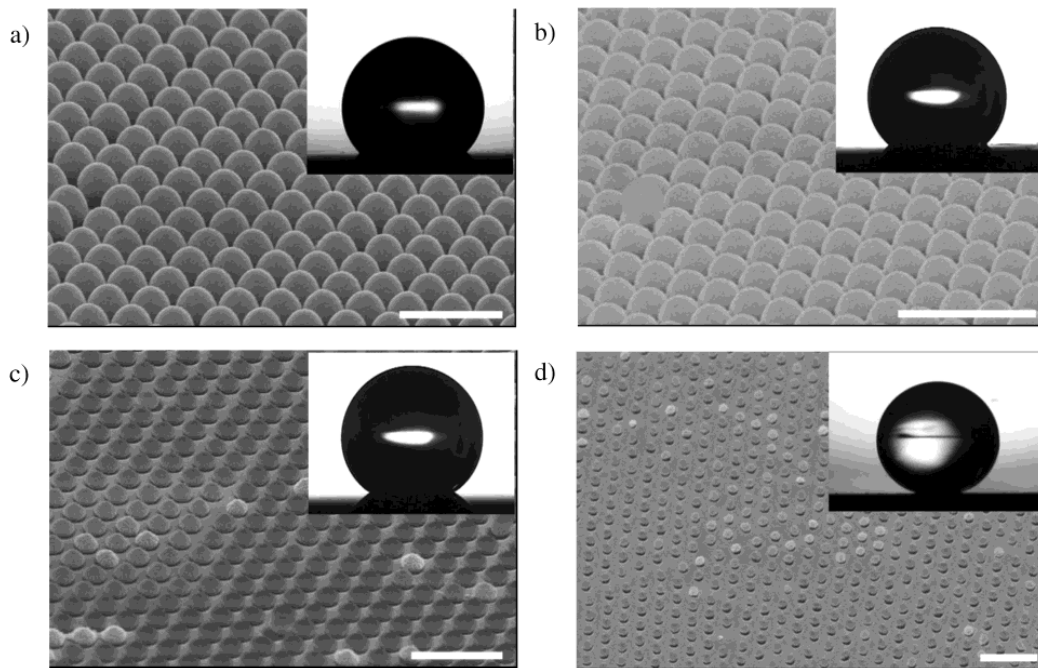
Figure 2.3. Nanosphere lithography. A range of packed nanosphere lithography-produced surfaces and their corresponding relative wetting properties. Reproduced from [117].

2.1.1.2. Plasma and Reactive Ion Etching

Etching represents a valid alternative for reaching the minute dimensions and highly ordered structures typical of highly hydrophobic surfaces, using polymeric substrates to be patterned.

The conventional **plasma** process (see section 2.3.3) also known as **reactive ion etching** (RIE) [118] uses gases such as CF_4, C_4H_8, SF_6, Ar, and O_2 [119] to functionalise the surface depending on the exposition modes and time. Whether combined with lithography or templating techniques, plasma etching enables large textured areas with high fidelity and reproducibility.

Plasma etching requires a vacuum chamber filled with the relevant gases, to be excited by a radiofrequency field. The co-presence of an excited and ionised species produces highly accelerated, directional molecules and ions, impacting the target surface. Thus, plasma etching, due to the combination of both chemical and physical effects, yields important advantages for the nanofabrication. RIE and plasma etching have successfully addressed the requirements of control and reproducibility, crucial for development of optically-active and electronic components, further improving the fabrication outputs in comparison to the other available etching techniques.

2.1.2. Bottom-Up Techniques

2.1.2.1. Molecular Self-Assembly

Molecular self-assembly is an important branch of science, known as supramolecular chemistry. This technique deals with all the weak forces and non-

covalent bonds such as, van der Waals, hydrogen bonds and dipole interactions, which have almost no impact on an individual level however, once combined, they result in a strong interaction driving a large number of natural process.
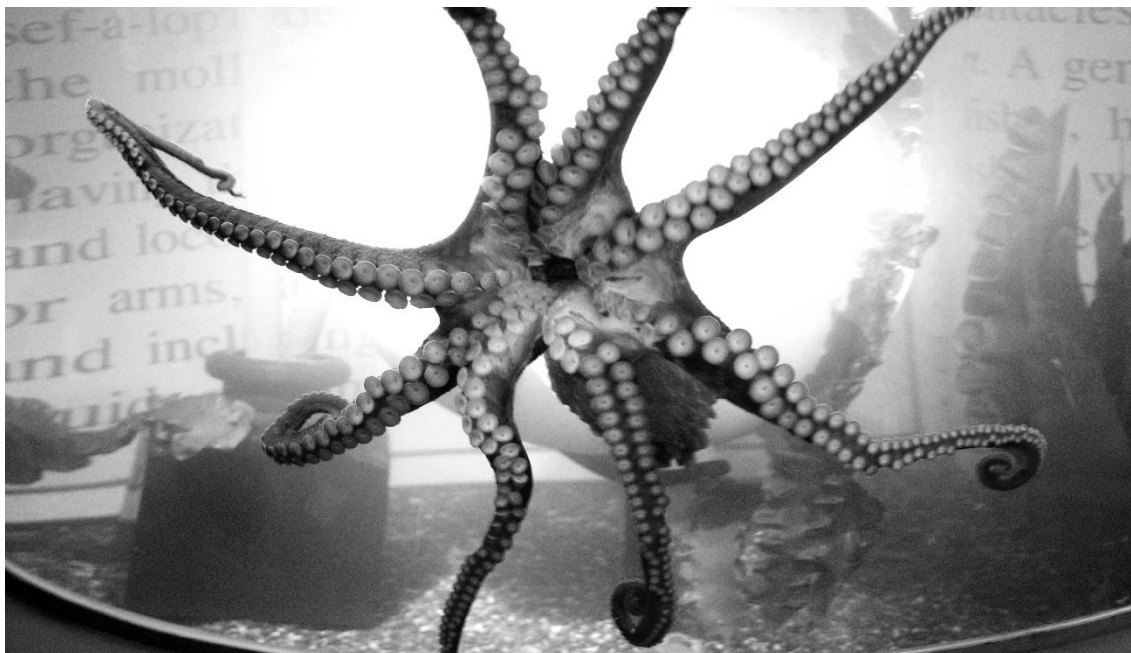
Figure 2.4. Supramolecular forces. The Octopus tentacles are comprised of a large amount of suckers, which, individually, cannot apply a large force when sticking to a surface. On the contrary, when a whole tentacle and all the suckers are attached, the resulting force makes it almost impossible to detach the animal. Similarity weak forces, when taken individually, can reach a maximum of 1/10 of the strength of a covalent bond, while, when combined together, are extremely strong.

In addition to the well-established importance of the coordination and hydrogen bond for living beings recently, after more than two decades of research, the role of supramolecular forces was demonstrated as a pivotal point in nanofabrication, including the π-π stacking, hydrophobic, colloidal, magnetic, electrical and optical forces [120–124].

2.1.2.2. *Electrochemical and Electroless Deposition*

Electrochemical deposition (or electrodeposition) of precious metals has a fundamental role in modern technology, especially for the production of thin microelectronic coatings and catalytic surfaces [125,126]. The basic processes were developed in the 19th century, and during the past three decades, the mechanisms have been widely exploited given the range of industrial uses and superior performance.

Nowadays, electrodeposition is considered as a cost-effective and efficient technique to produce uniform thin films by applying a constant voltage for specific amounts of time, usually stable for small variations at room temperature and pressure. The operating conditions allow the strict control of the amount of charge within the cell and consequently, the amount of deposited material, upon full understanding of the chemical reactions involved at each stage of the plating process. Defects and composition of the film can be monitored over time by accumulations, observing the correlation between the potential applied and the current passing in the system. This sort of experimental technique is known as *cyclic voltammetry* (CV), while the *chronoamperometry*, as the name implies, allows the monitoring of the current at a fixed potential by the time passing.

The majority of the industrial processes for noble metals, such as gold and silver, involve cyanide (CN^-) baths, which are usually comprised of stable components at various acidic pH values. Thus, three bath categories can be outlined depending upon the acidity of the solutions [126]. The stability of the cyanide bath is given by the equilibrium constant (pK_a) for HCN from aqueous to gas form,

28

which for pH > 8 (mildly basic conditions) shifts the equilibrium (Eq. 2.2) to the right of the reaction, leaving free and stable cyanide in the bath.

Equation 2.2. Cyanide disproportion reaction.

$$HCN_{(g)} \longrightarrow H^+ + CN^-$$
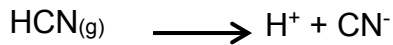
Gaseous cyanide is developed from the solution at a pH < 8 or at a temperature above 26°C. Thus, health concerns arise regarding the use of these facilities as $HCN_{(g)}$ is highly toxic and requires a dedicated ventilation system.

Alternatively, various baths were developed in particular, using gold sulphite and thiosulphate to reduce the risks for the operator, however, these types of baths do require highly controlled experimental conditions especially, in terms of temperature and pH. Whenever substantial deviations from the outlined standard conditions occur, by-product formation can be observed, mostly as a disproportion product of the gold from Au(I) to metallic gold and Au(III) as gold sulphite is unstable at a pH < 7. Thus, modern baths include additional stabilising agents for limiting such by-reactions which, at the occurrence, will inhibit the full plating potential of the baths. Nowadays, sulphite baths are preferable to the cyanide ones especially, in micro and optoelectronics applications, due to their low toxicity and better performance in the final deposition steps producing smoother and brighter films [127].

Moreover, electrodeposition media are usually comprised of water-based electrolytes and solutions, allowing coating on biomaterials such as proteins, viruses and DNA.

Electroless deposition is a well-known procedure since the beginning of 1800's, though the term "electroless" was introduced for the first time by Brenner and Riddle in 1946 for identifying the autocatalytic process of nickel and cobalt plating and later, commercialised in 1970 by Bell Laboratories [128–131].

Electroless deposition can be defined as a spontaneous chemical reaction which requires no external power [131] and therefore, insulating substrates can be easily plated. In the last few decades, electroless deposition has acquired a more prominent role, especially in the electrical and high-density semiconductor industry continuously requiring smoother and more homogeneous coatings.

The chemical reactions occur at the electrodes and described by Eq.2.3.

Equation 2.3. Electroless deposition complete reaction.

$$M^{z+}_{solution} + Red_{solution} \xrightarrow[\text{surface}]{\text{Catalytic}} M_{lattice} + Ox_{solution}$$
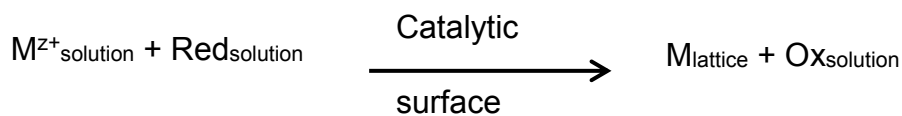
Where, *M* is the metal to be deposited, *Red,* is the reducing agent and *Ox* is the oxidation product.

Each species is characterised by a specific reduction potential. Hence, in order to have all the reactions occurring at the same time at the two electrodes, it is

necessary that the potential for the cathodic partial reaction (Eq. 2.4) to be more positive than the partial anodic reaction (Eq. 2.5).

Equation 2.4. Electroless deposition cathodic partial reaction.

$$M^{z+}_{solution} + ze^- \xrightarrow{\text{Catalytic surface}} M_{lattice}$$
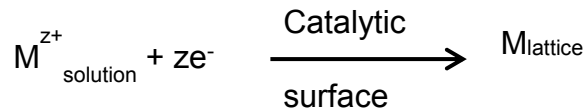
Equation 2.5. Electroless deposition anodic partial reaction.

$$Red_{solution} \xrightarrow{\text{Catalytic surface}} Ox_{solution} + me^-$$
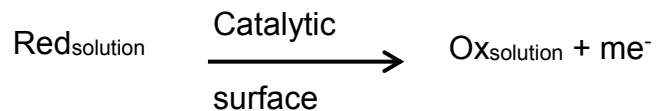
Electroless deposition is considered as performing well-functioning technique for coating non-conductive or insulating substrates thus, enabling a whole new range of otherwise unachievable substrates, such as insulating polymers or poorly conducting biomaterials.

2.1.2.3. *Chemical Vapor and Atomic Layer Deposition*

Chemical vapour deposition (CVD) is a well-established deposition technique [132,133] which utilises chemical precursors in a vapour phase, mixing them in a reaction chamber where they deposit a layer on a substrate. The prior modelling of the systems allows to predict possible by-products, reaction mechanisms and the structure of the thin layer, which combined with the high control over the

process parameters [133,134] including pressure, temperature, gas-flow and chemistry of the precursors, enable the deposition of the expected thin films.

Noteworthy, CVD is also one of the main techniques used for carbon nanotube (CNT) fabrication (see Chapter 3.3), which can be used in combination with lithography to orderly pattern substrates into arrays and grids.

Furthermore, **atomic layer deposition** (ALD) [133,135] enables epitaxial layer growth through chemisorption of one of the precursors onto the substrate. Once the first layer is saturated and excess is removed, the second precursor is introduced, following the same procedure as the first one. Therefore, the sequence can be repeated as needed until the desired thickness is reached.

2.1.2.4. Electrohydrodynamic Lithography

Electrohydrodynamics, a field investigating the deformation of a liquid phase upon application of an electric field, was firstly demonstrated in 1800, and since then it has vastly developed in the last decade [136], into a cost-effective, versatile, yet robust, technique for patterning of thin films on the micro-to-nanoscale.

Electrohydrodynamic lithography (EHD) represents a viable technique for patterning thin (< 200 nm) films comprised of a wide range of polymers while liquefied above their glass transition point (T_g) yet, below their melting temperature, with no dimensional limitation in the final pattern set by the experimental setup and conditions. To note, in experiments described herein, polymers are in their *glassy state* at room temperature. At temperatures above their Tg the segments of the chains become free to move and polymers can be

described as incompressible viscous fluids. The motion of an incompressible Newtonian fluid with viscosity is subsequently, fully described by classical hydrodynamic theory for known external pressure and an average velocity thus, governing the underlying theoretical principle of the EHD patterning.

The importance of defect-free homogeneous films as protective layers or components is essential for a large number of technological applications especially, in microelectronics or as coatings. Liquid thin films may vary in composition, from water to oil and polymers [137] although, when subjected to various stresses such as thermal, electrical or mechanical, they show dynamic properties (such as wave propagation) which are entirely different from those of bulk or thick films. Liquid film surface and interfacial pressure (or tension) overcome the other' forces, when the length scales involved are below the capillary length. The **capillary length** is defined as specific length scale at the interface of two fluids, both experiencing gravitational acceleration (g) and surface tension (γ). The capillary length is given as, $r_c = \sqrt{\gamma}/_{\rho_f g}$ where, ρ_f is the density of the fluid.

Therefore, when using a liquid thin film, different behaviour and properties than the bulk will likely be observed. In particular, within the capillary regime, the surface free energy acts as a dominant force over the thin film's intrinsic forces, while pressure acts as a destabilising force over the intrinsic stability of the liquid films.

The destabilization forces, coupled to the spectrum of capillary waves of a fluid (defined as the waves induced by the Brownian motion, which travel along the interface in a fluid and whose properties are defined by the surface tension) enable a single-capillary mode characterised by a specific wavelength, which experimentally, translates in a well-defined oscillating mode of the fluid surfaces. In turn, such instabilities can be affected by external factors such as gravity, temperature, or electromagnetic fields.

Thus, with accurate adjustment of the external factors, the liquid film instabilities can be forced to build-up into specific, well-defined structures at the micro-to-nanoscale by using a homogeneous thin (< 200 nm) polymer layer as a starting substrate.

A basic EHD experiment is usually comprised of different stages to achieve the desired architecture. As a first step, a homogeneous thin polymer layer with thickness h_0 is spin-coated onto a silicon substrate. This assembly is then connected by a conductive paste to an electrical conductor, which both impedes macro-movement of the substrate and allows the generation of high-electric fields in such a capacitor-like device. On top, another electrode, in this case comprised a Si wafer, is placed at a specific distance determined by the spacer dimensions. To enhance the electric field, the backside of the top electrode can be gold coated, and to enhance the hydrophilicity of the top electrode, facing the liquefied film, plasma cleaning can be used.

Once the assembled system is in place, a voltage (V) is applied, together with a temperature gradient across the micro-capacitor until reaching well above the glass transition point (T_g) of the polymer.

Since the z-scale of the liquid film is considerably smaller than the xy-dimensions, the temperature fluctuations primary affect the lateral capillary waves along the lateral direction forming a capillary wave spectrum at the liquid film surface.

The liquid film can be considered an incompressible Newtonian fluid in the zero-frequency limit, which translates into a range of properties, *i.e.,* the shear force per unit area is proportional to the local velocity gradient; the proportionality constant is the viscosity. Therefore, its motion is described by the classical hydrodynamics laws which take into account the external pressure and an average velocity.

The liquid material transport mechanism through the interface, including the velocity profile, is described by the Navier-Stokes (NS) equation (Eq. 2.6). The NS equation is comprised of two parts, each describing the two significant contributions to the fluid thermodynamics and kinetics where, u*, v, and w* represent of the velocity components.

Equation 2.6. Navier-Stokes equation.

$$\rho\left(\frac{\partial v}{\partial t}\right) + \rho\left[u\left(\frac{\partial v}{\partial x}\right) + v\left(\frac{\partial v}{\partial y}\right) + w\left(\frac{\partial v}{\partial z}\right)\right] = -\frac{\partial \rho}{\partial x} + \eta\left(\frac{\partial^2 v}{\partial x^2} + \frac{\partial^2 v}{\partial y^2} + \frac{\partial^2 v}{\partial z^2}\right) + \rho g$$

The first term represents the product of the fluid acceleration and the convective gradient, while the second term describes the force balance acting on the fluid itself.

NS equation for thin films can be simplified by making a few assumptions, as following:

   i.   The high viscosity polymers have a low flow velocity. Therefore, the quadratic terms tend to 0 and can be neglected.

  ii.   The dynamics of the system is slow. Thus, the velocity profile is assumed as a (*quasi*) steady-state.

 iii.   Since the film thickness is smaller than the capillary constant, gravity does not influence the interfacial shape.

 iv.   The film flow is approximated to a steady laminar flow with the velocity gradient varying only along the z-direction.

Therefore, for calculating the main wavelength of the capillary spectrum, the equation is calculated for simply one- coordinate, while neglecting all the wavelengths with amplitude smaller than the fluid thickness.

The pressure is known as a constant parameter thus, the pressure gradient is null, and the velocity assumes a parabolic profile which can be calculated from known values of both solid-liquid and liquid-vapour stress.

The system is assumed to behave within the lubrication approximation [138], where $v_{(z=0)} = 0$ and therefore, for $z = 0$ (which represents the liquid-vapour interface) the surface forces counterbalance the liquid intrinsic stress.

Since it is assumed that no stress arises from the vapour phase, the sum of both the elements *i.e.,* the viscous and the surface stress are set to zero. As a result, the surface stress is null.

Assuming that the slip component is zero and no lateral stress is present at the liquid surface, the mean velocity in the film is expressed by Eq. 2.7, where, h is the initial film thickness and η is the viscosity), which describes a Poiseuille flow for a liquid gradient. In a 1D case, the pressure gradient along the film drives the lateral volume flow rate.

Equation 2.7. Mean velocity within the film.

$$\vec{v} = \frac{1}{h} \int_0^h v(z) \mathrm{d}z = \frac{h^2}{3\eta} \left(-\frac{\partial p}{\partial x} \right)$$

The interface profile is derived from the mass conservation of a small volume in an incompressible fluid. In turn, the difference in volume observed for the element passing through distinct points within the fluid is calculated as, $\frac{\partial volume}{\partial t} = \frac{\partial A}{\partial x} dx$, where A is a cross-section of the film. For the 1D case, A equals h, any changes in height lead to redistribution of the fluid in a flow along the *x*-direction.

At the same time, the interfacial pressure within two phases determines the dynamic phenomena at the interface itself. Although the interfacial pressure is assumed uniform across the film thickness, the pressure does depend on the latter parameter. Consequently, the contributions to the overall pressure are given in Eq. 2.8.

Equation 2.8. Overall pressure contributions across film thickness.

$$p(h) = p_0 + p_{vdW}(h) + p_L(h) + p_{ex}(h)$$

In Eq. 2.8, the ambient air pressure (p_0) is independent of the film thickness and when it is smaller than the capillary length, p_{vdW}, it represents the van der Waals forces acting at a molecular level within the film with p_L is the Laplace pressure, arising from the interface curvature. Additionally, p_{ex} accounts for all the excess surface pressure and in particular, for the electrostatic pressure (p_{el}) arising from an external electric field applied to the system during the EHD patterning process.

In a liquid film at a constant temperature, when a sufficiently strong electric field is applied, the electrostatic interactions overcome the vdW contributions. In this case, the pressure distribution is given by (Eq. 2.9), where p_{vdW} term is neglected.

Equation 2.9. Overall pressure contribution in a liquid film for T=const.

$$p(h) = p_0 + p_L(h) + p_{el}(h)$$

For a perfect dielectric, when the liquid film in a capacitor is subjected to an external potential difference between two electrodes, not in contact, a strong electric field, E_f, is generated. E_f produces a charge displacement at the dielectric interface, which results in an effective surface charge density. Moreover, E_f induces the parallel alignment of the interfaces to the electric field lines, while the free electrostatic energy is minimised. Thus, the two main forces, *i.e.*, the destabilising electrostatic pressure at the liquid-vapour interface and the stabilising surface tensions, determine the stability of the liquid film and the EHD patterning development.
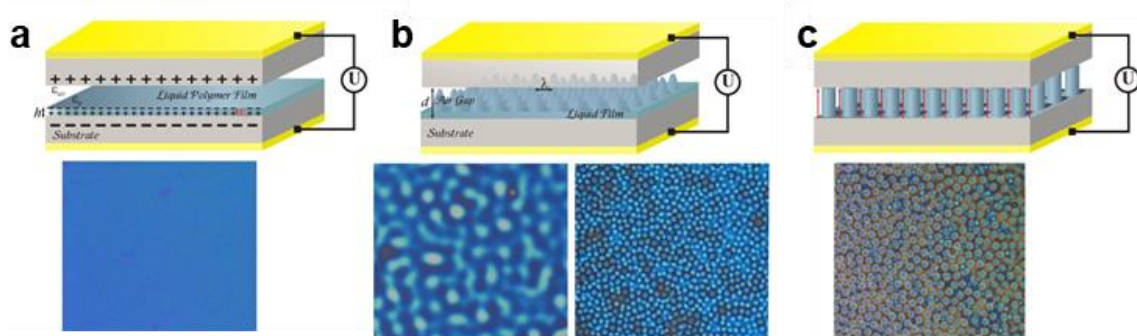
Figure 2.5. Experimental setup of EHD capacitor-like system. a). An electric field is applied to a homogeneous thin polymer film ($h \approx 100$ nm) deposited on the bottom electrode of the capacitor-like device, increasing T>T$_g$. **b)** These produce an amplification of the surface undulation at the characteristic wavelength which, eventually, leads to **c)** hexagonally-packed pillars. Adopted from [139].

2.2.   Polymers

Polymers are widely-known macromolecules comprised of many structural units, i.e., *monomers*, ordered and repeated in a specific fashion. Polymers are usually characterised by high molecular mass, which further defines their physical properties such as viscosity, thermal and electrical conductivity and the crystalline form. Since polymers can be either natural or lab-synthesised, they can have various forms, and their intrinsic organisation may lead to either branched or linear structures, determining other properties such as melting and glass transition points, solubility and density. Additionally, the presence of defects could also affect these properties.

Polymer nanofabrication is used in many different fields for producing highly sensitive, accurate devices. For instance, polymers are commonly constituting

drug delivery systems [140], micro- and nanosensors [141], and in basic research for polymeric matrixes [142].

2.2.1. From Block Copolymers to a DNA Scaffold: an Alternative Fabrication Technique for Metamaterials

Block-copolymers (BCPs) are a class of polymers comprised of two or more homounits, arranged in a specific fashion along the chain, and depending on the number of homopolymers, two- and tri-block copolymers can be produced [143,144]. Such units are naturally prone to self-assemble in periodically-ordered nanostructures which can be tuned in position and dimension, depending on the relative molecular weight and number of units. Hence, such an arrangement can be tailored to specific domains or features, which serve as building blocks for nanoengineered bulk materials or surfaces. BCPs have attracted interest from those research fields that require highly ordered features or the coexistence of two (or more) domains simultaneously, with applications predominantly for solar cell devices, thermoplastic elastomers or fabrics [145–147]. In the last decade, research has mostly focused on BCPs as nanocomposites, substrates for lithography and also, as templates for metamaterials [47,148,149]. Since the arrangement of the spacing and the domains can be tuned by tailoring properties such as the molecular weight of each subunit or by varying the filling ratio of the metal, complex structures like *gyroid* can be produced [144]. For these particular structures, BCPs' chain parts are the building units for the larger 3D structures. The deposition of a thin layer or a bulk material around the templates enables the

production of features with nano-scaled roughness and cavities, which can also be comprised of the template itself [143,144]. Furthermore, the scaffolds can be described as a *sacrificial template* [81,150,151] either when the composing material is removed within the steps toward the production of the final structures or when it acts as a precursor for the designed architectures. These kind of templates are not limited by the possible shape and dimensions that can be achieved since their fabrication is carried out with independent and well-established synthetic strategies usually, falling within the range of elementary *click-chemistry* or self-assembly procedures [33,148,152,153]. Nowadays, micro-to-nano materials either biological or inorganic, are commonly used as sacrificial scaffolds for metamaterials nanofabrication [150,154] mostly, due to being cost-effective. Therefore, DNA represents a potential candidate for templating materials towards the aim of achieving novel nano-scaled 3D features. The versatility and tunability of the DNA molecules, allows the design of miniature yet, accurate *moulds* for engineering the nanoworld [155–157].

2.2.2. "The Road so Far": DNA Origami Building Blocks

The DNA molecule, since being first identified in 1953, has gained a prestigious role spanning various fields from chemistry to nanotechnology. Nowadays, DNA is widely acknowledged as one of the most powerful tools in modern nanoscience [158–161], largely because: i) it possesses the ability to complementarily interact between strands without almost any mismatching [162], ii) is versatile and can

arrange in 2 and 3-dimensions [163,164] and, iii) has the ability to form intricate patterns when binding with other molecules [165–169].

A wide range of applications, spanning from targeted drug delivery [170–172] to nanocircuits manufacturing [165,173] are in fact achieved by using the DNA as a blueprint for structures with various functionalities. DNA molecules, for instance, can be arranged to obtain contiguous wires which, after metallisation, act as a nanoscale electrical networks [112,169,174,175]. On the other hand, it is possible to use the self-assembled 3D DNA structures or *origami,* as docking sites or as a "breadboard" for favouring other chemical species reactions (Fig 2.6) [31,176–178].
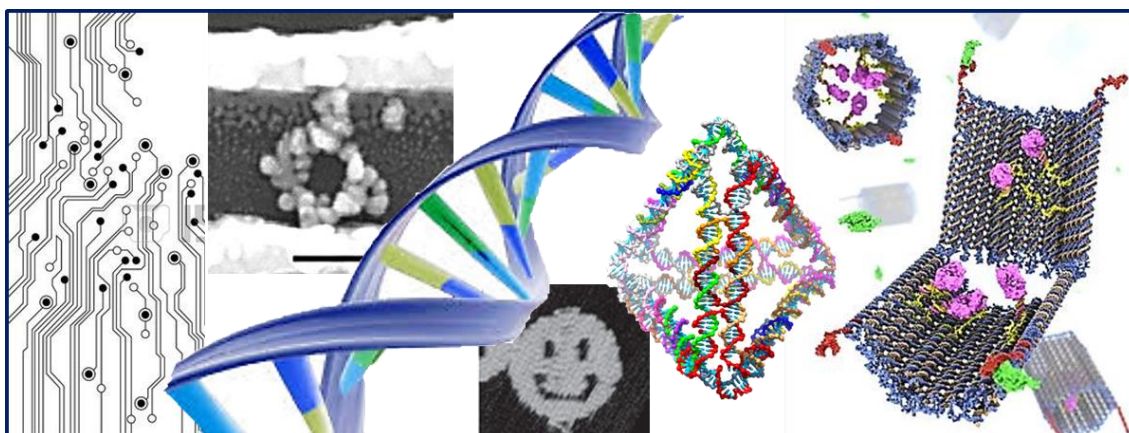
Figure 2.6. DNA nanoengineering. DNA engineering enabled the fabrication of robust, yet versatile structures such as DNA origami, cages, and arrays. The direct assembly of the structures eliminates purification steps in the synthesis hence, achieving high-yield and pure products. The DNA molecules can be arranged as arrays which, after metallisation, work as nanowires and nanocircuits [179,180]; barrel-like structures allow drugs to be linked and protected by external enzymes [170], ensuring a targeted *in situ* release. Additional use of DNA origami includes scaffolding and the formation of docking point in otherwise inaccessible surfaces.

The DNA's properties are derived from its structure [177,178], which is comprised of a phosphate-deoxyribose backbone that attaches to four nucleotides (or bases): adenine (A), guanine (G), cytosine (C) and thymine (T). In turn, these

bases exclusively interact in pairs of A-T and C-G. The specificity of the interactions between the DNA bases has led to the design of scaffolds [176,181,182] and structures with pre-determined geometry and length, which allowed accurate nanoscale features. DNA usually arranges as a double helix formed by two complementary and antiparallel strands (double-stranded DNA) [183] though, it can be reduced to single strands (ssDNA) [183,184] *via* melting at high temperature with low salt concentration buffer [155,185–188].

DNA engineering started to attract interest in 1970, when for the first time two sequences were attached by their interacting "sticky ends" [34], which are short single-strand nucleotides, protruding from the main, double-stranded DNA sequence. The real leap forward to the actual design of DNA "origami" was taken by Nadrian "Ned" Seeman who, inspired by Escher's woodcut "Depth", synthesised a cube-like structure in 1991 [189]. Seeman considered the DNA molecule from a new perspective and designed its structure within an organised 3D space thus, enabling a whole new range of versatile structure with potential applications spanning different fields such as bioscience, nanotechnology and medicine [169].

The production of DNA motifs by assembling pre-designed strands leads to branched structures which are not formed in nature and therefore, consisting of *synthetic 3D* features with intricate folding such as polyhedrons or DNA origami [165]. The potential of these motifs was finally exploited by Paul W.K. Rothemund in 2005, who developed a novel, non-expensive strategy for assembling DNA origami [163,164], which was comprised of a *2D* self-assembled DNA sequence, folded on itself and structurally "glued" together by complementary "staples". The

low-cost, resiliency and potential to tune the dimensions and geometric orientation of the DNA origami exploited DNA nanotechnology as an evolving field with numerous applications such as drug delivery, nanoelectronics, and photonics [178,181,190–192]. So far, DNA origami has mostly been developed in 2D although, specifically annealed structures such as DNA cages can achieve 3D orientation and result in intricate shapes and dimensions on the nanoscale - usually below 50 nm [171]. In particular, the real potential of DNA cages relies on their size and further functionalisation with chemical groups or metal nanoparticles (NPs), which can extend their uses for drug delivery systems, nano-circuits or molecular robots [166,193,194].

From the early 2000s, simple procedures for synthesising spatially-oriented polyhedrons were established, starting with Goodman and Tuberfield's work [195]. Further complexity was added by tuning the assembly with the introduction of intermediate products, which lead to the formation of various polyhedrons such as truncated octahedron, octahedron, dodecahedron and icosahedron [196,197].

The key role in the formation of such intricate assemblies is played by specific DNA structures, highly organised as a fork-motifs, which, in turn, arrange in such way to interact and attach to one another, forming a larger 3D assembly. The wide range of possible structures, coupled with their high resilience and stability at pH values far from neutrality, has further enabled the use of these structures as possible templates for manufacturing devices and surfaces at the nanoscale, using the so-called *bottom-up* approaches [34,157,186].

2.2.3. Design of 3D DNA Polyhedrons

DNA is a well-known store of genetic information [198,199]. However, its role as a scaffolding material for nano-engineering has only just started to be explored. Arrays of polyhedrons and origami have a pivotal role in modern nanotechnology mainly because of the high robustness and versatility enabled *via* their nucleotide sequence design. When tailoring complex molecules, it is fundamental to maximise the interaction of the desired sequences, while minimising the by-products from undesired interactions. The free energy of the molecular assembly (ΔG°) is the driving force in determining which kind of interaction will prevail. This, coupled with an accurate design of the sequences, eliminates identical parts within the sequence and increases the binding sites within the interacting domains [185,186]. The obtained patterns are stabilised by hydrogen bonds between the bases, thus, driving the self-assembly between complementary sequences. The achieved *inter*-strands arrangement is the result of using specific software for calculating the mentioned parameters, such as the minimum ΔG°, the nucleobases (nb) sequences and their interaction points. Goodman *et al.* highly recommend the use of NANEV [200,201], a Windows-based software for nanosystems design based on *sticky ends* sequences. The user is solely required to input the desired connectivity rules among the selected number of strands. The output is sequenced population, depending on the likelihood of energy minimisation, coupled with an accurate choice of nucleobases for avoiding repetitive parts. Alternatively, an independent platform called CaDNAno [168,186] has also been emerging as the standard software for specifically designing 3D DNA origami nanostructures. The software possesses user-friendly

2D and 3D interfaces which lead to fast-processed and customised DNA features, following similar rules to the NANEV interface. Supported by such tools, Goodman was able to design a DNA molecule connected as a tetrahedron [171] which has demonstrated versatile applications in nanoengineering and nanomedicine and has been exploited for instance, in protein encapsulation [193].

Goodman has further developed a synthetic fabrication strategy using four single-stranded DNA (ssDNA) sequences, which had the same sequence length and concentration. These were mixed and heated to their melting point, which is dependent on their length and constituent nucleotides, separating the double-stranded DNA into single-stranded sequences. The solution is then cooled down to a temperature which allows the single strands to complementary interact and form the final structures.

Analogous strategies usually outline the assembly of DNA molecules with the connectivity of polyhedrons, icosahedrons and prisms [157,171,177,186,193,195,202,203] although, a fundamental step is further introduced as a reaction intermediate. The initial single strands assemble to produce preliminary building blocks, defined as *tiles*, which arrange as three-point star motifs with unpaired single-stranded nucleotides at their ends also known as, *sticky ends* [165,169,171,196,204]. The concentration and flexibility of the tiles can be tuned accordingly to initial sequence concentration and length. Similarly, the final polyhedral structure, comprised of a different number of tiles interacting by their sticky ends, also depends on the concentration of the intermediates.

In 2004, Rothermund suggested a different approach to the DNA origami synthesis, proposing a controlled folding of a long single strand of circular genomic DNA from the virus M13mp18, which bends on itself while it is "glued" together by *staples* [164], short single-stranded DNA sequences (16 to 25 nucleobases).

This simplified origami production eliminates the majority of the synthesis problems especially in terms of final yield, which is >70%, with occurring misfolding almost entirely eliminated. The annealing reaction is a straightforward *one-pot reaction*, in which all the strands involved, in a solution are mixed together at once [205]. The symmetry of the assembled features depends on the stoichiometry of the mixed *staple* strands, and a variety of structures can be achieved when parts of the sequences are repeated.

Such DNA origami assembly technique requires five key steps starting from the design to the actual synthesis [163]:

i.   Design of a geometric model of the desired structure, filled by evenly organised parallel helixes. Each sequence is subsequently divided and idealised as cylinders of the same size. Each row of cylinders is held together by sequence crossing points, called crossover.

ii.   Folding of a long single-stranded sequence (> 900 nb, also called the scaffold) following the model. One strand of the helixes will be represented by the long strand, which will create additional crossovers.

iii. Tailoring the short strands, called "staples", as complementary sequences for the scaffold to be placed on the crossovers. Due to the double helix asymmetry and the presence of staples, the crossovers are not balanced.

iv. Minimising the strain that arises from the presence of the staples, which destabilise the overall structure. By doing so, the staples sequences are computed again and changed in places.

v. Increasing the interaction between staples and scaffold, by merging two staples together. In addition, to strengthen the structure at its weakest point of connection (the "seam" that separates the two branches of the scaffold), staples are bridged between the sides [163,164].

Experimentally, Rothermund used the DNA from M13mp18 bacteriophage as the skeleton of the origami structure, as a naturally single-stranded ~7,000 nb sequence, which nowadays is the standard scaffold in DNA origami synthesis.

Since 2006, when the first DNA origami was proposed, the arbitrary folding of DNA has been mastered and far more complicated 3D structures have been easily designed and produced [112,168,177,206,207]. The original procedure has been maintained, though an overall change in perspective has occurred in the design approach that focuses more on the final product stability than on the "building rules". In line with this experimental process, the production of larger and highly composed *superstructures* has been enabled. In fact, since the design of such assembly is particularly focused on the occurring intra-molecular interactions, which are defined by the position and interaction of nick points, crossovers and edge-to-edge stacking, multiple DNA origami can be arranged in large networks as scaffolds and other frameworks in a more flexible and controlled manner [206,208].

2.2.4. Deposition of DNA Polyhedrons at Allocated Sites

As previously described, plasmonic band-gap (PBG) and meta- (MM) materials consist of subunits characterised by the high level of periodicity in their mutual position, affecting the incident electromagnetic waves and thus, yielding unique optical properties, otherwise unachievable in nature [78,83,86]. However, in more recent studies it has been demonstrated that the ordered disposition of the subunits may not necessarily occur in every PBG and MM materials [40,63,64,77,209].

In these studies, the subunits are comprised of DNA polyhedrons which, require firm attachment to the chosen substrates, creating a suitable structure for further metallisation. Due to the large area that DNA origami can occupy on a 2D nanoscale surface, immobilisation of such structures has been solved by procedures that include metal coordination and physisorption on a wide range of conductive and insulating substrates.

Layer-by-layer deposition (LbL), based on alternate adsorption upon a surface of oppositely charged polyelectrolytes, is a well-established technique that allows both plasmidic and chromosomial DNA to be embedded in polycation layers due to its negative charge [187,210–214]. This property enables the fabrication of ordered multi-layered films which find their primary use in medical applications such as gene transfer, drug delivery systems and sensors [215–217].

Over the last few decades nanomaterials-based technology has been directed toward the generation of modified surfaces, tailored functional groups and effective detection devices that are all based on the direct adsorption of DNA

[218,219]. For instance, *Indium Tin Oxide* (ITO) film on glass has attracted a broad interest because of its high conductivity and transparency in the visible spectrum. Recent research [218,220] has recognised the ITO glass as a suitable substrate for DNA loading from aqueous solutions since the surface charge of SnO_2 and In_2O_3 nanoparticles is highly dependent on the pH of the solution. Moreover, the growing demand for faster, smaller and more sensitive DNA based chips for diagnostics has led to the development of cost-effective techniques for the modification of *silicon*-based substrates to achieve inexpensive binding surfaces. *Plasma* treatment [174] is of particular interest since it allows one to tune the binding sites for the DNA using different gases, while the chip itself can be easily washed-off the load and reused. Alternatively, irreversible binding systems to anchor origami rafts and pads [31,176,221] in ordered multiarrays were developed by combining well-established lithography techniques with chemical modification of the surfaces to improve the DNA-surface affinity. In particular, the introduction of a *self-assembled monolayer* (SAM) of (3-Aminopropyl) triethoxysilane, or APTES [155,176,221], in predesigned and lithographically accessible areas, allows the DNA nanostructures to dock exclusively at the binding site, without the risk of being washed off.

2.3. Overview and Background of Substrate Cleaning Methods

In a silicon-based technology world, wafer cleanliness and minimisation of residues have a vital importance [222] in the manufacturing processes for guaranteeing excellent quality of the final product. Since silicon is one of the most dominant components in majority of the modern technological devices, a broad range of well-established cleaning procedures is available, of which the most notable are described below.

2.3.1. RCA Wafer Cleaning

Developed in the mid-50s by Werner Kern while working at the Radio Corporation of America (RCA, therefore the denomination), this procedure involves numerous steps of a wet chemical substrate cleaning [222]. Generally, the wafer undergoes three stages for removing all the possible contaminants, including:

i.   Organic residues, *via* an aqueous solution of ammonium peroxide and hydrogen peroxide.

ii.   Oxidation layers, *via* treatment with hydrofluoric acid (HF).

iii. Ionic residues, *via* an aqueous solution of hydrochloric acid and hydrogen peroxide.

Alternatively, treatment with *piranha solution* - sulfuric acid (H_2SO_4) and hydrogen peroxide (H_2O_2), 3:1 - produces similar effects for organic residues, while at the

same time, introduces OH- groups on the silicon surface, increasing the wettability.

2.3.2. Snow-jet Cleaning

Snow jet cleaning is a well-established and straightforward technique developed for surface cleaning and systematically studied from the early 1990s by Hoenig and Whitlock, which produced the first data demonstrating the effectiveness of snow cleaning for micro-to-nano particle [223,224]. Snow-jet cleaning is mainly employed in automotive, optoelectronics, medical, basic and applied research. Snow-jet cleaning (Figure 2.7) is a process based on the transfer of the linear momentum and the properties as an organic solvent of dry ice and liquid CO_2. The direct high-velocity impact of the liquid and solid CO_2 stream with high momentum is able to remove sub-micron and micron-sized particles on the surface with the liquid CO_2 dissolving organic residues.
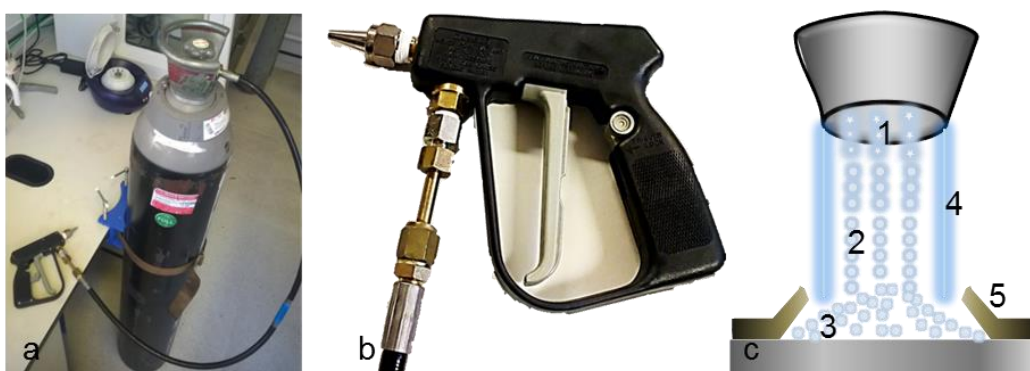
Figure 2.7. Snow-jet cleaning components and schematics. a-b) Snow-jet cleaning system, with a close-up to the gun. **c)** The action of the CO_2 stream begins at 1) the concentric nozzle, where the core jet, comprised of 2) snow CO_2 crystals, is ejected. While approaching the surface and losing velocity, 3) the CO_2 snowflakes start sublimating if the system is provided with an additional N_2 or air flow, the 4) compressed gas lifts the 5) organic residues, which are lately removed by the CO_2.

As the compressed fluid carbon dioxide is ejected from the nozzle, it expands to form a snow/ gas mixture, which forms the core jet flow. The combining thermal, mechanical and sublimation functions produce excellent cleaning results.

2.3.3. Plasma Cleaning

Plasma cleaning is a process to remove impurities from a surface through the use of plasma which can be produced by gases such as argon, oxygen and nitrogen.

Plasma is a partially ionised gas where electrons, ions and neutral species coexist together, without the release of thermal energy. The plasma is formed when a radio frequency oscillating electric field and the vacuum are generated in the chamber where the gas flows into. The combination of these factors allows the gas to gain kinetic energy, enough to start the ionisation of the gas, to break chemical species and create radicals, to excite atoms or molecules and also to transfer species kinetically from the treated surface.

The air plasma used in these experiments removes organic contaminants and cleans surfaces such as silicon wafers with micron-scale porosity. Plasma treatment enhances the hydrophilicity of the substrate surface, without affecting the bulk properties of the material. It promotes the substitution of the H- terminal groups with the OH- groups at the surface.

2.4.   Spin-Coated Polymer Films

Spin-coating is a process used to deposit a homogeneous thin, *i.e.,* sub-micrometric, polymer layer on a substrate. The process involves the deposition of a drop of the polymer solution onto the substrate and then the rotation at a specific speed that it is calculated as revolution per minute (RPM) and time (Fig. 2.8) [100].

The centrifugal forces spread the polymer solution across the substrate forming a homogeneous film. The higher the angular spinning speed, the thinner the film. The centrifugal force, the solvent evaporation rate, the initial solution concentration and the solution viscosity determine the thickness of the final homogeneous thin polymer film.
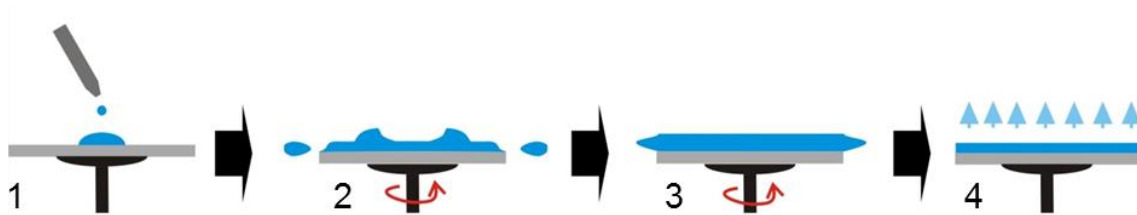
Figure 2.8. Spin-coating process schematics. The process can be summarised as follows: **1.** Deposition of polymer solution onto the substrate; **2.** Acceleration and spreading of the polymer; **3.** Constant rotational speed leading to homogenous spreading; **4.** Evaporation of the solvent.

2.5.   Characterisation Techniques

Characterising the morphology and the generated sub-micron structures is essential when specific properties are required from the materials of interest.

Various imaging techniques were used to observe patterns and colours of the samples, in particular, optical microscopy (OM). Further insights were provided by atomic force microscopy (AFM), scanning electron microscopy (SEM) and transmission electron microscopy (TEM) which yielded accurate information of the three-dimensional (3D) structures and properties of the materials on both the micro and the nanoscales (Fig. 2.9).
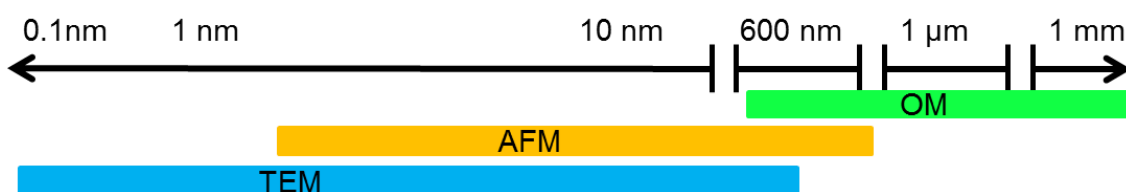
Figure 2.9. Comparison of the characterisation techniques and the imaging length scales that can be achieved with the various methods.

2.5.1. Optical Microscopy

Patterns and colours are dominant and visible, following the spin coating of the polymer films. Thin films, when deposited onto Si wafers, yield a wide range of colours depending on their thickness and their refractive index and these colour variations can be observed by optical microscopy (OM), providing preliminary information on the film thickness, enabling visualisation of the smallest differences down to the sub-100 nm scale and eventually capturing the micro and nano-patterns generated on or from the film. The thickness of the films could be indicatively and qualitatively determined by the observation of the *interference spectrum* [139]*,* where there is a direct correlation between the film thickness and its colour which arises from the interference of the two beams reflected from the polymer/air and polymer/ substrate interfaces. As the interference can be either constructive or destructive, depending on the coherence of the reflected beam

phases, which in turn depends on the distance between the two interfaces, even a slight change in the film thickness gives a drastic colour change. OM is a cost-effective and simple technique which allows observing the micro and nano (> 500 nm) structures. The main limitation of this technique is the resolution, which depends on the numerical aperture of the instrument and the wavelength of the incident light.

2.5.2. Atomic Force Microscopy

All the materials assembled in this work were characterised by features on the micro-to-nanoscale thus, scanning probes microscopies (SPM) had a fundamental role in acquiring experimental parameters such as height and distance between the features, their cross-section and their detailed dimensions. In particular, atomic force microscopy (AFM) was widely used due to the high versatility of different materials and the possibility to observe simultaneously different properties of the sample.

AFM was firstly developed in 1982 by Binning *et* al. and consequently, commercialised in 1989. Nowadays it is one of the most powerful tools for nanomanipulation and imaging. As with all the SPM techniques, AFM is based on the interaction of a physical probe with the sample. Usually, the probe for the AFM is a tip located at the end of a cantilever. The cantilever is held by a support arm that can be moved by a piezoelectric actuator (Figure 2.10). Any bending of the cantilever is monitored by a laser bouncing off the back of the cantilever and reflecting into a detector, which feedbacks an electric signal to be processed.

Imaging is mostly performed in two modes, contact and non-contact, which can be carried out either in liquid or dry state.

Contact mode was the first mode developed for the early models of AFM, and it measures directly how the cantilever is deflected when scanning the surface. In this mode, the forces detected from the cantilever are increasingly attractive when approaching the surface (Fig.2.11) until the cantilever moves into contact with the surface where the forces regime becomes repulsive.
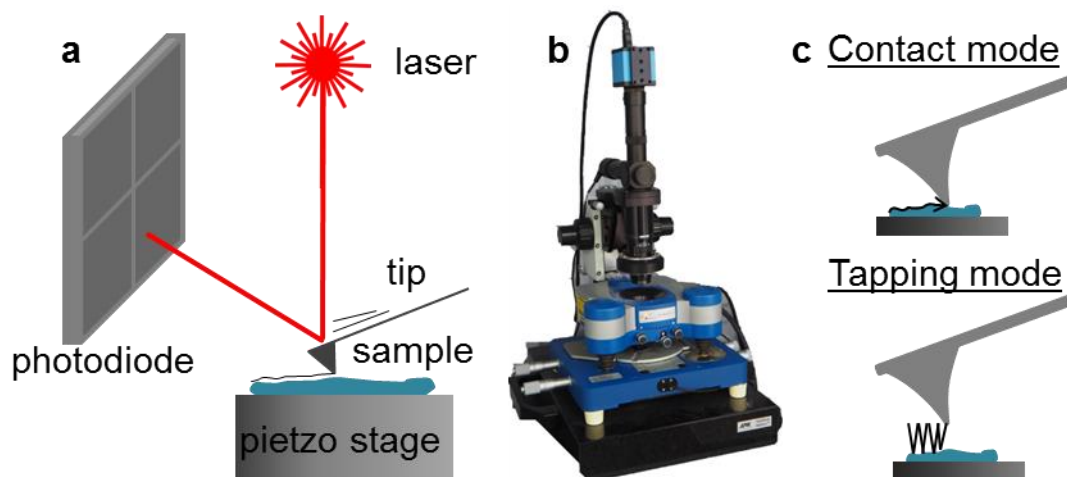
Figure 2.10. AFM technical details. a) Atomic force microscopy functioning schematic: the tip reacts to the sample, and the changes are recorded by a signal to a photodiode which is transmitted by an incident laser beam onto the back of the cantilever. **b)** Nanowizard instrument, used for imaging in this work. **c)** The two main modes for imaging: contact mode, where the tip actually "touches" the surface, and non-contact mode, where the tip continuously oscillates, and it is never touching the sample.
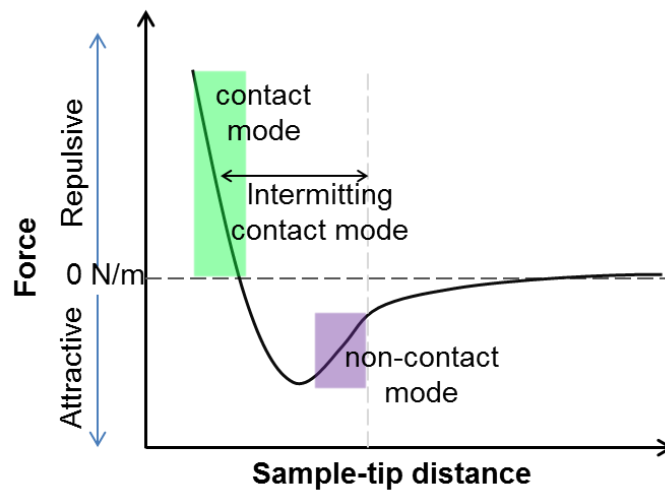
Figure 2.11. AFM forces and possible cantilever approaching positions and forces acting upon it.

Contact mode might damage the sample and the tip especially when scanning soft materials such as biomaterials or soft polymers, typical to this work. Hence, it is beneficial to imaging in a non-contact mode, which is based on the signal obtained from cantilever deflection when oscillating at its resonance frequency. As shown in Fig. 2.12., the surface is approached by the cantilever, and the oscillation is modified and monitored. Adjustments occur since the non-contact mode uses a feedback loop which maintains the tip-surface interaction constant.

2.5.3. Scanning Electron Microscopy

Scanning Electron Microscopy (SEM) in a powerful tool aimed for the in-depth investigation of the topography and composition of samples, with a possible imaging resolution that can reach sub-nanometre range. The first functioning instrument was invented in 1937 by Manfred Von Ardenne, who assembled a

microscope scanning with an electron beam. This kind of scanning enabled higher magnification using various modes of detection.

SEM scans are typically performed by irradiating the sample surface with a high-energy focused electron beam. After the beam hits the surface, secondary electrons and high-energy backscattered electrons are emitted and then detected. Relevant information about composition, crystallographic structure and topography, combined with the lateral resolution data, provide 3D images of the specimen.

The electron beam is produced by field emission from a very sharp tungsten needle. The electrons are accelerated towards the sample throughout a series of lenses and focused onto the sample. Scan coils scan the beam over the sample. The size of the spot and the beam current can be adjusted along the beam path by condenser lenses and the final objective lens, in order to modify the resolution in 2D and 3D images.
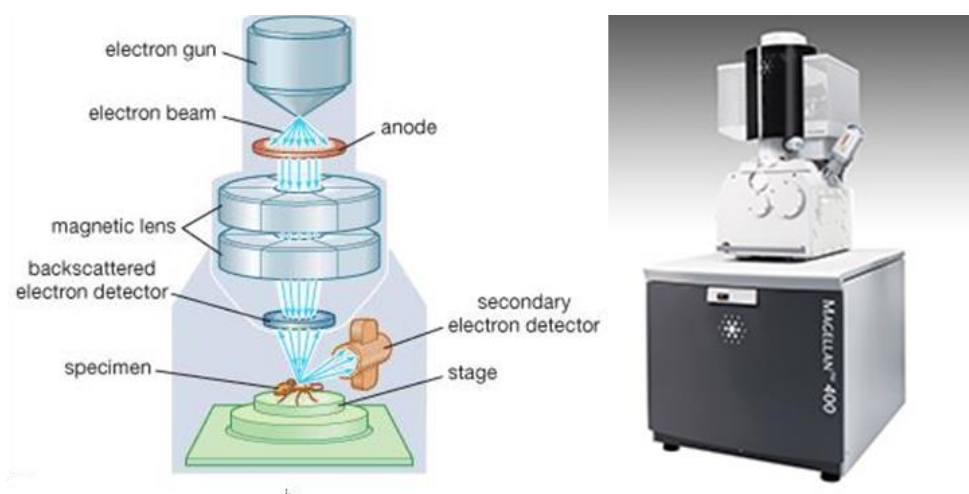
Figure 2.12. SEM instruments. On the left is a schematic of the SEM adopted from Encyclopedia Britannica, and right is a photograph of a Magellan microscope.

The interaction of the beam and a sample produces either elastic or inelastic scattering, which results in the emission of backscattered electrons (BSEs, high energy electrons) and secondary electrons. The bigger the atom then there is a higher probability of a BSE emission. BSEs provide information about the composition of the sample, while the topography is a result of the secondary electrons, due to their low energy (> 50 eV) and the small angles they are reflected.   The emitted electrons are detected depending on their energy, producing a signal which is amplified by a photomultiplier tube and finally displayed on a screen.

2.5.4. Transmission Electron Microscopy

Transmission electron microscopy (TEM) is a powerful technique with high resolution (<1 nm) which can also provide information about crystal orientation and electronic structure.

Developed initially by Knoll and Ruska in 1931, and further refined in 1939, TEM utilises the interaction of an accelerated electron beam with ultra-thin specimens. TEM typically comprised of an electron beam source, electromagnetic lenses acting as condensers, objective and projector lens.

A high voltage electron gun (that operates above 100 kV) can generate a high-energy electron beam, which is then guided and focused onto the sample by a series of electromagnetic lenses and apertures for reducing the scattering, as shown in Fig. 2.13. As the beam is transmitted through the thin sample volume,

the collected electrons are focused and magnified, forming an image which can be observed on a screen. The contrast in TEM images depends upon the direction of the deflected electrons which pass through the analysed volume, and it is calculated as the difference between scattered and transmitted electrons.
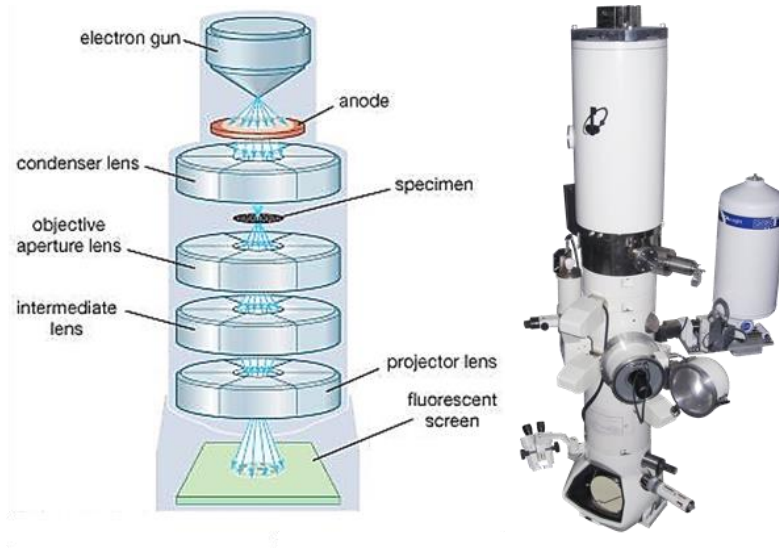
Figure 2.13. TEM instruments. From the left: schematic representation of a TEM (adopted from Encyclopedia Britannica) and a photograph of a working instrument.

2.5.5. Contact Angle

As mentioned in Section 1.3., the contact angle (CA), θ, macroscopically and quantitatively describes the interaction of a liquid on a solid. When a water droplet is wetting a solid surface, for determined conditions of pressure and temperature, the three states of matter coexist in mutual equilibrium. This can be quantified by measuring the contact angle value which in the case of a dynamic system, could range between a maximum value, also called advanced CA, θ_{adv}, and a minimum one called receding CA, θ_{rec}. Thus, measuring the exact CA provides crucial information about the prevailing energy in the total system either in static or

dynamic conditions. Optical and force tensiometers are usually employed for determining the wetting parameters using various methods, e.g., the 'pendant drop' method and the static and dynamic sessile drop technique (Fig. 2.14). The latter one in particular, can be performed by using a goniometer or tensiometer, which allows measuring the interface tension of a water droplet on a solid surface by fitting the parameters of the droplet profile, captured by a camera, with the theoretical model.
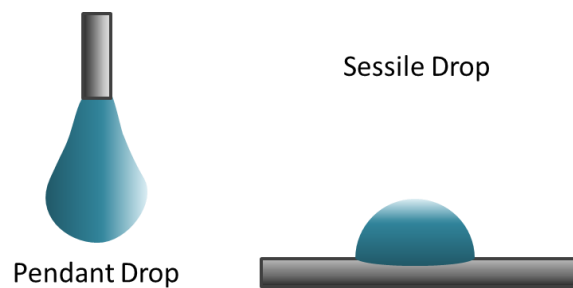
Figure 2.14. Contact angle measurement methods. Sessile and pendant drops.

3 Experimental Details and Methods

In this section, we describe the materials and the procedures used for fabricating micro-to-nano-structured materials and the treatments for increasing the already-existent hydrophobic properties arising from the double-layered arrangement. We further provide a theoretical background of the characterisation techniques used to analyse the fabricated surfaces, followed by experimental details for each set-up.

3.1. Materials Used for the EHD Patterning

3.1.1. Polymers and Solvents

Polymers are the predominant materials in the Electrohydrodynamic lithography (See Section 2.1.2.4). In this work, a selection of three well-known polymers, characterised by scarce hydrophilicity, was chosen for patterning, due to their availability and physical characteristics such as density, glass transition point (T_g), polarity and optical properties. The natural hydrophobicity of the polymers has been enhanced by increasing the surface roughness, coupling it with an

accurate choice of the chemical modification of the outer layer. The chosen

polymers were polystyrene (PS), poly methyl methacrylate (PMMA) and poly (9-

vinyl carbazole) (PVK) and Polychlorotrifluoroethylene (PCTFE) [225].

Table 3.1. Polymers used for EHD and related properties. The polymers indicated were used during different phases of EHD patterning. When available, properties such as molecular weight, density, glass transition point, melting pint, boiling point and surface energy are listed.

	M_w (g/mol)	Density (25°C)	T_g (°C)	T_m (°C)	Surface Energy (mN/m)
Polystyrene (PS)	~400,000	1.05 g/ml	~105	~212	40.7
Poly methyl methacrylate (PMMA)	~100,000	1.2 g/ml	~106	~165	41.1
Poly (9-vinyl carbazole) (PVK)	~1,100,000	1.2 g/ml	~200	n/a	n/a
Polychlorotri-fluoroethylene PCTFE	~n/a	2.1 g/ml	~103	~210	30.2
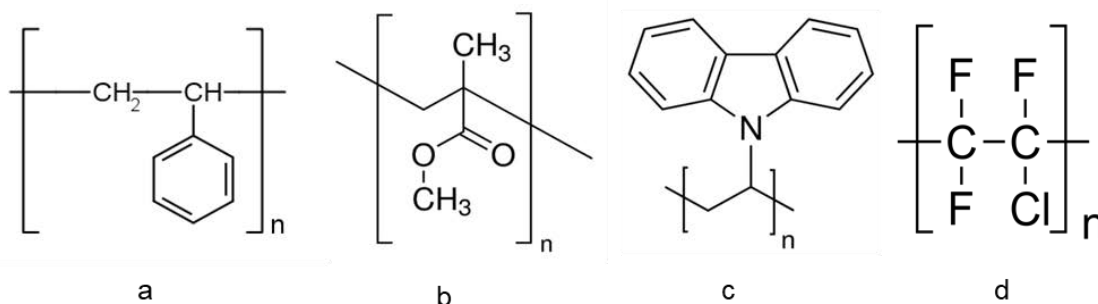
Figure 3.1. Representation of the polymers used as polymeric hosts. a) polystyrene, **b)** poly methyl methacrylate, **c)** poly (9-vinyl carbazole) and **d)** polychlorotrifluoroethylene.

The chosen polymers are characterised by a high solubility in organic solvent especially, aromatic hydrocarbons, chloroform and chlorobenzene as well as methylene chloride and tetrahydrofuran [226]. Thus, toluene was chosen as a solvent of preference [227,228], while chloroform ($CHCl_3$) use was limited by its toxicity and volatility. The purity of the solvent was determined by analysing the solutions with UV spectrophotometry (Varian Cary® 50 UV-Vis Spectrophotometer).
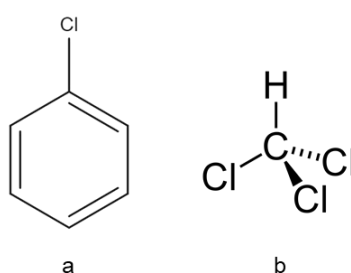
Figure 3.2. Representation of the solvents used. a) Toluene and **b)** Chloroform chemical structures of the compared solvents used for dissolving the polymer which will be later used as a support surface for further modification and nanopatterning.

3.1.2. Superhydrophobic Polymers and Solvents

Superhydrophobicity can be achieved by changing either the chemistry of the active surface or its roughness and topography. In this work, the two strategies were combined to enhance the desired properties. After the hierarchical structures were obtained, organometallic solutions were deposited on top of the nanopatterned surface to create an outer nanofilm to chemically improve the water-repellent behaviour of the final assembled system.

Bis(trimethylsilyl)amine (HMDS) and octadecyl trichlorosilane (OTS) were purchased from Sigma-Aldrich and tridecafluoro-1,1,2,2-tetrahydrooctyl-1-

trichlorosilane (FTS) from Gelest.Inc. (USA). According to the polymers solubility, isooctane, toluene and dichlorobenzene were the used solvent [229].

Table 3.2. Superhydrophobic polymers and related properties. The polymers listed were used during different phases of EHD patterning. When available, properties such as molecular weight, density, melting point, and surface energy are listed.

	M_w (g/mol)	Density	T_b (°C)	Surface Energy (mN/m)
FTS	481.55	1.05 g/ml	85	n/a
OTS	387.93	1.2 g/ml	223	28.05
HMDS	161.39	1.2 g/ml	125	43.57

a

b

c
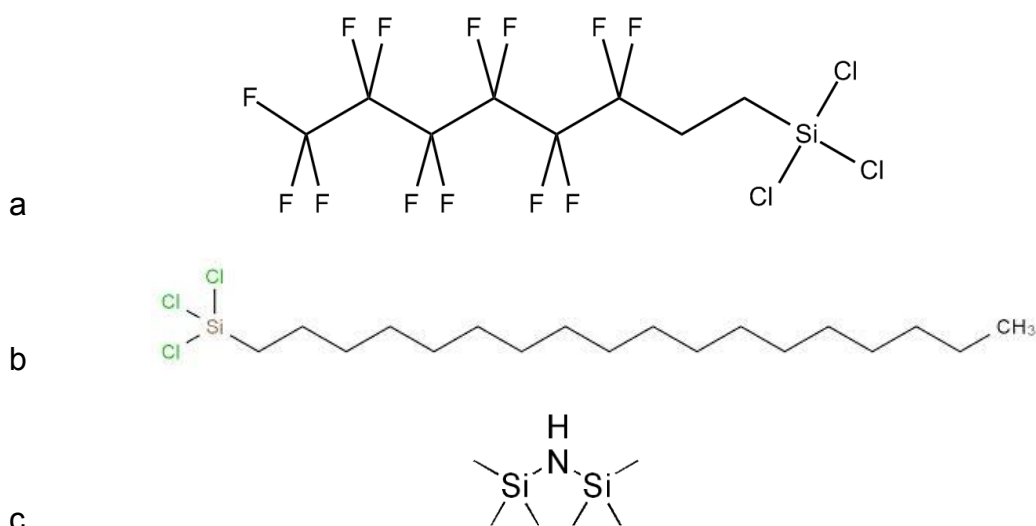
Figure 3.3. Representation of the superhydrophobic chemicals used. Structural formulas of the superhydrophobic compounds: **a)** FTS, **b)** OTS and **c)** HMDS.

3.2.   Thin Films for the Bottom EHD Electrode Production

Various consequent steps are required for preparing homogenous substrates, as described in the following sections.

3.2.1. Preparation of Solutions

PS, PMMA and PVK solutions were prepared in Pyrex glass vials using toluene as the solvent, in 3, 5, 10 and 20 % w/w ratio. Solutions were prepared at room temperature (T_r) and left equilibrating under fume cupboard for at least 24 hours before use. The film quality and properties can change upon different concentration, likely due to the incomplete solubility of the excess polymer.

PCTFE solutions were prepared in Pyrex glass vials using chloroform ($CHCl_3$) as the solvent, in 3, 5, 10 and 20 %w/w ratio. Solutions were prepared at room temperature (T_r), sonicated at 37 kHz for 15 minutes and left equilibrating in a fume cupboard for at least 24 hours before use.

3.2.2. Cleaning of the Substrates

The substrates used in the EHD experiments were Silicon wafers (Si), *n*-type with crystal orientation <100> and resistivity 1-100 Ω/cm^2 (Silicon Materials, Germany) and pre-cut square Indium-Tin Oxide glass, 1.5 x 1.5 cm^2 slides, with resistivity 70-100 Ω/sq.

The Si wafers were cut into 1.5 x 1.5 cm^2 and cleaned by snow-jet cleaning on the polished side. Undesired artefacts in the film can be produced by imperfections or poorly-cleaned substrates thus, it is necessary to remove all physical, chemical and organic residues from the surface.

In this experimental work, for increasing the hydrophilicity of the substrates, a compact, table-top PDC-32G from Harrick Plasma (US), has been used for both cleaning and modifying the wettability of the substrates [230].

3.2.3. Spin-Coated Polymer Films: Technique and Parameters

Preliminary studies were carried out on polymer solutions in toluene before introducing the metal complexes. The conditions have been optimised building upon the known protocols for standard polymers such as PS and PMMA to establish additional procedures for each polymer. The optimal conditions for the PS were already known and were used as a starting point for studying the other polymers as they all have similar viscosity and density [231]. A homogeneous thin film (of a typical thickness of 100nm) was spin-coated using a WS-650 Mz-23NPPB spin-coater (Laurell Technologies, USA) onto a silicon wafer. The density and the experimental conditions are summarised in Table 2.2.

Table 3.3. Experimental conditions of spin-coating for PS, PMMA, and PVK. The listed density values are provided by the supplier (http://www.sigmaaldrich.com/united-kingdom.html).

	Density	Rpm	Time (sec)
Polystyrene (PS)	1.05 g/ml	3000	30
Poly methyl methacrylate(PMMA)	1.2 g/ml	1000 3000	60 30
Poly (9-vinyl carbazole) (PVK)	1.2 g/ml	2000	30

3.3. Top Electrode Fabrication

3.3.1. Growth of the Vertically Aligned Carbon Nanotube Forests

CNT forests were grown on 5×5 mm^2 silicon wafers as substrates, which have been sputter-coated with a catalyst layer consisting of Al_2O_3 buffer and iron catalysts, using the cold-wall system of the catalytic chemical vapour deposition (CVD) process [232]. During the growth process, initially, 500 sccm of H_2 was heated to 750° C for 5 min under a controlled system pressure of 15 mbar. CNTs growth proceeded at 750° C with a gas flow of H_2: C_2H_2 (460:40 sccm). Upon the completion of the growth, the substrate was cooled to room temperature under the flow of 500 sccm of hydrogen.

3.3.2. Fabrication of Patterned CNT Arrays

CNTs arrays were produced using electron beam lithography coupled with CVD growth process, where initially a layer of photoresist was spin-coated on a silicon wafer, which was further annealed at 120° C for 2 minutes. Consequently, the resist was exposed to the electron beam with (pre)written dimensions. Finally, it was post-baked at 140° C for 2 minutes and developed in CD26 for 30 s, and the CNT-based pillar arrays were obtained.

These structures were further filled by depositing 10 nm alumina and 1.3 nm of iron through a sputtering process, followed by lifting-off the resist using acetone. The CVD process was utilised using a combination of H_2: C_2H_2 (70: 30 sccm) at 750° C for 2 minutes. Eventually, CNTs arrays with desired dimensions and pitches were grown on top of the patterned catalysts.

3.3.3. Fabrication of the Inverted CNT Forests

Initially, a homogeneous poly (methyl methacrylate) (PMMA) film was spin-cast on a silicon substrate, followed by placing the VACNTs facing the PMMA layer and annealing at 180 °C for 1 minute. The substrate was then cooled down below the glass-transition temperature of the polymer film, and this results in the film solidifying while embedding the upper ends of the CVD-grown CNTs forest. The VACNTs were subsequently peeled off the original silicon wafer, exposing well-defined straight tips.

3.4. EHD Patterning

3.4.1. Thin Film Patterning

EHD lithography is the technique that was used for the production of micro and nanostructures from the spin-coated thin films [100].

As shown in Fig. 3.4, the EHD experimental setup is assembled by using two parallel electrodes, separated by a distance *d* and then connected to an external voltage supply. The bottom electrode is usually comprised of the Silicon (Si) wafer coated with a thin layer of a desired polymer while the top electrode can either be a plain Si wafer or a patterned silicon electrode which, when coupled with the voltage applied to the electrodes, drives the lithographic process.
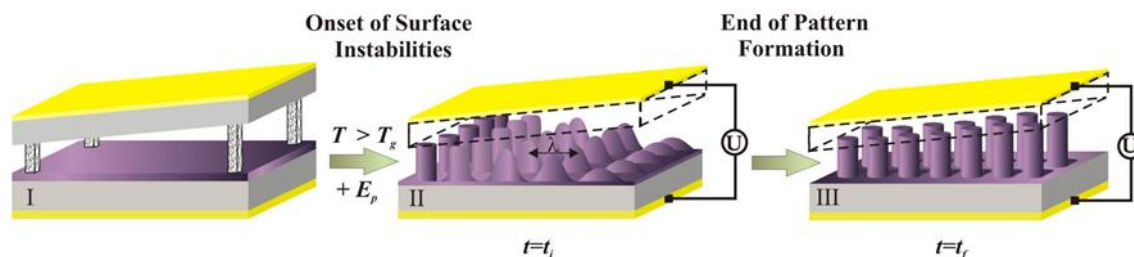
Figure 3.4. Electrohydrodynamic Lithography experimental setup schematics. In **I)** the nearly parallel position of electrodes and spacers is set, with a slight tilting of the top electrode. In **II)** the temperature of the systems is raised above the glass transition point (T_g), where the polymer thin film liquefies. The potential applied, E_p, triggers the surface instabilities, which increase with the time and finally pin to the top electrode, **III)** forming discrete pillars [233].

Initially, to establish the correct parameters, the EHD experiments were carried out on PS films, obtaining the values of temperature, voltage and film thickness. Since PMMA has similar properties to the PS, the parameters were not changed during the subsequent experiments. However, these were optimised in the later stages (Table 3.4). PVK, due to the different values of properties such as viscosity and conductivity required a more careful selection of experimental parameters. However, the PVK film was not successfully patterned, most likely due to the neutral and slightly hydrophobic nature of the polymer, which creates several domains and segregation areas in the film area while patterning (Fig 3.5).
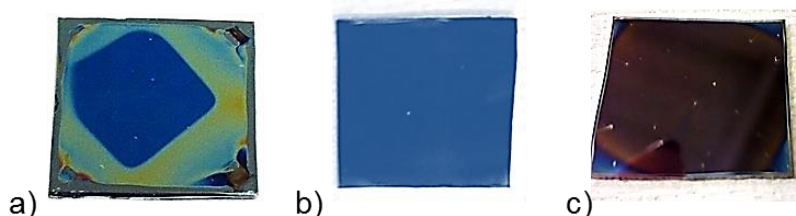
Figure 3.5. Polymeric thin films. a) PVK film on silicon wafer. Two areas are clearly visible: the deep blue film, 150 nm thick, is the desired area for patterning, while the degrading yellow-blue area thickness is > 20 nm, therefore unsuitable for EHD. **b)** PS film, spotless, of deep blue colour which indicates 100 nm thickness; **c)** PMMA film 200 nm thick, with high presence of residues.

Table 3.4. Experimental conditions for EHD patterning of polymers. Pure polymers films were in solutions with 3, 5 and 10% w/w ratios.

	Temperature (°C)	Voltage (V)	Time (hours)
PS	170	40	24
PMMA	170	50	18-20
PVK	n/a	n/a	n/a

The film obtained from PMMA solution (5% w/w ratio) provided the best results in terms of smoothness and the lack of artefacts and therefore, the subsequent EHD experiments, which are strictly dependent on the film quality and thickness, were predominantly based on the above-established parameters.

Further optimisation of the experimental procedure was carried out during the lithography process, to decrease the dimensions of the obtained pattern towards the nanoscale. A few parameters such as the distance between the film and the upper electrode could be varied since the dimension and shape of the final patterns are directly influenced by these. The described experimental protocol has been followed changing the necessary experimental parameters, e.g., reducing and increasing the inter-electrode distance while maintaining all the other parameters. Patterning was also carried out on top of Indium-Tin-Oxide glass (ITO) to obtain a transparent and conductive substrate, ideal for the further characterisation.

3.4.2. CNT-EHL Patterning

The fabricated CNT-based electrodes were coated with a silicon layer (Kurt J. Lesker Si sputtering target 99.999% purity). To ensure the reusability of the CNT-based electrodes, these were increased in their hydrophobicity by the deposition of a 1,1,1,2H-perfluorodecyltrichlorosilane (FTS) self-assembled monolayer to reduce the adhesion between the mask and the EHL patterned polymer. Alternatively, a non-stick self-assembled monolayer was deposited from liquid octadecyl trichlorosilane (OTS) phase. Silanisation was performed by immersion of the substrate in the freshly prepared silane solution (0.25% OTS in hexadecane).

Highly polished p-doped silicon (Si) wafers, with <100> crystal orientation (Wafernet Gmbh, Eching, Germany) covered by a 100 nm thick silicon oxide layer were used as substrates. Initially, the substrates were cleaned in a `Piranha' solution consisting of 3:1 H_2SO_4 (98%): H_2O_2 (30%), followed by thorough rinsing with deionised water and dried under N_2. Thereafter, silicon wafers were cleaned using a snow-jet gun immediately before film deposition and capacitor patterning assembly. Transparent indium-tin oxide (ITO) covered glass slides with a resistivity of 80 Ω cm^2 were also used as substrates, allowing the *in-situ* optical tracking of the pattern formation or replication process. Thin films of PCTFE were spin-coated onto a silicon wafer with typical concentrations of 2-3% polymer by weight. Facing it, a top electrode comprised of the silicon coated VACNT (as-grown and inverted) forests and arrays was mounted at a specific distance, leaving a thin air gap, *d*. The silicon wafers were electrically contacted by evaporating a 10 nm chromium layer, followed by a 100 nm gold layer on the

unpolished backside. When ITO glass was used as bottom electrodes, these were contacted by scratching the polymer film at two corners before applying the silver paste.

The experiment was initiated by liquefying the spin-cast PCTFE (see Section 3.1.2) films by annealing above the softening/glass transition temperature of the polymer while the voltage was applied to the electrodes and subsequently, cooling the sample to room temperature solidifying the polymer before the voltage was removed, terminating the patterning process. A laterally varying electric field density was introduced to the system by mounting a topographically structured CNTs-based master electrode onto the polymer film. Expressed by the ratio between the intrinsic wavelength, λ_i, and the lateral periodicity (or lateral size of nonperiodic structures) Λ_m of the master electrode structure, three replication cases can be described: (i) $\lambda_i < \Lambda_m$, (ii) $\lambda_i \approx \Lambda_m$, and (iii) $\lambda_i > \Lambda_m$. After freezing in the samples by reducing the temperature to room temperature, the electric field was disconnected, and the upper electrode was removed. Pattern replication was monitored and recorded by a microscope and a connected computer throughout the experiment. After removal of the top electrode, the quenched polymer film was further characterised by the atomic force microscopy (AFM).

3.5.   Fabrication of the Superhydrophobic Surfaces

Patterned polystyrene films have been fabricated by various techniques as described in Section 3.3 [100]. The pattern obtained from EHD lithography forms pillar-like features on the micro-to-nanoscale. In order to create a

superhydrophobic hierarchical surface, a higher level of roughness is introduced by adding PS nanospheres. Standard PS nanospheres of 100, 200, 500 nm in diameter were spin-coated onto PS films both, the EHD- patterned and the smooth ones.

The initial film has been modified to achieve higher roughness thus, chemical modifications were required to further increase the superhydrophobicity of the structures. For this purpose, organometallic silane-derived monolayers (HMDS, OTS and FTS) have been deposited on top of the entire surface. HMDS was directly spin-coated onto the patterned surface (2000 rpm for 1 minute) while the OTS, as well as FTS, were added as self-assembled monolayers (SAM) [53]. The substrates were hydrated in water steam for 1 minute until the formation of water droplets and subsequently, blow-dried with N_2 flow. A 1wt % FTS solution in 2,2,4-Trimethylpentane (or isooctane, from Sigma-Aldrich) was used as an immersion solution where the samples were left for 10 minutes. The samples were then removed and rinsed with dichloromethane (Sigma-Aldrich) and finally, dried with nitrogen gas (N_2).

3.6.   Preparation of the DNA Templates

3.6.1. DNA Strands

There are multiple strategies for obtaining resilient and stiff structures for the production of 3D DNA origami [189,234,235]. In this work, the 3D DNA preparation derives from three well-established procedures [195–197].

Based on the original work by Goodman [195], a 20 base-pair regular tetrahedron with the side ranging from 6 to 9nm, was synthesised. The DNA tetrahedron has six sides of the same length and four open hinges, formed by one single unpaired base, which provides the structure with its flexibility. The final annealing requires four different single-stranded DNA (ssDNA) sequences, as detailed in Table 3.5

Table 3.5. SsDNA strands used for producing Goodman-like 3D tetrahedron structures.

S1	AGGCAGTTGAGACGAACATTCCTAAGTCTGAAATTTATCACCCGC CATAGTAGACGTATCACC
S2	CTTGCTACACGATTCAGACTTAGGAATGTTCGACATGCGAGGGTC CAATACCGACGATTACAG
S3	GGTGATAAAACGTGTAGCAAGCTGTAATCGACGGGAAGAGCATG CCCATCCACTACTATGGCG
S4	CCTCGCATGACTCAACTGCCTGGTGATACGAGGATGGGCATGCT CTTCCCGACGGTATTGGAC

In collaboration with Professor James Tucker group's (University of Birmingham, UK), the four strands were synthesised using a Synthesiser (Applied Biosystems ABI 394, Department of Chemistry, University of Birmingham) obtaining samples with 90% yield and 85% purity as determined by preliminary characterisation by high-pressure liquid chromatography (HPLC).

The chemical DNA synthesis cycle is explained in Appendix 1.1 (from http://med.stanford.edu/sgtc/resources/chemical_DNA_synthesis.html), as discussed and recommended by Tucker's group. A further purification step was carried out using an HPLC/ Electrospray ionisation (ESI-MS) spectroscopy integrated device, to confirm the calculated mass (Appendix 1.2).

According to the procedure described in Goodman's original work, an additional set of strands was purchased from Eurofins Genomics [201] (Appendix 1.3). The samples, provided with the documentation, were purified by High Purity Salt-Free, a routine purification method by the supplier. The method is documented as accurate and reproducible, using a cartridge purification method based on reverse-phase chromatography. It enables the delivery of oligonucleotides purified from by-products, free of salt residues and therefore, is ready to use. The HPSF purification is guaranteed to a purity of > 70%.

Thus, the production of the strands through the synthesiser was terminated due to the higher purity of the commercial products. The following, larger 20-nm and 30-nm structures were ordered directly from Eurofins Genomics since the base sequence length of these was superior to the instrument maximum reliability of 100 nucleobases (Appendix 1).

According to well-established procedures [196,197,200], stiff and resilient polyhedron structures were further synthesised following the various synthetic strategies [196]. He *et al.*, as reported in Table 3.6, achieved the assembly of 3D DNA structures using three different DNA single strands: a short sequence (21 bp), a medium one (42 bp) and a long one (78 bp). Different folding pathways lead to various structures with different dimensions although, in this work, the tetrahedron shape, with size dimensions ranging from 16 to 25 nm, was preferred due to the high yield, as shown in Figure 3.6 [197].
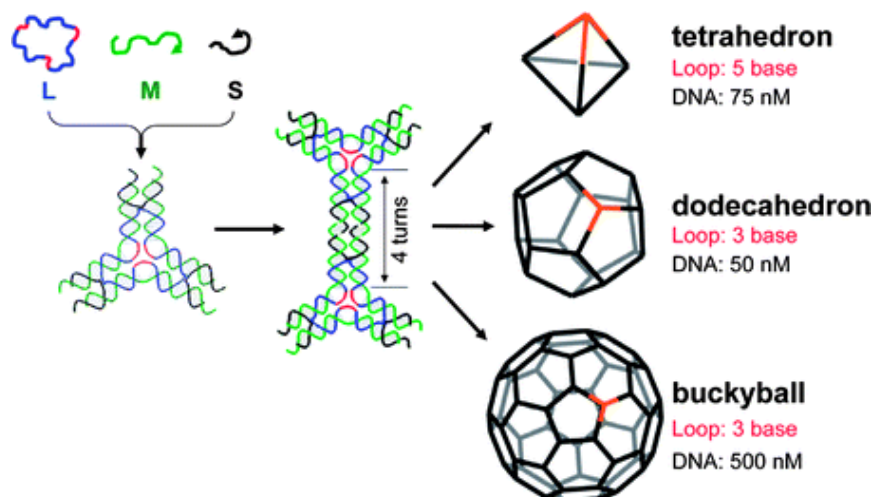
Figure 3.6. **Self-assembly of DNA polyhedrons**. The self-assembly procedure starts with three different types of DNA single strands (L, M, and S) which forms an intermediate product called a tile, a symmetric 3-point-star motif. The tiles assemble into polyhedra in a one-pot reaction. Image reproduced from [236].

Table 3.6. **DNA strands used for producing 3D 20-nm DNA structures**. Since the same precursors are used to achieve different polyhedron structures than polyhedrons, the number and concentration of the strands may vary.

Long	AGGCACCATCGTAGGTTTAACTTGCCAGGCACCATCGTAGGTTT AACTTGCCAGGCACCATCGTAGGTTTAACTTGCC
Medium	TAGCAACCTGCCTGGCAAGCCTACGATGGACACGGTAACGCC
Short	TTACCGTGTGGTTGCTAGGCG

The produced DNA tetrahedron has *closed hinges*, and this structural optimisation is believed to provide increased stiffness and rigidity to the structure, which are essential prerequisites for a stable structure, which otherwise will bend and collapse in the dry state.

One of the main goals of this project is to show how a wide range of nanopatterned materials can be produced. Therefore, it is fundamental to

demonstrate the dimensional tunability of the DNA structures which have been used as templates [196,197] and for this reason, we have also assembled larger structures in the shape of octahedrons with typical dimensions of 20 to 40 nm. The synthetic procedure involves the production of DNA tiles as intermediate products, which later are annealed in a specific fashion, depending on the concentration of the intermediate tiles, as shown in Fig. 3.7 [196]. The strands required for obtaining such a structure are as summarised in Table 3.7.
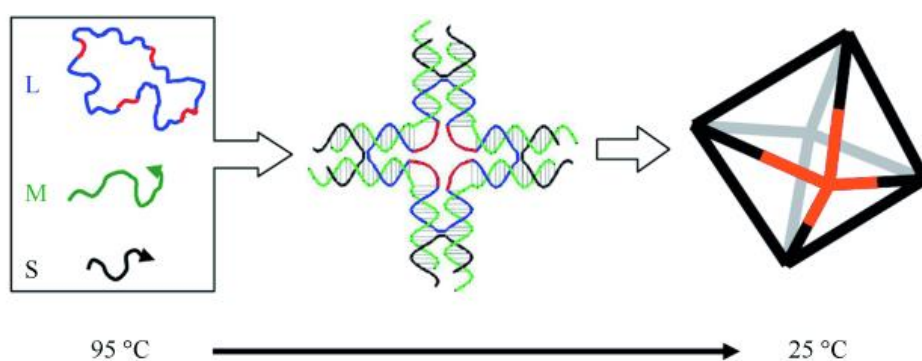
Figure 3.7. Self-assembly of DNA octahedron. Schematic procedure of the one-pot self-assembly reaction of DNA octahedra from three DNA single strands (L, M, and S). In a similar fashion to the process explained in Fig 2.8., the one-pot reaction involves the formation of an intermediate product known as a tile which, in turn, assembles into the final octahedron. Image adapted and reproduced from [196]

Table 3.7. DNA strands for producing 3D 30-nm DNA structures. In line with the synthetic strategy used to assemble DNA polyhedrons, the number and concentration of the strands may vary depending upon the desired structure.

Long	AGGCACCATCGTAGGTTTAACTTGCCAGGCACCATCGTAGGTT TAACTTGCCAGGCACCATCGTAGGTTTAACTTGCCAGGCACCA TCGTAGGTTTAACTTGCC
Medium	TAGCAACCTGCCTGGCAAGCCTACGATGGACACGGTAACGCC
Short	TTACCGTGTGGTTGCTAGGCG

Due to a strict similarity with the described 20 nm-side DNA polyhedron, this structure also yields high stability and yield. The stiffness is derived from the closed hinges, which help in maintaining the structure in the dry state, essential for further characterisation.

3.6.2. DNA Sample Preparation

According to the procedures developed by Goodman [195] and He [196,197], robust yet flexible polyhedrons have been assembled, once again demonstrating the potential of DNA-based structures, which allow to span from 9 to 30 nm side length structures. Interestingly, these assembled macromolecules are extremely resilient in dry state and at room temperature thus, without biological requirements when treating the samples.

3.6.2.1.   9 nm Side Tetrahedron

Initially, all four single strands are mixed in a stoichiometric mixture in TM buffer (10 mM Tris, 5 mM MgCl$_2$). The temperature is increased to 95°C for 2 minutes and then cooled to 4°C for 30 minutes. Subsequently, the DNA mixture is treated with gel purification (Figure 3.8). A diluted solution of DNA polyhedrons is run on a 6% PAGE gel (19:1 acrylamide: bisacrylamide mixture) with 1×TAE (Tris base, Acetic acid and EDTA) buffer and stained with SYBR Gold by Fisher Scientific. The DNA is quantified and characterised by using the UV transilluminator (wavelength 320 nm). Electrophoresis is a consolidated technique which allows

separating components of a solution depending on their different weight using an applied static electric field.

The set of strands purchased from Eurofins Genomics [201] was also assembled into polyhedrons in an analogous experimental procedure and characterised by electrophoresis.
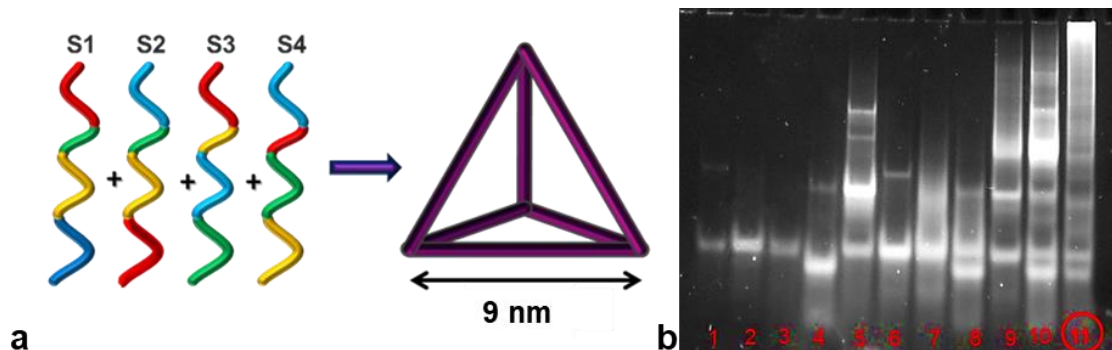
Figure 3.8. 9-nm DNA polyhedron assembly strategy and gel electrophoresis. a) ssDNA sequences and tetrahedron: the single strands self-assemble in the final polyhedron, in a *one-pot* reaction. **b)** With proper control of the DNA single strands concentration and the temperature, it is possible to form a polyhedron structure with regular sides. DNA quantification by UV transilluminator: single strands (1-4); mixed strands (5-10); DNA tetrahedron (11).

3.6.2.2. 20 nm Size Tetrahedron

The polyhedron annealing requires three single strands DNA sequences (L, M and S) in a 1:3:3 ratio. Differences in the stoichiometric mixtures of these sequences could lead to bigger and more complicated structures such as dodecahedrons and icosahedrons [196]. The main discriminating parameter in obtaining the different structures is the concentration of the intermediate product, the *tiles*, as shown in Figure 3.9.
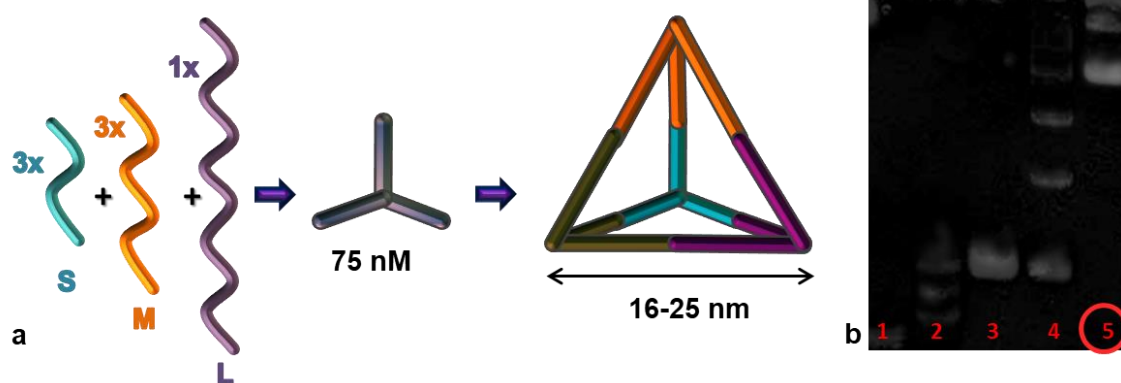
Figure 3.9. 20-nm DNA polyhedron assembly strategy and gel electrophoresis. a) Synthesis scheme for 3D DNA annealing with a lateral size of 16-25 nm. Seven strands are required for obtaining a single tile with an intermediate concentration of 75 nM, which combine with each other will anneal into the final polyhedron. **b)** Gel electrophoresis comparing the single strand L (1), L+M 1:1 (2), L+M 1:3 (3), L+M+S 1:3:1 (4), L+M+S 1:3:3 (5).

The tiles are the building blocks which are assembled into a pre-designed tetrahedron. Seven strands are required to have 50 nM of tiles concentration, which cannot be altered, as otherwise will result in different (undesired) polyhedrons. The annealing process, *per se,* is similar to the procedure explained for polyhedrons of 9 nm side. Typically, seven strands were mixed in an Eppendorf, which is then inserted into a thermal cycler machine (also known as PCR). The cooling process, which allows the DNA polyhedrons annealing, reduces the temperature from 98°C to 4°C, takes 48h, and follows a pre-determined temperature decrease ramp.

Once the annealing is completed, the DNA structures are stored at -4°C and kept in an amber glass container to minimise interaction with the UV light, which could lead to denaturation of the DNA, destroying the structure. The final product is also characterised by gel electrophoresis.

3.6.2.3. 30 nm Side Octahedron

The production of these polyhedron requires three sequences (L, M, and S) in a 1:4:4 ratio [196] as shown in Figure 3.10. The assembly procedure is similar to the above-described steps. The nine strands are mixed all together in a PCR Eppendorf tube and inserted into the PCR machine. Inside the instrument, the temperature decreases from 95°C to 25°C over a period of one hour. The final structure annealing is driven by the formation of 50 nM intermediate tiles, which interact with each other via the connecting sequences, generally called *sticky ends*.
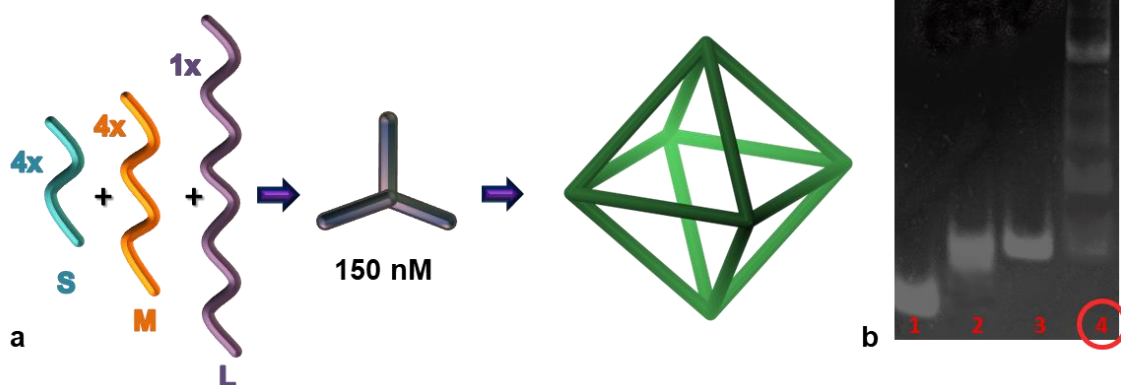
Figure 3.10. 30-nm DNA polyhedron assembly strategy and gel electrophoresis. a) Synthesis scheme for 3D DNA octahedron annealing with a lateral size of 28-30 nm. Nine strands are necessary for obtaining a proper concentration of single tiles with an intermediate concentration of 150 nM, which will be annealed into the final polyhedron. **b)** Gel electrophoresis comparing the single strand L (1), L+M 1:2 (2), L+M 1:4 (3), L+M+S 1:3:4 (4).

3.7.   Substrates for the DNA Deposition

The DNA samples were immobilised onto different substrates such as silicon wafers, mica, transmission electron microscopy (TEM) grids or Indium-Tin-Oxide

(ITO) glass. A short description of each of the substrates used is detailed in Table 3.8 and further shown in Figure 3.11.

Table 3.8.**Substrates used in the process and their corresponding properties.**

	Dimension (mm x mm)	Resistivity ($\Omega \cdot$ cm)
Silicon wafer	10 x 10	1-100
TEM grid	3.5 x 3.5	<1
ITO glass	10 x 10	70-100
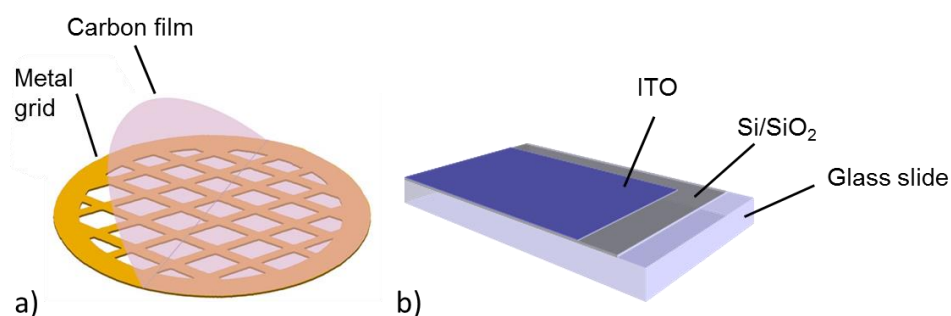
Figure 3.11. Substrates representation and schematics. a) Schematics of the TEM grid: a copper grid with a specific mesh size is typically covered by a carbon film, on top of which the substrate is deposited, http://www.agarscientific.com/tem/carbon-support-films/carbon-films.html. **b)** Schematic representation of **ITO**: typical composition of an Indium-Tin-oxide coating on a glass slide.

The DNA polyhedrons attach onto the surface *via* physisorption thus, eliminating the need for chemical modification [204,237,238], which otherwise requires additional and time-consuming steps.

All samples have been spin-coated onto the substrates for various periods of time ranging from 1 to 10 minutes and then washed with 10^{-2} mM magnesium acetate solution. The following procedures have been used to anchor the DNA nanostructures onto surfaces:

1.	Attaching the polyhedra onto a silicon wafer, which has been initially pre-coated with a 30 nm gold layer, using sputter-coating. During these experiments, using a polaron E5400 Sputter Coater, the chamber was under vacuum and filled with rarefied Argon. The gold coating is required as the DNA polyhedron in aqueous solution has a residual partial negative charge which will equilibrate with the partial positive one from the gold [187].

2.	Attaching the polyhedra from buffer solution directly onto clean silicon wafer. It has been established that similar structures attach to a smooth surface such as silicon or mica when treated with magnesium acetate [204].

3.	Drop-casting the DNA solution directly on a carbon film of a TEM grid.

4.	Firstly, treating silicon wafer with (3-Aminopropyl)triethoxysilane (APTES). The DNA from a buffer solution was then directly deposited onto the APTES treated surface [239].

5.	Immobilising the DNA onto the ITO glass without washing. As reported by Liu [218] the DNA directly attaches onto the conductive glass surface due to the opposite charge. Washing after immobilisation has been proven to remove both samples and the buffer.

3.8.   Plating Techniques

The production of metallised 3D nanostructured materials requires a step in which the soft 3D DNA structures are replicated by forming a metallic layer over the structures. Various plating procedures were attempted and carried out as described below and finally, establishing the optimal one.

3.8.1.   Gold Electrodeposition

The replication of insulating nano-scaled features through electroplating is still a challenging step, even on conductive substrates such as ITO glass or metals.

In fact, each kind of substrate reacts differently when subjected to plating with the same type of solution, depending on the conductivity properties of the material. In line with the acknowledged differences, a preliminary substrates characterisation step was carried out to determine the optimal conditions for producing homogenous and smooth layers of only a few nanometres thickness on the bare surface. Well-established procedures suggest using a three electrode system through all the steps [126]. The gold solution (ECF60) was purchased from Metalor Technologies (UK) Ltd. which is a most commonly used solution for plating of thin films especially, for electronic coating purposes.
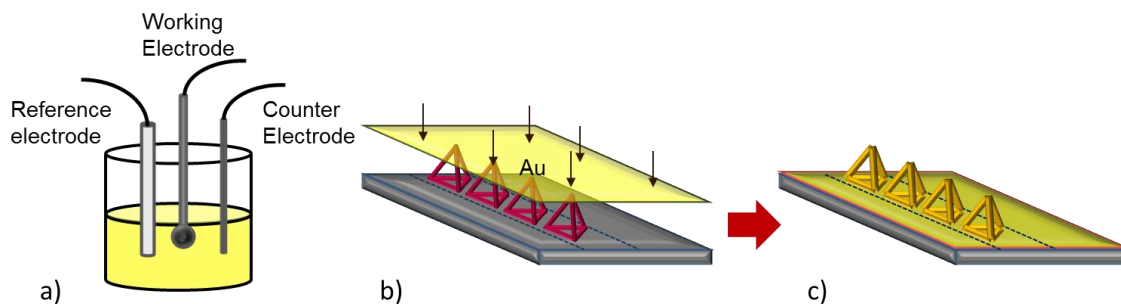
Figure 3.12. Schematics of the electroplating setup and plating processes. **a)** All the experimental procedure has been carried out maintaining the three-electrodes arrangement for minimising current oscillations. Figures **b)** and **c)** shows the replication of the 3D DNA structures, which involves the deposition of 10-20nm gold layer on top and inside the structures when the dimensions allow the gold grains to penetrate the polyhedrons.

Three different plating strategies were performed for each sample to determine the most suitable plating conditions of the nanostructured substrates, as described below.

a) *First Procedure*

According to previous studies [125,240] the plating process involves various steps, which were repeated for both the bare substrate and the diluted sample (50 nM) immobilised onto the substrates. Such a low concentration of the sample is essential to avoid modifying the conductivity of the substrates after the immobilisation, which otherwise may affect the plating process. In fact, the presence of vast insulating areas may lead to the formation of gold nuclei on the conductive parts of the substrates, with the following gold grains growth localised around the insulating structures, while not inside them.

1. A *cyclic voltammetry scan* (CV) allows understanding the occurring electrochemical reactions when the increasing voltage is progressively applied to the electrodes immersed into the solution. Each type of substrate leads to slight changes in the voltage applied for electrodeposition [127].

2. A *corrosion test*, coupled with the determination of the open-circuit potential (OCP), defines the upper and bottom thresholds of voltage for the reactivity of the substrates.

3. A *linear sweep voltammetry* (LSV) scan is run to determine the potentials where the electrodeposition occurs.

4. *Chronoamperometry* scans are recorded for 10 minutes to define the best voltage to be applied to the substrates.

5. *Electroplating* is carried out for a short period (<1 minute) at a constant voltage which has been determined in step 4. As previously mentioned, each substrate possesses specific conductivity properties and therefore, the voltage range to be applied for plating might differ.

b) *Second Procedure*

According to previous experiments [241] performed in similar conditions, the plating process can be carried out in two main steps:

1. *CV* scan (one to three times) which produces the nuclei for starting the deposition, over a wide voltage range where the deposition will occur. In this experimental procedure, the voltage has spanned from 0 to -1.1 V and from -0.5 to -0.9 V;

2. *Electrodeposition* at a constant voltage (-0.8 V) for a specific amount of time (10, 20, 30, 40 seconds), as it is well-established that a 100±5 nm thick layer is produced in 50 seconds, at the same conditions [241].

c) <u>*Third Procedure*</u>

Typically for electroplating processes, a constant potential or current is used, depending on whether working in galvanostatic or potentiostatic conditions. It is further possible to modulate the current or voltage as pulsed series [242]. The process uses alternate potential (or current) between two values, one of which is set to zero. This results in a series of equal pulses in terms of amplitude and duration, separated by a constant period of zero current, where the species involved in the process first move towards the electrode surface and then equilibrate. This kind of electrodeposition is especially interesting as the layer thickness and the grain dimensions can be tuned according to the amount, separation and length of the pulse [243,244]. Experimental *pulse electrodeposition* (PED) was performed in potentiostatic mode, setting the pulse duration for 1 and 5 ms, and the no-pulse duration for 20 ms; the entire procedure was repeated for 60 seconds to observe how the deposition time affects the grain dimension and deposition.

3.8.2. Electroless Deposition

The procedure involves preparing a gold thiosulfate/ascorbic acidic bath, where the sample to be deposited is immersed into. Depending on the desired thickness of the final layer, the bath is accordingly quenched and the sample removed. A critical parameter in electroless deposition is the lifetime for the species involved, which in this experimental work was expected to be 2 hours. Table 3.9 [245] summarises the parameters for this experimental procedure.

Table 3.9. Electroless conditions for gold thiosulfate/ascorbic bath. The experimental parameters have been used for directly plating the 3D DNA nanostructures.

$Na_3Au(S_2O_3)_2$	0.03 M
Na L-ascorbate	0.05 M
Citric acid	0.4 M
pH (KOH)	6.4
Temperature	30°C
Plating rate	760 µm/h

3.8.3. Sputter Deposition

The gold sputtering deposition process, based on plasma, is described in Section 2.3.3. In this experimental part, the sputtering parameters have been changed to obtain a smooth 1 - 10 nm thick layer of gold.

The gold target position has been calibrated and kept constant for the experiments in order to minimise the possible interaction of the plasma "plume" with the substrates, which may detach the sample from the surface. The sputtered atoms have a wide energy distribution (around 100,000 KeV) and may hit the substrate directly and cause re-sputtering as the sample is physisorbed onto the surface. Introducing high gas pressure, which may vary from 0.2 to 0.1 mbar and increasing the gold target distance create the conditions for the least interaction with the substrate while the mean free path of the ions remains the same.

3.9. Characterisation Techniques

3.9.1. Optical Microscopy

All the samples have been investigated with an Olympus BH2 optical microscope in reflective mode, using a 20 W halogen lamp.

3.9.2. AFM

All the AFM measurements were carried out using a JPK Nanowizard instrument. Further details for particular samples will be provided in the following chapters. Different kinds of cantilevers were tested for obtaining the best results in terms of tip convolution and highest resolution.

3.9.2.1. *Imaging of DNA-Templated Surfaces*

Imaging of 3D DNA polyhedrons with sides of 9 to 30 nm is still a challenge, due to the very small dimensions of the samples and the probes. It is important to avoid any electrostatic and physical interaction between the tips and surface. Hence, soft tapping or force mapping (FM) cantilever has been used. FM tips enabled a better resolution for detecting the nano-scaled features in a dry state after the buffer has been washed from the substrate.

Two types of cantilevers have been used in this work, in every characterisation step:

1.   FESP cantilevers, by Veeco: 60-100 MHz drive frequency (f0), and 1-5 N/m force constant.

2.   Point Probe Plus, by NanoSensors: 190 kHz drive frequency (f_0), and 48 N/m force constant. This kind of cantilever was suggested in the original work [196,197].

As suggested in previous DNA related studies [196,197,246], AFM imaging was carried out predominantly in tapping mode, setting the appropriate set-point values in order to minimise the interaction between the samples and the tips. Three simultaneous independent images were recorded: height, phase and amplitude. The comparison between the different images provides valuable information about the topography and the presence of different materials.

3.9.2.2. *Superhydrophobic Surfaces*

One of the main concerns when characterising polymeric film with AFM in contact mode is the shear force, which may deform the sample surface. On the contrary, intermitting contact mode eliminates almost entirely lateral forces yet, mismatch between the amplitude and the set-point values may lead to sample damage. After preliminary analysis of the polymeric features, the imaging has been carried out in intermitting contact mode.

AFM measurements were performed using a Nanoscope IV Dimension 3100 (Veeco Instruments Inc.) and a JPK Nanowizard microscopes, operating in tapping mode using two kind of cantilevers: NSG 20 cantilevers with a resonance frequency of 260 kHz and a force constant (k) of 28 Nm^{-1}, and PPP-NCL with a f_0 of 170 kHz and k = 40 N/m. Image processing and analysis were carried out with the instrument's software version V612r2 and V530r2 for the Nanoscope data, and V4.2 of the data processing software for the JPK instrument. *AFM* measurements yielded the geometric dimensions of the CNT-EHL and PS structures including the aspect ratio, the pitch between the generated morphologies, their heights and diameters.

3.9.3. SEM

Scanning electron microscopy was used to characterise the polymeric nano features produced in the following chapters. The scanning electron microscopy (*SEM*) measurements were performed using a LEO ULTRA 55 SEM including a Schottky emitter (ZrO/W cathode) at acceleration voltages of 1−5 KV with a lateral resolution of 2−5 nm. Low-angle backscattered electrons imaging mode was

used to contrast the non-coated VACNTs, and those sputtered with silicon, providing the atomic number contrast.

3.9.4. TEM

Transmission electron microscopy was used to characterise the polymeric and DNA nano-features and the CNTs. The samples were analyzed using a FEI Technai 12 transmission electron microscope at acceleration voltages of 80 or 120 kV. STEM images were also obtained using a Hitachi s5500 scanning transmission electron microscope with a cold field emission source and lens detector with 4 Å resolution, allowing adjustable acceptance angle STEM imaging.

3.9.5. Contact Angle Measurements

Contact angle and hysteresis were measured in 3 different areas *per* each sample. Every sample was repeated in a minimum number of 3 and a maximum of 5. A computer-controlled telescopic goniometer (KSV CAM 200) with a digital image acquisition was used at this stage. A numerical fitting algorithm was applied to determine the advancing and receding contact angles from the side-view of drops.

3.9.6. Optical Properties Measurements

As the last step into the manufacturing of optically-active surfaces with DNA generated micro-to-nanofeatures aimed for in this work, the preliminary characterisation of optical properties was further carried-out.

The detection of the optical signal is of fundamental importance when dealing with optically active materials such as plasmonic bandgap-or metamaterials. In this work, such signal has been recorded with a bespoke, home-built bench-top optical set up in the Cavendish laboratory (University of Cambridge, UK). Measurements were taken in collaboration with Dr Silvia Vignolini's Group (University of Cambridge, UK).

As shown in Figure 3.13, the beam is produced by a halogen lamp (a). The light passes through a polariser (b) and then to a condenser (c) and then, the sample (d) is placed. Passing through the latter, the light splits beam into an array of different wavelengths, *i.e.,* transmitted and scattered light, which is then collected by a 20x objective (e) and subsequently, collimated into parallel paths, which are selected by a second linear polariser (f). Undesired specular reflection [247] is blocked by keeping the polarisers perpendicular to each other. After the light gets to the beam-splitter (g), the beam is divided into two different paths toward the CCD and toward the spectrometer, where both are collected and analysed.

The term ballistic light, typical of the medical field imaging, refers to photons that that crosses a scattering medium, non-deviating from the direction of incident light.

In order to probe the **linear birefringence,** polarising measurements were taken by rotating the polariser (b) while and keeping the other polariser perpendicular (f) to it. Additionally, specular light is also blocked by keeping the polarisers perpendicular to beam-splitter (g).

When taking **spectral measurements**, the beam-splitter (g) is by-passed in order to avoid the polarisation-dependent attenuation and to double the signal intensity. After that, during the path to the spectrometer, a 50 µm fibre (h) is required to capture only the crystal signal, while minimising the background noise.

optical fibre (**h**)

Spectrometer

CCD

beam splitter (**g**)

linear polariser (**f**) — 90°, 105°, …

20x objective (**e**)

sample (**d**)

condenser (**c**)

linear polariser (**b**) — 0°, 15°, …

Lamp (**a**)

INCIDENT LIGHT → SCATTERED LIGHT →
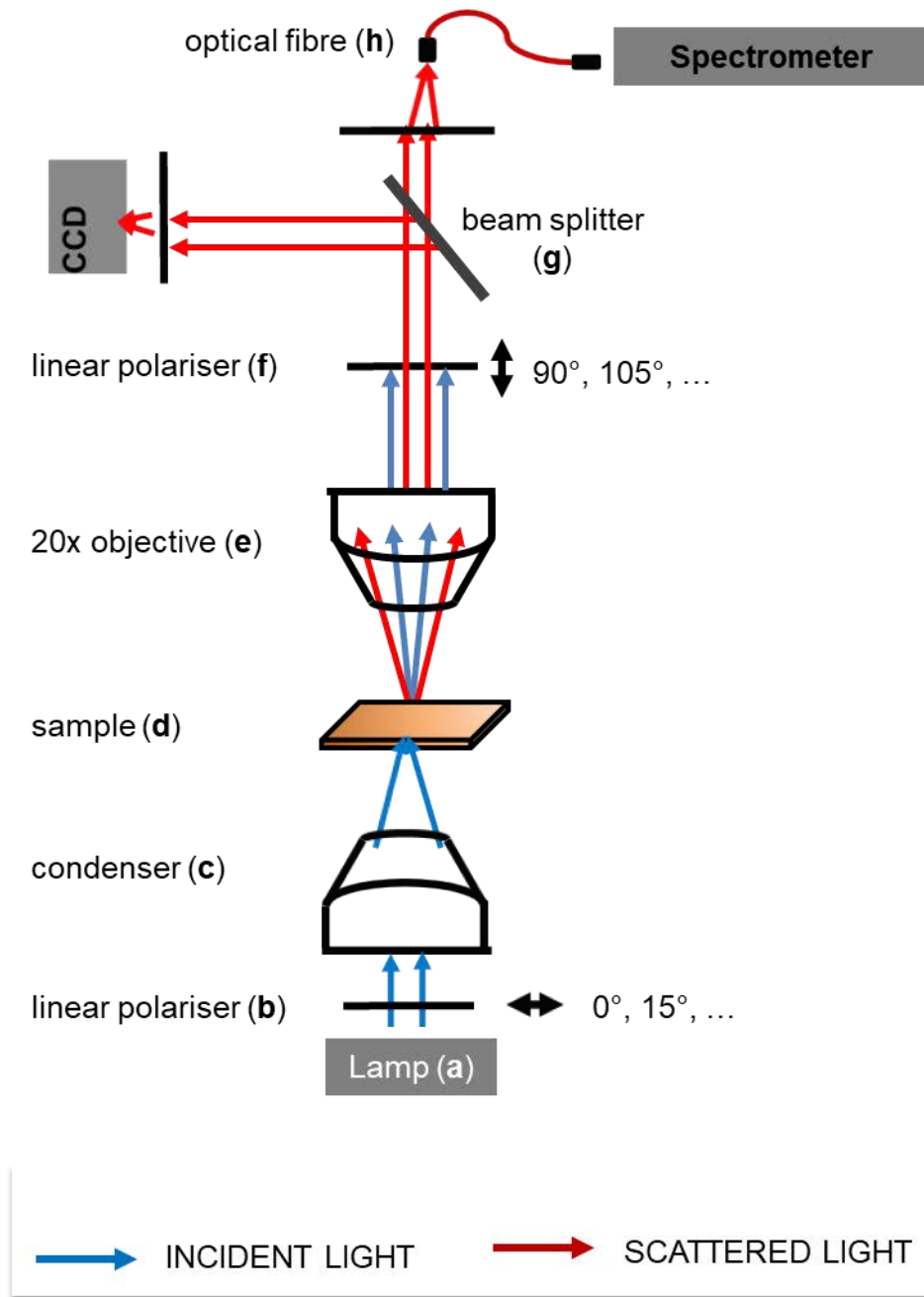
Figure 3.13. Schematics of the bespoken transmission setup. The components are typically mounted on optical bench.

4 Superhydrophobic Surfaces: Superapolar Lotus-to-Rose Hierarchical Nanosurfaces *via* Vertical Carbon Nanotubes Driven by Electrohydrodynamic Lithography

Novel evolving nanoscale structures have paved the way for manufacturing materials suited for the modern world demands, spanning from self-cleaning to anti-fogging materials. The high level of control and robustness from the macro to the submicron scale permits the production of perfectly tuneable materials, mostly using polymeric blends while combining various properties such as electrical and thermal conductivity, mechanical resiliency and hydrophobicity [11,17,53].

Concurrently, during the last decade, carbon nanotubes (CNTs) have attracted a wide research interest due to their unique electrical and thermal properties, coupled with robust structures, which allow the manufacturing of flexible, yet resilient devices [248–250]. Blending CNTs in polymeric matrixes enables an overall control over dispersion, orientation and surface chemistry of the materials as well as the tuning of the CNTs properties [39].

This chapter focuses on the development of a robust, cost-effective, scalable and simple technique that allows the design and construction of well-controlled large area superhydrophobic surface structures which can be easily switched from *lotus-leaf* to *rose-petal* state.

In this study, we introduce the carbon nanotubes-based electrohydrodynamic lithography (CNT-EHL), to fabricate unique multiscale structured cones and nanohair-like architectures with tuneable periodicities and dimensions, successfully enabling surface energy minimisation. The possibility of contact-less lithography *via* the CNT-EHL morphology replication combined with the electric field coupling to smaller self-assembled patterns within the film provides a way for hierarchical structure control spanning many length scales along with tunable wetting capabilities. By controlling the hierarchy of micro-to-nano cones and spikes, these morphologies offer a range of architectures with sufficient roughness for very low wettability, with the highest contact angle achieved of 173° and their properties can be easily switched between *lotus-leaf* to *rose-petal* behaviour.

4.1.   A Novel Approach towards Super-Apolar Surfaces

While electrohydrodynamic patterning was previously used to pattern dielectric, conductive and crystalline materials [101,233,251,252], in this work, for the first time, vertically aligned CNTs are exploited to generate master electrodes, which are further employed as top masks to produce and control the fabricated morphologies *via* the EHD. A wide range of reusable CNT-based electrodes with

99

various morphologies and dimensions is, therefore, fabricated, enabling a direct patterning with tuneable dimensions from the material of choice and with no need of functionalisation (*i.e.,* inexpensive, no processing equipment), obtaining robust and highly reproducible structures which exhibit hexagonal packing symmetry. Nanohair-like structures, cones, coupled with sharp spiky micro and nanoarrays which are typically difficult to manufacture, are successfully produced *via* the CNT-EHL [39,232]. The single-step EHD process, which allows easily tuning dimensions, pitch, aspect ratio and cone tip curvature, enables the fabrication of micro-to-nanoscale roughness while utilising low-energy materials. A precise tailoring and a controlled hierarchical geometry are determined by adjusting the patterning parameters which significantly influence the surface wetting properties and enable the mimicking the various regimes found in nature. Therefore, EHD enables alternating systems between the "lotus-leaf" and "rose-petal" states, mostly due to the controllable experimental approach, which leads to the ultimate morphologies generated while patterned from the same initial material (Fig 4.1.). The fabricated superhydrophobic surfaces possess either self-cleaning and adhesive properties, which stand as promising prospects for both the fundamental research of submicron scale superhydrophobicity and also toward broader applications, for instance, in anti-fouling and microfluidics. CNT-EHL therefore, opens a new path for the production of a broad spectrum of high-fidelity superhydrophobic patterns in a straightforward and low-cost fashion, requiring no vacuum processing or no hazardous organic compounds, with possibilities of exploiting biodegradable and environmentally-friendly apolar polymers, rendering this technique even more technologically appealing.
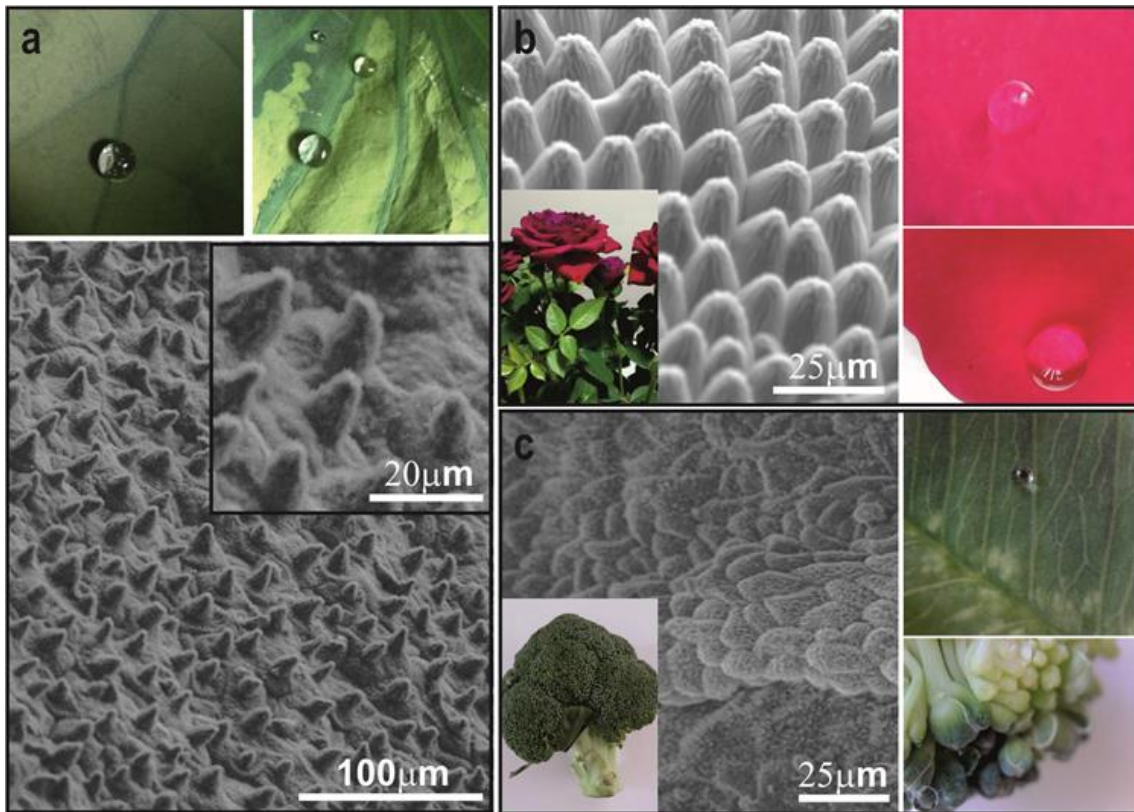
Figure 4.1. Optical images of natural hierarchical superhydrophobic materials. a) Optical images of the spherical water droplets rolling-off the natural *Nelumbo nucifera* (lotus leaf) and the corresponding scanning electron microscopy (SEM) image of the surface topography of the lotus-leaf with the higher magnification of the lotus surface shown in the inset. **b)** SEM image of the structure found on the *rose* petal and the corresponding photograph pictures of spherical water droplets sticking to the rose-petal surface. **c)** SEM image of the microstructure found in *broccoli* and the corresponding optical images of its superhydrophobic properties

4.2.   Superhydrophobic Surfaces and Overview of the Wetting Regimes

As a requirement for a living organism, water has a fundamental role at each stage of life. Mammals, plants and insects, all have at least a water content of 60% in their bodies and without its continuous exchange with the surrounding environment, existence would not be possible. Similarly, whenever water is in

large excess organisms are also threatened [253,254]. In turn, water-repellent systems are common in the natural world and the various structures that allow such superhydrophobic behaviour have been widely studied [255,256]. Superhydrophobicity is defined as the property of "repelling water to the degree that droplets do not flatten but roll off instead" or even bounce away [257,258]. Water-repellent surfaces are acknowledged to have a high-potential in modern devices which require anti-splash or complete dryness of their parts, for example, mobile phones or cameras [57]. Thus, in our work, we have been exploiting an alternative pathway to manufacturing a range of novel superhydrophobic surfaces properties which can be easily tuned by modulating the fabricated surface structures.

Super-apolar (or superhydrophobic) surfaces show unusual self-cleaning properties which find various applications in modern technologies, ranging from coatings for windows, clothes and car windshields to the anti-corrosive covering for aircraft and marine vessels to antifogging and anti-icing finishes [57]. The combination of the surface topography and chemical composition at the air-liquid interface enables the ability to let liquid droplets, in contact with the surface, to roll off at low angles [257]. Therefore, six different models were developed to describe the correlation between the surface roughness and the wettability properties, that will be discussed below in more details [259–262].

The fundamental parameter characterising these wetting models or states is the *static contact angle* (CA) formed by a liquid droplet on a surface [257–263]. The surface roughness, coupling with surface energy, determines the angle, which is also dependent on the cleanliness of the materials. The liquid may wet the

surface forming a CA < 90°, and the substrate is considered *hydrophilic*; whereas, when the CA is 90° < θ < 180° the surface shows *hydrophobic* properties. However, for extreme values such as CA below 10°, surfaces are defined as *superhydrophilic*, and for CA values above 150° as *superhydrophobic* (Fig. 4.2).
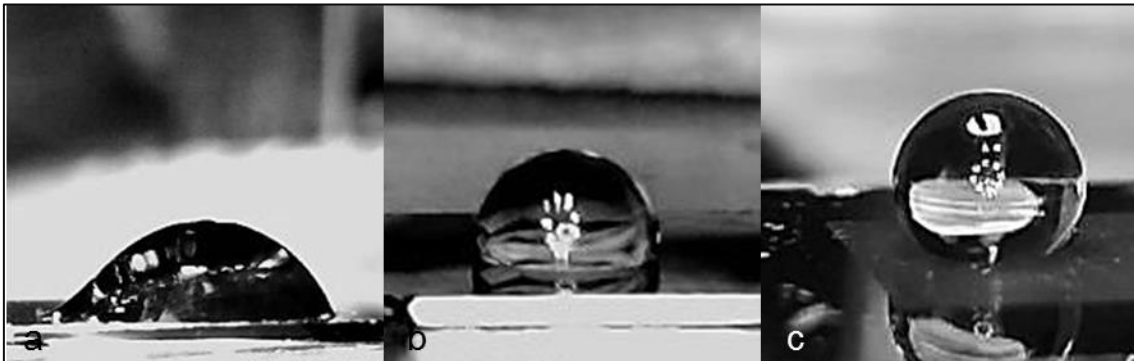
Figure 4.2. Behaviour of a water droplet when deposited on surfaces with an increasing hydrophobicity. a) 100 nm Polystyrene film on silicon; **b)** micro-to-nano patterned Silicon; **c)** Fluorinated micro-to-nano patterned Silicon.

It is well-established that high energy surfaces, usually formed by polar components, have the tendency to be hydrophilic while low energy surfaces, formed by apolar components, tend to be hydrophobic [264–266]. At the same time, the surface atoms (or molecules) in both solids and liquids have a smaller number of bonds compared to the bulk atoms. Hence, their energy is higher than the internal ones. Thus, whenever a liquid is in contact with a solid, attraction forces will lower the energy of the whole systems compared to the energy of two individual surfaces [53,267]. The equilibrium of the liquid and solid will result in a characteristic static CA, which relates to the surface energies formulated by *Young*'s equation (Eq. 4.1):

Equation 4.1. Young's equation.

$$\gamma_{\mathrm{SV}} = \gamma_{\mathrm{SL}} + \gamma_{\mathrm{LV}} \cos\theta$$

where γ is the surface tension, θ is the contact angle, and SV, LV, SL are the solid-vapour, liquid-vapour and solid-liquid interfaces, respectively [261,266]. According to the Eq. 4.1, a hydrophobic material has an inherent water contact angle above 90°, and a hydrophilic material has an inherent water contact angle below 90°. This is because, for most materials $\gamma_{\mathrm{SV}} + \gamma_{\mathrm{LV}} > \gamma_{\mathrm{SL}}$, and therefore, it is energetically favourable for a liquid to wet a solid surface, whereas the presence of air pockets and surface roughness, which enhances the wetting properties of the materials, is unlikely to happen [264–266]. Also, a solid in direct contact with air is an energetically more favourable condition in comparison to a liquid entirely covered by another liquid and therefore, the CA depends on the local surface energy and molecular arrangement, excluding any dependence on the liquid contact area [262].

When the solid surface is progressively tilted, the equilibrium among the three phases, vapour, solid and liquid, starts to change and the resulting contact angle will be defined as *dynamic* CA [268]. The CA at the front of the droplet (advancing CA, θ_{adv}) will differ from that at the back (receding CA, θ_{rec}) and the difference between the two values represent the contact angle *hysteresis* (Hys), which has a fundamental role for self-cleaning surfaces [53,267,269]. Hysteresis has also been discussed whether being a key condition for superhydrophobicity, as the typical high CA is mostly accompanied by a small CA hysteresis, which is related to the surface roughness and homogeneity and a further contribution is given by

the surface energy which also includes an "adhesive hysteresis" factor [270] (Fig. 4.3).
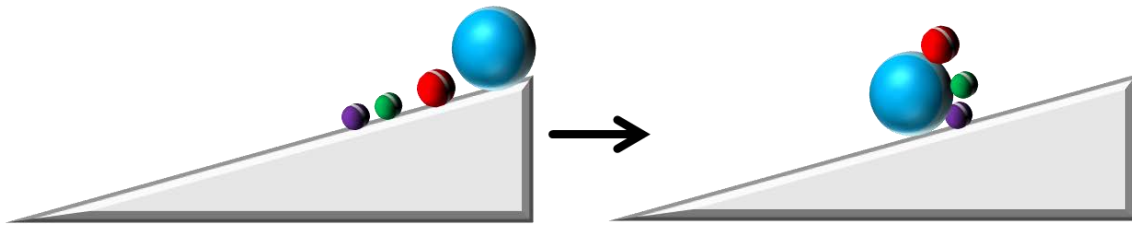
Figure 4.3. Contact angle hysteresis. CA hysteresis has a fundamental role in self-cleaning surfaces, since it has a direct correlation with the adhesive properties and effectively allows the water droplet rolling off the surfaces as well as to "stick" to the particles or contaminations and therefore, remove the residues on the surface.

In recent years, due to the broad potential, the unique water-repelling properties known as the '*Lotus-Leaf*' effect [262,271–273], have centred research efforts towards developing artificially engineered surfaces, able to biomimic these properties.

Natural patterns exhibit different wettability behaviour predominantly depending on the surface roughness, that can be divided among six main models: the classical Wenzel, Cassie-Baxter and the transitional regime between the Wenzel and Cassie-Baxter. In addition, the "Lotus", "Gecko" and the "Petal" states have been lately differentiated [12,55,108,110,259,262,269,274–276].

4.2.1. Wenzel's Model

Wenzel's theory [262,277–279] is built upon the assumption of complete contact between the liquid and the surface, establishing that, regardless the roughness and the hydrophobicity of the surface in contact, the liquid completely penetrates every asperity of the solid part. The wetting behaviour of a droplet

homogeneously adhering to the surface during the contact is described by the *Wenzel*'s equation (Eq.4.2):

Equation 4.2. Wenzel's equation.

$$\cos\theta = \rho \cos\theta_0$$

Where ρ is the roughness, θ_0 is the static CA for a smooth substrate and θ is the static CA for a rough surface [259,280–282]. Wenzel has described the roughness factor as the ratio between the actual surface and the geometric surface and the mutual dependence with the contact angle (Fig.4.4.a).
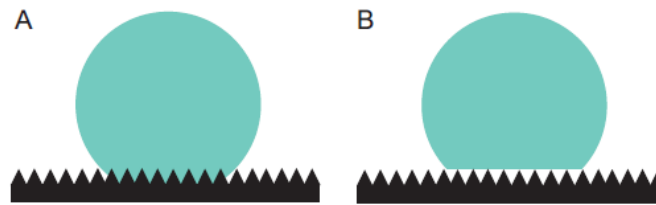
Figure 4.4. Wenzel and Cassie-Baxter wetting regimes schematics. Wetting on hydrophobic rough surfaces with a **a)** Wenzel drop and with a **b)** Cassie-Baxter drop.

4.2.2. Cassie-Baxter Model

The *Cassie-Baxter's* model exploits the most energetically favourable state for a water droplet when in contact with a composite dual-layered surface structure [277,283–285]. In *Cassie-Baxter's* theory, the droplet can bridge across the top of the asperities of the surface, trapping air pockets beneath the liquid and thus, enhancing the superhydrophobicity. Furthermore, the small contact area between the liquid and the solid phase and the resulting small contact angle hysteresis, allow the drops to easily 'roll off' a surface due to the presence of air pockets [17].

Cassie-Baxter wetting (Fig. 4.4.b) is characterised by the drop located on the peaks of the surface structures which does not penetrate into the deeper holes. This air-pocket state corresponds to partial non-wetting of the surface, which is the most favourable solution for the energy equation for very rough hydrophobic materials:

Equation 4.3. Cassie-Baxter's equation.

$$\cos\theta = \varphi_s(cos\theta) + (1\text{-}\varphi_s)\,cos\theta_X$$

where, φ_s is the fraction of surface available at the top of protrusions, and θ_X is the contact angle with the vapour in the gaps (usually taken as 180°).

Cassie-Baxter model is often called the superhydrophobic wetting, and it has been observed by Barthlott *et al.* [17] on the surface of *Nelumbo Nucifera*, commonly known as the 'Lotus Leaf Effect'. Superhydrophobicity has been studied on various surfaces including, for instance, periodically structured micropillars, biomimetic superhydrophobic structures, carbon-nanotubes based surfaces, alumina nanowires, silicon 'nanograss' and fibrous textile surface structures [263,271,273,279,286,287].

4.2.3. Cassie Impregnating and Rose-Petal Wetting State

The *transitional regime* between the *Cassie-Baxter* and *Wenzel* state [262,282,288] usually exhibits high contact angle hysteresis and depends on the dimensions and gaps between the surface roughness structures as well as the

chemical hydrophobicity, thought the history of the whole system might change

the water repellent behaviour intensity [289].

As a transition from the "traditional" models, the *Cassie-Baxter* wetting

impregnating state is mostly applied to inhomogeneous surfaces with varying

roughness. For this model, it is fundamental to introduce the concept of *apparent*

contact angle (Figure 4.5.b) as the inhomogeneous advancing of the wetting

front, which depends on the surface roughness. In turn, the triple-phase line is

pinned to a range of values which differ from the observed macroscopic CA, as

shown in Figure 4.5.a-b [290–292].
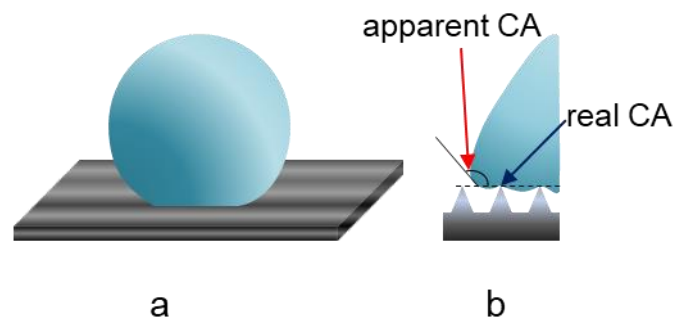
Figure 4.5. Apparent contact angle schematics. Example of **a)** a water droplet on a rough surface and **b)** the difference between the macro- and the microscopic CA, which leads to the definition of apparent CA.

In particular, the *Cassie-Baxter wetting impregnating* model is acknowledged for

specific solid/ liquid couples which show lower values of the apparent contact

angle compared to the expected ones following the Wenzel and Cassie-Baxter

models. This is due to the three-dimensional heterogeneity of the surface.

The impregnating state [270,284], depicted in Figure 4.6 can be determined using

the following equation (Eq 4.4):

Equation 4.4. Cassie impregnating wetting state equation.

$$\cos\theta = 1 - f_s + f_s cos\theta$$

where, f_s is the solid fraction underneath the liquid drop. However, for this Cassie impregnating state to be viable, it must satisfy (Eq. 4.5):

Equation 4.5. Cassie impregnating state's condition.

$$cos\theta = \frac{1 - f_s}{r - f_s}$$

where, *r* is the radius of the surfaces topographies. A classic example in nature of a Cassie impregnating regime is the *Rose*'s petal, also known as the '*Rose Petal* Effect' [262,288]. The water film is able to impregnate the surface by seeping into the larger crevices, but not the smaller ones. Therefore, the water drop, depending on its size, can attach to the surface due to the very high adhesive forces.
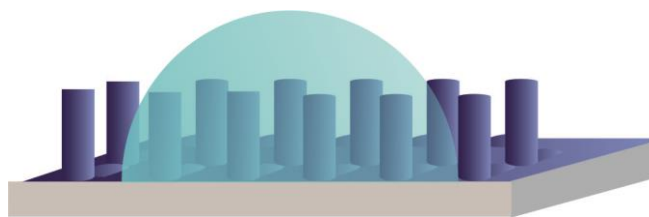
Figure 4.6. Schematic representation of the Cassie-Impregnating wetting state.

4.2.4. Combined Rose-Petal and Lotus-Leaf Wetting Regimes

An additional possibility exists when a liquid droplet may not bridge the gap on a rough surface completely. Unlike Wenzel's model, where a liquid film must be

present before the droplet is deposited on the surface, the combined wetting

model requires an initially dry rough surface [260,269,293–295]. Without a liquid

film, the drop might spread below the flat surface, as occurs on surfaces such as

sol-gels and soils, where internal spreading can occur rapidly, resulting in a

combined Wenzel's and the Cassie-Baxter model, which gives the effective

macroscopic water contact angle for Cassie-Baxter wetting [285] (Eq. 4.6):

Equation 4.6. Combined Wenzel and the Cassie-Baxter model's equation.

$$\cos \theta_{CB} = f \cos \theta + f - 1$$

where *f* is solid fraction of the surface structures.

The roughness of the fraction of the surface in contact with the liquid, r_f, also

controls the surface wetting properties, and a more specific definition of the air-

pocket state can be given by (Eq. 4.7):

Equation 4.7. Air-pocket state's equation.

$$\cos \theta_{CB} = r_f f \cos \theta + f - 1$$

Ishino *et* al. have theoretically studied the cross-over between *Wenzel* and

Cassie-Baxter wetting [293] for pillar arrays and suggested that the penetration

versus air-pocket state wetting depends strongly on the roughness r_f and the solid

fraction *f*. The roughness of liquid/ solid contact was further calculated according

to the threshold value of slope and the top hemispheric model taking into the

consideration the roughness of both micro and nanostructures [296]. The contact

angle of rough surfaces (*i.e.,* cone structures and CNT-like surfaces) with *lotus-

leaf* effects can be extracted from the modified *Cassie-Baxter* equation (Eq. 4.8):

Equation 4.8. *Lotus-leaf* model equation.

$$\cos \theta_r = \rho f_s \cos \theta - f_v$$

where, θ_r is the apparent contact angle of the micro- and nano-structured surfaces, f_s is the fraction of the areas occupied by the solid-water interface and f_v is the fraction that corresponds to the vapour gaps, θ is Young's contact angle and ρ is the roughness factor, which can be simplistically calculated from triadic curve for fractal geometry [297] (Eq. 4.9):

Equation 4.9. Roughness factor.

$$\rho = (R/r)^{D-2}$$

where R and r are respectively, the upper and the lower dimensional limit of the fabricated and studied features.

For a hexagonal array of cones, the area fraction of the solid surface that is in contact with the liquid is given by $f_s \approx \frac{\pi}{4\sqrt{3}}(r/R)^2$.

More recently, the existence of additional wetting modes has been fully established [57,261,291], recognising super water-repellent modes such as the renowned 'Lotus-Leaf' state, which is characterised by the combination of a strong water adhesion and super-hydrophobicity. Hence, the distinction among wetting regimes of a surface has been focused on the level of organisation of the roughness and if achieved, the hierarchical levels within.

The *Lotus-leaf* wetting regime was proposed by Barthlott and Neinhius in 1997, following observations of the self-cleaning and superhydrophobic behaviour of

the *Nelumbo Nucifera* [298]. The combination of the hierarchical surface structure and low surface energy enables a wetting mode which minimises the adhesion with the leaf itself while capturing and removing the "dirt" in the water that is repelled. In fact, the "dirt" is usually comprised of more hydrophilic materials than the wax-based surface [298,299] and moreover, these particles are larger than the minute leaf mesostructure. Thus, since the interfacial area between the liquid and solid phase is minimised, trapping the air within the nanogaps, the "dirt" particles are captured by the water droplet while rolling off (Fig 4.7).
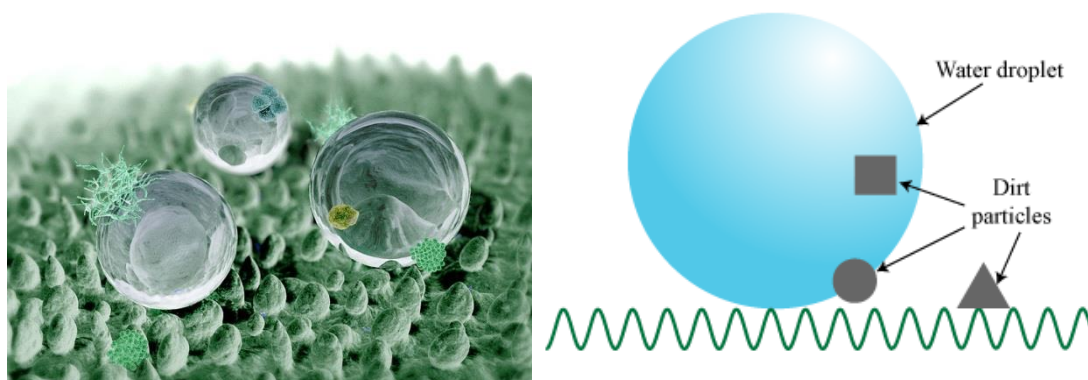
Figure 4.7.Lotus-leaf wetting regime and self-cleaning properties. a) Digital image of a Lotus-leaf surface at the micro- and nanoscale, reproduced from William Thielicke's website More pictures and bionics. **b)** Lotus-leaf self-cleaning effect schematics.

4.3.   Carbon Nanotubes

Carbon nanotubes (CNTs) were first observed in the early 1950's although, their full potential was fully realised by Iijima [300] as late as in 1991 when the crystalline structure of hollow CNTs was observed for the first time. It was a unique carbon (C) structure with a sp^2 C hybridisation, shaped as nano-metric tubular hollow fibre yet, 100 times stronger than steel and dramatically lighter,

with thermal and electrical conductivity properties comparable to the well-known conductors such as, copper or aluminium [248].
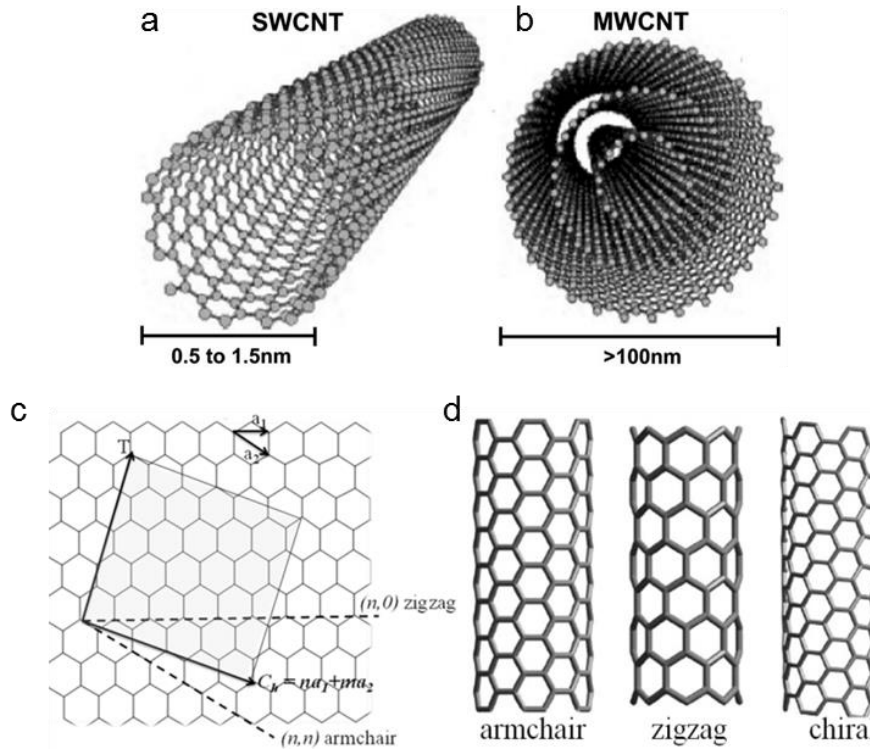
Figure 4.8.Carbon nanotubes. a-b) Carbon nanotubes (CNTs) can be synthesised as single-walled (SWCNTs) or as multi-walled (MWCNTs), which are comprised of several layers of SWCNTs. **c-d)** Three relative mutual orientation of the carbon atoms, depending on the axis upon which the CNTs have been rolled up, are named as armchair, zigzag, and chiral and determine wide differences in the mechanical properties of the CNTs [301].

Carbon nanotubes can be generated as single-wall CNTs (SWNTs), comprised of a single graphite sheet seamlessly rolled on itself in a 1 nm diameter tube or, as multi-wall CNTs (MWNTs), with diameters varying from 2.5 to 70 nm, depending on the number of concentric graphite sheets comprising the MWNTs (Fig 4.8.a-b). CNTs can be produced with different length and diameter, and are always characterised by an extremely high aspect ratio since the length can easily achieve several microns (Fig 4.8.c-d) [250]. Carbon nanotubes are also

known to be highly hydrophobic and therefore, insoluble in water or polar solvents. However, when subjected to chemical or electrical treatments, CNTs' properties can be switched to the hydrophilicity.

Importantly, carbon nanotubes have been used for producing superhydrophobic surfaces, mostly using *top-down* techniques such as soft lithography. For instance, Sun *et al.* [302] widely studied the changes in the wetting behaviour of vinyltrimethoxysilane (VTMS) and (2-(perfluorooctyl) ethyl)trimethoxysilane (FETMS) before and after treatment with arrays of CVD-grown CNTs, depicted in Fig. 4.9.
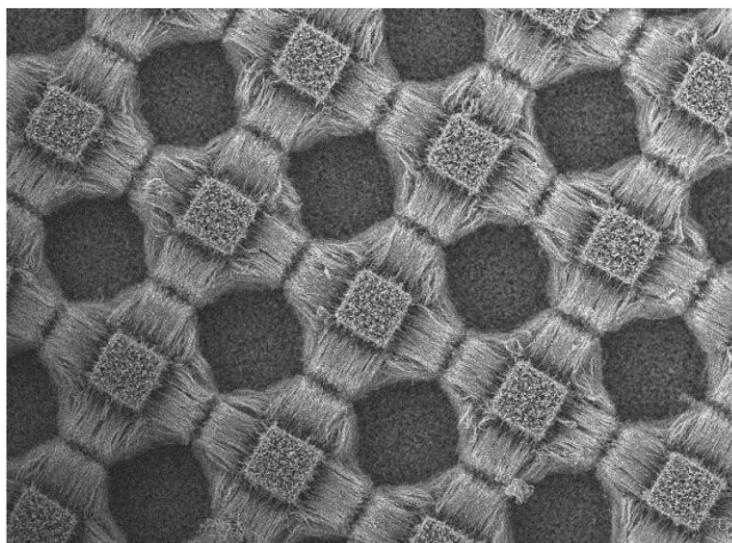
Figure 4.9. Carbon Nanotubes in arrays. Reprinted with permission from [302]. Copyright 2003 American Chemical Society.

4.4.　　Roadmap of the Study

The manufacturing of hierarchical superhydrophobic structures is comprised of the following stages as described in Fig 4.10.

The production of both top and bottom electrodes represents a preliminary step, prior to the water-repellent surface production process.
While the bottom electrodes carry the liquid film to be patterned, the top electrode can be comprised of various structures. All the features were characterised by Scanning Electron Microscopy (SEM) imaging.

In a later stage, a capacitor-like device comprised of both top and bottom electrode separated by a distance, d using standard polystyrene beads as spacers was assembled. After being placed in an oven for controlling the overall temperature, a voltage (V) was applied to the assembled device. The various features of the top electrode have driven the film build-up into micro-to-nano structures. The surface topography was characterised by AFM and the wettability properties were observed with a goniometer.
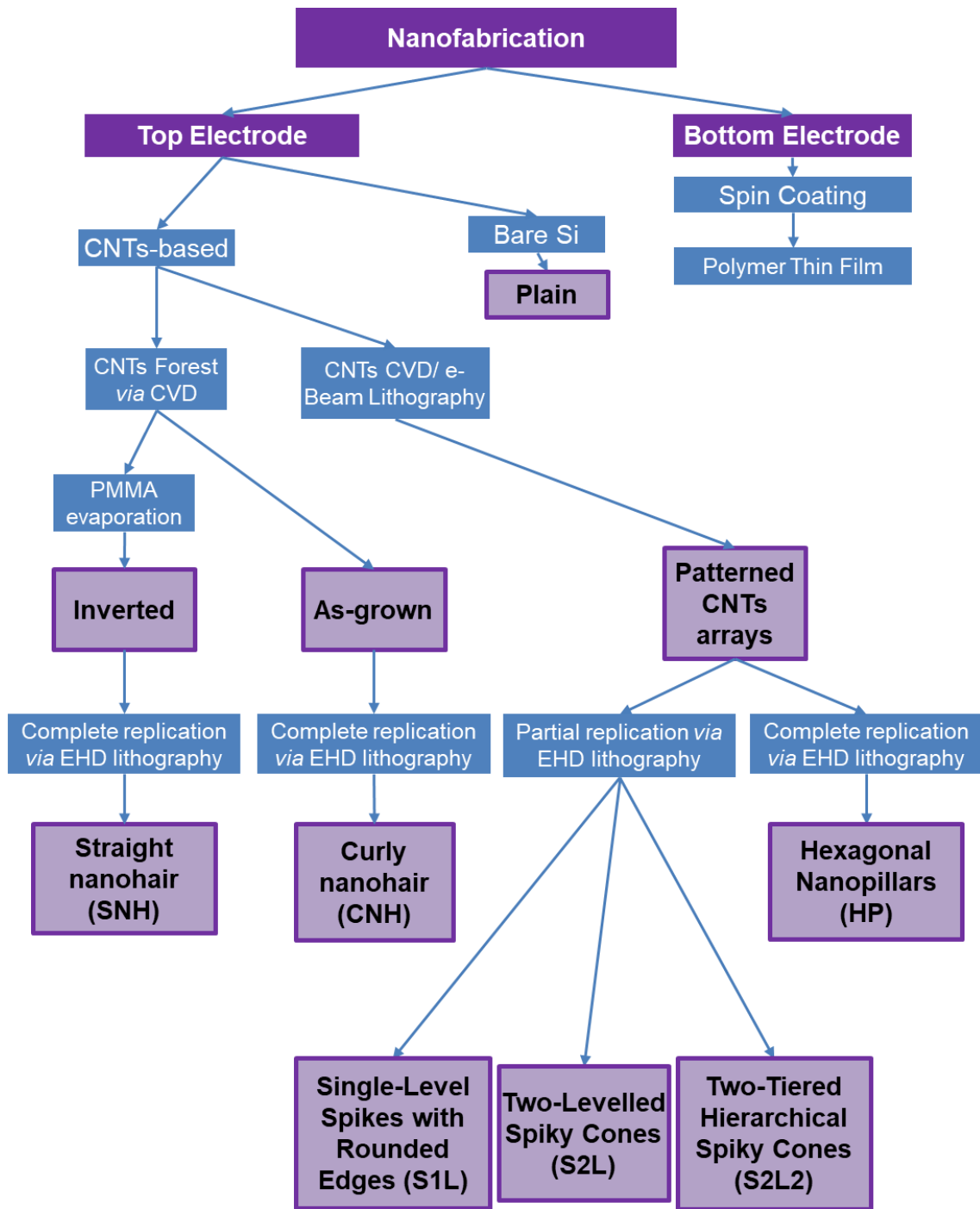
Figure 4.10. Carbon-Nanotubes (CNTs) EHD lithography flow-chart overviewing the roadmap of this study.

4.5.　　Fabrication of the Top Electrode for CNT-EHL

The CNT-EHL method requires assembling a miniaturised capacitor-like device, which is comprised of two parallel electrodes. The bottom electrode is comprised of silicon wafer topped with a thin nanofilm spin-casted from the polymer to be patterned, while the topographically structured top electrode carries a pattern of interest to be replicated.

A range of master electrodes were fabricated based on vertical CNTs including vertically aligned carbon nanotube (VACNT) forests both *as-grown* and *inverted* (as seen in Figure 4.11), as well as a range of VACNT-based micro- and nanostructures (Fig. 4.13).
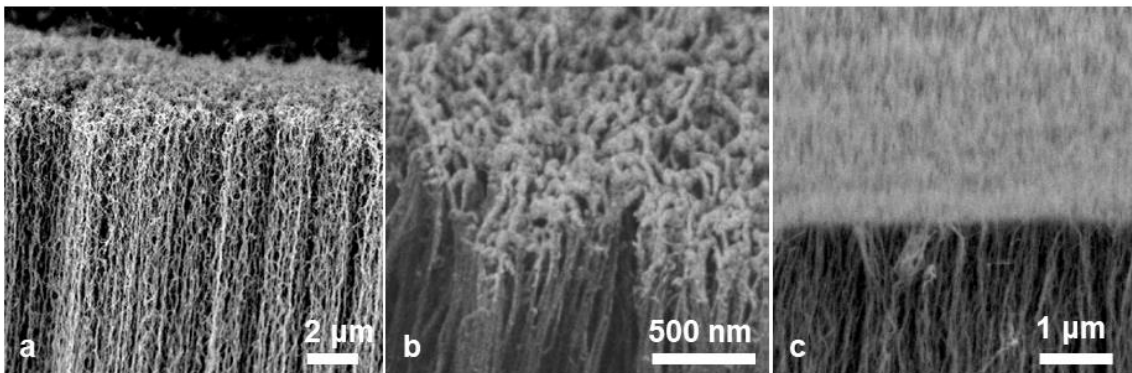
Figure 4.11. CNT electrodes SEM images. a-b) *As-grown* CNTs forest at different magnifications, b) inverted CNTs forest after being flipped over.

The overall procedure for the fabrication of the CNT-based master electrodes for the EHL is illustrated in Figure 4.15 (also, see Section 3.3.3). Vertically oriented CNT forests were either grown *via* chemical vapour deposition (CVD) to achieve substrates of nanotube arrays with well-defined and stable large area (Figure 4.14.a-b, top) or were flipped over to generate better defined, straighter CNT tips

(Figure 4.14.b, bottom). Various VACNT site-densities can be obtained *via* CVD process, allowing to control the nanogaps in the final masks used for the CNT-EHL, as shown in Figure 4.12. Throughout carefully monitored CVD process, a range of site densities of the VACNTs between 7% and 30% were accomplished and have been quantified by *liquid-induced compaction* method. Isopropanol was added to the samples and been allowed to dry leading to the collapse of the CNT forests. The percentage of the aggregated CNTs was then calculated by the fraction of the number of pixels of the aggregated forest areas divided by that of the entire image.
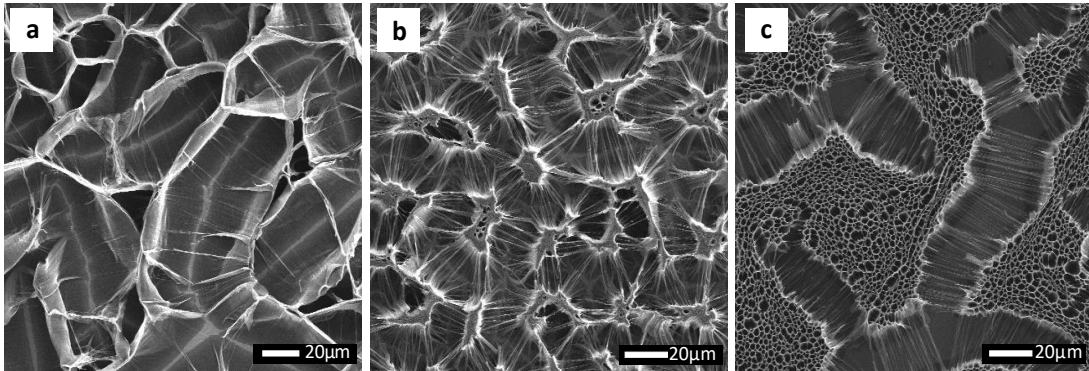
Figure 4.12. Top view SEM images of coagulated CNTs forests following the liquid-induced densification by isopropanol. a-c) CNTs with various densities (10^{10}-10^{12} cm^{-2}) and coverage of 7%, 15% and 30%, respectively.

Furthermore, VACNT-based morphologies were also designed and fabricated by prewriting the location and dimensions of CNT growth areas, generating patterns of arrays of pillars with various pre-designed height, diameters and pitches (*e.g.,* arrays with ranges of 1-5 µm diameter and with a 1.5-5.5 µm pitch between the individual pillars (Fig. 4.13).
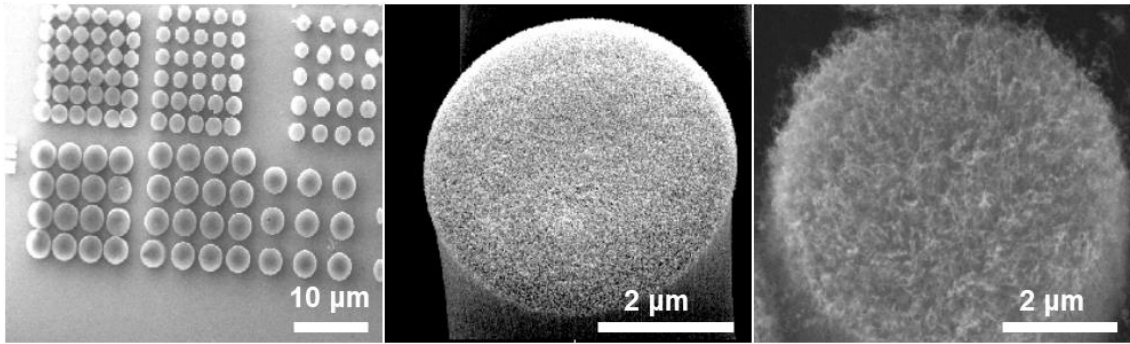
Figure 4.13. VACNT-based morphologies as top electrodes. Growth from the careful combination of e-beam lithography and CVD, electrodes were orderly patterned into arrays of pillars of various dimensions and pitch.

The bare VACNT arrays were transformed into master electrodes by sputter-coating the arrays with a 10 nm thin silicon layer, which uniformity was confirmed by high-resolution scanning electron microscopy of the uncovered CNTs masks (Figure 4.13.) and the low-angle backscattered SEM images of the Si-coated VACNT electrodes.

Additionally, a simple silanisation process (see Chapter 3.1.2) enabled rendering the oxidised Si surface increasingly apolar [303], leading to the consequent reduction in adhesion of the CNT-EHL patterned material to the silicon surface. Therefore, the fabricated CNT-based master electrodes can be used numerous times for CNT-EHL process without undergoing any deformation or damage. The coated VACNT arrays were then used as master top electrodes in the EHL assembly (Fig 4.14).
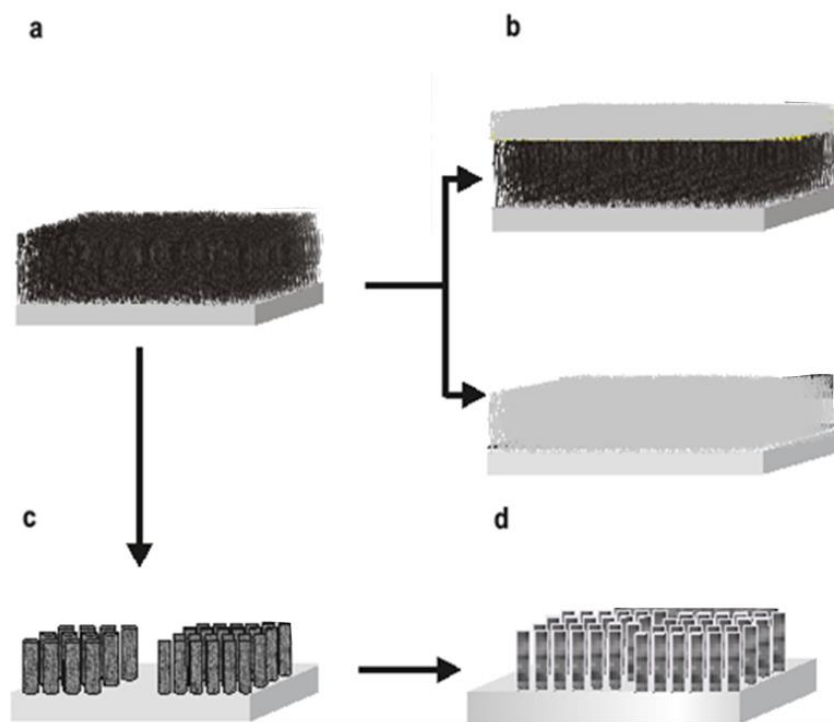
Figure 4.14. **Fabrication of novel vertically aligned CNTs-based electrodes for the EHL patterning.** Schematic representation and the corresponding SEM images of **a)** CNTs arrays fabricated using the chemical vapour deposition process (CVD) and electron beam (e-beam) lithography combined with CVD growth process and **b)** subsequently coated with a thin silicon layer to produce a range of top electrodes for EHL. Either as-grown (top) or inverted (bottom) arrays can be generated. **c)** Small-diameter VACNT forests patterned into predesigned pillar structures with various dimensions, and pitches are further utilised and coated with silicon **d)** generating a broad range of masks for the CNT-EHL.

The careful control of parameters such as the inter-electrode spacing (d), the applied electric field (E_f), the initial film thickness (h_0), the patterning and termination times (τ_0 and τ_f) allowed to fine-tune the desired hierarchical morphologies from the polymer of choice. Since accomplishing the superhydrophobicity of the manufactured surfaces requires a combination of both physical structure and chemical properties, we have exploited Poly(chlorotrifluoroethylene) (PCTFE) with a static contact angle (θ_0) of water

drop on a smooth film of 119 ± 3° for the EHL patterning to obtain the lowest possible surface energy properties from the final morphologies [99].

The inter-electrode distance, *d* and tilting angle in EHD lithography concur in providing favourable conditions for initialling the polymer bridges which lead to the final patterning. The position of the standard PS nanospheres (3000 Series Nanosphere™ Size Standards by Fisher Scientific) used as separators were investigated by AFM imaging, which also allowed cross-section calculation. As expected, the mean radius of the 200 nm standard nanospheres measured 201 ± 4 nm, against the provided information of 202 ± 3 nm. Figure 4.15 illustrates a possible surface disposition of the nanospheres after drying, showing a single monolayer, which separates the top and bottom electrode.
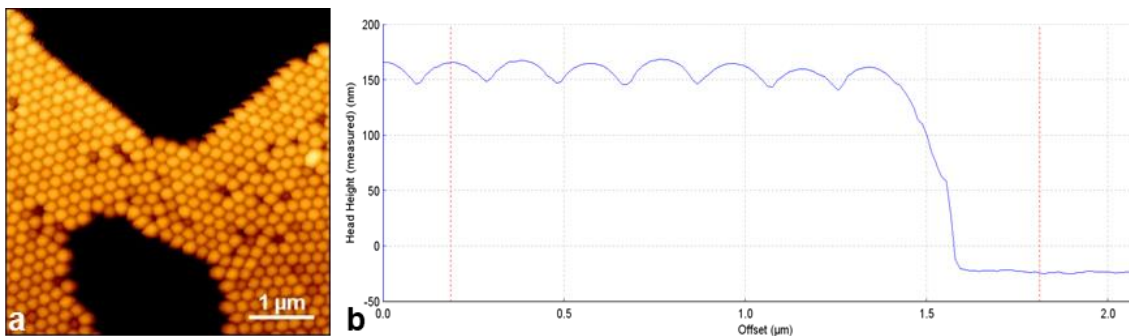
Figure 4.15. PS standard nanospheres as spacers. a) PS nanospheres deposited onto polymers layer on Silicon wafer before capacitor assembly, and **b)** the related cross-section.

The processes involved in CNT-EHL patterning are shown in Figure 4.16. A topographically structured top electrode (comprised of either CNTs arrays or CNTs forest) induces high lateral electric field variations in the capacitor-like device. In addition, (see Eq. 4.10) since the electrostatic pressure, p_{el}, is inversely

proportional to the square of the capacitor gap, *d*, the downward protruding structures of the top mask generate locations with the highest electrostatic pressure. In turn, the evolving wave pattern instabilities in the thin polymer film are coupled to the heterogeneous electric field and driven upwards, eventually spanning the capacitor gap. Once the correct sample parameters are identified, high-fidelity pattern replication over the entire electrode area is obtained during the patterning process, as also previously successfully demonstrated for the elctrohydrodynamic patterning method [39, 100-101]. The top mask, once fabricated, can be used numerous times for patterning (following cleaning with a snow-jet and sonication), reproducibly generating morphologies of interest, given that the identical excremental settings *i.e.,* initial film thickness, electric fields strength, inter-electrode spacing and patterning time are used.

In Eq. 4.10., ε_0 and ε_p are, respectively, the medium permittivity in a vacuum and of the polymer, *V* is the voltage applied, *d* is the inter-electrode distance, and h is the polymer film thickness.

Equation 4.10. Electrostatic pressure.

$$p_{el} = -\frac{\varepsilon_0 \varepsilon_p V^2}{2[\frac{\varepsilon_p d - h}{(\varepsilon_p - 1)}]^2}$$

The CNT-EHL pattern replication kinetics, shown in Figure 4.16.a-c, consists of three integral, yet well-separated, parts [304,305].

Thus, the overall process includes (a) the *amplification* of a capillary surface instability triggered by applying an external voltage, which with time causes (b)

the *formation of liquid bridges* between the two electrodes and eventually, (c) this seamless sequence of capillary instability results in *the coalescence* of the initial capillary plugs bridging the substrates and the protruding parts of the top electrode, forming positive replicas of the imposed master pattern (Fig. 4.16.c).
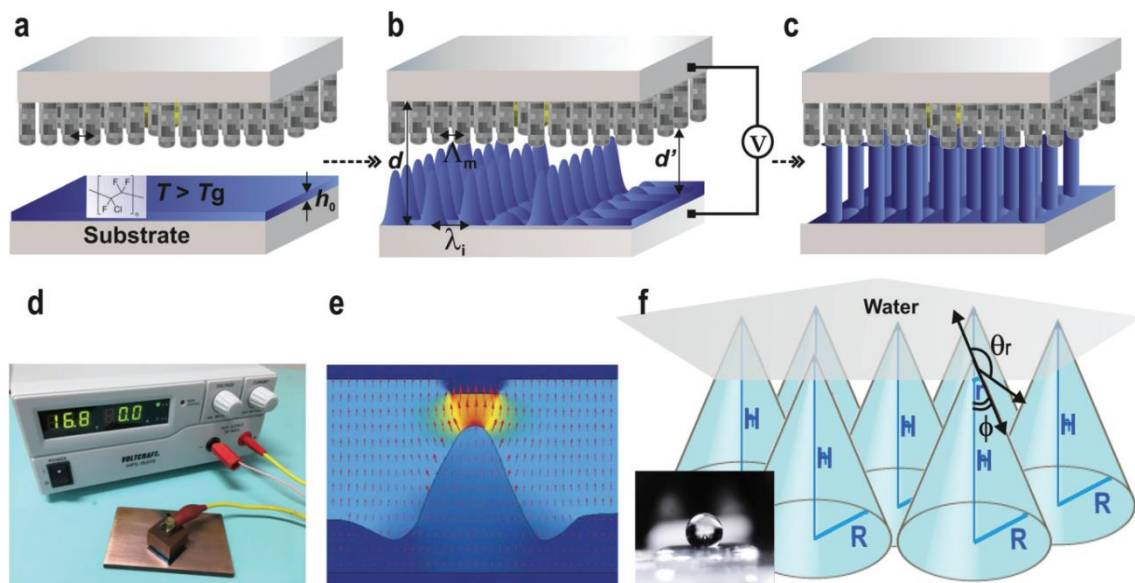
Figure 4.16. CNT-EHL based method. Placing the CNT-based top electrode above the **a)** initially homogeneous thin PCTFE film with thickness, h_0, **b)** liquefying it above the glass transition temperature (Tg) and subsequently, **c)** applying a voltage, V, into the capacitor-like device with the controllable inter-electrode distance, d, triggers the amplification of a surface instability with the intrinsic film undulation wavelength, λ_i. This instability, with time, leads to the formation of liquid bridges between the two electrodes. The kinetics of pattern formation allows the termination of the patterning process in each stage of either the **b)** cones or **c)** pillars with locations predetermined by the top electrodes, at which the electrostatic pressure is the highest. The profile of the generated pattern depends on the ratio of λ_i and the lateral periodicity of the master top plate, λ_m. The sharp tips of the VCNTs-based electrode enable to obtain the spiky replicas as well as 'sharp' cones. **d)** A photograph of a representative experimental CNT-EHL rig consists of an assembled miniaturised capacitor device with the patterned film on the bottom electrode and the CNT-based top master electrode connected to an external voltage supply. **e)** Electric field distribution during EHL pattern formation [251]. **f)** Schematic of the geometrical parameters of the cone/spike-like structure upon wetting and a representative optical image of a water drop on the CNT-EHL patterned surface (inset).

Since the confinement of the redistributing fluid polymer morphologies is organized accordingly to the ratio of the electrode spacing and the initial height of the polymer film in the capacitor gap, *i.e.,* the filling ratio, f_r ($f_r = h_0/d$) the pattern

selection during the early stage of the EHL process is a sinusoidal surface undulation and *f* determines the further stages of pattern formation (Fig 4.16.a-c). Well-established is the role of the effective surface. Thus, *S* is defined as the surface area ratio of the topography, *i.e.,* fraction of the template surface that protrudes downward the polymer film. The patterning process might proceed in various ways, mainly depending on two parameters, the intrinsic film undulation wavelength, λ_i and the lateral periodicity of the master top plate, Λ_m. The λ_i/Λ_m ratio describes the three EHL replication possible case-scenarios: (i) *periodicity mismatch-small wavelength regime ($\lambda_i << \Lambda_m$)*, where the initial structure formation is followed by lateral coarsening of material yielding partial positive replication; (ii) p*eriodicity match-similar wavelength regime ($\lambda_i \approx \Lambda_m$ and S $\approx$ f)*, where positive replica of the templates is obtained and (iii) *periodicity mismatch-large wavelength regime ($\lambda_i >> \Lambda_m$)*, where the pattern develops certain number of defects, and every protrusion of the electrode does not faithfully generate a liquid column.

4.6. CNT-EHL Pattern Replication for Superhydrophobic Surfaces

The CNT-EHL patterning process can be controlled and fine-tuned by both tailoring the design of the top electrodes and carefully choosing the experimental parameters as well as by the ability of terminating the lithographic process at any

chosen pattern formation steps, which allows to "freeze" each individual stage of the replication kinetics of CNT-EHL and thus, the obtained structures.

The produced geometries can be summarised as straight nano-hairs (SNH), curly nano-hair (CNH), single-level spikes with rounded edges (S1L), two-levelled spiky cones (S2L), two-tiered hierarchical spiky cones (S2L2) and hexagonal pillars (HP) surfaces generated with various CNT-based top electrodes that will be explained in the following sections. 3-5 patterned surfaces were fabricated for each of the above morphologies, exhibiting high-fidelity replicas with consistent reproducibility.

When the non-patterned *as-grown* VACNTs-based electrodes were used, it resulted in the replication of dense nano-needles with typically a top surface consisting of curly nano-roughness over large substrate areas. The removal of the non-aligned nanotubes by flipping over the as-grown VACNTs yielded better defined, straighter, nanohair-like PCTFE structures. Imposing the VACNT-based columns with different pitch spacing between the pillars and diameters, thus yielding a range of morphologies, depending on the degree of master electrode periodicity match/mismatch in the presence of the laterally varying electric field, the filling ratio of the PCTFE and the corresponding **patterning termination times** (τ) [139].

To establish the precise τ during patterning of the PCTFE into the desired morphologies, the evolving pattern formation of the sandwiched polymer was

observed *via in-situ* imaging with an inverted optical microscope through a transparent ITO glass electrode [233].

The electric field formed within the micro-capacitor between the two electrodes causes a displacement of charges at the polymer-air interface, which results in energetically unfavourable build-up and consequently, aligns the final morphology along the field lines to lower the overall electrostatic energy.

Typically, a top electrode formed by protruding pillars comprised of densely packed VACNT-based nanostructures generates higher electrostatic pressures at the centres of each ''pillar'' giving rise to spike-like, pointing cones (Figure 4.16.b). Additionally, the lateral field components, which arise during intermediate stages of the EHL process, induce the growing undulations to arrange in a cone-like fashion, before pinning to the top electrode and reorganise into pillars (Fig. 4.16.c).

4.6.1. Straight (SNH) and Curly Nano-Hair (CNH) Surfaces

As previously mentioned, the CNT-based electrodes can be employed as master electrodes in two variations, depending on the desired final pattern.

On one hand, the as-grown CNTs-based master electrode, which yields curly nano-hair (CNH) like roughness, the patterning of the PCTFE film evolves as shallow peaks and valleys, generating a superhydrophobic surface which exhibited the *rose-petal* effect with a contact angle of 167±2° and characterised by strong adhesive forces, with a typical contact angle hysteresis of 15±2°. On the other hand, using the inverted CNT forest-based top electrodes, that yield

well-defined, sharp CNTs brush-like structures (SNH), the EHD process leads to dense straight nano-hair like morphologies, establishing hierarchical nanoscale structure (*intra* an *inter* CNTs) thus, mimicking the *lotus-leaf* behaviour with a contact angle of 165±3°and a hysteresis of 8±2°.

The patterned fluorine-terminated polymer yielded in SNH-like structures, which exhibited considerably increased water repelling properties. In particular, this is due to combining both chemical and physical modifications and effects, accounting for both the PCTFE low surface energy and the pinning effect of the large surface contact area between liquid droplet and the nanohair-like surface. Interestingly, on the mesoscopic scale, the PCTFE patterned film appears predominantly smooth. Additionally, both the topography and roughness also drive the wettability properties of a surface (see section 4.2.3), as the air pockets trapped between the water droplet and the surface asperities may produce the conditions for increased water repellent behaviour.

Since in this work, while a densely packed porous network of CNTs-roughness characterised by *minute* variations in heights, such as CNH, is in contact with a water droplet, a thin layer of liquid results in a spreading on top of the surface, with an increased solid fraction penetrated by the liquid and therefore, yielding the high solid–water adhesion with a typical high contact angle hysteresis. On the contrary, closely packed needle-like structures, such as the generated SNH nano-architectures, restrain the droplet spread, leading to a smaller contact angle hysteresis and roll-off, super-apolar surfaces closely resembling the *Lotus* state.

Summarising, while the curly-like nano-roughness with shallow peaks and valleys (CNH) exhibits *rose-petal*-like behaviour creating a thin water layer upon wetting, the sharp needle-like surface (SNH) with a measured contact angle of 167 ± 2° and the contact angle hysteresis of 13.0 ± 2.0°, inhibits liquid from remaining on the surface behaving like a *lotus-leaf* surface.
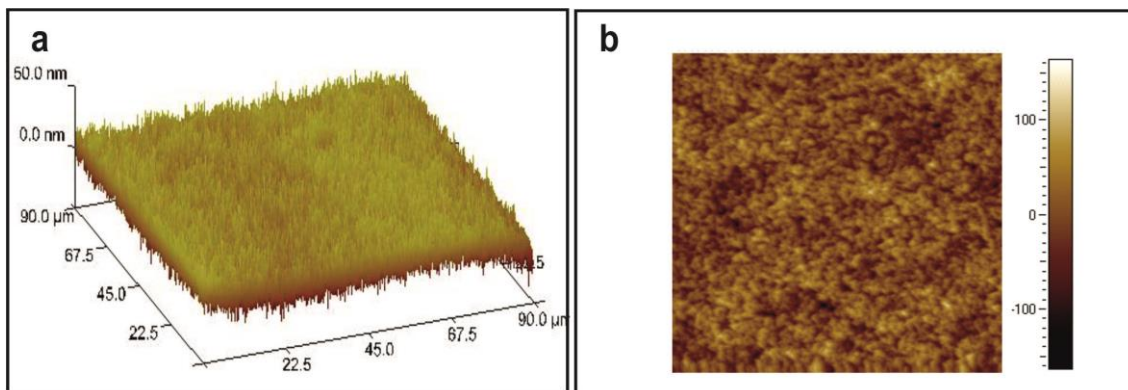
Figure 4.17. CNT-EHL replicated patterns from SNH and CNH top electrodes. Atomic force microscopy height and three-dimensional images and the corresponding cross-sections of **a)** of straight nano-hairs (SNH), **b)** curly nano-hair (CNH) surfaces.

4.6.2. Hexagonal Pillars (HPs)

Subsequently, a similar master electrode, generating patterns of arrays of pillars with various pre-designed height, diameters and pitches (*e.g.,* arrays with ranges of 1–5 µm diameter with a 1.5–5.5 µm pitch between the individual pillars) was used maintain the previous initial experimental parameters, such as the air gap and the polymers film thickness, however, the CNT-EHL replication was terminated at stage (iii) of the formation kinetics. This yielded well-defined pillars with hexagonal packing symmetry which have fully spanned the capacitor gap, as shown in Figure 4.16.c, which were replicated from the imposed CNT-based electrodes (Figure 4.18).

The HPs show a "traditional" Wenzel wetting regime, a high hydrophobic behaviour with 155 ± 3° as CA and 18 ± 7° as hysteresis.
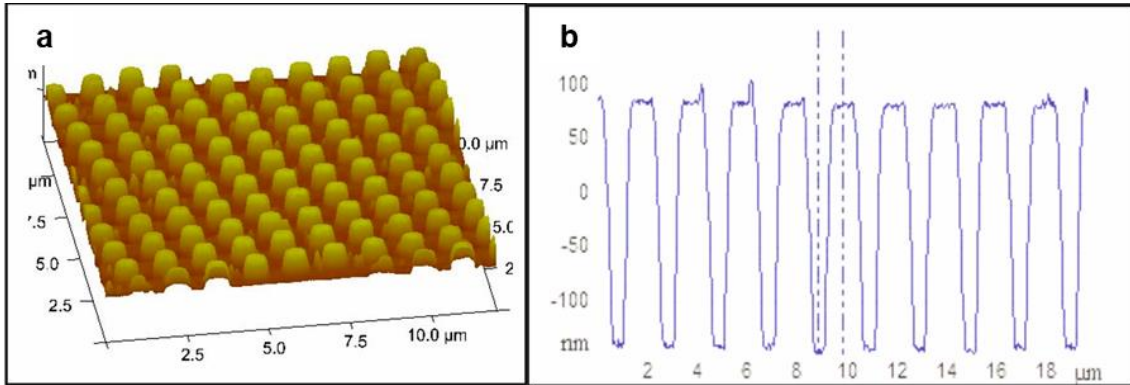
Figure 4.18. Hexagonal nanopillars a) Three-dimensional height AFM image and **b)** the corresponding cross-section.

4.6.3. Single-Level Spikes with Rounded Edges (S1L)

Single-level spikes with rounded edges (S1L) were obtained by using a top electrode structured in arrays of pillars with 1µm diameter, a 2 µm pitch and a 100 ± 10 nm PCTFE film on Si wafer as the support as the bottom electrode.

It is observed that, in the case of the similar wavelength regime where, $\lambda_i \approx \Lambda_m$, a high-fidelity replica of the top electrode was obtained terminating the patterning process at stage (ii). As a result, arrays of periodic cone-like PCTFE structures are obtained, characterised by a typical centre-to-centre distance of 3.0 ± 0.4 µm, a base diameter of 2.5 ± 0.3 µm and a peak diameter of 0.30 ± 0.07 µm (Fig. 4.13.c).

For the *spiky cone-like* (S1L) structures, shown in Fig. 4.19, generated *via* CNT-EHL, the measured contact angles of 169.0± 5.0° is higher than for the forest-like (SNH/CNH) nano rough surfaces, with a contact angle hysteresis of 8.0 ± 2.0° resulting in low adhesive forces between the liquid and the surface, which allows the water droplet to roll-off the substrate easily. The S1L surface is comprised of hexagonally packed cones with nano-scaled, slightly rounded triangular peaks which exhibit CA hysteresis < 10° thus, resulting in a non-wetting (behaviour) between the spikes due to the air pockets formed between the solid-liquid phases. Furthermore, the air trapped in-between the spikes yields a heterogeneous surface comprised of both air and solid.
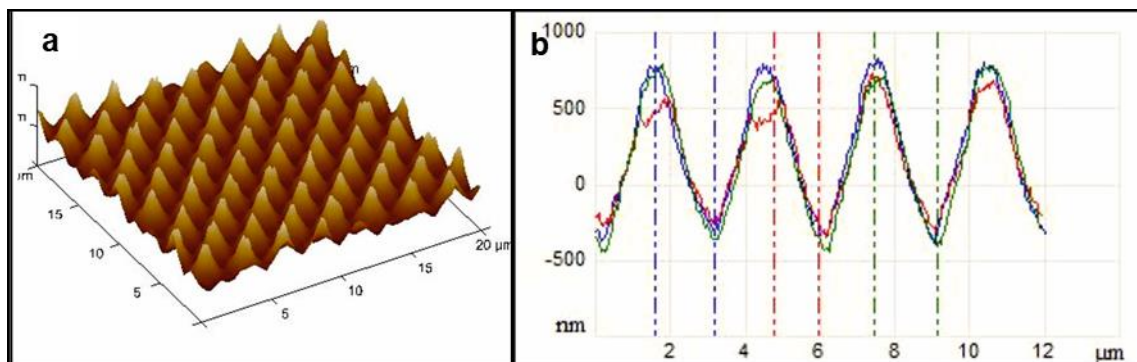
Figure 4.19. Single-level spikes with rounded edges (S1L). a) 3D image of the obtained topography and b) related cross-section. Three colours visible in the cross-section of this S1L surfaces roughness, represent the replication of three samples, exhibiting highly similar structures fabricated with occasional, local artefacts in geometry.

4.6.4. Two-Levelled Spiky Cones (S2L) and Two-tiered Hierarchical Spiky Cones (S2L2)

In Figure 4.14.d, a grid pattern alternating sharp 1.0 ± 0.2 μm height cones and intermediate 300±7 nm height cones were replicated from an initial 93 nm

thickness film (τ =45 mins, d = 230 nm, $1/f$ = 2.5, $1/S$ = 1.5) by superimposing an appropriate pitch/distance top electrode. Insufficient polymer material was available to reproduce the CNT-based top electrode topography precisely. This is indicated by a mismatch in the plate spacing to film thickness (h_0/d) ratio and the value for the lateral periodicity (Λ_m) of the master electrode.

Eventually, the process was terminated just before the polymer pillars entirely span the inter-electrode gap, resulting in sharp spiky cone structures with the top diameter of 270 ± 4 nm.

On the contrary, the hierarchical microstructure of tapered cones S2L (Figure 4.20.a-b) yielded highly apolar surfaces (CA = 168±1°) along with the sticky properties, retrieved by hysteresis values of 75±2°, mimicking the rose-petal effect.

On the other hand, the similarly comprised hierarchical dual structure of tapered cones shown in Figure 4.20.a-b yielded highly apolar surfaces (CA = 168±1°) along with the adhesive properties (hysteresis of 13±2°), mimicking the *rose-petal* effect.

As described in section 4.5, an upper electrode patterned with CNTs features produces a periodically modulated surface with localised charge dispositions and gives rise to an electric field contribution which is proportional to the CNTs curvature, yielding local enhancement of the electric field. Since p_{el} is proportional to E_f^2 and inversely proportional to the inter-electrode distances (see Eq. 4.10), the instabilities evolve towards their final forms focusing in the direction of the

highest electric field (Fig. 4.16.e), inducing structures with sharper ends. Therefore, the termination of the pattern formation at this stage yields cone-like micrometric features with nano-scaled spiky asperities.

Similarly, maintaining the initial parameters of the experiments such as, the film thickness, d, $1/f_r$, and $1/S$ and superimposing the relevant electrode with the CNTs arrays, two-tiered hierarchical spiky cones (S2L2) arrays were accurately replicated (Figure 4.20.c-d). The S2L2 final dimensions were of 300 nm top radius of the cone and 1500 nm in height.
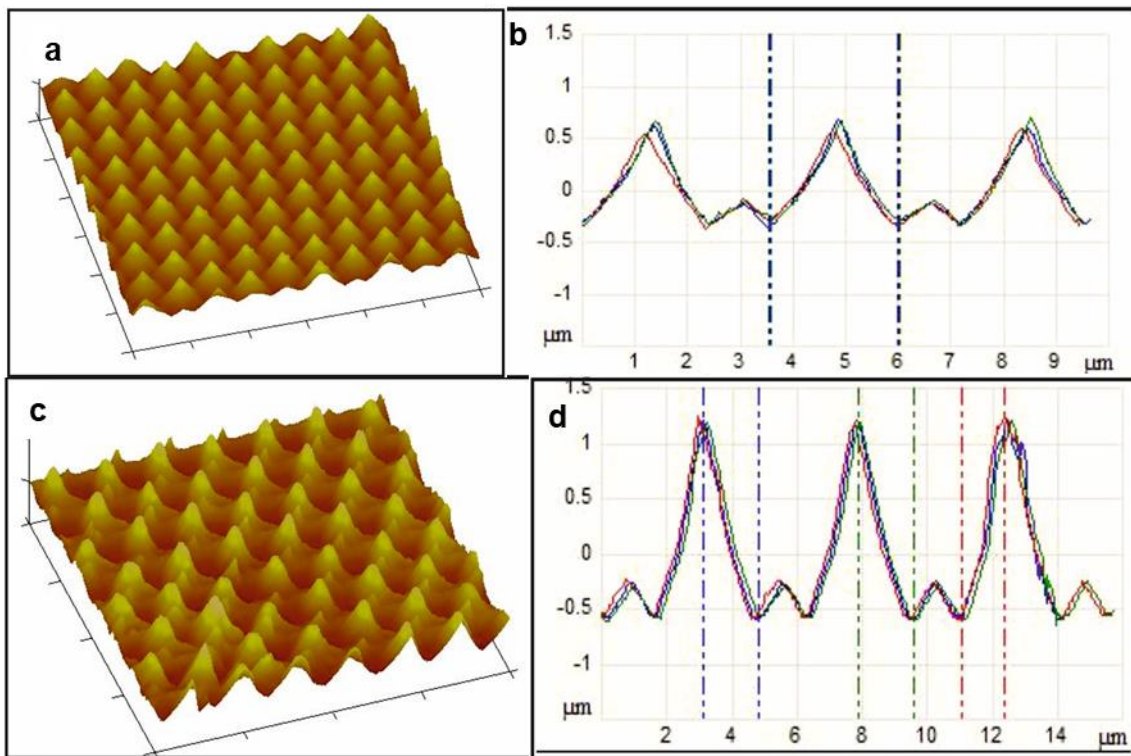
Figure 4.20. CNT-EHL replicated patterns with **a-b)** two-levelled spiky cones (S2L), **c-d)** two-tiered hierarchical spiky cones (S2L2) with the corresponding cross-sections. High-fidelity reproducibility is evidenced by the three colours of the cross-sections of three samples for each morphology.

4.7.   Hydrophobic Properties of the CNT-EHL Fabricated Architectures

Chemical modifications of a surface are known to enhance surface hydrophobicity. As described in Section 4.2 , *Young's Equation* for flat surfaces is given by Eq 4.1:

Equation 4.1.

$$\gamma_{SV} = \gamma_{SL} + \gamma_{LV} \cos \theta$$

where, γ is a surface energy, θ is a contact angle (CA), while the subscripts refer to the states solid (S), liquid (L) and vapour (V).

Taking into an account the surfaces roughness, for surfaces with CA larger than 90°, it is energetically more favourable for the liquid drop to wet a smaller area in order to reduce the total interface energy, $\gamma_{SV} < \gamma_{SL}$. In particular, above a critical roughness value, a cone structure with the contact area for a known vertical force is given by $A \propto [sin\varphi \, cos^2 \, (\theta - \varphi)]^{-1}$ where φ is the fraction of the area of the solid surface that is wetted by liquid. Thus, it is energetically more favourable for the water drop to contact only a very small fraction of the surface asperities and move up the cone structure.

Therefore, since the cone-like sharp tips enable the minimum solid-liquid contact with maximum vertical force per contact area, as demonstrated in Figure 4.16.e, conical structures are favourable geometries to obtain superhydrophobic surfaces. Coupled with the highly hydrophobic chemical properties of the

patterned polymer, these physical structures lay the platform for optimal surface topography, which in turn gives rise to the super-hydrophobicity. Furthermore, these sharp and rounded cone surfaces closely resemble structures of natural systems both in their morphologies and dimensions, as can be clearly seen from the SEM images of Figure 4.1.

The contact angle of rough surfaces (*i.e.,* cone structures and CNT-like surfaces) with *rose-petal* and *lotus-leaf* effects can be extracted from the modified *Cassie-Baxter* equation:

Equation 4.11. Modified Cassie-Baxter equation for rough surfaces

$$\cos \theta_\mathrm{r} = \rho f_\mathrm{s} \cos \theta - f_\mathrm{v}$$

where, θ_r is the apparent contact angle of the micro- and nanostructured surfaces, f_s is the fraction of the areas occupied by the solid-water interface and f_v is the fraction that corresponds to the vapour gaps, θ is Young's contact angle and ρ is the roughness factor, calculated from triadic curve for fractal geometry [29]:

Equation 4.9. Roughness factor.

$$\rho = (R/r)^{D-2}$$

For a three-dimensional space, the factor $D \approx 2.2618$, where R and r are the upper and the lower limits of the surface topographies [29, 30]. As shown in Figure 4.21, for a cone-like structure, the area fraction of the solid surface that is in contact with the liquid is given by $f_s \approx \frac{\pi}{4\sqrt{3}}(r/R)^2$, which can be further extended to the hexagonal array of cones. For the surface morphologies S1L, S2L and S2L2, shown in Sections 4.6.3 and 4.6.4, and only considering the top of the nano-hair like surface roughness, the contact angle can be extracted from the Eqs. 4.11. and 4.9.
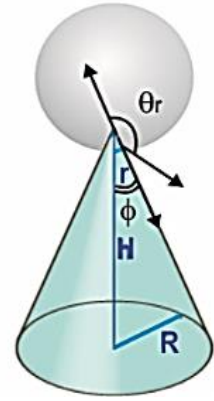
Figure 4.21. Cone geometry in contact with a single water droplet.

Based on the surface geometry considerations depicted in Figure 4.21, the *Cassie-Baxter* equation can be reformulated exploiting the evident dependence on the structure's hexagonally packed cone geometry, typically generated during the EHL process (Eqs. 4.12, 4.13):

Equation 4.12. f_v factor for hexagonally packed cones geometry.

$$f_v = (2\sqrt{3}H^2 - \pi h^2)\frac{r^2}{h^2 + r^2}$$

Equation 4.13. f_s factor for hexagonally packed cones geometry.

$$f_s = \frac{\dfrac{\pi h^3 r}{h^2 + r^2}}{\dfrac{\pi h^3 r}{h^2 + r^2} + \dfrac{2\sqrt{3}H^2 r^2}{h^2 + r^2} - \dfrac{\pi h^2 r}{h^2 + r^2}} = \frac{\pi h^3 r}{\pi h^3 r + 2\sqrt{3}H^2 r^2 - \pi h^2 r} =$$

$$= \frac{\pi h^3}{\pi h^2 (h-r) + 2\sqrt{3} H^2 r} = \frac{h}{(h-r) + \frac{2\sqrt{3}}{\pi} (\frac{H}{h})^2 r}.$$

Therefore, the Cassie-Baxter equation can be rearranged as follows:

Equation 4.14. *Cassie-Baxter* equation for hexagonally packed cones geometry (part I).

$$cos\theta_r = \frac{h}{(h-r) + \frac{2\sqrt{3}}{\pi} \left(\frac{H}{h}\right)^2 r} cos\theta - \left[1 - \frac{h}{(h-r) + \frac{2\sqrt{3}}{\pi} \left(\frac{H}{h}\right)^2 r}\right] =$$

$$= \frac{h}{(h-r) + \frac{2\sqrt{3}}{\pi} (\frac{H}{h})^2 r} cos\theta - \frac{\frac{2\sqrt{3}}{\pi} \left(\frac{H}{h}\right)^2 - 1}{\frac{h}{r} + \frac{2\sqrt{3}}{\pi} \left(\frac{H}{h}\right)^2 - 1} =$$

$$= \frac{\frac{h}{r}}{\frac{h}{r} + \frac{2\sqrt{3}}{\pi} (\frac{H}{h})^2 r - 1} cos\theta - \frac{\frac{2\sqrt{3}}{\pi} \left(\frac{H}{h}\right)^2 - 1}{\frac{h}{r} + \frac{2\sqrt{3}}{\pi} \left(\frac{H}{h}\right)^2 - 1}.$$

Equation 4.15. *Cassie-Baxter* equation for hexagonally packed cones geometry (part II).

$$cos\theta_r = \frac{\left(\frac{h}{r}\right) cos\theta - [\frac{2\sqrt{3}}{\pi} \left(\frac{H}{h}\right)^2 - 1]}{\left(\frac{h}{r}\right) + [\frac{2\sqrt{3}}{\pi} (\frac{H}{h})^2 - 1]}.$$

Resulting in Eq. 4.16:

Equation 4.16. *Cassie-Baxter* equation for hexagonally packed cones geometry (part III).

$$cos\theta_r = \frac{\left(\frac{H}{R}\right)cos\theta - [\frac{2\sqrt{3}}{\pi}\left(\frac{R}{r}\right)^2 - 1]}{\left(\frac{H}{R}\right) + [\frac{2\sqrt{3}}{\pi}\left(\frac{R}{r}\right)^2 - 1]}$$

The effects of structure morphologies and dimensions, fabricated *via* the CNT-EHL, on the water contact angle and hysteresis, can be observed by their wettability properties, as summarised Table 4.1, comparing experimentally measured and theoretically calculated values.

Table 4.1 provides details of the analysed features such as the measured values for R and r as the maximum and minimum value of the radius, H as the height, while the measured CA (°) and hysteresis (Hys°) values, with their associated standard deviations, are compared with the expected value $\theta_r°$.

Table 4.1. Geometrical effects of the CNT-EHL generated surfaces on the contact angle and hysteresis (Hys). The experimental results in comparison to the theoretical predictions as a function of varying surface roughness.

	R/nm	*r*/nm	*H*/nm	θ/°	Std θ/°	Hys/°	STD Hys	Wetting regime	Expected θ_r°
PCTFE Film	-	-	100	119	1	-	-	-	-
HP	1750	-	250	155	3	28	7	Wenzel	156
SNH	1.3	1	1250	165	3	8	1	Lotus	167
S1L	2500	300	1500	169	5	8	2	Lotus	174
S2L2	3000	300	1400	173	1	5	3	Lotus	174
CNH	3.5	1.3	1150	167	2	83	2	Petal	169
S2L	1000	300	1200	168	1	75	2	Petal	170

The direct comparison of the wetting behaviour of the produced structured surfaces and the flat surfaces from the same material shows the enhanced super-apolar properties. Figure 4.22 shows the experimental contact angles and hysteresis of the fabricated surfaces as well as the variation of these as a function of the morphological parameters. All the CNT-EHL patterned structures show super-apolar properties as demonstrated from the CA values, which considerably exceed 160°, especially in the case of the cylindrical pillars (Figure 4.22.c) and the S2L2 geometries, both exhibiting the most superhydrophobic properties with contact angle as high as 173°.

Nevertheless, whilst SNH, S1L and S2L2 structures exhibit roll-off superhydrophobicity mimicking the *Lotus-leaf* like behaviour, the CNH and S2L structures (Fig. 4.22.b and c), water is likely to be penetrating a few nanometers into the voids and therefore, facilitates strong adhesive forces combined with the superhydrophobicity thus, mimicking the *Rose-petal* effect (Fig. 4.22.a and c). Whereas for the hierarchical S2L structures both levels of roughness contribute to the pinning effect, with the larger spikes completely in contact with the liquid and the smaller cones contributing to the second order of roughness with the air trapped within, in the case of the S2L2 surface, where similar morphology is observed, the effect of the second order roughness of the small spikes is considerably lower than the primary cones and therefore, their effect is negligible. According to the *Cassie-Impregnating* wetting regime, the liquid wets the larger-scale structure and penetrates the smaller nanoscale valleys, and therefore, the adhesive force between the water drop and the surface is very high, supporting the droplet even when the surface is tilted at an angle or turned upside down (Fig.

4.22.a). In addition, the critical role of defects and artefacts on the mesoscale (micro-to-nano) have been widely acknowledged since they have demonstrated to yield the high localised surface energy, possibly penetrating into the static drop and increasing the adhesion forces resulting in adhesive surfaces on the macro scale [306,307]. The opening angle of the cone structures has also been shown to influence the transition from the slippery to sticky behaviour [307].
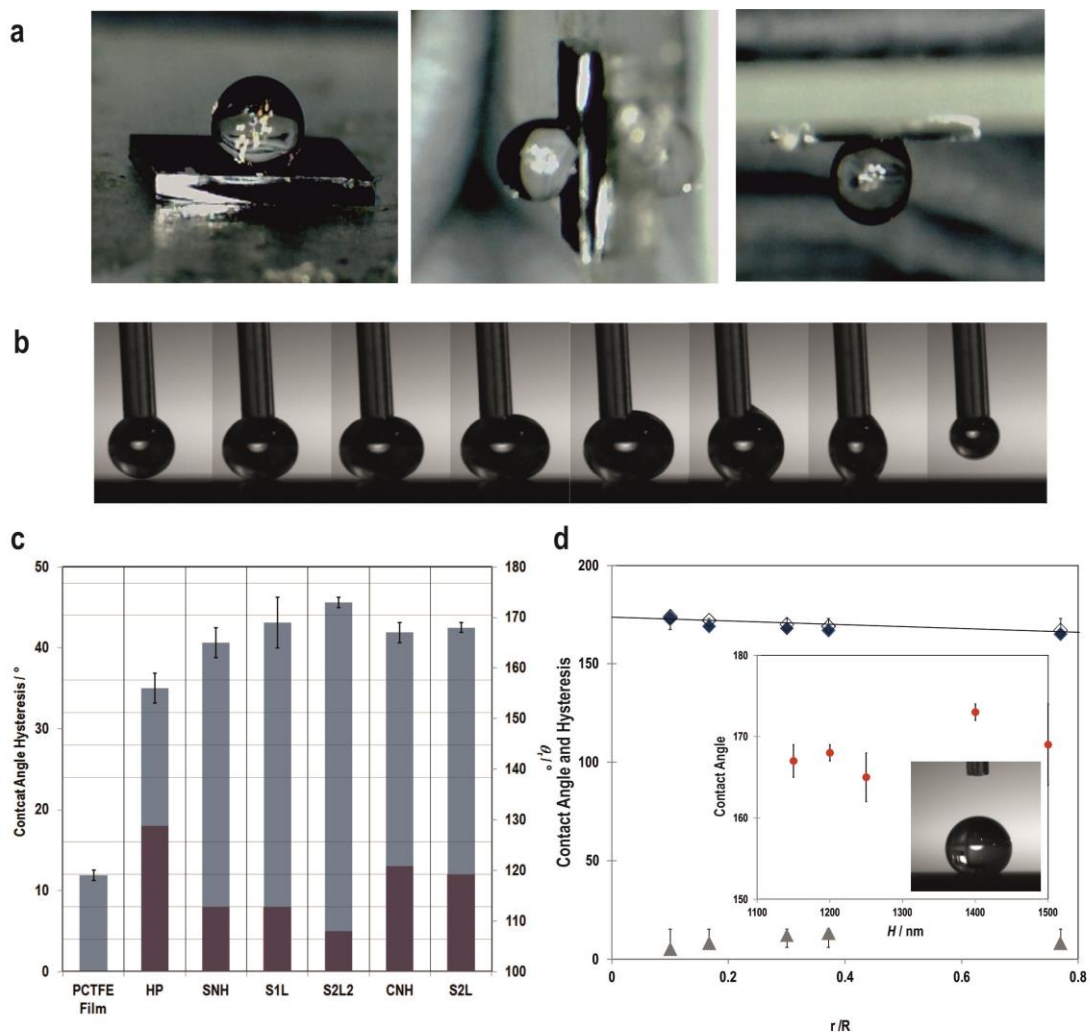
Figure 4.22. Wetting properties of the CNT-EHL fabricated surfaces. a) Optical image sequences on the (i) flat, (ii) 90° tilted and (iii) 180° tilted CNH surface. **b)** Images of the water drop are advancing and receding on the S2L surface indicating its superhydrophobic contact angle of 168°, the shape of the suspending water drop of 5μL and its complete receding without rupture while withdrawing the water droplet with $\theta_{Adv} \approx \theta_{Rec} \approx \theta_r$. **c)** Different wetting states of all the

experimental samples showing the measured contact angles (right) and the measured hysteresis (left) with SNH, S1L and S2L2 exhibiting roll-off (*lotus-leaf*) behaviour and CNH and S2L demonstrating sticky (*rose-petal*) properties not observed in the case of hexagonal pillars in comparison to the reference sample of the flat PCTFE thin film. **d)** Variation of the measured contact angle (blue diamonds) and the corresponding hysteresis (grey triangles) with the geometric parameters is in agreement within their error margins and are well described by the theoretical prediction (line) of the Eqs. 4. 12- 4.16. The theoretical data follow the same trend but are offset towards slightly higher values. Inset: Variation of the contact angle as a function of the structures' height. Over a height variation of 350 nm, the contact angle changed by only 22% compared to a variation as a function of *r/R* by a factor of 7.

From Figure 4.22.d, it is evident that the contact angles as a function of the geometric parameters of the surface roughness of the CNT-EHL patterned surfaces have linear dependence, indicating that the larger the fractional contact area, the smaller the apparent contact angle (Fig. 4.22.d). As qualitatively extracted from Figure 4.21, the marked conical height has only a minor influence on the contact angle. This is quantitatively shown in the inset of Figure 4.22.d, where θ_r changed by only 22% of height variation, despite a relative variation of the water penetration by a factor of 7, indicating a considerably smaller influence of the height on the superhydrophobicity in comparison to the surface roughness factor.

In conclusion, our results highlight the importance of the ratio of the surface roughness factor and heterogeneity parameters, R_s for tuning the superhydrophobic properties. Typically, the ratio of the roughness factor, as well as the fractional area of contact, can be calculated by averaging the surface roughness over a given area which is smaller than the liquid droplet. The contact angle hysteresis is influenced by the value of the surface roughness which can modify the ability of the interface to pin the triple line, therefore, decreasing the R_s relative to the liquid drop size eventually rendering the contact angle hysteresis

of a negligible value. For the hexagonally packed cone structures, the dependence of the surface roughness in Figure 4.22.c-d implies that the triple-phase contact length has a linear dependence on the contact angle hysteresis. For rough superhydrophobic surfaces [306], it has recently been demonstrated the importance of using the triple line length, ω_{tf} over the drop's diameter. For cone structures with hexagonal symmetry:

Equation 4.17. Triple line length for cone structures with hexagonal symmetry.

$$\omega_{tf} = 2r\left(\frac{1 - \dfrac{Rh}{H}}{\dfrac{RH}{H}} + 1\right) = 2r\left(\frac{1}{R} - \frac{h}{H} + 1\right) = 2r(\frac{1-r}{R} + 1)$$

Plotting the dependence of the cones' surface roughness in Figure 4.23 reveals that the triple-phase contact length has a linear dependence on the contact angle hysteresis.
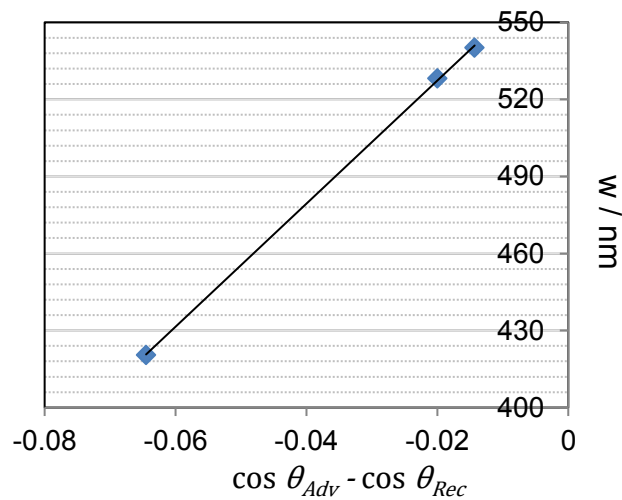
Figure 4.23. Triple-line length versus the contact angle hysteresis dependence for cone structures

141

4.8.   Conclusions

In summary, we have demonstrated an innovative, controllable and facile yet scalable method to fabricate a broad range of super apolar surface morphologies with a single or multi-level hierarchy. Vertically aligned carbon nanotube forests were exploited in an unconventional way to produce a range of robust lithographic electrodes, further exploited in conjunction with electrohydrodynamic patterning. A range of configurations was produced by verifying the top electrode design and the experimental parameters during the CNT-EHL patterning process yielding various hierarchical architectures, mimicking the *lotus-leaf* and *rose-petal* like surface morphologies and properties. The generated hierarchical structures enable enhancing the hydrophobicity *via* different length scales of roughness. When the water can penetrate the larger-scale texture, but cannot enter into the smaller structures, the patterned surface effectively mimics the '*lotus-leaf*' effect. However, when the larger micro- and nanostructures are impregnated by water, this gives rise to high solid–water adhesion and therefore high contact angle hysteresis. The tunable wetting properties can be easily switched between the various states including, the *sticky* or *roll-off* superhydrophobicity and super-hydrophilic surfaces can also be fabricated on demand from a simple switch between alternative polymers and morphologies. Furthermore, thin EHL patterned films can be easily floated off the supporting substrates and transferred onto different support surfaces and therefore, can be used as advanced superhydrophobic coatings which conformably adhere to underlying substrates with any dimension and morphology. The versatility of the CNT-EHL technique

142

renders it easily extendable for a broad range of more complex, adjustable geometrical microstructures enabling direct biomimetics of nature's unique wettability. In this perspective, CNT-EHL is a promising prospect for the robust, straightforward, and low-cost fabrication of sub-micrometre patterned substrates to facilitate a plethora of low energy surfaces for coatings, fabrics and microfluidic device technologies with high mechanical durability and optical transparency.

5 Three-Dimensional DNA-based Nanoarchitectures for Optically Responsive Surfaces

5.1.   Introduction

During the last decade, metamaterials have been attracting increasing interest due to their unique electromagnetic properties, which could rarely be found in natural materials [78,241]. For instance, negative and near-zero refractive index (NIMs) and plasmonic bandgap (PGB) materials introduce a whole new, usually impossible to find in nature, range of properties arising from the interaction of the light with their constituents, called *meta-atoms*. Nowadays, extensive research is focussed on assembling optically-responsive platforms such as cloaking devices [308,309], plasmonic filters [310–312] and super-lenses [74,313–315], as potentially powerful tools for detection and sensing. With an increasing demand from the medical, technological and military fields, the production of robust and cost-effective devices has focused on the manufacturing of scalable, controlled surfaces with high performance and optical properties such as NIMs and PGBs.

In this study, we present an innovative route for the fabrication of tunable 3D DNA-based optically-active nanoarchitectures, introducing a novel perspective of employing biological materials as templates.

The results of the experimental procedures investigated for producing the DNA-templated (sub-micron) metallic features, provide relevant data for determining the feasibility of such techniques with biological samples. In this regard, the DNA employed in this work was not derived from any tissue, bacteria or living being, but was designed and artificially synthesised.

This approach is potentially scalable for patterning areas on a micron scale, whilst the sub-100 nm features are precisely dictated by the DNA templates.

5.2. Tuneable 3D DNA-based Nanoarchitectures for Optically Responsive Surfaces: Overview and Roadmap

This chapter proposes a novel, alternative and cost-effective route for manufacturing optically-responsive materials *via* gold replication of the 3D DNA nanostructures. As previously detailed in Section 2.2., in 2005, the assembly of DNA origami by Rothermund [163] set a turning point in the approach to new biological materials enabling, in the years to follow, accurate designs of a broad range of DNA-based morphologies. A few years later, self-organised block copolymers were assembled into *gyroid* geometries [144] and then replicated with noble metals enabling tuneable optical responses by tailoring the intrinsic structure of such objects.

In this work, the two approaches were combined into a novel strategy for manufacturing scalable, optically-responsive features on a sub-50 nm length scales. Independently assembled 3D-DNA polyhedrons were used as scaffolds for producing free-standing self-assembled gold replicated architectures while preserving the sub-50 nm details of the original structures.

Historically, gold plating involved the use of toxic cyanide baths as an electrolytic solution for transporting metal ions to the surface to be plated (see Section 2.1.2.2). However, since the modern micro- and nano-electronics industry has increased the demand for high-quality gold-plated components for integrated devices, novel techniques have been evolving aiming at minimising the hazards arising from the traditional plating processes. Using baths based methods has nearly eliminated the presence of cyanide especially in gaseous form, with the further electroless techniques permitting to coat even insulating surfaces *via* the *click-chemistry* processes.

In the flow diagram in Figure 5.1 all the experimental procedures for achieving nanopatterned metal surfaces are detailed. The production of gold nanostructured materials is a complex process which involves numerous steps [196,197,200,234], described in Section 3.6, will be explained in detail in this chapter.

The first steps involve the production of the DNA polyhedrons followed by the characterisation steps according to the well-established procedures, developed by Goodman *et al.* [200] and He *et al.* [196,197].

In this thesis, optimisation steps were carried out (see Section 3.6). Plating techniques were also attempted and optimised for depositing a suitable < 20 nm gold layer covering the DNA features, which have been deposited onto solid substrates. Characterisation steps were also optimised. Optical properties deviating from the natural behaviour of the materials were measured as preliminary results, in collaboration with the Vignolini's group (Department of Chemistry, University of Cambridge, UK).
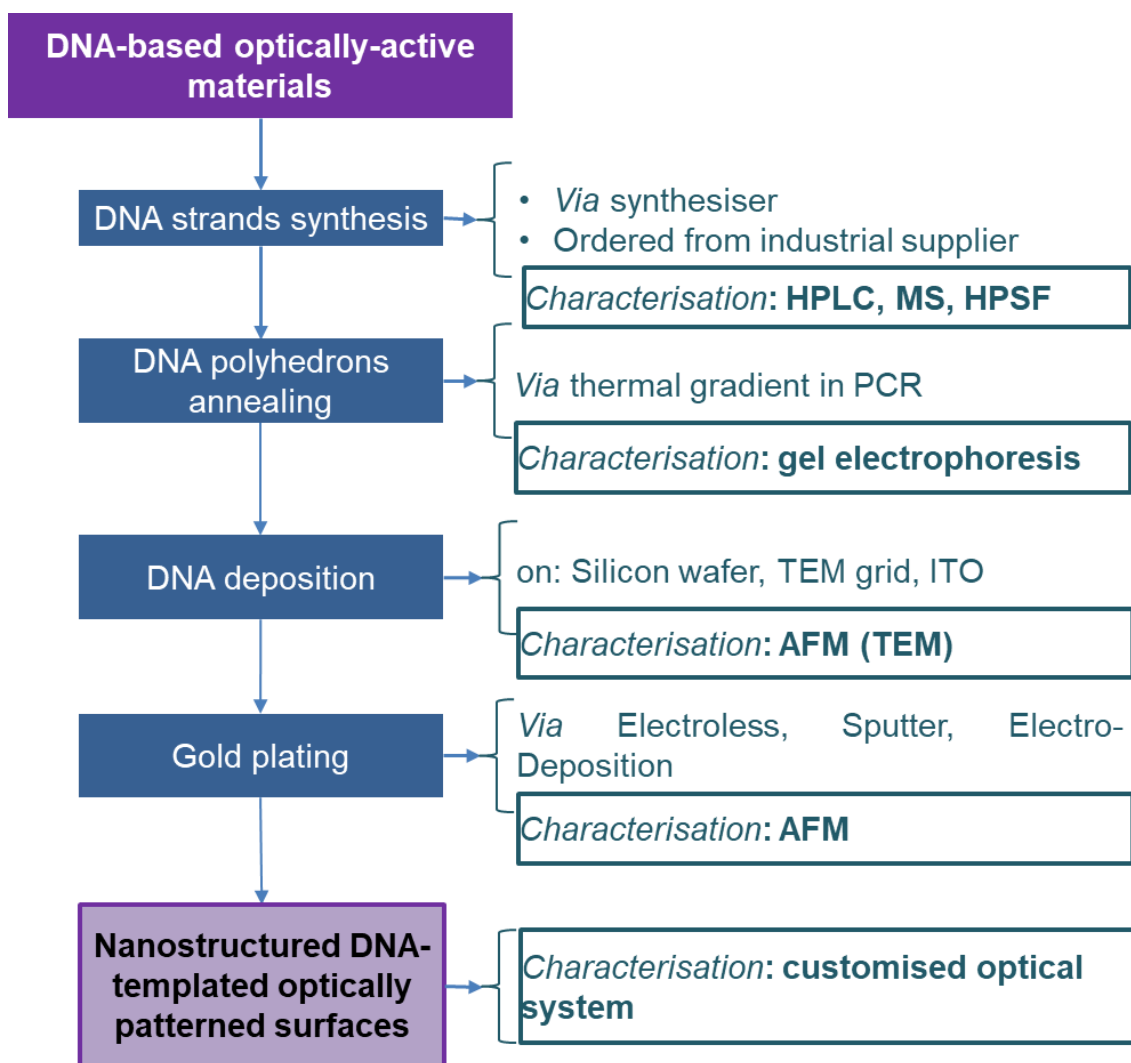
Figure 5.1. Process diagram flow for the fabrication of tuneable 3D DNA-based nanoarchitectures for optically responsive surfaces.

5.3.   DNA Polyhedrons as Robust Scaffolds

The preliminary step for the fabrication of nanostructured surfaces using the DNA polyhedrons as *sacrificial templates* for patterning involves the independent production of DNA nano-architectures. According to well-established procedures [195–197,316] listed in Section 3.6.2, fully-annealed DNA polyhedrons with various shapes and dimensions ranging between 9 and 30 nm were synthesised with final yields between 70 and 90%.

Since the design and assembly procedure of DNA polyhedron structures is not within the goals of this thesis, well-established procedures [195–197] were used, including the characterisation steps, which utilise gel electrophoresis and AFM (or TEM) imaging for revealing the post-annealing yield and structures. While dynamic light scattering measurements were not possible in our case, given the low concentrations and volume of the solutions, DNA polyhedra were analysed and quantified by UV transilluminator and electrophoresis (Fig. 3.9b: DNA quantification by UV transilluminator showing single strands (1-4), mixed strands (5-10) and DNA tetrahedron (11)), which allows separating components of a solution depending on different weight using an applied static electric field. It was found from these analyses that the single strands self-assemble into the final polyhedron, in a one-pot reaction and at in a controlled environment and temperature, form a polyhedron structure with regular sides.

As illustrated in Chapter 3.5, gel electrophoresis was run for each sample, comparing them with the single strand (ssDNAs) run for establishing the amount

of residual, un-annealed ssDNAs in the final batches. Further quantification was not possible, as the sample amounts did not suffice for analytical techniques such as dynamic light scattering (DLS), which requires high volumes and concentrations compared to the produced batches.

Although dimerisation is possible, the electrostatic stacking between the bases comprising the DNA molecules does not affect the stability or the shape of the polyhedron, and therefore, it has not been taken into account.

For the deposition, of the DNA origami structures, the samples were immobilised onto three kinds of substrates including, mica, polished silicon wafer, ITO and carbon films on a TEM grid, each characterised by different conductivity and transparency (see Section 3.7 for full details). Preliminary AFM images of the three polyhedrons immobilised onto the various substrates were taken as control for later comparison, *i.e.,* after the coating processes. While the DNA structures showed high affinity with all the surfaces, the intrinsic roughness of the latter ones increased the difficulty of measuring using AFM imaging compared to very smooth, freshly cleaved mica. It was concluded that all the chosen supporting substrates are suitable for DNA structure immobilisation and the following replication processes.
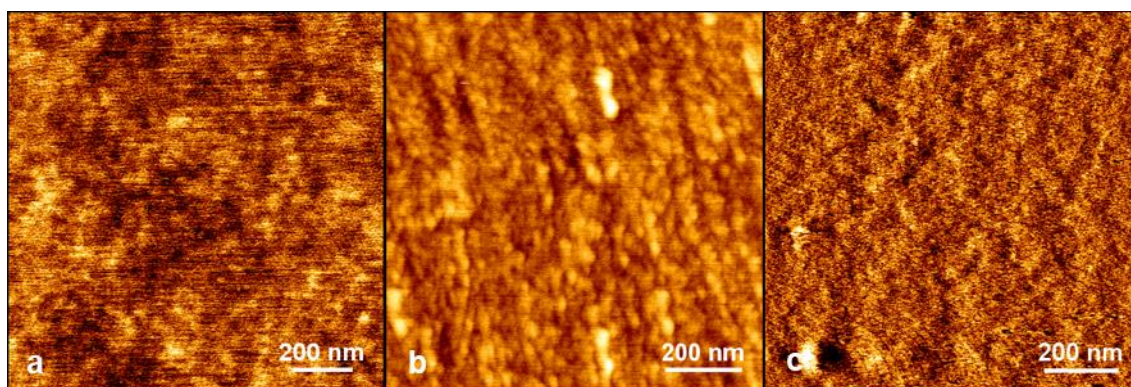
Figure 5.2. AFM images of the substrates. a) Silicon wafer, average roughness of 534±20 pm, **b)** ITO, average roughness of 586±42 pm, and **c)** carbon film on TEM grid, average roughness of 293±56 pm.

The **9-nm DNA structures** of various shapes are seen in negatively stained TEM images (Fig. 5.3) which reveal the presence of a mixture of triangular and square-like shapes of the sub-10 nm features. Negative staining enables contrasting and visualising the DNA (appearing as white nano-shapes) by staining the background while leaving the actual specimen untouched, and thus visible. The co-presence of several distinctive geometries, which can be retrieved from the various possible orientations of a polyhedron-like structure in the 3D space are shown in the inset of Fig.5.3. In particular, in the inset of Fig. 5.3.a, a triangular shape is highlighted in the middle of the picture while at the same time, square-like locally assembled structures are observed in Fig 5.3b. Scanning, transmission electron microscopy image in the inset of Figure 5.3b demonstrates the resolved DNA-based nanostructures with a characteristic 10nm scale. It is worth noting, that since these DNA structures are on sub-10nm scale, high resolution imaging is very difficult and furthermore, the high current density required for such images appeared to damage the assembled morphologies.
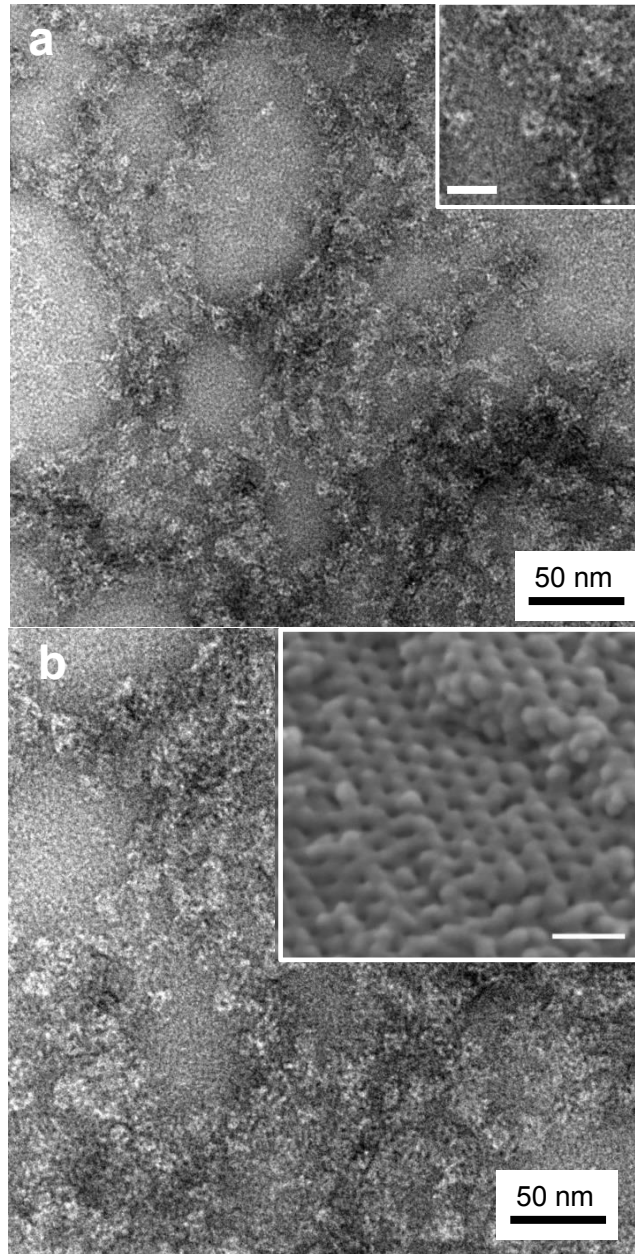
Figure 5.3. 9-nm DNA features TEM images. The various 3D orientations of the polyhedrons are mirrored by the disposition of the fabricated DNA polyhedrons when immobilised on supporting surfaces. **a-b)** TEM images of 10 nm polyhedrons on TEM grids from aqueous solution. Different areas highlight the various morphologies achieved after drying. b, inset) Scanning transmission electron microscopy image of polyhedral nanostructures assembled on a grid.

The overall disposition of the polyhedrons on a sub-micron area, as seen in Fig.

5.3., varies upon the deposition time and likely, the amount of residual salt from

151

the Mg^{2+} washing solution, which can act as an aggregating agent due to the carried positive charge, which counteracts the negatively charged DNA. Hence, the average density of the DNA nanostructures on the surface cannot be calculated, since the immobilisation process is yet to be optimised.

The AFM imaging in the Goodman's original work [200] was carried out in a liquid state, i.e., environmental AFM, using an ultra-sharp AFM tip (typical radius of 2-3 nm), which produced high resolution of both shape and edge lengths, with the height of the polyhedron measured as 10.5 nm [193].

In this work, we have aimed to reproduce high-quality AFM images (512 x 512 pixels) in tapping mode, using commercial tips with a tip radius < 8 nm using a Nanowizard II instrument.

AFM imaging in tapping mode, as described in Chapter 2, is a non-destructive technique, based on the interaction of a probe (or tip) with sample surfaces, allowing high resolution down the 1 nm scale. It is important to notice the difference between the two kinds of AFM tips used in our and previous works which is based on the concept known as *tip convolution*, which is also known to affect the quality of the produced AFM image and can be corrected by calculating the deconvolution, according to the previously established models [317–323]. As shown in Fig 5.4, both the vertical (*z-plan*) and the lateral (*xy-plan*) imaging can be affected by a wide range of undesirable inaccuracies during the scanning, usually leading to artefacts and a reduction in the achieved resolution. Nevertheless, the vertical resolution is typically high and strongly dependent on the shape and sharpness of the tip (Figure 5.4). With the tip radius being r_{tip}, the convolution error ranges from 2 - 0.9 r_{tip} depending on the height of the examined

sample [322]. The convolution error of lateral resolution must also take into account the aspect ratio, A, of the sample, defined as the ratio between the height and width of the analysed features, $A = H/w$. Additionally, the size of the scan can largely influence the image resolution, with it being calculated as the number of nanometres *per* pixel (nm/pxl), it determines the amount of points collected for each scanned line (Fig. 5.4). Therefore, the *de*convolution of the tip is an essential step for the reconstruction of the real topography of a surface. The *de*convolution of the tip plays a substantial role in sample imaging and is mostly based on the correct estimation of the probe geometry. This can be either provided by the supplier or obtained *via* an electron microscopy characterisation of the tip.
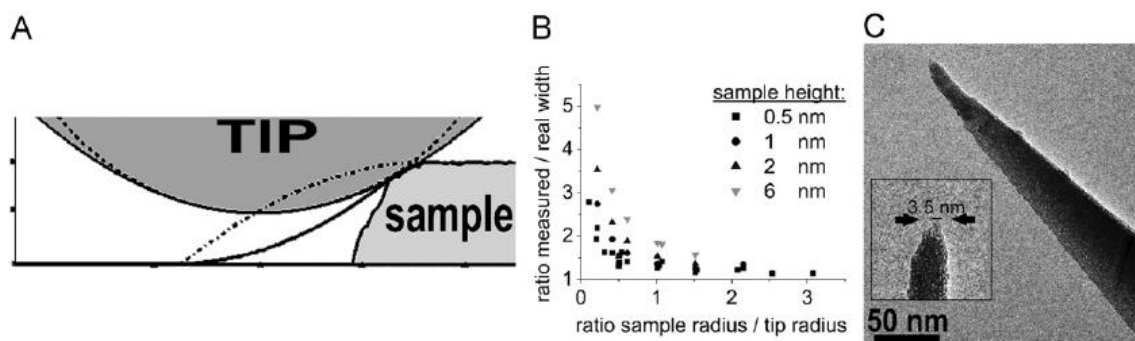
Figure 5.4. AFM tip convolution schematics. a,c) The tip shape and radius have a fundamental role in determining the convolution of the image. **b)** The resolution, expressed as the ratio between the measured and the real width, is relative to the sample/tip radius ratio, also depending on the sample height. Reproduced from Winzer, 2012 [317].

Over the years, few possible solutions have been developed to overcome the convolution effects arising from the cantilevers. One method was the manufacturing of a new set of single-walled carbon nanotube (SWCNT)-based tips. These ultra-sharp probes exhibited high-performance, however, were of

higher cost and in certain cases also required well-trained operators, due to their frailness and specific handling requirements.

In this study, the tips with the radius < 8 nm were used for producing the AFM images were purchased from the Windsor Scientific (UK). Since the feature side (R_p) is expected to measure approximately 10 nm [171,193], it is assumed that $R_p - r_{\text{tip}} \ll R$, while the aspect ratio of the structures, A, is ideally 1 [317,321– 324]. Therefore, after absorbing the assembled DNA polyhedrons using standard methods on mica with Mg^{2+} as counterions and setting the experimental conditions for high-resolution AFM imaging, the vertical side of the polyhedron is expected to be 3.2±1 nm [196,317].

According to the several previous studies [317,319], DNA polyhedrons tend to collapse on themselves during the deposition and drying steps, leading to a dramatic decrease in the samples' vertical dimensions. Such structure 'failure' has been widely documented [188,195,196] as an effect of the drying process, where the liquid medium is removed, withdrawing the "support" in the vertical dimension.

Coupled with this effect, at the same time, the mechanical force of a few nN applied during the scanning produces a compression of the biological material [317]. The cross-section analysis of the images allowed measuring the lateral dimension of the samples, yielding the dimensions of 10±2 nm. The measured values are slightly bigger than the original structure dimensions shown in literature (9±1.5 nm) [195] although, are within the expected experimental error range especially if taking into an account our choice of a commercial tip with r_{tip}

≤ 8 nm which introduces an additional error in the *xy*-plane (Figure 5.4) [317,318,320]. The polyhedron dimensions were additionally confirmed by TEM and AFM characterisation, which also indicated a tendency to aggregation after drying. As shown in Fig 5.5.b-c., the triangular shape of each side of the polyhedrons is usually preserved, however, after the solvent is washed away, the polyhedrons slightly deform, arranging in square-like features.
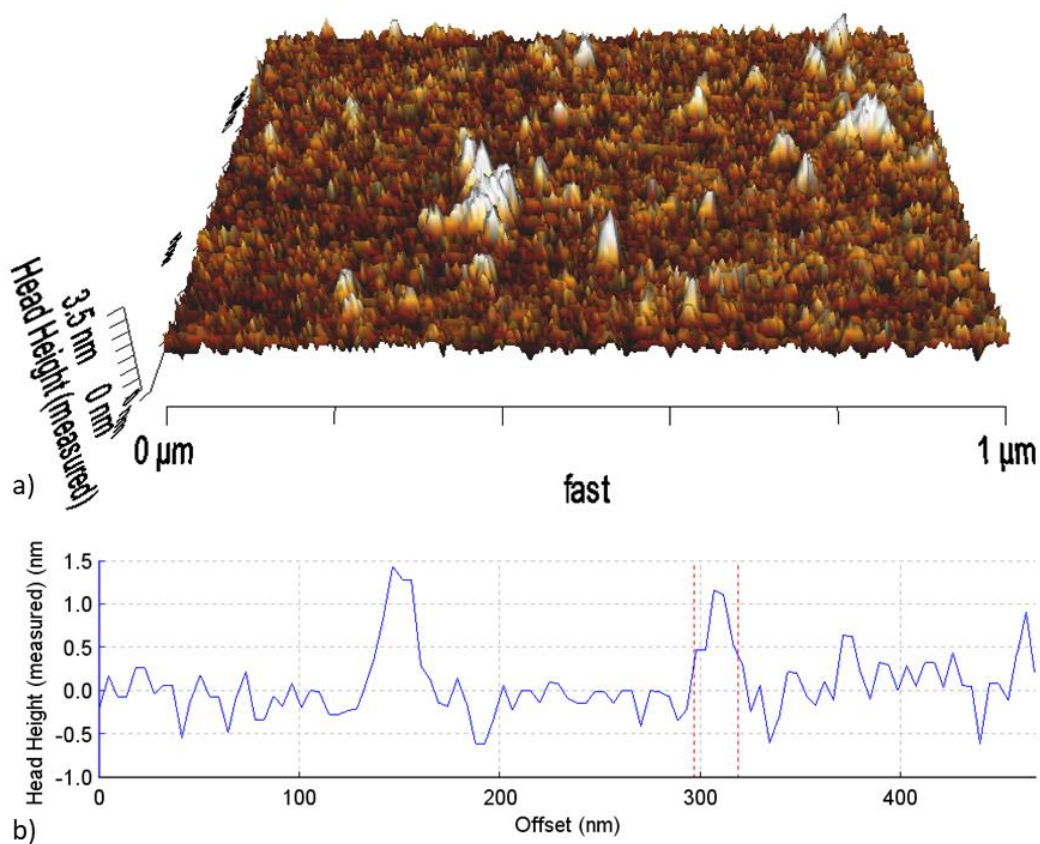
Figure 5.5. 9nm polyhedron AFM profiles. a) 3D AFM map of 1 x 1 µm^2. The white peaks represent the 9-nm polyhedra on mica, which, upon collapsing, results in an average of 3.5 nm height. **b)** Image-related cross-section.

When investigating the **20-nm DNA polyhedrons**, similar effects related to the AFM tip convolution were taken into the account as well as the role of the Mg^{2+}-

based salt. TEM imaging was not carried out for the larger 20-nm and 30-nm nanostructures.

The deformation effect is due to the combination of the washing procedure, which eliminates the Mg^{2+} salt from the structures' cavity, and the polyhedrons *open-hinges* (each corner of the structure is formed by an hairpin-like structure in the DNA sequence, see Section 3.6.2), which affect the rigidity of the 3D DNA structures. As previously described, the Mg^{2+} salt has a fundamental role in stabilising the polyhedrons in solution, besides acting as an anchoring site for the DNA onto the substrates.

According to the previous models [318–320,322], the structure dimensions reduce the error associated with both the vertical and lateral AFM scans, under the same experimental condition. Due to the fundamental differences in the annealing process reported in Section 3.6.2, the side of the 3D structure [202,316] ranges between 16 and 20 nm, in contrast to the 9 nm- feature for which the triangular side shape is mostly preserved during the drying. In this case, the presence of the *tiles* (star-like intermediates in the synthesis which are positioned at each vertex of the assembled tetrahedron) provides additional stability to both the hinges and the edges.

Nevertheless, the structure is still expected to collapse due to the DNA dehydration [197] and which was found to measure of 4 ± 1 nm in height.

Two significant structure populations were revealed by the AFM imaging (Fig 5.6.a-b). The brightest, uneven features exhibited dimensions and shapes which would be suggesting impurities from the rinsing solution (2 mM $Mg(OAc)_2$), as a result of the sample immobilisation procedure, *i.e.,* salt crystallisation. Large areas (Figure 5.6b) are covered by less bright triangular features, corresponding in size to the expected polyhedrons (approximately 3 nm).

Since the points of adhesion with mica change upon the geometric orientation of the nanostructures (in a 3D space) (Fig 5.6), two key dispositions were identified including, (i) triangular-like and (ii) square-like morphologies.
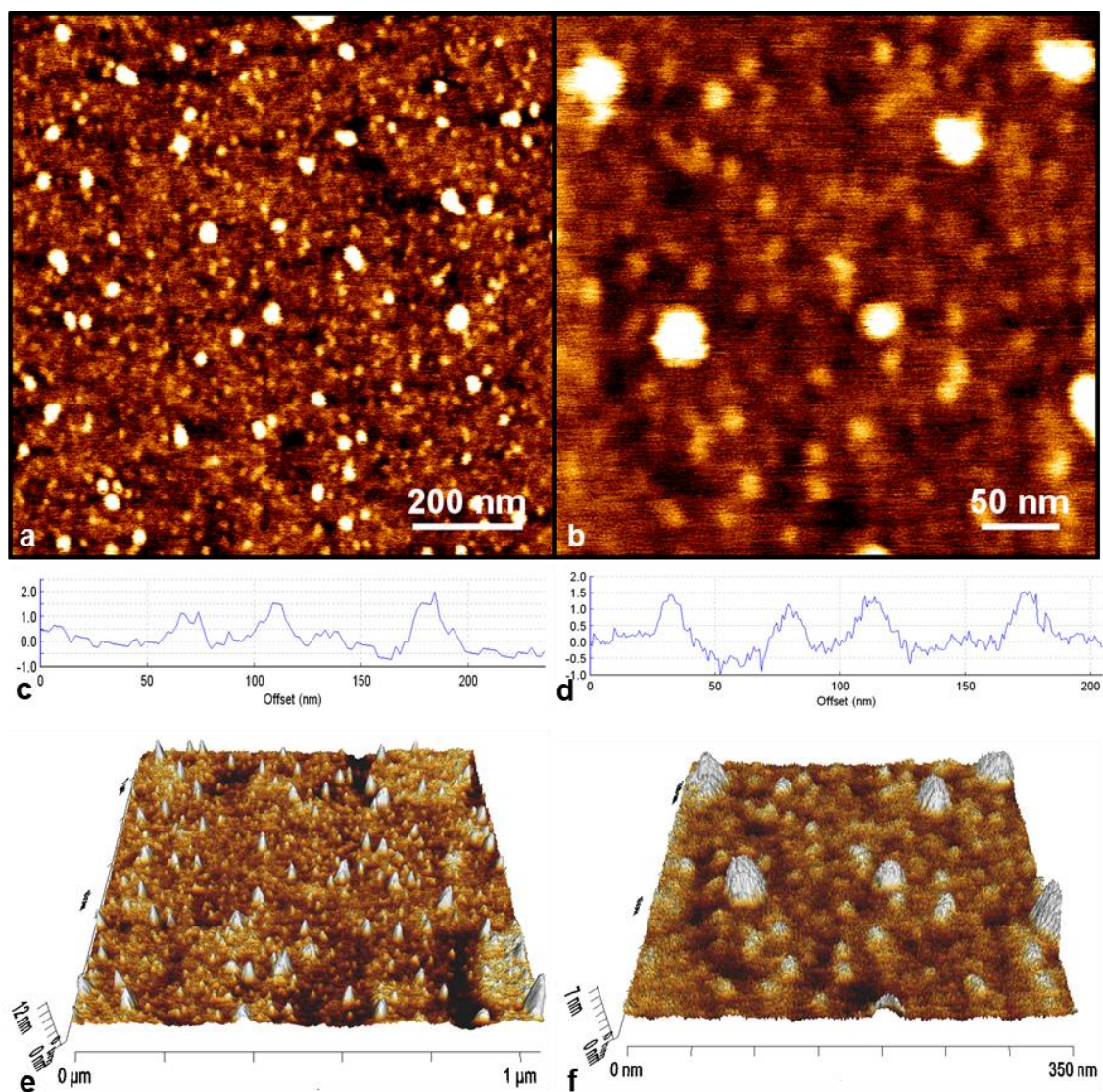
Figure 5.6. AFM height image of 20 nm DNA on mica. Due to their robustness, the yield is > 90%. **a-c-e)** The large area scan shows the presence of bright white points, which are assumed as an aggregation of the structures and residual salts (a). The height of selected features is highlighted in the cross-section (c), while the 3D image allows observing the whole system disposition in a 1x1 μm^2. **b-d-f)** The AFM image shows the presence of 20-nm features as the less bright triangular-like shapes (b), with height profile (d) showing close values to the ones reported in the literature [197]. The 3D image allows observing the whole system disposition in a 350x350 nm^2.

Roughness data of the sample after immobilisation was compared with the freshly cleaved mica values, indicating an average peak-to-valley difference of 3.63 nm. Additional cross-section analysis of a single polyhedron highlights the height

profile of the observed features and set it to 4±1 nm, closely correlated with the previously reported values [202].

Finally, AFM height images were taken for **30 nm DNA structures**, according to the described assumptions taken in the previous sections for tip convolutions and the Mg^{2+} role in the system.

These features, similarly to the 20-nm polyhedrons, are comprised of basic, identical *tiles* branching in four directions, which are connected by their *sticky ends*, easily forming the polyhedrons as the smallest stable structure. As reported by He *et al.* [196], the dehydrated and collapsed DNA polyhedrons are expected to measure 29±1 nm in lateral dimensions with a height of 2.5 nm while showing the edges for pointed out-of-plane vertex orientation (Fig 5.7). In our work, the produced structures, previously immobilised on mica with well-established protocol by using Mg^{2+} as counterion, are variously oriented on the surface. In each case scenario, the structures exhibit a side of 37±6 nm and a height of 5±2 nm.
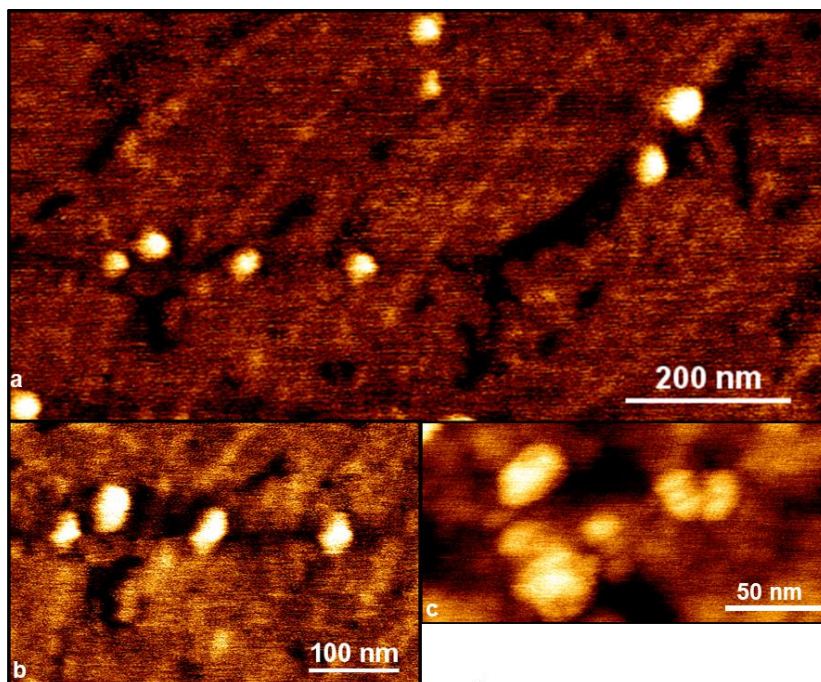
Figure 5.7. AFM images of 30 nm DNA structure on mica. a) AFM height images of the possible geometric orientation in a 3D space of an ideal polyhedron with typical dimensions of approximately 30 nm. **b)** AFM images of DNA assembled polyhedrons on mica, using Mg^{2+} as a counterion for immobilisation. Polyhedrons are observed in correspondence of the white spots, where the brightest point points at the top vertex. The four polyhedrons likely lie on the side. **c)** High-resolution image of a 30-nm polyhedron, outlined by its vertexes, on the top-left corner of the image.

5.4. DNA Polyhedrons Surface Distribution

As illustrated by the TEM and AFM analysis, the precise DNA polyhedra surface organisation at this stage of research cannot be determined, although the effects of a local organisation are observed.

Figures 5.3 and 5.5 show areas of high aggregation for the 9-nm DNA polyhedrons in a dry state, where the medium has been entirely removed and the structures have collapsed. However, further areas show no presence at all of the DNA features. This aggregation phenomenon can be ascribed as a direct

consequence of the Mg^{2+}-based salt presence, which, due to the strong positive dipole, attracts the negative dipole carried by DNA features [34,196,325,326]. Furthermore, the quick-drying process of the DNA samples may also concur in immobilising the structures in specific local arrangements driven by energy minimisation and dipole-dipole interactions.

Different local organisations are seen in the AFM images in Figure 5.6, where the 20 nm polyhedrons are (more) discretely distributed over the surface, and fewer aggregation points are localised. This arrangement is likely due to the larger dimensions of the structures which lead to weaker directional interactions and in turn, to a weaker attraction to the salt grains.

Similarly, preliminary images of the large 30 nm features (Fig. 5.7) do not show any localised organisation and appear as discrete, well-separated particles, although not enough data was collected to confirm this behaviour.

At this stage of research, the surface distribution of the DNA structures has not been taken into account, since the sought optical properties were demonstrated as uncorrelated to specific spatial arrangements of the meta-atoms, as recalled in Chapter 1.4. In fact, surface plasmon polaritons and negative-refractive index (SPP and NIM) can arise from randomly organised media [327–329] and since the goal of this work is to demonstrate the feasibility of the described procedure for possible applications for metamaterials, no adjustment in the DNA features surface arrangement has been undertaken. Viable alternatives for immobilising the structures were taken into consideration, though, at this stage, were less

prioritised due to focusing on the production of a preliminary optically-responsive surfaces, since optical properties can also directly arise from the observed distributions.

5.5. Preliminary Studies of 3D DNA Polyhedron as Replication Moulds with the Corresponding Advantages and Disadvantages and Further Required Optimisation

In this section, electroless plating and gold sputtering results are discussed, highlighting the advantages and disadvantages, while demonstrating the unfeasibility of such techniques for bio- and soft-material replication.

The 3D DNA polyhedrons, characterised by their shapes and dimensions after drying, were further used as replication templates with various coating techniques. Due to the stiffness and the physical properties of the structures, it is assumed that the plating process does not affect the polyhedrons in both dried and wet conditions. To complete the replication of the nanostructures both the sides and the cavity of the polyhedrons are aimed to be reproduced with a noble metal.

Initially, we pursued the direct replication of the assembled 9 nm-features. Since the DNA conductivity properties are still under debate [330–332], we assumed that their reported slow electron transfer rates (*i.e.,* electrical conductivity) would not suffice to attempt electroplating processes, which are typically performed on highly conductive substrates. In line with this hypothesis, *electroless deposition* (see Section 3.8.2), a spontaneous chemical reaction reducing the gold in solution (Au^{3+}) to metallic gold (Au), was chosen as an initial technique for replicating the DNA polyhedrons. The electroless deposition enables the patterning of non-conductive substrates and therefore, could be suitable for the direct plating of the DNA-based material. However, the limited amount of solution (< 30 ml) coupled with the polyhedrons low concentration (≤ 1 nM) set unfavourable experimental conditions for the complete coating of the structures. Additionally, the dimensions of the Au^0 grains obtained by ascorbic acid [333,334] although in the sub-25 nm scale length, were not highly compatible with the 9 nm side of the small polyhedrons to further coat the structural part of the cavity. AFM characterisation of the samples was hampered by the presence of high concentration of salt which has crystallised after several washing steps. Additionally, the dimensional polydispersity of the gold grains was unsuitable for fabricating a homogenous sub-25 nm thick coating, as shown in Figure 5.8, which also highlights the presence of > 40 nm particles.

Following several attempts, it was concluded that the electroless deposition is an unsuitable tool for the 10 nm polyhedrons replication, and therefore, other deposition techniques such as electroplating and plasma sputtering were further performed on the 20 and 30 nm-polyhedrons samples.
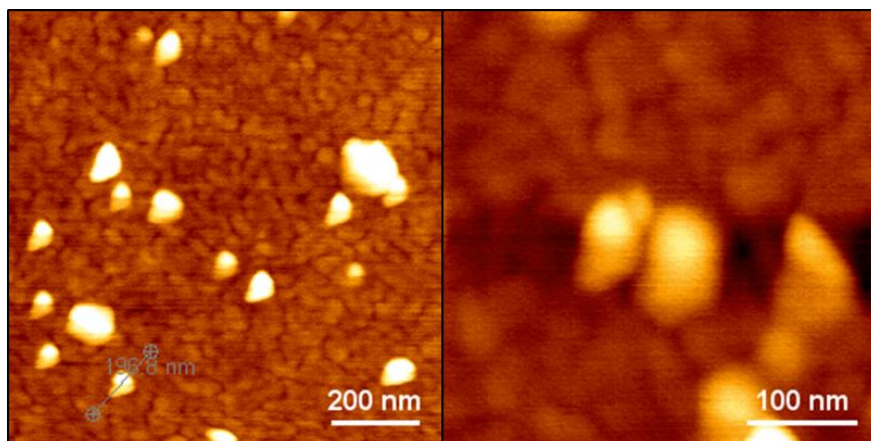
Figure 5.8. Electroless coated surfaces. Large particles, with the unsuitable dimensions of the DNA features to be plated, can be clearly observed in the shown area.

In addition, *plasma sputtering* (Chapter 2.3.3), a coating process where particles are emitted from a target, set at a specific distance from the sample, was also tested as a replication method for 3D DNA morphologies. Due to the high energy of the ejected gold particles, this technique is usually considered highly unsuitable for treating biological samples. After careful considerations of the experimental conditions including, in particular, the gold emitting height and the Argon atmosphere pressure, controlled deposition of homogeneous gold films was obtained, producing gold nanolayer with dimensions comparable with the 3D DNA polyhedron side, as plotted in Figure 5.9, in the calibration curve.
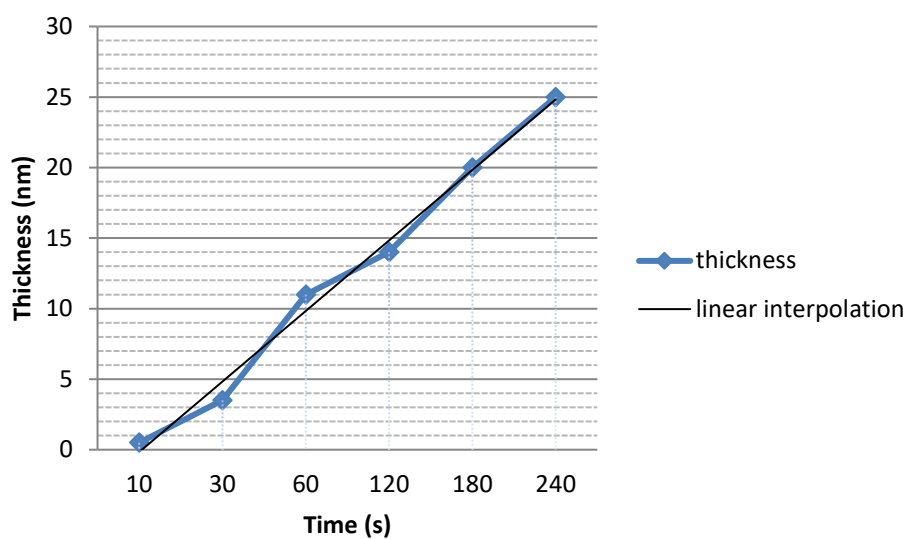
Figure 5.9. Average thickness of gold nano-layers sputtered on top of a silicon wafer *vs* time.

Since the homogeneity of the sputtered film is consistently reproduced with deposition time ≥ 60 s, which corresponds to a layer thickness of 12 nm, the 10 nm DNA structures were not coated, as shown in Figure 5.10.

Since plasma sputtering is a physical process, the emitted particles travel in a straight direction before finally depositing onto the substrate, thus, while a uniform layer is easily deposited, the emitted particles can not reach the central cavity of the polyhedrons.
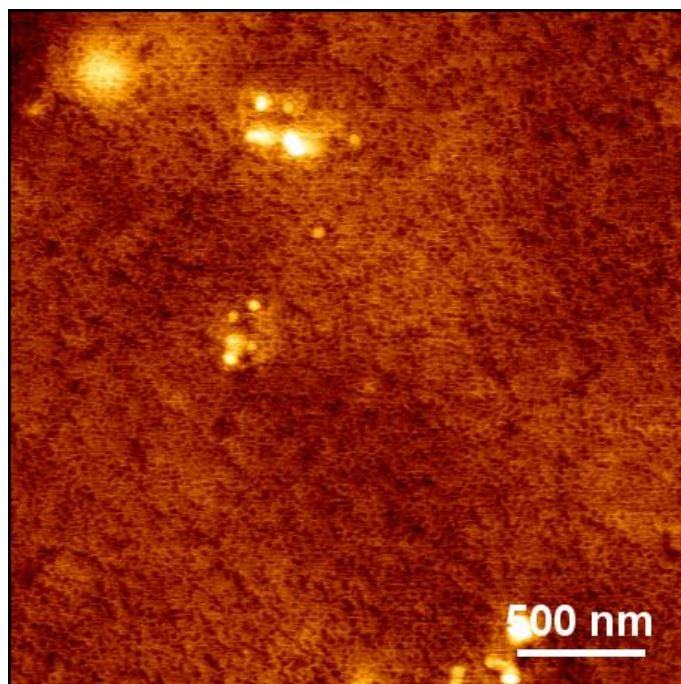
Figure 5.10 AFM image of gold sputter deposition for 60 s.

Gold sputtering as a deposition technique enables the fabrication of a thin layer on simple templates such as, grids or lamellae [335]. In turn, this kind of patterned film can be lifted-off and detached from the substrates, making it applicable for potential application in integrated nanoelectronics and biosensing devices [336,337].

In contrast, the use of intricate structures characterised by cavities such as, DNA polyhedra has been confirmed unsuitable for complete replication on all the sides, since the emitted particles cannot reach the hollow spaces and asperities of the features.

5.6. Determination of Suitable Substrates and Operating Conditions for 3D DNA Polyhedrons Replication *via* Electroplating Deposition

So far, the fabrication of robust micro-to-nano metal arrays has widely utilised plating processes for producing stable coatings on a wide range of substrates. In fact, electroplating is frequently used in the fabrication of nano- and bio-devices, due to the capability of modifying the nature and mechanical properties of the electrodeposit by changing the electrolytic bath composition and tailoring deposition parameters (temperature, convection, deposition technique). In this work, the replication of the 3D DNA nanostructures represents a challenging step, mostly due to the sub-30 nm dimensions of the polyhedrons and their organisation on a surface upon drying.

It needs to be recalled that the polyhedrons are immobilised onto the substrates by non-covalent bonds, and thus, a partial loss of sample is to be expected, although, it has not been quantified accurately.

Experimentally, as shown in Fig 5.11.a., the three-electrode setup for the electrodeposition is comprised of the substrate to coat as the working electrode (WE), an Ag/AgCl 1 M KCl (0.222 V vs. SHE) reference electrode (RE) and a Pt wire as counterlectrode (CE). The role of each electrode in the set-up is explained in detail in Section 3.8, along with the chosen configuration.

The relative position of the electrodes plays an essential role in the yield of the electrochemical process since the *inter*-electrode distance modifies the amount of deposited material (Fig 5.11). More specifically, the physical distance between the WE and the RE should be minimised to reduce the ohmic drop ascribed to the inherent resistance of the aqueous electrolyte employed, whilst the CE should be kept as distant as possible to avoid redepositing of by-products formed at the CE surface.

In this work, the ideally parallel orientation of the WE (Fig 5.11.a) with respect to the gold solution, was achieved by use of a meniscus configuration, to ensure that the applied current flux solely comes in contact with the area of the carbon film modified with the DNA polyhedrons. In particular, this configuration was attempted when using TEM grids as substrates, in order to minimise the interactions with the uncoated copper side of the grid and the plating solution. Experimentally, the WE position was modified by partial immersion of the grid, perpendicularly oriented, therefore enabling further coating and by-reactions at the copper interface, which were further minimised by careful consideration of the experimental parameters.

Initially, while attempting to maintain a parallel geometry, the grid was pasted with conductive glue to a copper sheet, as a conductive support and orientated parallel to the liquid surface (Fig 5.11.b-d) although, the deposition was eventually ineffective due to the unstable position of the WE. The copper sheet was replaced by conductive metal tweezers which enabled the stable positioning of the grid,

preventing any contacts with the solution and the support itself which would interfere with the overall electroplating process.
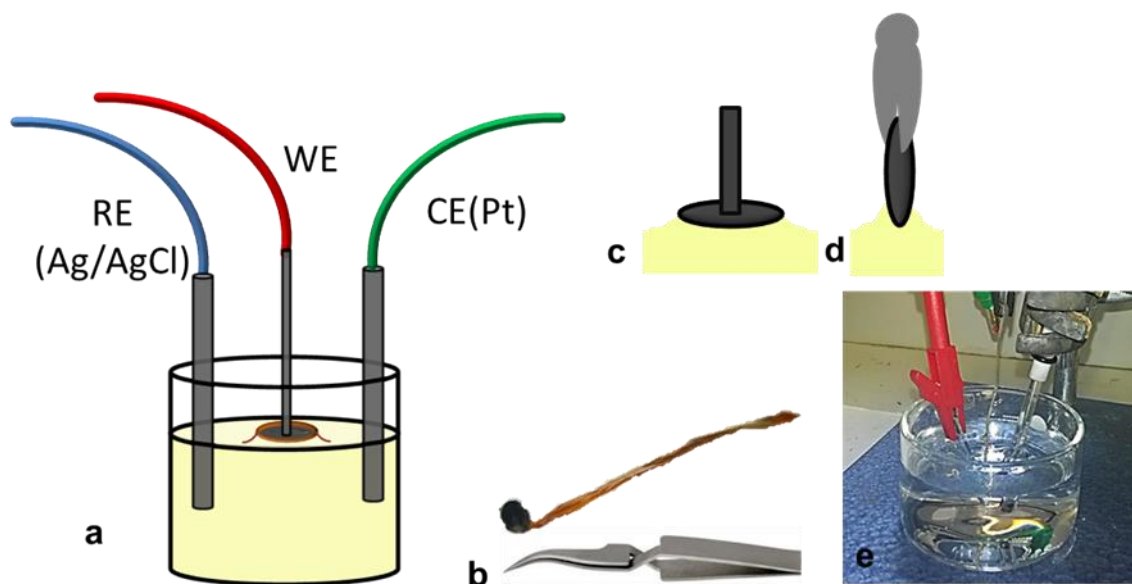
Figure 5.11. Electrochemical setup and details. a) Three-electrodes setup for electrodeposition, comprised of a working electrode (WE) where the sample to be coated is placed, reference electrode (RE), in our case a silver/ silver chloride electrode (E = +0.197 V) and a Platinum wire as counterlectrode (CE). **b-d)** Two of the working electrodes support are used. **c)** A copper wire glued to a TEM grid upon which the sample was immobilised, held in parallel position to the solution, forming a meniscus to ensure the direct deposition onto the grid. In **b)** an inverted tweezer allowed to hold the grid and eventually all the substrate partially immersed in the solution. **e)** An image of an assembled experimental setup ready for the electrodeposition process.

The cyanide-free bath, on the contrary of the traditional ones, eliminates the health hazards from the formation of $HCN_{(g)}$ which forms after disproportion of the $Au(CN)_2$ for T > 26° C. In this work, the use of a commercial solution, ECF60 (Metalor Technologies Ltd, UK) formulated for fine patterning on semiconductors, enables coatings on conductive surfaces with insulating features, resembling the nature of the samples to be electrochemically modified.

5.6.1. Preliminary Tests for Substrates and Solution Stability

Preliminary tests were necessary to determine the activity and stability windows for both the plating solution and the substrates.

Preliminary studies of the plating solution are shown along with the Pourbaix diagram [338] (Fig. 5.12.a-b), which indicate the different oxidation status of a gold aqueous solution at varying pH and applied voltage (E), also defined as a *potential/ pH* diagram.

In this work, the oxidation state of the gold is strictly dependent on the potential applied, the pH and also, on the temperature of the solution. Additionally, this latter factor has a cumbersome role in preserving the DNA structures during the plating, which otherwise may affect their stability and thus, the 3D arrangement. The diagram proposed in Figure 5.12.a refers to 25°C bath conditions.

From the Pourbaix diagram, it emerges that metallic gold (Au) is majorly present for E < 0.2 V at every pH value, while upon applying a potential difference it can reach various oxidation states and therefore, originate different species.
On the one hand, beyond the upper limit of the *stability window* of the electroplating setup, as shown in Fig 5.12, Au_2O_3 is formed (E ≥ 1 V), although voltage values above -0.2 V also result in corrosion of the copper grid originating CuO_x. On the other hand, below the minimum threshold of the stability windows, for E ≤ -1 V, solvent breakdown occurs as water disproportion, releasing gaseous H_2.
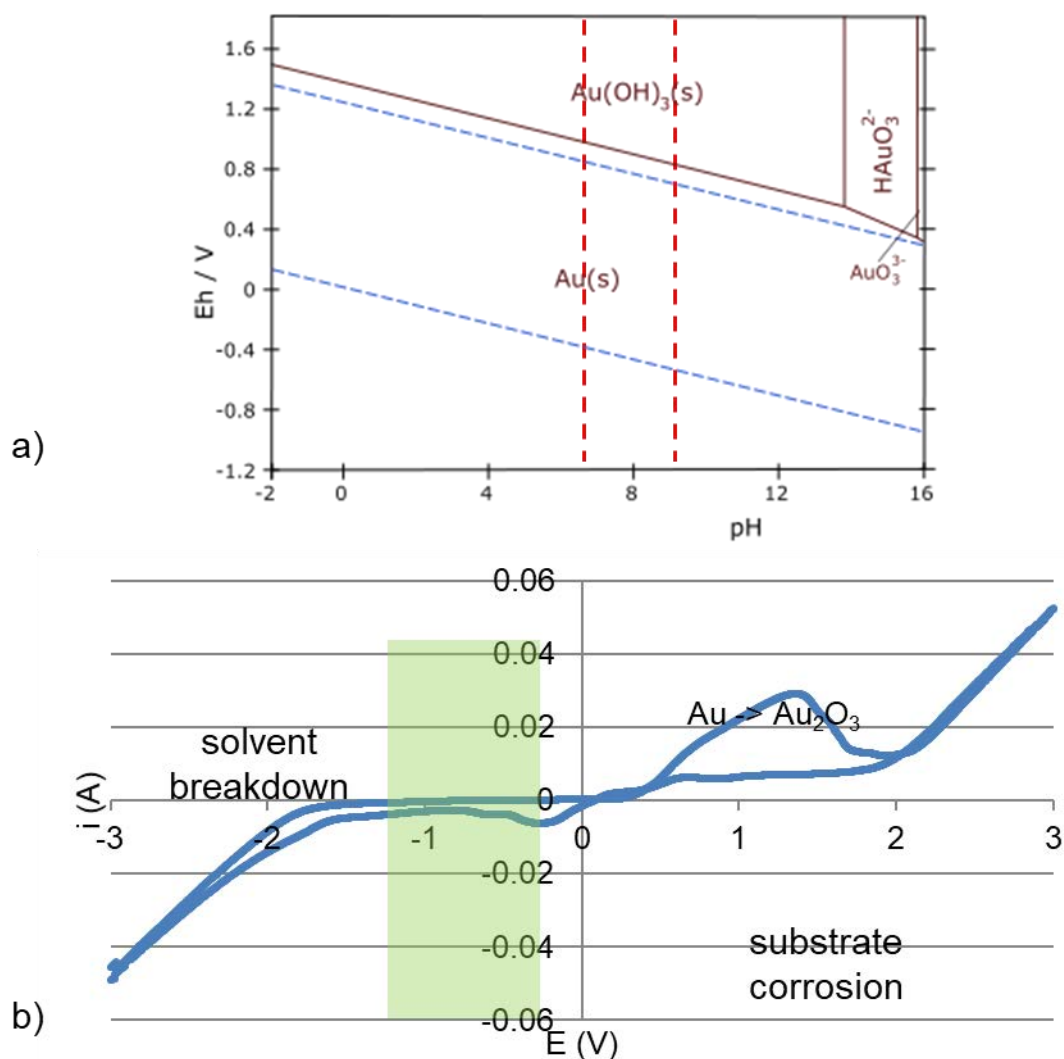
Figure 5.12. Electrochemical window for ECF60 and related Poubaix diagram. a) Pourbaix diagram is highlighting the different species originating from the gold various oxidation states, upon changes in the voltage applied and the pH of the solution. **b)** Voltammogram of ECF60, upon determination of the OCP, at approximately -0.2 V. The stability area, in the green box, has the OCP as a maximum threshold, while the minimum value is determined by the solvent breakdown.

The stability limits of the substrates in the solution were established by corrosion test, determining the open-circuit potential (OCP test). Potential limits were set between -1 and -0.2 V for the carbon film TEM grid (Fig 5.12.b) and between -0.75 and 0 V for the ITO glass slide, which were similarly analysed.

The by-reactions occurring while plating silicon (Si) wafers, coupled with the harsh bath conditions required, concurred in considering silicon substrates unsuitable for biological sample treatments thus, leading to perform the Au electroplating directly onto polyhedron-modified TEM grids and ITO glass.

After OCP determination, the *linear scanning voltammetry* (LSV) (see Section 3.8.1) recorded within the sample stability window (Fig. 5.12.a.) allowed to gather insight on the Au deposition process. A *reaction kinetics*-controlled region (from -0.2 to -0.75 V) was followed by a *mass transport*-controlled region (from -0.8 to -1 V), featuring a cathodic peak characteristic of *diffusion*-controlled electroplating processes. As the electroplating process is used to obtain sub-30 nm Au layers, the Au growth rate should be slow enough to enable careful control over the deposition process. This level of control is generally achieved in the kinetics-controlled region, where the applied over-potential with respect to the OCP value is small and therefore, acts as the Au deposition driving force. At high overpotentials, which is defined as a mass transport-controlled region, the deposition rate would be very fast, promoting bulk Au deposition.

Consequently, the electrodeposition potential was set at -0.7 V, where the reactions occurring at the WE are mostly kinetics-controlled, as shown in the LSV diagram (see Section 3.8.1) in Figure 5.13.
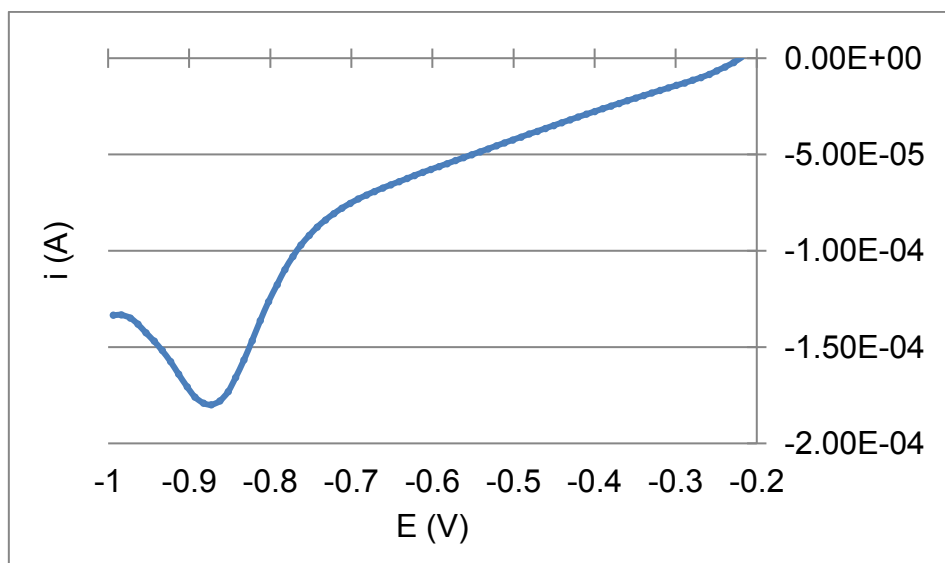
Figure 5.13. LSV diagram derived from OCP determination. The cathodic peak, typical of diffusion-controlled processes, is followed by a kinetic-controlled region, which lasts until -0.2 V.

Therefore, a set of bare substrates were electrochemically coated for testing the reliability and reproducibility of the methods, for both E = -0.7 V and E = -0.8 V, in order to justify these assumptions.

As recalled, when plating at E = -0.8 V, the electrochemically-driven Au^{3+} reduction occurs at the WE with a high deposition rate, leading to the formation of a large number of initial nuclei which ultimately grow to overlap and form a full layer.

As shown in Fig. 5.14, the deposition time (*t*) has also a fundamental influence on the thickness and shape of the plated gold nanolayers. For instance, lamellar-like structures can be identified on a substrate coated for over 60 s (Fig 5.14.c-d), while, for *t* = 40 s, nano-islands are formed (Fig 5.14.a-b). Both structures, due to the elevated amount of formed *nuclei*, had an elevated roughness with an average peak-to-valley distance of approximately 20 nm thus, resulting in an unsuitable coating for the DNA polyhedrons. For *t* < 40 s, the deposition was

173

highly irregular and sporadic all over the substrate, with fewer *nuclei* than the *t* = 40 s sample, localised at the surface defects of the substrate.
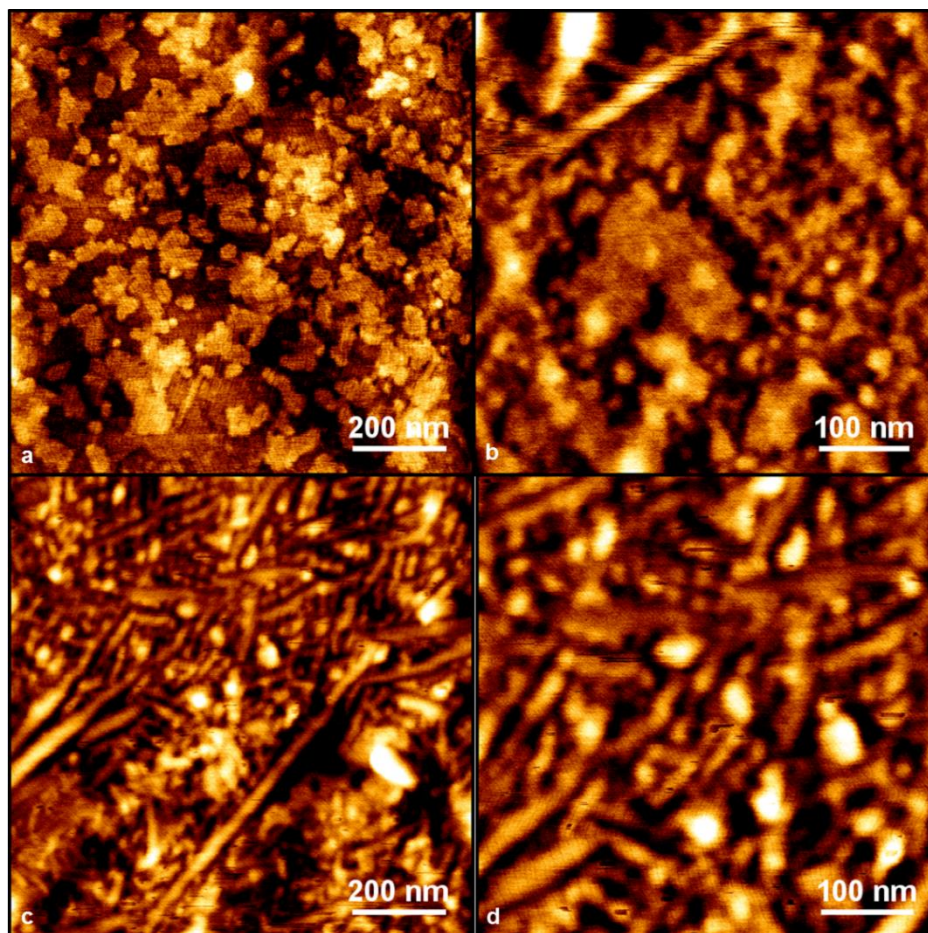
Figure 5.14. Gold formation on substrates after electroplating. a-b) Nanoisland formation after a 60 seconds deposition at -0.8 V. Since E is close to the cathodic peak, and the occurring reactions are diffusion-controlled, the great amount of material deposited does not allow a homogeneous film to form. Similar assumptions in **c-d)**, where the gold deposits as *lamellaes*.

On the contrary, the deposition carried out at E = -0.7 V, for *t* = 20, highlighted the formation of a 7.5±2 nm layer, evenly distributed. The dimensions of the resulting grains are comparable with the DNA nanostructures, therefore, setting the ideal conditions for the replication of the polyhedron nanopatterns.

Consequently, the determination of the gold deposition conditions on ITO has followed similar to the above-described assumptions. The ITO thin film has

usually an electrochemical window from -0.5 V to 1.5 V (*vs.* SHE), although the analysis performed on our sample showed an extended window to -0.55 V (*vs.* SHE). The electroplating potential was then set to 0.2 V (*vs.* SHE) and the produced layer roughness results with a maximum peak-to-valley distance of 3±0.5 nm for a 20 s deposition, while the thickness modulated by the deposition time (Fig. 5.15), with a maximum of 40 s.
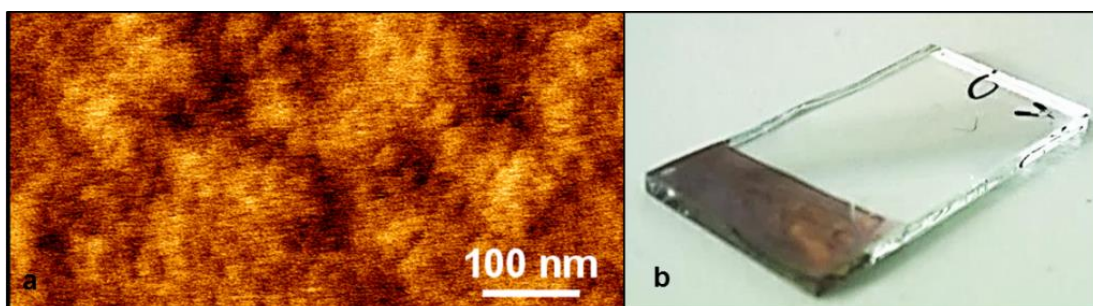
Figure 5.15. Gold plating on ITO. a) AFM image of gold coated ITO. In **b)** the picture shows an extensively coated ITO glass, much above the desired thickness. Sub-10 nm structures are nearly transparent and therefore, difficult to observe.

Once the electroplating parameters were established, further tests were carried out for demonstrating the method's feasibility when coating insulating features immobilised onto the surface. At this instance, 100 nm polystyrene nanoparticles (PS-NPs) were coated while maintaining the experimental conditions determined above.

The PS-NPs diameter was monitored before and after the plating. PS-NPs are inert at the varying applied voltages (see Figure 5.16) on both TEM grids and ITO glass, and no changes in the shape of the spheres were observed.

ImageJ software was used as a tool for analysing the diameter of the particles before and after the plating, showing a homogeneous increase of 9±3 nm, for t = 20 s, and 11 ± 2 nm for t = 40 s.
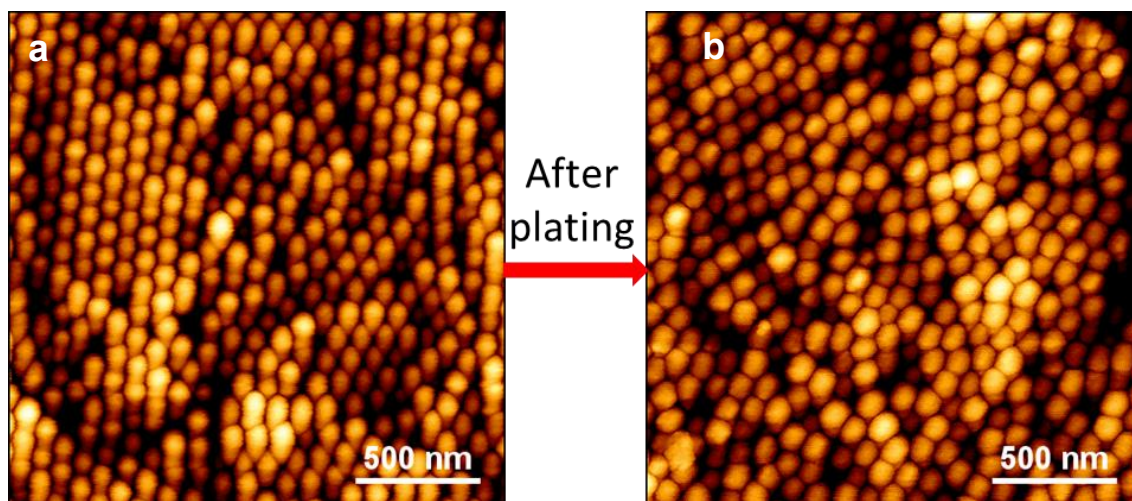
Figure 5.16. Gold plating control. Comparison between PS nanospheres **a)** before and **b)** after gold electroplating, for a deposition time of 20 seconds. The particles diameter was measured before and after the plating treatment, and an overall increase of approximately 9 nm was calculated.

5.6.2. Replication of 3D DNA with Gold Electroplating

The 3D DNA polyhedrons were replicated upon immobilisation on the substrates, which were previously electrochemically characterised. A close gold replica of the DNA polyhedrons, reproducing both edges and cavities with no loss in the structural details, was produced. Thus, illustrating a proof-of-concept of a novel procedure, which enables DNA molecules to be exploited as templates for fabricating a range of 3D nanostructures.

The accurate dimensional tuneability of the structures, as demonstrated in synthesising various polyhedrons with varying side length, allows manufacturing tailored templates, which can be further reproduced with various noble metals targeting a range of applications.

The previous sections provided detailed insights into various plating techniques, eventually narrowing these to the electrochemical deposition as the most suitable one, due to its high performances and compatibility with the biological samples. The dimensions of the gold grains, usually ranging from 2 to 5 nm [126,127,339], are comparable with the polyhedrons dimensions and enable the replication of a sub-10 nm thick gold film while preserving the structures during the process. Upon completion of the replication process, the resulting features can be up to 4 to 5 times larger than the moulds, dimensions which can be tuned depending on the deposition time.

The first 3D structures replicated were the 10-nm and the 20-nm polyhedrons. Their position on the surfaces and their shapes were prior characterised in dry conditions (Fig 5.4-5.6).

According to the general growing mechanisms [340,341], it is assumed that the plating process, in the first place, occurs on the conductive substrate and later proceeds toward the edges of the deposited, insulating DNA features (see Figure 5.17). The position of these latter structures was recorded showing a range of geometrical structures, which are considered as the DNA polyhedra [171,196,197,200]. Thus, it is expected to observe similar shapes, whose dimensions will increase with the plating time. The growing process is shown schematically in Figure 5.17.
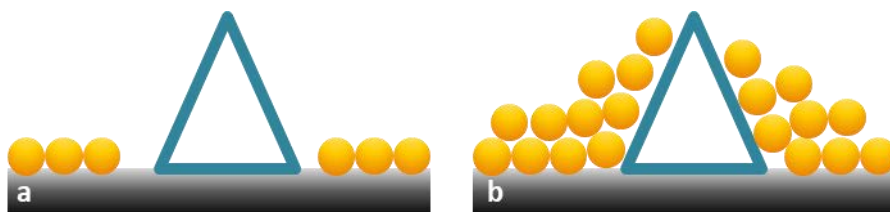
Figure 5.17. Cross-section schematics of the layer-based growth mechanism.

As, the plating of the 9-nm features resulted in a homogeneous layer, where the gold grains and the polyhedra were essentially indistinguishable, as shown in Figure 5.18.
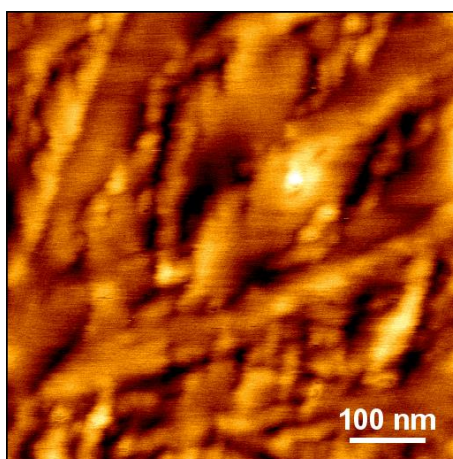
Figure 5.18. Gold-plated layer on 9-nm polyhedrons. The gold grains forming an irregular layer are visibly indistinguishable from the DNA features.

The AFM images of the gold replicated features (Fig 5.19) show the deposited gold layer, initially still comprised of single gold grains, visible in the early stages of the gold replication, indicating the nucleation sites for the further nanolayers. As determined by the preliminary plating of the bare substrates, the deposition occurred homogeneously on the conductive surface although, the presence of insulating DNA polyhedrons affects the coating, creating grove-like features, as shown in Fig 5.17.c-d.

178

Experimentally, the low conductivity of the DNA structures produces insulating points on the conductive substrates, where the plating first occurs. Therefore, as, expected, gold deposition on the polyhedrons occurs at a later stage of the electrodeposition, with an almost complete coating of the substrates.

The structure details of the polyhedrons can be recognised by the presence of the hole-like features (Fig 5.19 and 5.20), which indicate the pyramid shapes of the polyhedrons patterned surface. These areas are the replicas of variously oriented polyhedrons, which result in measured structure sides of 55±15 nm. Surface roughness measurements determined the average peak-to-valley distance to be 15±4 nm, with an overall roughness of 9±4 nm, as expected after the gold deposition.
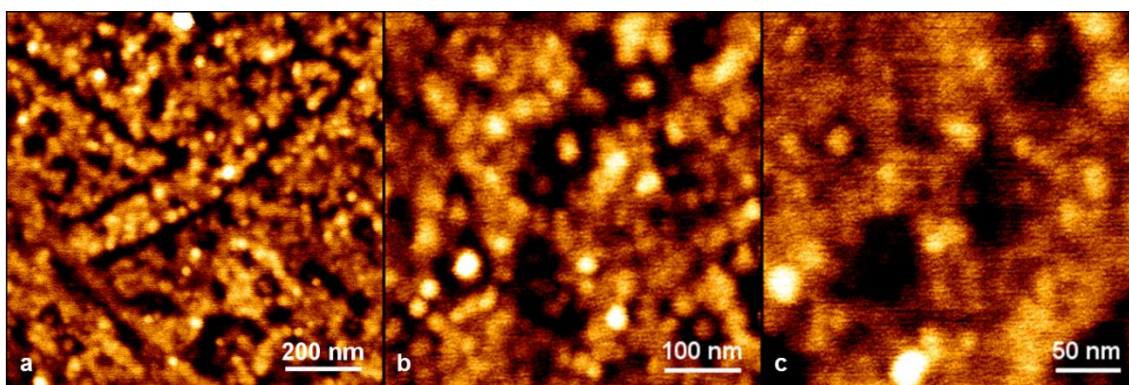
Figure 5.19. Gold-coated 20 nm samples on substrates. a) 1 x 1 µm^2 AFM images show the deposition on 3D DNA sample on TEM grid. **b-c)** Zoom–in of the areas shown in **a)** where holes-like shapes determine the presence of upward oriented DNA polyhedrons used as a plating template.

From the preliminary characterisation of the bare substrates, the deposited layer thickness for t = 20 s is approximately 7 nm thus, the increase in the height of the

179

structure is due to the preliminary coating of the conductive substrate, which forms an initial layer with thickness consistent with the expected value.

Thus, limiting the applicability of DNA templates directly replicated from the TEM grid substrate. To note, the direct deposition on TEM grids was very useful due to their conductivity as well as the direct TEM imaging of the nanostructures in the transmission and scanning modes. To further overcome this limitation, however, preliminary gold replication was carried out on the DNA polyhedrons and in particular, on the 30-nm DNA features, immobilised on the ITO glass.
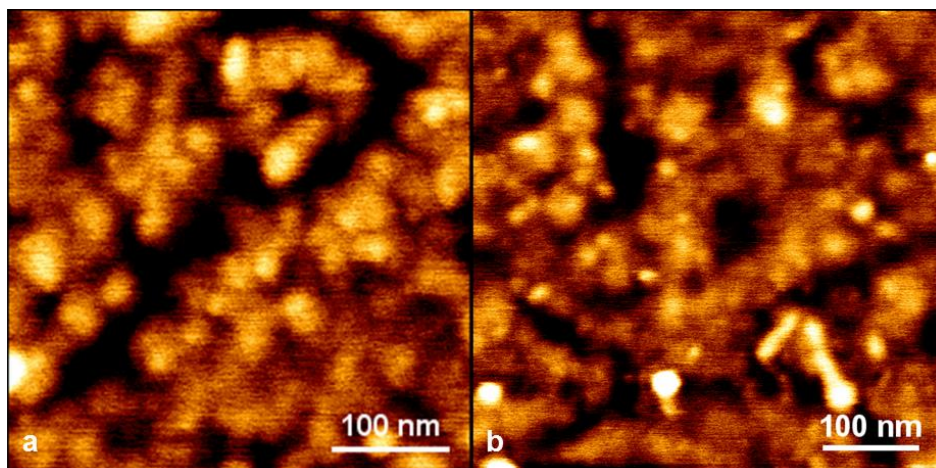
Figure 5.20. Gold-coated 20 nm samples on substrates a-b) AFM images of gold patterned areas where the triangular replicas can be observed.

Since the presence of the triangular-like structures is interpreted as evidence of accurate completion of the DNA features replication, the procedure was also applied to the synthesised polyhedrons immobilised on the ITO glass. Here, the initial roughness of the surface is compensated by the homogeneous conductivity, which enables coating of sheer, transparent gold layers. A set of preliminary deposition studies on 30-nm DNA polyhedrons and 20-nm

polyhedrons, upon immobilisation on ITO, showed a uniform coating on the surface although, clear images of the octahedron gold replicas were of an insufficient resolution at this stages and further studies are required to optimise this procedure.

Table 5.1 summarises the results of roughness measurements taken for each system, before and after the plating, on a number of various substrate.

Table 5.1. Roughness measurements were taken for each polyhedron before and after plating at -0.7 V.

Roughness measurements (nm)	9-nm polyhedron		20-nm polyhedron		30-nm polyhedron	
	grid	ITO	grid	ITO	grid	ITO
Before plating	3.2±1	n/a	3.1±0.5	4.3±0.5	5.1±2	7.3±0.8
After plating	1.3±0.5	n/a	9.2±3.9	10.5±3.2	15.8±2.1	17.1±2

5.7.   Preliminary Characterisation of the Optical Properties of the 3D Gold Replicated DNA Polyhedrons

Following the successful fabrication of the 3D gold plated nano-polyhedrons, preliminary results of optical properties were collected in collaboration with Dr Vignolini's group (University of Cambridge, UK).

Since this section aims to show a set of preliminary data as a *proof-of-concept* for future investigation of similar systems, this set of results focuses on the optical properties arising from the gold surfaces templated by the **20-nm polyhedrons**.

As observed in the previous sections, the assembled nanostructures show the tendency to self-assemble into localised areas which were chosen as analytical sites for the transmission and birefringence spectral investigation.

Preliminary results for the effect of polarised light on the 20-nm DNA-templated gold-plated surface in a chosen micron-scaled area are shown in Fig. 5.21.

Cross-polarised images are obtained by using a cross-polarised analyser or similarly, using a second polariser perpendicularly positioned to the first. Thus, the original plane-polarised light is eliminated while the perpendicular one is transmitted. In fact, as shown in Fig. 5.21, from the same analysed area, the transmitted light drastically changes depending on the transmitted light interacting with the sample itself.
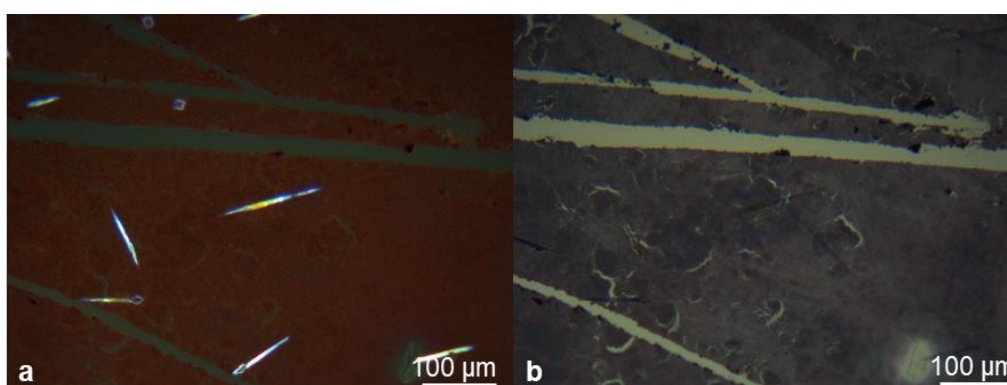
Figure 5.21. **Effect of polarised light on nanostructured gold surfaces. a)** Cross-polarisation 20x in transmission and **b)** cross polarisation 20x, in transmission, of the same location when the polarisers are rotated 45 degrees.

A preliminary spectrum of the analysed area was also taken for better understanding of the properties arising from the interaction of the sample with varying polarised light, between 350 and 800 nm as wavelength (λ) range. The spectrum arising from the analysed area (Fig 5.22 - red line), compared with the control spectrum obtained by the gold-plated bare ITO (Fig 5.22 - blue line), showed that the red background (for λ between 600 and 700 nm) has a prominent signal stretching into the IR. Therefore, this was interpreted as a plasmonic effect and was further investigated, despite the disturbance arising from the red background.
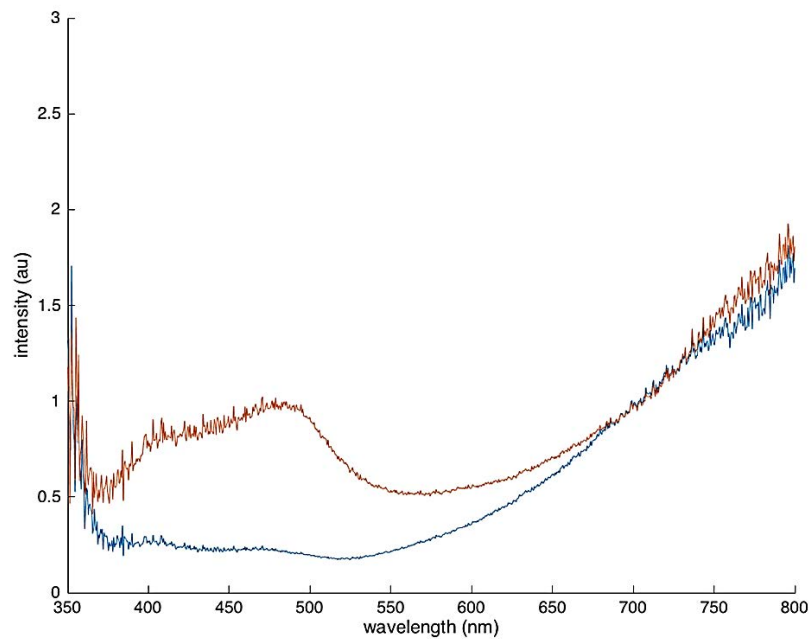
Figure 5.22. Preliminary transmission spectra. The spectrum of the area anaysed in Fig 5.21 (red line) is depicted against the control spectrum from the gold-plated bare ITO (blue line).

5.7.1. Optical Transmission Measurements

Further investigations were carried out on specific sites, restricting the analysed area to singular spots, as shown in Fig. 5.23.

In this bespoken setup, the optical fibre captures spectra from the centre of the image, where the region of interest (ROI) is located (Fig 5.23, black circle).
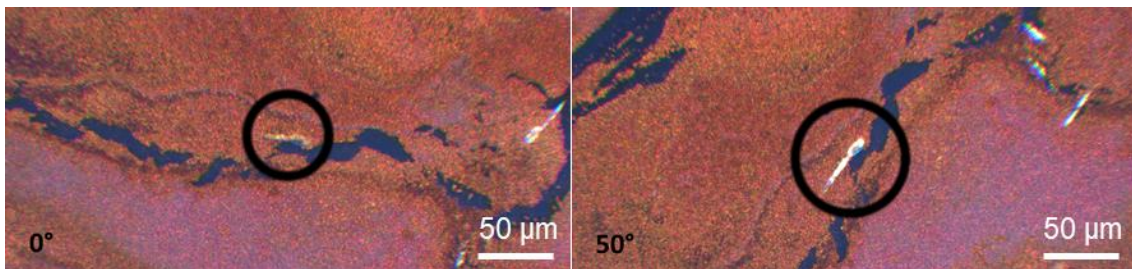
Figure 5.23. Areas investigated by transmission polarised light.

Spectra in Figure 5.24 are related to the ballistic light (see Section 3.9.6) filtered by a polariser at the same angle. While a strong birefringence can be seen centred around 490 nm (left arrow in Figure 5.24), the red background area (circled are with an arrow on the right-hand side of Figure 5.24) should be less polarisation sensitive, indicating that we potentially have polarisation dependent attenuation in the light path. Future investigation will focus on reducing this effect. The ITO slide was used as a reference sample while keeping the polarisers parallel to measure the total incident light. Measurements were taken between cross polarizers, rotating the sample.
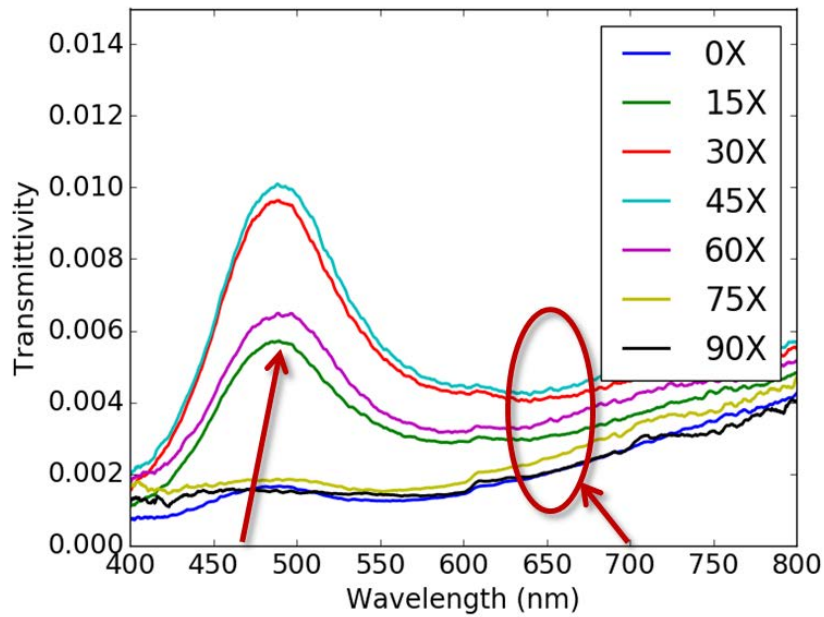
Figure 5.24. Transmissivity spectra of ballistic light filtered by a polariser at the same angle. The red left arrow indicates a clear birefringence at approximately 485 nm, while the red background (600-700 nm) area is less sensitive to polarisation.

Figure 5.25.a-b shows the normalised transmission intensities in the wavelengths range of 400-800 nm, as a function of different angles with the angle of 0° indicating the position where the sample is parallel to the polarization of the incoming light (which is the same in both reflection and transmission).

Furthermore, a periodicity of about 100° is evident in the peak intensity seen in Figure 5.26, whilst no periodicity is observed for the other peak's features in terms of width and spectral position. The position of the transmission peak is 485 nm for all the spectra (Fig. 5.26).
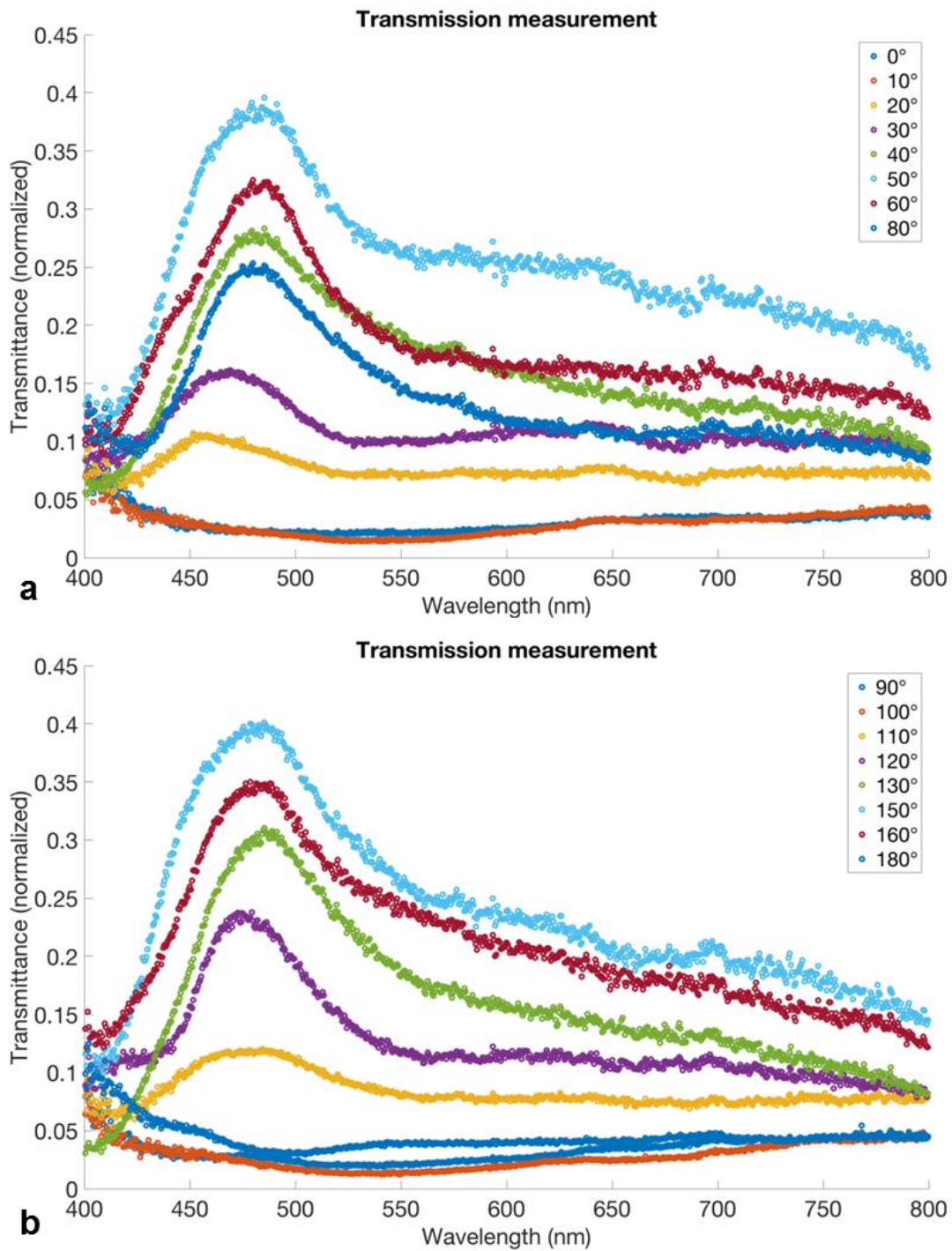
Figure 5.25. Normalised transmission intensities as a function of the sample angle and the light beam. a-b) Taken for the 400-800 nm wavelength window, measurements were obtained between cross polarisers, rotating the sample.
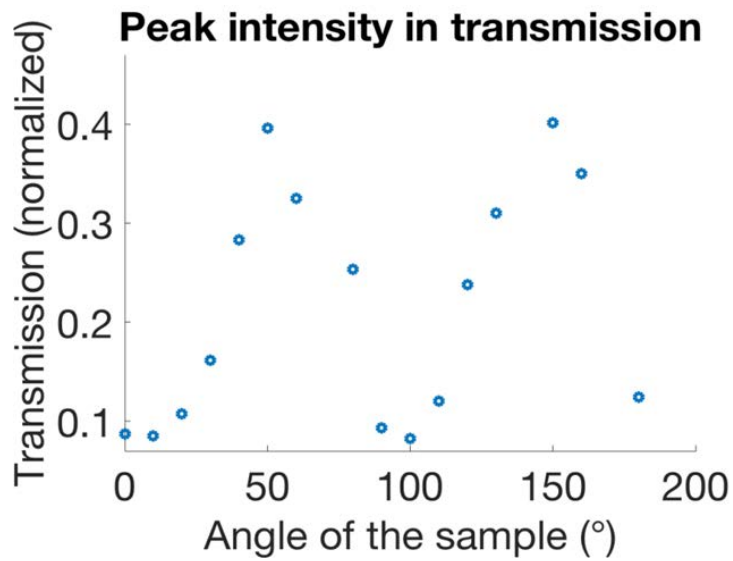
Figure 5.26. Normalised transmission at 485 nm for tilting sample angle from 0 to 180°. A 100° periodicity in intensity is observed.

5.7.2. Optical Reflection Measurements

Similarly, the 20-nm DNA-templated gold surfaces were investigated in the reflection mode. The total incident light was measured with a reference setup with parallel-aligned polarisers, using a gold-plated ITO slide. The measurements were obtained rotating the sample.

As observed in the transmission investigation, reflection measurement showed a 100° periodicity, which is present both for the peak and the minimum, in terms of intensities.
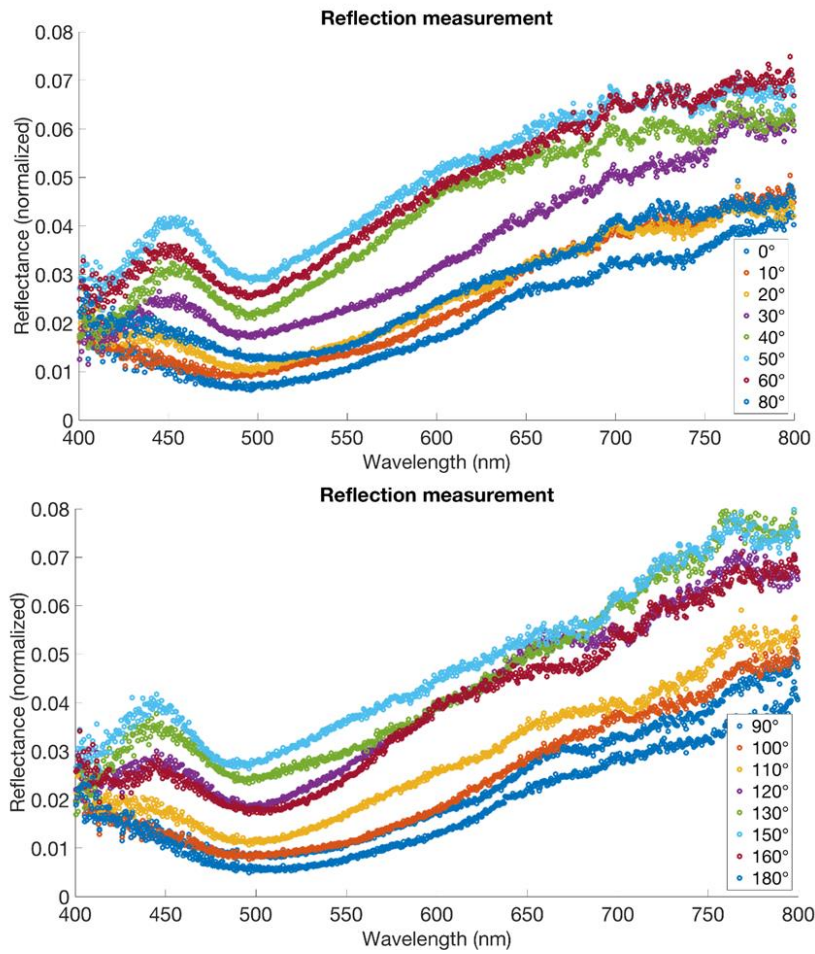
Figure 5.27. Reflection spectra. The angle in the legend is the one of the rotation stage where the sample is placed

Noteworthy, the position of the peak and the minimum do not show any shifting, being found, respectively at 450 nm and 495 nm.

Finally, the transmission and reflection spectra were compared, showing both the maximum (50°) and minimum (100°) positions (Figure 5.29).
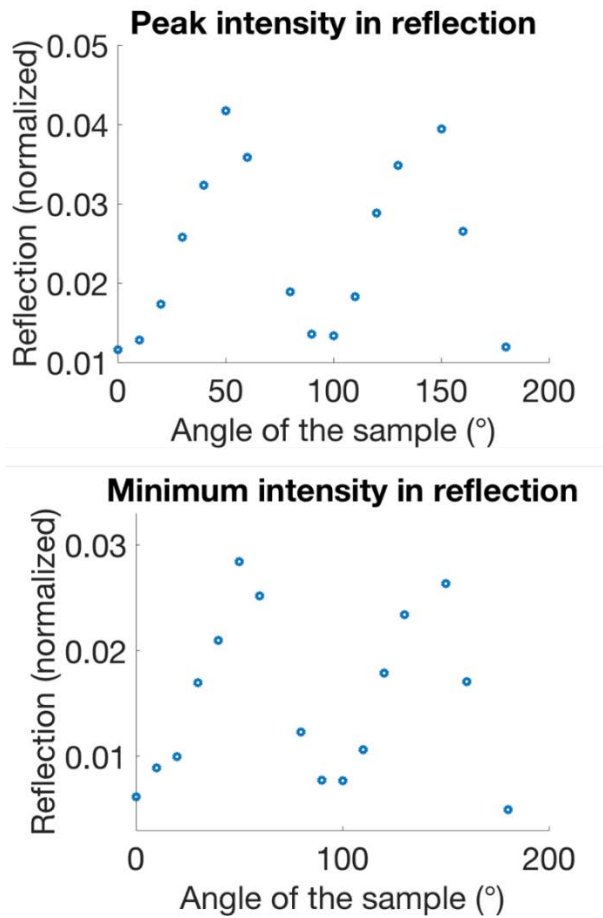
Figure 5.28. Reflection peak and minimum. The peak is located at 450 nm and the minimum at 495 nm.

5.8.   Conclusions

In conclusion, in this study, we have successfully demonstrated a novel, cost-effective and robust method for replicating sub-50 nm 3D DNA structures *via* gold electroplating. Furthermore, preliminary optical responses were collected from

such patterned areas showing interesting properties arising from the organised micro- and nanostructures.

Initially, the sub-50 nm 3D DNA polyhedrons were fabricated and characterised in dry state on solid supports, and subsequently, were used as sacrificial templates for manufacturing gold nanopatterns *via* controlled electrochemical deposition, enabling highly detailed replicas. Interesting optical properties are revealed by the interaction of polarised light with the replicated polyhedrons, with a strong birefringence peak arising at 485 nm in transmission, and later confirmed by the reflection data.
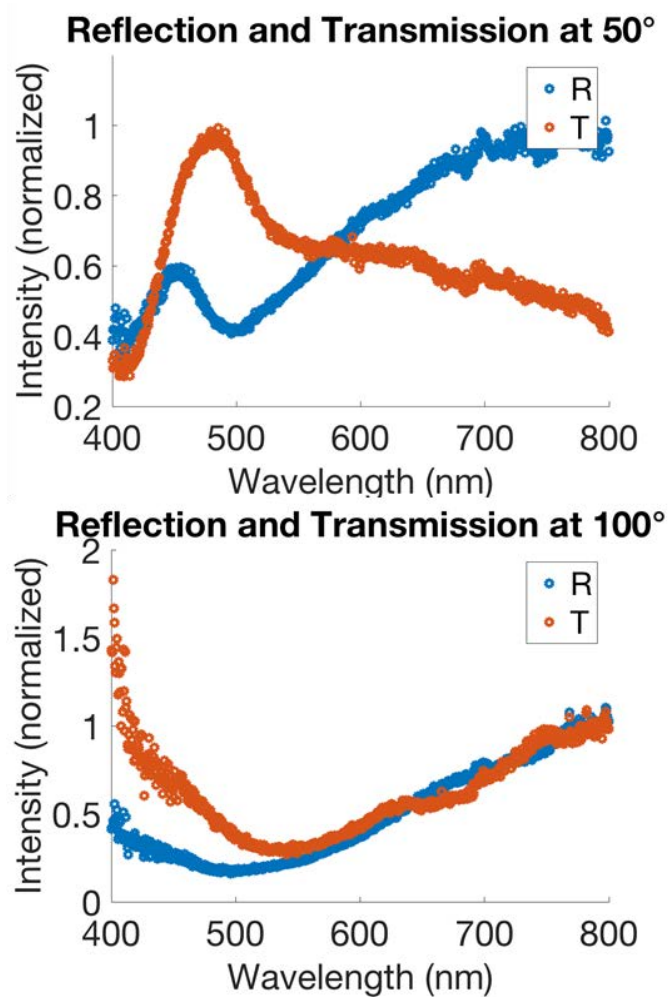
Figure 5.29. Comparison of the reflection and transmission at 60 and 100 degrees with the two spectra normalised to their values at 800 nm.

The results obtained for the 20-nm DNA polyhedron's replica provide preliminary yet, fundamental, information about the properties of free-standing three-dimensional gold nanostructures, delivering a proof-of-concept that new fundamental methods can be used to further develop tuneable three-dimensional nanostructures. Further into-depth studies are required to develop robust, reproducible and tuneable DNA nanostructures that will be able to act as templates for the fabrication, through molecular recognition, of sub-100 nm porous metal (or metal-oxide) 3D-nanoarchitectures. Theoretical modelling and simulations, optimisation of assembly conditions, reproducibility and tuneability, spectroscopic characterisation and extensive testing of evolving optical properties are all subjects for further research and studies.

Establishment of all the above listed parameters will in turn, enable this unique and successful procedure to further, lay the foundations for an innovative approach to nanomaterials manufacturing, using cost-effective materials and techniques. The scalability of the protocol toward large areas patterning whilst preserving the sub-50 nm length scale details of the original DNA polyhedrons templates may represent a step forward in bio-nanomanufacturing. Furthermore, the tunability of the polyhedron 'scaffolds' enables an endless pool of structures to be replicated which in turn, can allow modulating the optical properties. Finally, to summarise, potential applications of the nanoscaled gold 3D replicas can broadly range from, for instance, sensing devices through the ultra-sensitive diagnostic platforms to military devices for environmental surveying and camouflaging.

6. Conclusions and Future Outlook

The work presented in this thesis shows two of the many possible ways to develop nanopatterns that are technologically appealing. Due to the increasing demand for miniaturised devices, research has exploited alternative pathways for decreasing cost and time of sub-micron fabrication. In line with this perspective, this work has focused on producing tuneable nanofeatures, using cost-effective materials through non-toxic techniques.

The **first and second chapters** introduce the main topics of the thesis and the overall aims and objectives, providing theoretical background on nanofabrication techniques and their uses, while a general introduction of photonic, plasmonic band-gap, meta-materials and superhydrophobicity provides fundamental information on hierarchical water-repellent surfaces and optically-active structures and their manufacturing.

The **third chapter** describes the experimental approaches and technical advancement for producing hierarchical patterns, with features on the micro-to-nanoscale. Early stage optimisation of the systems, deprived of any discussion, are listed in this section.

The subsequent chapters are dedicated to the two major research studies carried out and the corresponding experimental work, presenting the scientific outcomes and potential future applications.

The **fourth chapter** outlines the route taken to develop dimensionally-tuneable *lotus*-to-*rose* superhydrophobic surfaces with hierarchical micro-to-nano patterning *via* EHL method.

In this chapter, the hypothesis H_{1-EHD} was successfully verified by manufacturing a range of patterned *carbon nanotubes (CNTs)*-based top electrode for *electrohydrodynamic (EHD) lithography* on polymeric substrates. Careful determination of the EHD various stages and experimental parameters enabled the controlled replication of the top electrodes asperities introduced by the CNTs. Moreover, set aside the "traditional" complete patterning with polymers columns pinning to the master electrode, controlled partial replication was successfully achieved, enabling the fabrication of spiky-cones of various pitch and dimensions. The wetting properties of the produced surfaces were tested and confirmed obeying to *rose-petal* and *lotus-leaf* regimes.

An accurate insight into the various wetting regimes and the nature of carbon nanotubes (CNTs) as driving elements of EHD patterning provides additional background information to the overall procedure.

CNTs were grown by chemical vapour deposition as a forest and in predetermined arrays and then, covered by a silicon layer to preserve them for continuous, long-term use as top electrodes in the EHD process. The patterning was carried out on polychlorotrifluoroethylene (PCTFE), which due to its

hydrophobic properties and polymeric nature provided the ideal substrates for manufacturing super apolar surfaces with various morphologies. The results of the wettability properties, obtained by dynamic sessile drop, highlight the influence of the morphology on the hydrophobic behaviour, mostly dictated by the distance between the pattern units, enabling *Lotus* and *Rose*-like wetting states. Therefore, CNT-EHL represents a versatile technique easily applicable to a wide range of polymeric substrates enabling complex yet, tunable geometries, directly mimicking nature's unique micro-to-nano structures. The scaling-up of such low energy surfaces, which have a vast role in modern coatings, fabrics and technology devices is thus facilitated by the CNT-EHD as a robust and straightforward technique with high potential for future applications for mechanical resilient and optically transparent sub-micrometre patterned surfaces.

The **fifth chapter** presents an alternative pathway for manufacturing optically-active photonics-like materials by exploiting the role of DNA origami as a sacrificial template for scaffolding a metal backbone.

Herein, the principal hypothesis *($H_{1\text{-}OPT}$)* was successfully confirmed by the positive replication of self-assembled DNA polyhedrons *via* gold electroplating. Preliminary studies and characterisation of optical properties showed interesting results in terms of birefringence*.*

The unconventional use of DNA as a building block represents an innovative strategy for achieving controlled structures in the sub-100 nm scale by allowing accurate tuning of the template dimensions. Discussion of the experimental

details further introduces the manufacturing strategies which were exploited for the final gold nanostructures, stressing the importance of the correct DNA assembly into 3D polyhedrons, followed by careful choice of substrates and deposition techniques for immobilising these nano-architectures on a surface. Particular attention is given to the combination of techniques used for achieving structural scaffolds using DNA polyhedrons as templates for replication *via* gold plating. Accurate characterisation *via* atomic force microscopy (AFM) and transmission electron microscopy (TEM) allows visualising the minute sample structures while confirming their dimensions and mutual disposition after drying. The 3D polyhedrons, upon immobilisation on conductive surfaces such as indium-tin-oxide (ITO) glass or TEM grids, represent ideal replication moulds for gold electrodeposition. It is demonstrated that the scarce conductivity of the DNA polyhedrons does not affect the gold plating, which proceeds homogeneously, coating both the substrates and the 3D moulds at an equal deposition rate. The surface analysis *via* AFM imaging revealed the presence of polyhedron-like gold features, suggesting that the structures were preserved during the plating process and thus, enabling an innovative and robust procedure for producing nanopatterned surfaces with a scaling-up potential. The optical properties of the structures were later studied using the spectrometry analysis, showing interesting birefringence at 490 nm. Therefore, a novel nanopatterning strategy has been demonstrated in this study, using biomaterials such as, 2D and 3D DNA origami, organised viruses, and proteins, which will potentially broaden the spectrum of tools for manufacturing structures with novel photonic properties, plasmonic bandgap and negative refractive index. Noteworthy, this procedure might be

further expanded to plating with different metals such as, copper or silver, enabling robustly patterned surfaces with potential applications in sensing devices.

6.1. Future Applications

The remarkable advantages of the patterning procedures introduced in this work are also characterised by their cost-effective processes. The techniques used for the manufacturing the unique nanostructures are mostly comprised of bench-top instruments, either customised or purchased.

With regard to the **EHD lithography**, in general, an oven and a low-voltage power supply are suffice as the experimental setup, while conventional spin coating deposition is necessary for producing the top-facing capacitor plate. In this case, the production of CNTs arrays requires additional expensive procedures, which are compensated by the great control gained during the patterning, while achieving highly reliable and robust micro-to-nano structures. In line with the cost-effective manufacturing perspective, the fabrication of **optically-active materials** only requires a standard galvanostat during the plating process, while the DNA origami units can either be produced by a bench-top synthesiser or purchased as designed. Therefore, both versatile procedures will potentially enable increasing accuracy in the sub-micron fabrication techniques, while diminishing the costs of production. In particular, self-assembled high-yield DNA structures will provide ideal building blocks for large-areas patterning, and it is reasonable to suggest

their use in combination with traditional lithography, or even EHL, in the production of robust hierarchical surfaces.

The **combination of the two techniques** will enable highly controlled, robust micro-to-nano structures generated with the EHL method from polymers, without lower dimensional limits [100] upon which the DNA units could be immobilised in order to add additional tuneable sub-50 nm asperities [120,163,186,234]. The replication of the assembled hierarchical features *via* plating techniques such as electro and electroless deposition, sputtering, and chemical vapour deposition will enable large, controlled and robust patterned surfaces, feasible for potential application in photonics and sensing devices.

Furthermore, building upon the previously established work, which demonstrated that an accurate combination of soft-lithography, DNA origami and cages enables anchoring of these on specific sites *i.e.,* arrays, nanocavities, grids [178,181,335] in turn, yielding the fabrication of ordered nano-materials, the plating techniques can further enable a wide range of inorganic materials, to replicate these nanostructures into organised metal nanopatterns. Further modelling and theoretical simulations have also indicated potential, broad range of sub-50 nm morphologies as suitable substrates for novel optical responses in terms of plasmonic band-gap and negative-refractive index.

EHD lithography has been widely exploited for applications in integrated and diagnostic devices. Further projects, which we are currently working on (not shown here), have also demonstrated the EHL as a viable tool for manufacturing

high surface area components for multi-layered solar cells and organic light-emitting devices [227,228,342]. Our preliminary results indicate that chromophores were successfully blended into the polymeric matrix and patterned using the EHD method into sub-micron pillar-like structures. The presence of the chromophore metal centre inside the polymers enhances the overall conductivity compared to the pure polymer, while the patterning increases the active surface area at approximately 20-40%. Therefore, further electrical and optical characterisation of the nanofeatures will determine their potential roles for applications in optoelectronics devices, reducing the production costs and enhancing the use of eco-sustainable materials.

In conclusion, this thesis illustrates novel versatile and robust routes for achieving sub-micron and nanoscale features by a simple combination of well-established techniques and starting, 'raw' materials, while paving the way for a future assembly of a whole new range of hierarchical, functionalised micro-to-nano patterned surfaces.

Appendix 1.1
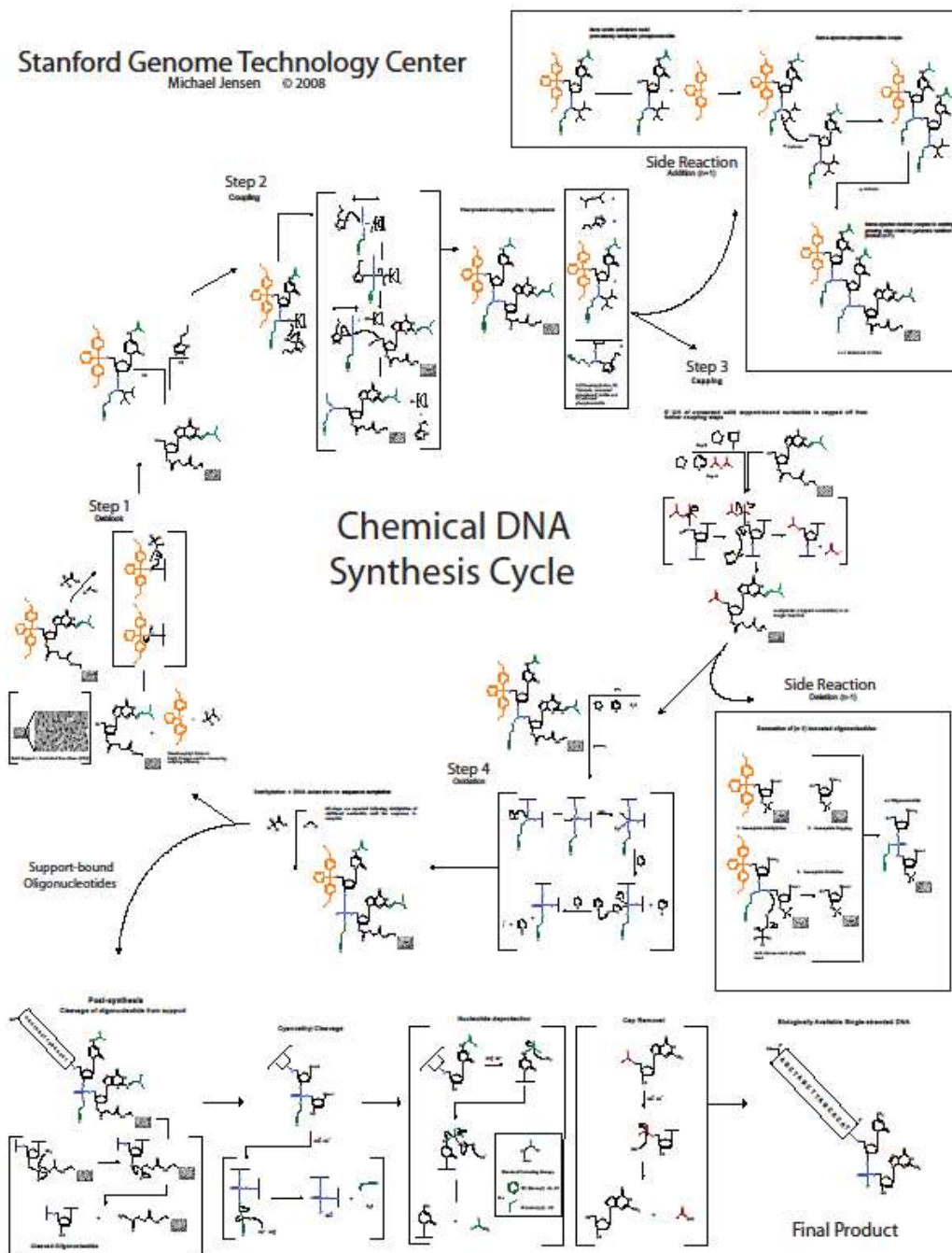
Appendix 1.2

Strand S1

151 Oligo 1124- larger injection

Sample Name:	Oligo 1124- larger injection	Injection Volume:	1000.0
Vial Number:	149	Channel:	UV_VIS_2
Sample Type:	unknown	Wavelength:	260
Control Program:	Long Thiol Ferro	Bandwidth:	1
Quantif. Method:	Gemma	Dilution Factor:	1.0000
Recording Time:	4/4/14 11:14	Sample Weight:	1.0000
Run Time (min):	40.00	Sample Amount:	1.0000

Thiol Ferro #151 [modified by burnseys a legend] UV_VIS_2 WVL:260 nm
%D: 0.0 %
6 - 17.452   100.0
4 - 15.742
3 - 15.136
5 - 16.345
2 - 14.500
18.0
1 - 13.609
Acetonitrile: 5.0 %
%B: 0.0 %   5.0
Flow: 3.000 ml/min
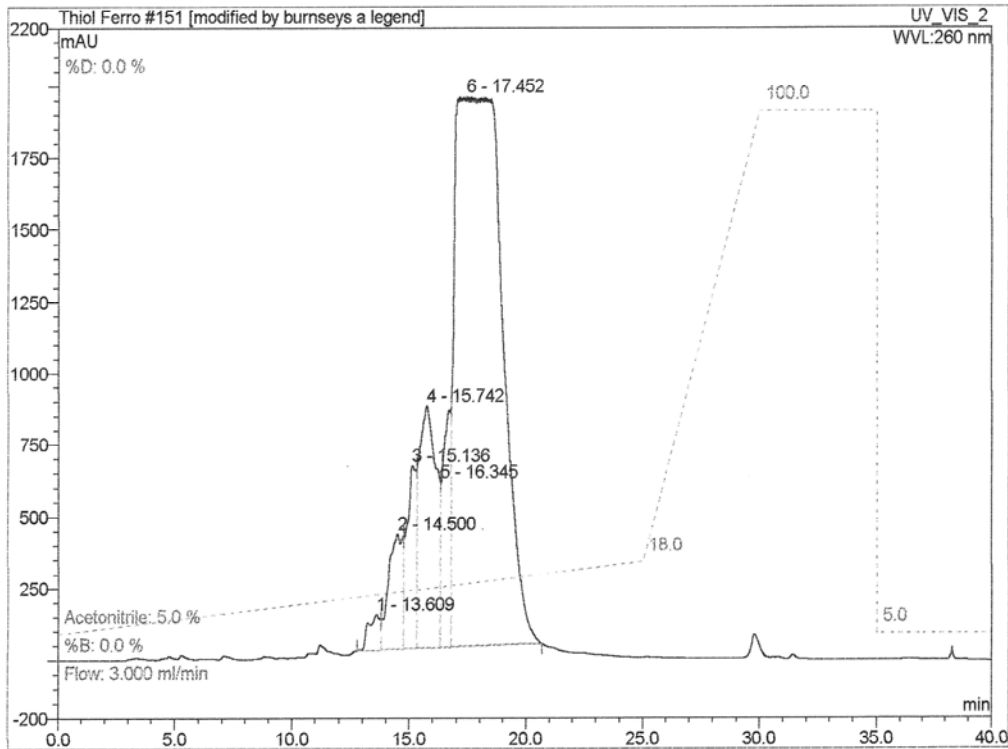
No.	Ret.Time min	Peak Name	Height mAU	Area mAU*min	Rel.Area %	Amount	Type
1	13.61	n.a.	122.850	68.436	1.12	n.a.	BM *
2	14.50	n.a.	401.732	273.353	4.46	n.a.	M *
3	15.14	n.a.	634.793	308.959	5.04	n.a.	M *
4	15.74	n.a.	840.169	709.450	11.58	n.a.	M *
5	16.35	n.a.	573.689	331.965	5.42	n.a.	M *
6	17.45	n.a.	1917.101	4436.063	72.39	n.a.	MB*
Total:			4490.335	6128.226	100.00	0.000	

Strand S2

152 Oligo 1125- larger injection

Sample Name:	Oligo 1125- larger injection	Injection Volume:	1000.0
Vial Number:	150	Channel:	UV_VIS_2
Sample Type:	unknown	Wavelength:	260
Control Program:	Long Thiol Ferro	Bandwidth:	1
Quantif. Method:	Gemma	Dilution Factor:	1.0000
Recording Time:	4/4/14 13:18	Sample Weight:	1.0000
Run Time (min):	40.00	Sample Amount:	1.0000
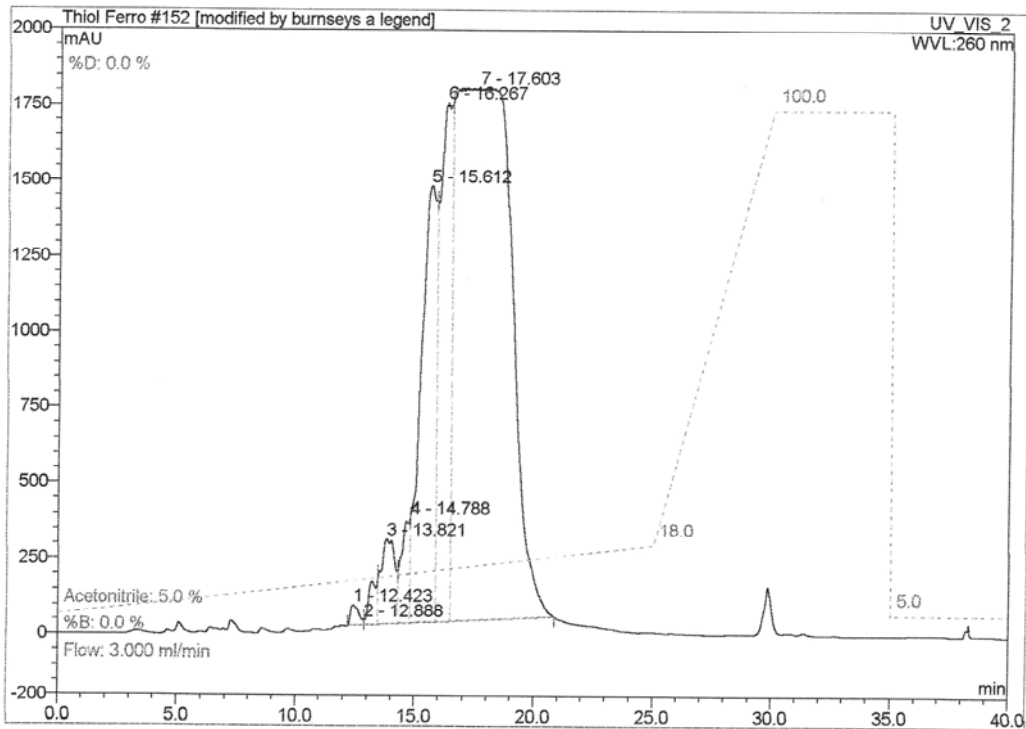
No.	Ret.Time min	Peak Name	Height mAU	Area mAU*min	Rel.Area %	Amount	Type
1	12.42	n.a.	68.895	26.960	0.37	n.a.	BM *
2	12.89	n.a.	15.281	58.670	0.81	n.a.	M *
3	13.82	n.a.	280.824	188.683	2.60	n.a.	M *
4	14.79	n.a.	348.015	135.614	1.87	n.a.	M *
5	15.61	n.a.	1443.395	1075.018	14.84	n.a.	M *
6	16.27	n.a.	1716.863	995.161	13.73	n.a.	M *
7	17.60	n.a.	1761.292	4766.158	65.77	n.a.	MB*
Total:			5634.564	7246.265	100.00	0.000	

Strand S3

153 Oligo 1126- larger injection

Sample Name:	Oligo 1126- larger injection	Injection Volume:	1000.0
Vial Number:	151	Channel:	UV_VIS_2
Sample Type:	unknown	Wavelength:	260
Control Program:	Long Thiol Ferro	Bandwidth:	1
Quantif. Method:	Gemma	Dilution Factor:	1.0000
Recording Time:	4/4/14 14:09	Sample Weight:	1.0000
Run Time (min):	40.00	Sample Amount:	1.0000
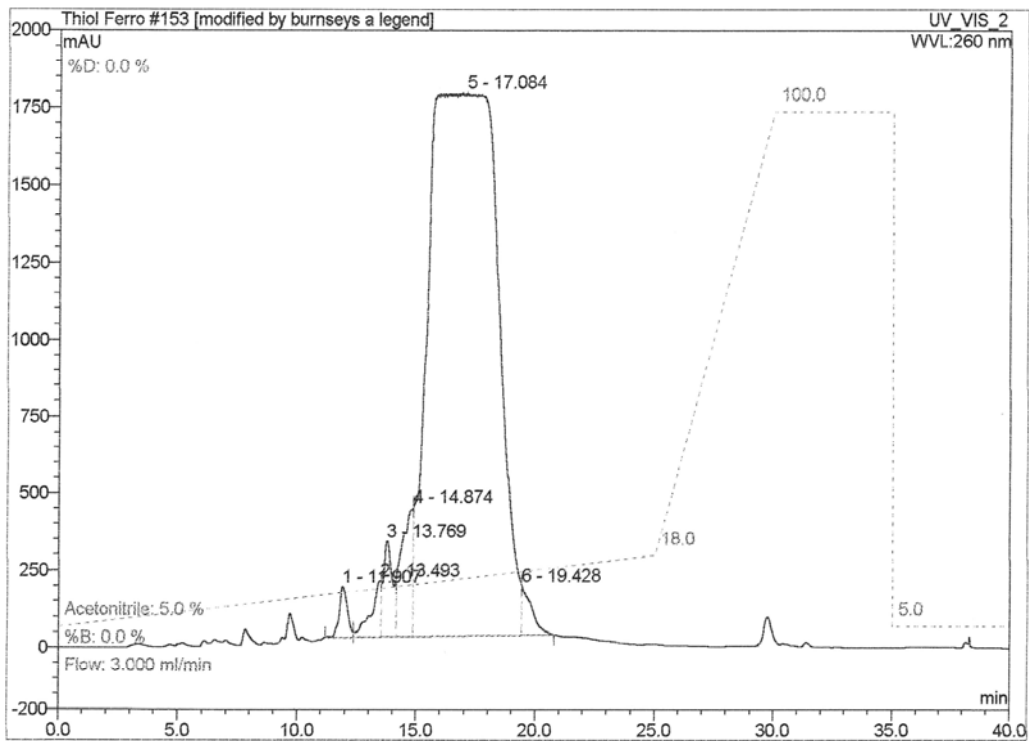
No.	Ret.Time min	Peak Name	Height mAU	Area mAU*min	Rel.Area %	Amount	Type
1	11.91	n.a.	165.019	64.978	1.01	n.a.	BM *
2	13.49	n.a.	182.137	86.969	1.35	n.a.	M *
3	13.77	n.a.	308.228	139.433	2.16	n.a.	M *
4	14.87	n.a.	420.604	231.496	3.59	n.a.	M *
5	17.08	n.a.	1759.993	5852.390	90.71	n.a.	M *
6	19.43	n.a.	160.536	76.780	1.19	n.a.	MB*
Total:			2996.517	6452.047	100.00	0.000	

Strand S4

154 Oligo 1127- larger injection

Sample Name:	Oligo 1127- larger injection	Injection Volume:	1000.0
Vial Number:	152	Channel:	UV_VIS_2
Sample Type:	unknown	Wavelength:	260
Control Program:	Long Thiol Ferro	Bandwidth:	1
Quantif. Method:	Gemma	Dilution Factor:	1.0000
Recording Time:	4/4/14 14:56	Sample Weight:	1.0000
Run Time (min):	40.00	Sample Amount:	1.0000
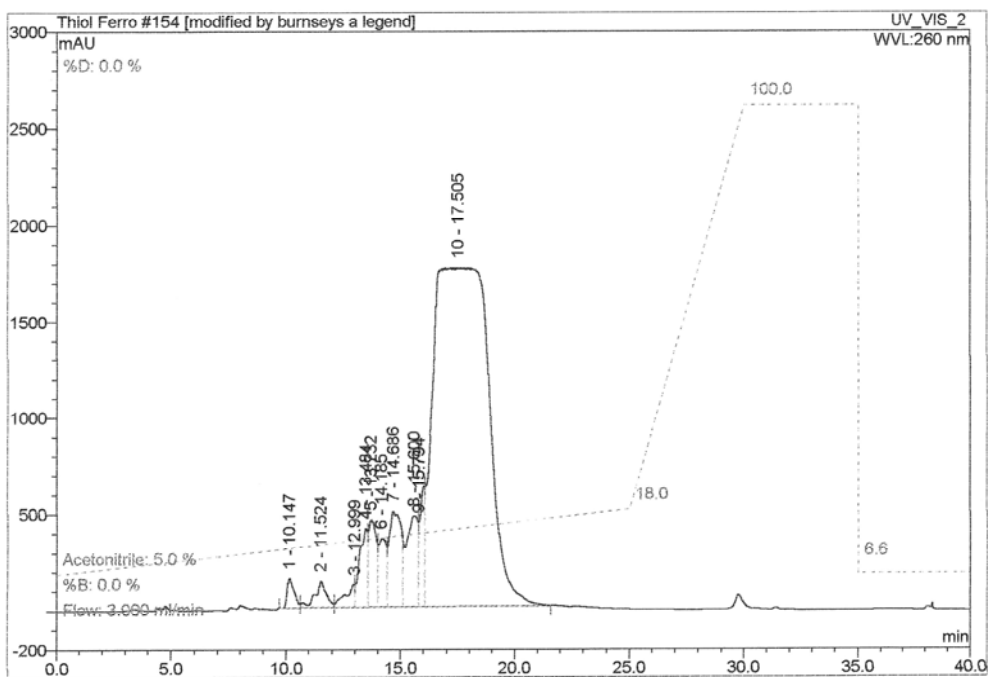
No.	Ret.Time min	Peak Name	Height mAU	Area mAU*min	Rel.Area %	Amount	Type
1	10.15	n.a.	152.012	52.432	0.84	n.a.	BM *
2	11.52	n.a.	136.047	79.386	1.27	n.a.	M *
3	13.00	n.a.	117.948	56.120	0.89	n.a.	M *
4	13.48	n.a.	406.427	169.469	2.70	n.a.	M *
5	13.73	n.a.	450.404	167.514	2.67	n.a.	M *
6	14.19	n.a.	354.823	141.271	2.25	n.a.	M *
7	14.69	n.a.	492.450	301.025	4.80	n.a.	M *
8	15.60	n.a.	468.781	268.631	4.28	n.a.	M *
9	15.79	n.a.	436.952	155.233	2.47	n.a.	M *
10	17.51	n.a.	1758.029	4884.385	77.83	n.a.	MB*
Total:			4773.874	6275.466	100.00	0.000	

Appendix 1.3

9 nm polyhedron

No.	Oligo Name	Sequence (5' -> 3')	Yield [OD]	Yield [µg]	Yield [nmol]	Concentration 100pmol/µl	Vol. for 100pmol/µl	Tm [°C]	MW [g/mol]	GC-Content	Synthesis Scale	Purification	Modification	Barcode IDO	QC Report
1	STRAND 1	AGG CAG TTG AGA CGA ACA TTC CTA AGT CTG AAA TTT ATC ACC CGC CAT AGT AGA CGT ATC ACC (63)	34.7	950	49.1	-	491	> 75	19342	44.4 %	1 µmol	HPSF	-	02082225505	-
2	STRAND2	CTT GCT ACA CGA TTC AGA CTT AGG AAT GTT CGA CAT GCG AGG GTC CAA TAC CGA CGA TTA CAG (63)	36.6	1010	52.0	-	520	> 75	19415	47.6 %	1 µmol	HPSF	-	020822506	-
3	STRAND 3	GGT GAT AAA ACG TGT AGC AAG CTG TAA TCG ACG GGA AGA GCA TGC CCA TCC ACT ACT ATG GCG (63)	36.1	980	50.2	-	502	> 75	19514	50.8 %	1 µmol	HPSF	-	020822507	-
4	STRAND 4	CCT CGC ATG ACT CAA CTG CCT GGT GAT ACG AGG ATG GGC ATG CTC TTC CCG ACG GTA TTG GAC (63)	38.6	1120	57.7	-	577	> 75	19390	57.1 %	1 µmol	HPSF	-	020822508	-

20 nm polyhedron

Certificate of Analysis and Identity

Miss Chiara Busa

School of Engineering
University of Birmingham
Edgbaston,
Birmingham
B15 2TT

Oligo code **D83629CB**

Edited 26 June 2015

Order no. EPS878025

Oligo name Strand S

5'
TTA--CCG--TGT--GGT--TGC--TAG--GCG---

3'

21 Bases   standard scale

Synthesis   Trityl OFF

Purification   Desalted - G25

Special bases

```
2 x residues of A
4 x residues of C
8 x residues of G
7 x residues of T
0 x residues of special
0 x residues of K = G+T
0 x residues of M = A+C
0 x residues of R = A+G
0 x residues of S = C+G
0 x residues of W = A+T
0 x residues of Y = C+T
0 x residues of B = C+G+T
0 x residues of D = A+G+T
0 x residues of H = A+C+T
0 x residues of V = A+C+G
0 x residues of N = A+C+G+T
```

Physical data

Refs:-
http://www.PremierBiosoft.com/netprimer.html
http://alces.med.umn.edu/rawtm.html

| Melting temp. | 63.6 C | Molecular weight | 6484 Da | |
| The vial contains:- | | 89 OD units | 2650 u.gram | 0.414 u.mole |

Dilution data

When diluted to 1ml, the concentration = 414 p.mole/ul

Dilute to 4138 ul, to get a final concentration of 100 pmole/ul

Certificate of Analysis and Identity

Miss Chiara Busa

School of Engineering
University of Birmingham
Edgbaston,
Birmingham
B15 2TT

Oligo code **D83626CB**

Edited 26 June 2015

Order no. EPS878025

Oligo name Strand M

5'
TAG--CAA--CCT--GCC--TGG--CAA--GCC--TAC--GAT--GGA--
CAC--GGT--AAC--GCC---

3'

---

42 Bases standard scale

Synthesis Trityl OFF

Purification Desalted - G25

Special bases

```
11 x residues of A
14 x residues of C
11 x residues of G
 6 x residues of T
 0 x residues of special
 0 x residues of K = G+T
 0 x residues of M = A+C
 0 x residues of R = A+G
 0 x residues of S = C+G
 0 x residues of W = A+T
 0 x residues of Y = C+T
 0 x residues of B = C+G+T
 0 x residues of D = A+G+T
 0 x residues of H = A+C+T
 0 x residues of V = A+C+G
 0 x residues of N = A+C+G+T
```

Physical data

Melting temp. 89.3 C   Molecular weight 12878 Da

Refs:-
http://www.PremierBiosoft.com/netprimer.html
http://alces.med.umn.edu/rawtm.html

The vial contains:- 126 OD units   3563 u.gram   0.282 u.mole

Dilution data

When diluted to 1ml, the concentration = 282 p.mole/ul

Dilute to 2817 ul, to get a final concentration of 100 pmole/ul

Certificate of Analysis and Identity

Miss Chiara Busa

School of Engineering
University of Birmingham
Edgbaston,
Birmingham
B15 2TT

Oligo code **D83625CB**

Edited 26 June 2015

Order no. EPS878025

Oligo name Strand L

5'
AGG--CAC--CAT--CGT--AGG--TTT--AAC--TTG--CCA--GGC--
ACC--ATC--GTA--GGT--TTA--ACT--TGC--CAG--GCA--CCA--
TCG--TAG--GTT--TAA--CTT--GCC---

3'

---
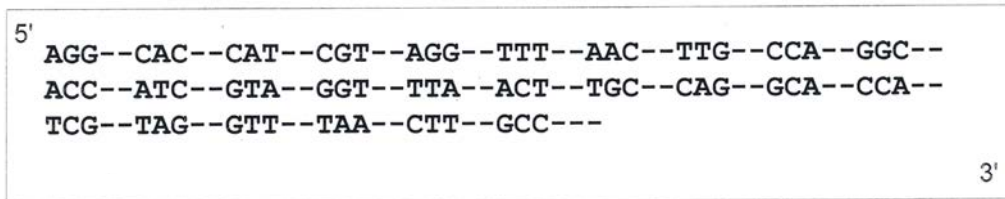
78 Bases   standard scale

Synthesis   Trityl OFF

Purification   Desalted - G25

Special bases

```
18 x residues of A
21 x residues of C
18 x residues of G
21 x residues of T
 0 x residues of special
 0 x residues of K = G+T
 0 x residues of M = A+C
 0 x residues of R = A+G
 0 x residues of S = C+G
 0 x residues of W = A+T
 0 x residues of Y = C+T
 0 x residues of B = C+G+T
 0 x residues of D = A+G+T
 0 x residues of H = A+C+T
 0 x residues of V = A+C+G
 0 x residues of N = A+C+G+T
```

Physical data

Melting temp. 95.9 C	Molecular weight	23962 Da	Refs:- http://www.PremierBiosoft.com/netprimer.html http://alces.med.umn.edu/rawtm.html
The vial contains:-	165 OD units	4740 u.gram	0.203 u.mole

Dilution data

When diluted to 1ml, the concentration = 203 p.mole/ul

Dilute to 2028 ul, to get a final concentration of 100 pmole/ul

30 nm polyhedron

No.	Oligo Name	Sequence (5' -> 3')	Yield [OD]	Yield [µg]	Yield [nmol]	Concentration [pmol/µl]	Vol. for 100pmol/µl	Tm [°C]	MW [g/mol]	GC-Content	Synthesis Scale	Purification	Modification	Barcode IDO	QC Report
1	long	agg cac cat cgt agg ttt aac ttg cca ggc acc atc gta ggt tta act tgc cag gca cca tcg tag gtt taa ctt cgc agg cac cat cgt agg ttt aac tcg cc (104)	75.0	2147	67.2	-	672	> 75	31955	51 %	1 µmol	HPSF	-	020822098	-
2	medium	Tagcaactgcctggcaagcctac gatggacacggtaacgcc (42)	28.5	801	62.2	-	622	> 75	12878	59.5 %	0.2 µmol	HPSF	-	020822099	-
3	medium	Tagcaactgcctggcaagcctac gatggacacggtaacgcc (42)	28.8	809	62.8	-	b28	> 75	12878	59.5 %	0.2 µmol	HPSF	-	020822100	-
4	medium	Tagcaactgcctggcaagcctac gatggacacggtaacgcc (42)	32.1	902	70.0	-	700	> 75	12878	59.5 %	0.2 µmol	HPSF	-	020822101	-
5	medium	Tagcaactgcctggcaagcctac gatggacacggtaacgcc (42)	23.2	652	50.6	-	506	> 75	12878	59.5 %	0.2 µmol	HPSF	-	020822102	-
6	short	Ttaccgtgtggttgctaggcg (21)	16.9	501	77.2	-	772	61.8	6484	57.1 %	0.2 µmol	HPSF	-	020822103	-
7	short	Ttaccgtgtggttgctaggcg (21)	17.1	507	78.2	-	782	61.8	6484	57.1 %	0.2 µmol	HPSF	-	020822104	-
8	short	Ttaccgtgtggttgctaggcg (21)	15.1	447	69.0	-	690	61.8	6484	57.1 %	0.2 µmol	HPSF	-	020822105	-
9	short	Ttaccgtgtggttgctaggcg (21)	16.4	486	75.0	-	750	61.8	6484	57.1 %	0.2 µmol	HPSF	-	020822106	-

Appendix 2

Tunable superapolar *Lotus-to-Rose* hierarchical nanosurfaces *via* vertical carbon nanotubes driven electrohydrodynamic lithography†

Chiara Busà,[a] Jonathan James Stanley Rickard,[a,b] Eugene Chun,[a] Yaw Chong,[a] Viroshan Navaratnam[a] and Pola Goldberg Oppenheimer*[a]

The development of a robust, cost-effective, scalable and simple technique that enables the design and construction of well-controlled large area superhydrophobic surface structures which can be easily tuned from *lotus-leaf* to *rose-petal* state is essential to enable progress in realising the full applied potential of such surfaces. In this study, we introduce the tuneable carbon nanotubes-based electrohydrodynamic lithography (CNT-EHL) to fabricate unique multiscale structured cones and nanohair-like architectures with various periodicities and dimensions, successfully enabling surface energy minimization. The possibility of contact-less lithography *via* the CNT-EHL morphology replication combined with the electric field coupling to smaller self-assembled patterns within the film, provides a way for hierarchical structure control spanning many length scales along with tuneable wetting capabilities. By controlling the hierarchy of micro- to nano cones and spikes, these morphologies provide a range of architectures with sufficient roughness for very low wettability, with the highest contact angle achieved of 173° and their properties can be easily switched between *lotus-leaf* to *rose-petal* behaviour.

Super-apolar surfaces which exhibit unique self-cleaning properties are very promising for a broad range of applications ranging from coatings for windows, cloths and car windshields, to the anti-corrosive covering for aircraft[1,2] and marine vessels to antifogging and anti-icing finishes.[3] Due to the exciting breadth of potential, considerable efforts have been focussed into developing artificially engineered surfaces to biomimic the extreme water repelling properties, notably known as the '*Lotus-Leaf*' effect. The classical Wenzel and Casie–Baxter models describe the correlation between the surface roughness and the wettability properties.[4,5] While the Wenzel regime explains the intrinsic wetting tendency of a liquid to adhere to the surface after contact, the Casie–Baxter mode refers to the state at which it is energetically more favourable for the water drop to bridge across the top of a composite dual-layered surface structure with air trapped within the asperities. The transitional regime between the Casie–Baxter and Wenzel state usually exhibits high contact angle hysteresis and depends on the dimensions and gaps between the surface

roughness structures as well as the chemical hydrophobicity. However more recently, it has been acknowledged that it is important to consider wetting modes beyond the classical and the broadly described Wenzel/Casie–Baxter states recognising existence of not only the '*Lotus-Leaf*' effect but also of a strong adhesion combined with super-hydrophobicity known as '*Rose-Petal*' state[6,7] and thus, distinguishing wetting regimes of a surface with a single level of roughness and the hierarchical ones (Fig. 1b).

The existence of such a spectrum of the wetting states can be understood through the competition of forces acting on the solid–liquid in terms of surface energy, which is inversely proportional to the contact angle adhesion of water molecules to the rough surface as well as impregnation of the hierarchical structures by water or air. For instance, small liquid–solid adhesion typically results in high contact angle and low contact angle hysteresis, facilitating super repellent surfaces. On the other hand, when strong adhesion coexists between molecules of liquid at the same time as low surface energy, surfaces tend to be both superhydrophobic and at the same time sticky. The adhesion hysteresis yields an asymmetry between the wetting and dewetting processes, with higher energy required for the latter. Natural super-hydrophobic systems such as the *Lotus* leaf consists of micron sized papillae spaced apart from each other by a micron scale distance and nano hair like mats on each micro-papillae, yielding the highly

[a]*School of Chemical Engineering, University of Birmingham, Birmingham B15 2TT, UK. E-mail: GoldberP@bham.ac.uk*

[b]*Department of Physics, Cavendish Laboratory, University of Cambridge, Cambridge CB3 0HE, UK*

†Electronic supplementary information (ESI) available. See DOI: 10.1039/c6nr08706j
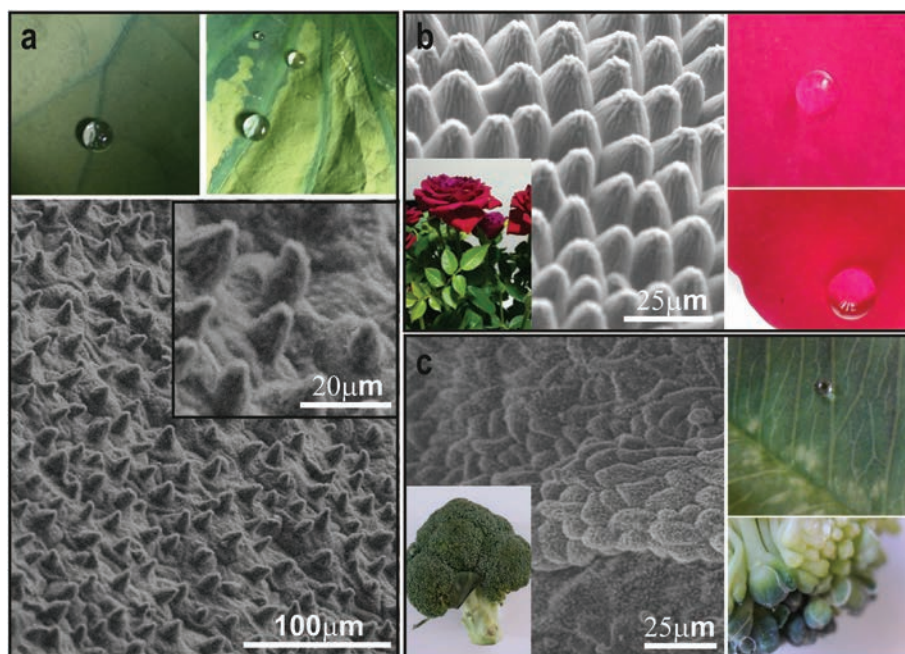
Fig. 1 Superhydrophobicity in nature. (a) Optical images of the spherical water drops rolling–off the natural *Nelumbo nucifera* (lotus leaf) and the corresponding scanning electron microscopy (SEM) image of the surface topography of the lotus-leaf with the higher magnification of the lotus surface shown in the inset. (b) SEM image of the structure found on the *rose* petal and the corresponding photograph images of spherical water droplets sticking to the *rose-petal* surface. SEM image of the microstructure found in *broccoli* and the corresponding optical images of its superhydrophobic properties.

apolar surface with very low contact angle hysteresis (Fig. 1a). The hierarchical texture of the natural systems allows enhanced water repellence (Fig. 1) for both static and dynamic conditions. Biological adhesive systems such as for instance Gecko's pads excel in terms of adhesive strength on virtually any surface due to the millions of densely assembled high aspect ratio adhesive setae, which are arranged in a grid-like pattern on the ventral surface of each scansor, branching out into hundreds of nanometer-sized spatular tips, allowing them to deform and adhere to nearly any surface. The red rose petals maintain spherical droplets on their surface which do not roll off even if the petal is turned upside down (Fig. 1b) thus, exhibiting both superhydrophobicity along with high adhesive force with the water. While technologically valuable, both high-density hierarchical fibrillar adhesives and precisely orchestred periodic micro-to-nano super apolar structures are difficult to manufacture in a straightforward manner from a material of choice and no scalable low-cost approach yet exist to create the required tuneable geometries.

The vast majority of previous routes to generate synthetic superhydrophobic morphologies using low surface energy materials with high or low adhesion are based on conventional patterning methods.[8–10] These are not cost-effective, and are time consuming, often cumbersome and necessitate an accurate combination of multistep processes, thus limiting the scalability of the resulting architectures. For instance, while photolithography[8,11] is an established method for generating structures optically, it is not a straightforward route to create

micro and nanoscale roughness simultaneously due to the sequential photoresist development and film etching processes involved, rendering it essentially a two-dimensional technique, where many steps must be iterated to create a three dimensional structure, it is also limited by the diffraction limit. Alternative approaches such as electron-beam lithography[12] require many sequential steps, are costly and highly susceptible to beam-drift occurring due to the long exposure times. Replication fidelity using the majority of the techniques employed to fabricate the sought after hierarchical superhydrophobic architectures on substrates with desired chemical and physical properties, is predominantly low and often results in a stochastic mixture of non-periodic and non-optimal packing of the final submicron structures, unlike the ones found in nature, (Fig. 1a–c) and frequently accomplished *via* using hazardous organic compounds and corrosive gases.[13,14] This in turn, results in inconsistent and partial wetting states on meso and macro scales. Fabrication of multitier morphologies with tuneable wetting exploiting biologically inspired routes, self-assembly processes, templating block-copolymer based approaches and various imprinting techniques are typically limited by poor mechanical stability, mold-pattern distortions, cost, difficulties to manufacture bicontinuous morphologies in all three spatial dimensions and the principal uncontrollability and irreproducibility.[15–21]

Here we demonstrate an unconventional route to reproducibly manufacture scalable nano to micro nanohair-like surfaces as well as hierarchical cone-structure arrays with various

curvatures, patterned from vertically aligned carbon nanotube-based master electrodes *via* advanced electrohydrodynamic lithography (CNT-EHL). While electrohydrodynamic patterning was previously used to pattern dielectric, conductive and crystalline materials,[22–25] this is the first time that vertically aligned CNTs are exploited to generate the master electrodes which are further employed as top masks to generate and control the fabricated morphologies *via* the EHL. This innovative approach allows fabricating a range of reusable CNT-based electrodes with various morphologies and dimensions, enabling direct and tuneable patterning from the material of choice and with no need of functionalisation (*i.e.*, inexpensive, no processing equipment) of robust and highly-reproducible structures which exhibit hexagonal packing symmetry. Importantly, the CNTs generated master electrodes, once coated with a metallic nanloayer, are of a high structural integrity and durability and can be used to consistently produce structures of interest from low-cost materials and therefore, enabling high-reproducibility, cost-efficiency and scalability of the generated nanosurfaces. Moreover, the versatile CNTs-based masks can be easily tailored and tuned in structural dimensions and nano-gaps by simply varying their growth densities. Nanohair-like structures, cones and sharp spiky micro and nano arrays, which are typically difficult to manufacture, are successfully fabricated *via* the CNT-EHL in a single step which can be easily tuned in dimensions, pitch, aspect ratio and the cone tip curvature. Utilising low-energy materials, the CNT-EHL fabricated micro to-nanoscale roughness allows precisely tailoring and controlling hierarchical geometries by adjusting the patterning parameters and thus, significantly influencing the surface wetting properties and mimicking the various regimes found in nature. This method enables tuning and alternating between the *lotus-leaf* and *rose-petal* behaviour due to the controllable experimental approach and the ultimate morphologies generated while patterned from the same initial material. The generated superhydrophobic surfaces with self-cleaning or adhesive properties are promising prospects for both the fundamental research of submicron scale superhydrophobicity and broader applications including, in anti-fouling and microfluidics. CNT-EHL therefore, opens a new avenue for the generation of a broad spectrum of high-fidelity superhydrophobic patterns in a straightforward and low-cost fashion, requiring no vacuum processing, no hazardous organic compounds with possibilities of exploiting biodegradable or environmentally-friendly apolar polymers, rendering this technique even more technologically appealing.

Results and discussion

CNT-EHL method, elucidated below, requires assembling a miniaturised capacitor-like device comprised of a bottom electrode topped with a thin nanofilm, spun-cast from the polymer to be patterned and the topographically structured top electrode with a pattern of interest to be replicated. The details of device assembly and characterization are given in the Experimental section. The physical principles underlying the destabilization of thin films by electrohydrodynamic lithography are well-established.[25–27] The detailed experimental configuration is schematically shown in Fig. 3. We have fabricated a range of master electrodes based on the vertical CNTs including, vertically aligned carbon nanotube (VACNT) forests both as-grown and inverted (Fig. 2a and b) as well as a range of VACNT-based micro and nano structures (Fig. 2c and d). The overall procedure for the fabrication of the CNT-based master electrodes for the EHL is illustrated in Fig. 2. Vertically oriented CNT forests were grown *via* chemical vapour deposition (CVD) process to yield well-defined stable large area substrates of nanotube arrays (Fig. 2a and b, top) or were flipped over to generate better defined, straighter CNT tips (Fig. 2b, bottom). Various VACNT site-densities in the range of 7–30% coverage grown *via* CVD process can be obtained, allowing control of the nano-gaps in the final masks (see ESI, S1†). Furthermore, VACNT-based morphologies were also designed and fabricated by prewriting the location and dimensions of CNT growth areas, generating patterns of arrays of pillars with various pre-designed height, diameters and pitches (*e.g.*, arrays with ranges of 1–5 μm diameter with a 1.5–5.5 μm pitch between the individual pillars) (Fig. 2c).

To transform the bare VACNT arrays into master electrodes, we sputter-coated the arrays with a 10 nm thin silicon layer (Fig. 2b and d). The corresponding high resolution scanning electron microscopy of the uncovered CNTs masks (Fig. 2a and c) and the low-angle backscattered SEM images of the Si coated VACNT electrodes (Fig. 2b) demonstrate uniformly covered VACNTs with a thin layer of silicon. Further, a simple silanization process enabled rendering the oxidized Si surface appolar (*i.e.*, low surface energy),[26] and thus, led to the reduction in adhesion of the CNT-EHL patterned material to the silicon surface. Therefore, the fabricated CNT based master electrodes can be used numerous times for CNT-EHL process without undergoing any deformation or damage.

The coated VACNT arrays were then used as master top electrodes in the EHL assembly. Controlling the inter-electrode spacing (d), applied electric field (E_f), initial film thickness (h_0), patterning and termination times (τ_0 and τ_f) allowed fine-tuning the desired hierarchical morphologies from the polymer of choice. Since accomplishing the super-hydrophobicity of the manufactured surfaces requires a combination of both physical structure and the chemical properties, we have exploited poly(chlorotrifluoroethylene) (PCTFE) with a static contact angle, θ, of a water drop on a smooth film of $119 \pm 3°$ for the EHL patterning to obtain the lowest possible surface energy properties from the final morphologies.

An overview of the CNT-EHL method is illustrated in Fig. 3. A topographically structured top electrode opposing the initially homogeneous film (Fig. 3a–d) induces high lateral electric field variations in the capacitor-like device. Since the electrostatic pressure, p_{el}, is inversely proportional to the square of the capacitor gap, d, the downward protruding sharp structures of the top mask generate locations with the highest electrostatic pressure and thus, the evolving wave pattern
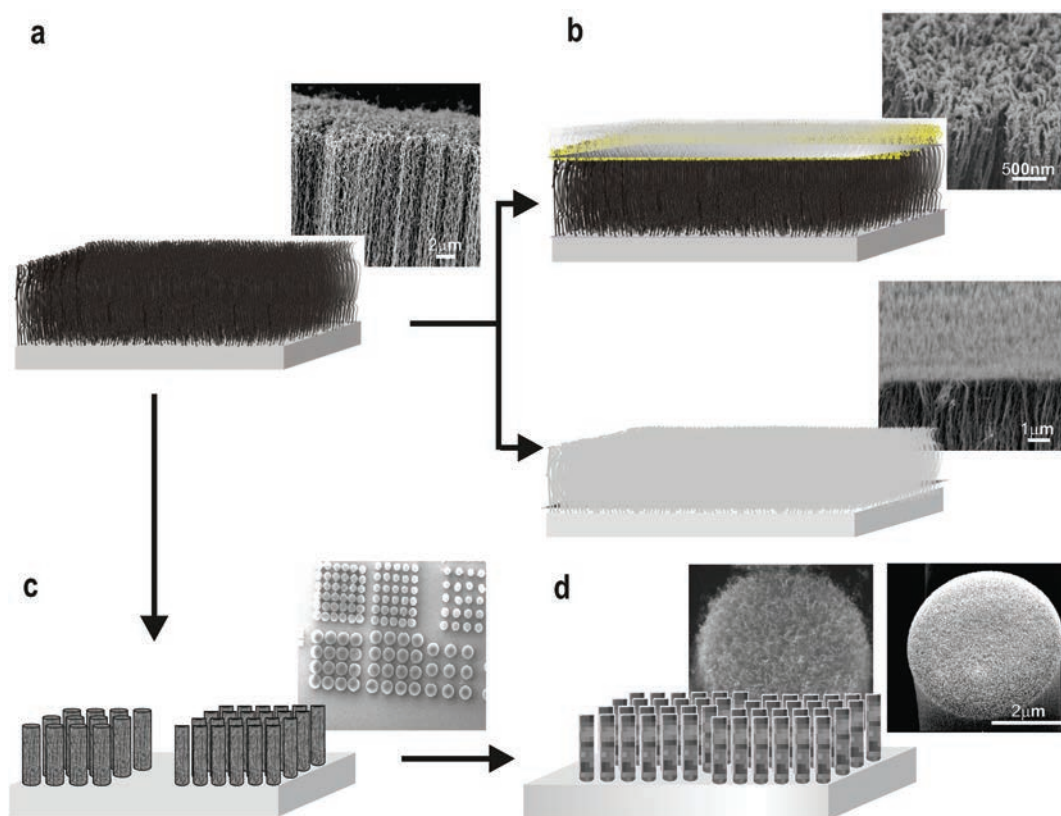
Fig. 2 Fabrication of novel vertically aligned CNTs-based electrodes for the EHL patterning. Schematic representation and the corresponding SEM images of (a) CNTs arrays fabricated using the chemical vapour deposition process (CVD) and electron beam (e-beam) lithography combined with CVD growth process and (b) subsequently coated with a thin silicon layer to produce a range of top electrodes for EHL. Either as-grown (top) or inverted (bottom) arrays can be generated. (c) Small-diameter VACNT forests patterned into predesigned pillar structures with various dimensions and pitches are further utilized and coated with silicon (d) generating abroad range of masks for the CNT-EHL.

instabilities in the thin polymer film are coupled to the heterogeneous electric field and driven upwards, eventually spanning the capacitor gap.

$$p_{el} = -\frac{\varepsilon_0 \varepsilon_p V^2}{2\left[\frac{\varepsilon_p d - h}{(\varepsilon_p - 1)}\right]^2} \tag{1}$$

The CNT-EHL pattern replication kinetics consists of three integral parts[25,27] including, (i) the amplification of a capillary surface instability triggered by applying an external voltage, which with time causes (ii) the formation of liquid bridges between the two electrodes (Fig. 3b and d) and eventually, (iii) this seamless sequence of capillary instability results in the coalescence of the initial capillary plugs bridging the substrates and the protruding parts of the top electrode, forming positive replicas of the imposed master pattern (Fig. 3c and d). Since the confinement of the redistributing fluid polymer morphologies is organized according to the ratio of the electrode spacing and the initial height of the polymer film in the capacitor gap, *i.e.*, the filling ratio, f ($f = h_0/d$), the pattern selection during the early stage of the EHL process is a sinusoidal surface undulation and f determines the further stages of pattern formation. S is the surface area ratio of the topography,

i.e., fraction of the template surface that protrudes towards the polymer film. Given that the profile of the generated pattern depends on the ratio of the intrinsic film undulation wavelength, λ_i and the lateral periodicity of the master top plate, Λ_m, three EHL replication scenarios are possible: (1) periodicity mismatch-small wavelength regime ($\lambda_i \ll \Lambda_m$), where the initial structure formation is followed by lateral coarsening of material yielding partial positive replication; (2) periodicity match-similar wavelength regime ($\lambda_i \approx \Lambda_m$ and $S \approx f$), where positive replica of the templates is obtained and (3) periodicity mismatch-large wavelength regime ($\lambda_i \gg \Lambda_m$), where the pattern develops certain number of defects and every protrusion of the electrode does not faithfully generate a liquid column.

Therefore, firstly by tailoring the-designing of the top electrodes and carefully choosing the experimental parameters it is possible to control and fine-tune the patterning process. Secondly, given the ability of terminating the lithographic process at each of the pattern formation steps, it is possible to capture the individual stages of the replication kinetics of CNT-EHL and thus, the obtained structures.

To establish the precise termination times during patterning of the PCTFE into the desired morphologies, the evolving pattern formation of the sandwiched polymer was observed *via*

Fig. 3 CNT-EHL based method. Placing the CNT-based top electrode above the (a) initially homogeneous thin PCTFE film with thickness, h_0, (b) liquefying it above the glass transition temperature (T_g) and subsequently, (c) applying a voltage, V, into the capacitor-like device with the controllable inter-electrode distance, d, triggers the amplification of a surface instability with the intrinsic film undulation wavelength, λ_i. This instability, with time leads to the formation of liquid bridges between the two electrodes. The kinetics of pattern formation allows the termination of the patterning process in each stage of either the (b) cones or (c) pillars with locations predetermined by the top electrodes, at which the electrostatic pressure is the highest. The sharp tips of the VCNTs-based electrode enable to obtain the spiky replicas as well as 'sharp' cones. (d) A photograph of a representative experimental CNT-EHL rig consists of an assembled miniaturised capacitor device with the patterned film on the bottom electrode and the CNT-based top master electrode connected to an external voltage supply. The profile of the generated pattern depends on the ratio of λ_i and the lateral periodicity of the master top plate, Λ_m. (e) Electric field distribution during EHL pattern formation.[28] (f) Schematic of the geometrical parameters of the cone/spike like structure upon wetting and a representative optical image of a water drop on the CNT-EHL patterned surface (inset).

the *in situ* imaging with an inverted optical microscope through a transparent ITO glass electrode.[25] The electric field generated inside the micro-capacitor device causes the energetically unfavourable build-up of displacement charges at the dielectric polymer–air interface and aligns the final morphology along the field lines to lower the overall electrostatic energy. Lateral field components, which arise during intermediate stages of the EHL process lead to a cone like arrangement of the growing undulations, prior to pinning to the top electrode and reorganising into pillars (Fig. 3c). A top electrode of protruding pillars comprised of densely packed VACNT-based nanostructures generates higher electrostatic pressures at the centres of each "pillar" giving rise to spike-like, pointing cones (Fig. 3e).

In Fig. 4 atomic force microscopy (AFM) images and the corresponding height cross section profiles of structured surfaces obtained after the application of voltage to the capacitor device using various fabricated Si-VACNT top electrodes exhibiting a range of features are shown. When the non-patterned as-grown VACNTs-based electrodes were used, it resulted in the replication of dense nano-needles with a typical a top-surface consisting of curly nano-roughness over large substrate areas (Fig. 4a). The removal of the nonaligned nanotubes by flipping

over the as-grown VACNTs (Fig. 2b, bottom) yielded better defined, straighter, nanohair-like PCTFE structures (Fig. 4b), otherwise impossible to obtain using the conventional top electrohydrodynamic electrodes.[22–24] Imposing the VACNT-based columns with different pitches between the pillars and diameters yielded a range of morphologies, depending on the degree of master electrode periodicity match/mismatch in the presence of the laterally varying electric field, the filling ratio of the PCTFE and the corresponding patterning termination times (Fig. 4(c–f)).[27]

In the similar wavelength regime where, $\lambda_i \approx \Lambda_m$, a high-fidelity replica of the imposed top template was obtained terminating the process at stage (ii) of the CNT-EHL patterning, resulting in periodic cone-like PCTFE structures with a typical centre-to-centre distance of 3 μm, base diameter of 2.5 μm and the peak diameter of 0.3 μm (Fig. 4c). Using similar master electrode and initial parameters yet, terminating the CNT-EHL replication at stage (iii) of the formation kinetics, yielded well defined pillars with hexagonal packing symmetry (Fig. 4f), which have fully spanned the capacitor gap. In Fig. 4d a grid pattern of sharp 1 μm height cones with additional intermediate 300 nm height cones was replicated from an initial 93 nm thickness film ($\tau = 45$ min, $d = 230$ nm, $1/f = 2.5$, $1/S = 1.5$).
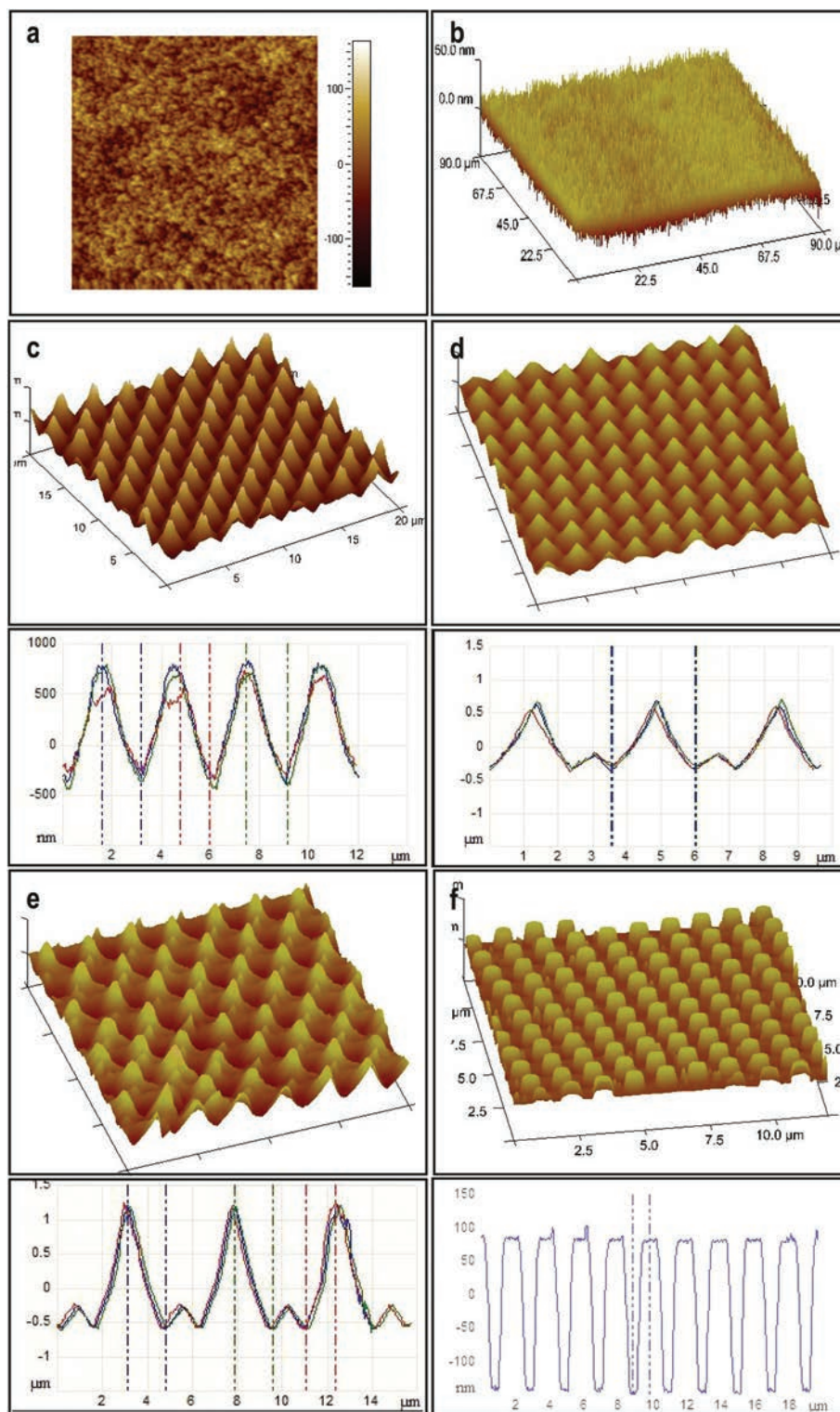
Fig. 4 CNT-EHL replicated patterns. Atomic force microscopy height and three-dimensional images and the corresponding cross-sections of (a) curly nano-hair (CNH) surfaces, (b) of straight nano-hairs (SNH), (c) single-level spikes with rounded edges (S1L), (d) two-levelled spiky cones (S2L), (e) two-tiered heretical spiky cones (S2L2) and (f) hexagonal pillars (HP) replicated from the various imposed CNT-based electrodes.

Insufficient polymer material was available to reproduce the CNT-based top electrode topography precisely. This is indicated by mismatch in the plate spacing to film-thickness ratio

and the value for the lateral periodicity of the master electrode. Terminating the process just before the plugs entirely span the inter-electrode gap resulted in sharp spiky cone (top diameter

of 270 nm) structures. An upper electrode patterned with features of CNTs generates a periodically modulated electrode with a charged surface giving rise to an electric field contribution which is proportional to the CNTs curvature yielding local enhancement of the electric field. Since $p_{el} \propto E_f^2$, which is also much stronger for smaller inter-electrode distances, the instabilities which still evolve towards their final forms are focused in the direction of the highest electric field (Fig. 3e) and the peaks of the forming structures become sharper thus, terminating the pattern formation at this stage yields spiky cones.

Using the as-grown CNTs-based master electrode yielded curly nano-hair (CNH) like roughness, with shallow but sharp peaks and valleys from the patterned PCTFE film, generating a superhydrophobic surface which exhibited the *rose-petal* effect with a contact angle of 167 ± 2° and strong adhesive forces, with a typical contact angle hysteresis of 83 ± 2° (Fig. 4a and 5a). On the other hand, the inverted CNT forest based top electrodes yielded well-defined, dense straight nano-hair (SNH) like morphology establishing hierarchical nanoscale structure (intra and inter CNTs) mimicking the *lotus-leaf* behaviour (Fig. 4b and 5b) with a contact angle of 165 ± 3° and a hysteresis of 8 ± 2°.

SNH fluorine terminated hydrophobic polymer exhibits considerably increased water repellent properties due to the large surface contact area between liquid droplet and the nanohair-like surface. Interestingly though, on the mesoscopic scale the PCTFE patterned film appears mostly smooth. In a densely packed porous network of CNH-roughness with minute variations in heights, upon wetting with a water drop a thin layer of liquid is left behind and the solid fraction in contact with liquid is increased with the network being penetrated by water, yielding the high solid–water adhesion and therefore, high contact angle hysteresis. On the other hand, closely packed needle like SNH nanostructure restrains the droplet spread, leading to a smaller contact angle hysteresis and roll-off super-hydrophobicity. However, the surface roughness must still be maintained, too dense a structure will slowly close the porous network, thus decreasing the water repellence. Since the surface roughness of the VACNT forests can be controlled, (see ESI, S1†) it is possible to also tune the degree of the apolar properties for the CNT-EHL replicated structures. While the curly-like nano-roughness with shallow peaks and valleys exhibits *rose-petal* like behaviour creating a thin water layer upon wetting, the sharp needle-like surface with measured contact angle of 165° and the contact angle hysteresis of 8°, inhibits liquid from remaining on the surface behaving like a *lotus-leaf* surface.

For the structures shown in Fig. 4c, generated *via* CNT-EHL, we measured higher contact angles of 169° ± 5° than for the forest like nanorough surfaces and contact angle hysteresis of 8° ± 2° resulting in low adhesive forces between the liquid and the surface, allowing the water drop to roll-off the substrate easily. This surface is comprised of hexagonally packed cones with nanoscale, slightly rounded triangular peaks which exhibit contact angle hysteresis <10°, resulting in a non-

wetting of the microstructures' spaces between the spikes. The air trapped in-between the spikes yields a heterogeneous surface comprised of both air and solid. The hierarchical dual structure of tapered cones in Fig. 4d yielded highly apolar surfaces (CA = 168 ± 1°) along with the sticky properties (hysteresis of 75 ± 2°), mimicking the *rose-petal* effect.

The physical principles underlying the wetting theory are well understood.[4–7] Here, we briefly summarize the principles of the wetting and superhydrophobicity on flat and rough surfaces (see 'ESI', S2† for the more detailed background on the wetting theory). For flat surfaces, the Young's Equation is given by:

$$\gamma_{SV} = \gamma_{SL} + \gamma_{LV} \cos \theta \qquad (2)$$

where, γ is a surface energy and θ is a contact angle (CA). For wetting on rough surfaces where the contact angle is larger than 90°, it is energetically more favourable for the liquid drop to wet a smaller area to reduce the total interface energy, $\gamma_{SV} < \gamma_{SL}$. In particular, above a critical roughness value, a cone structure with the contact area for a known vertical force is given by: $A \propto [\sin \varphi \cos^2(\theta - \varphi)]^{-1}$ where, φ is the fraction of the projected area of the solid surface that is wetted by liquid, it is energetically more favourable for the water drop to contact only a very small fraction of the surface asperities and move up the cone structure. Therefore, sharp coned CNT-EHL generated structures are favourable geometries to obtain superhydrophobic surfaces since their sharp tips enable the minimum solid–liquid contact with maximum vertical force per contact area as demonstrated in Fig. 4e, where a structured surface yields a contact angle of 173 ± 1° and a hysteresis of 5 ± 2°. These physical structures in combination with chemical properties of the cone-structured polymers lay the platform for optimal surface topography, which in turn gives rise to the super-hydrophobicity. Furthermore, these sharp and rounded cone surfaces closely resemble in their morphologies and dimensions found in the structures of natural systems, as can be clearly seen from the SEM images of Fig. 1a–c.

The contact angle of rough surfaces (*i.e.*, cone structures and CNT-like surfaces) with *rose-petal* and *lotus-leaf* effects can be extracted from the modified *Cassie-Baxter* equation:

$$\cos \theta_r = \rho f_s \cos \theta - f_v \qquad (3a)$$

where, θ_r is the apparent contact angle of the micro- and nano structured surfaces, f_s is the fraction of the areas occupied by the solid–water interface and f_v is the fraction that correspond to the vapour gaps, θ is the Young's contact angle and ρ is the roughness factor, calculated from triadic curve for fractal geometry[29]

$$\rho = (R/r)^{D-2} \qquad (3b)$$

For a three-dimensional space $D \approx 2.2618$ and R and r are the upper and the lower limits of the surface topographies.[29,30] Based on the surface geometry considerations described in Fig. 3f, the Casie–Baxter equation can be reformulated (see
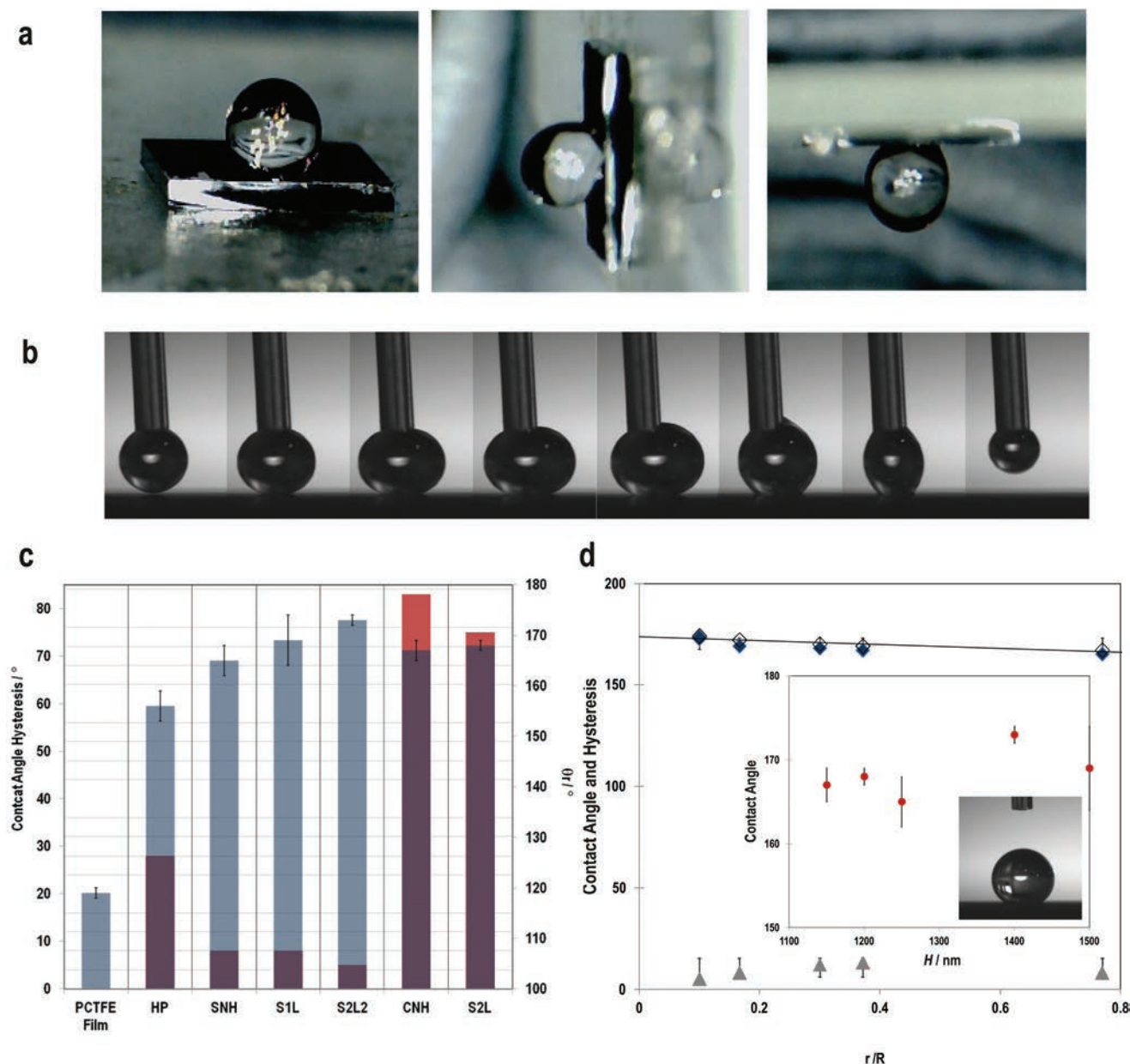
Fig. 5 Wetting properties of the CNT-EHL fabricated surfaces. (a) Optical image sequences on the (i) flat, (ii) 90° tilted and (iii) 180° tilted CNH surface. (b) Sequence images of the water drop advancing and receding on the S2L2 surface indicating its superhydrophobic contact angle of 173°, shape of the suspending water drops and the complete receding without rupture while withdrawing the water droplet with $\theta_{Adv} \approx \theta_{Rec} \approx \theta_{\gamma}$. This behaviour corresponds to a *Cassie-Baxter* wetting state. (c) Different wetting states of all the experimental samples showing the measured contact angles (right) and the measured hysteresis (left) with SNH, S1L and S2L2 exhibiting roll-off (*lotus-leaf*) behaviour and CNH and S2L demonstrating sticky (*rose-petal*) properties not observed in the case of hexagonal pillars in comparison to the reference sample of the flat PCTFE thin film. (d) Variation of the measured contact angle (blue diamonds) and the corresponding hysteresis (grey triangles) with the geometric parameters is in agreement within their error margins and are well described by the theoretical prediction (line). The theoretical data follow the same trend, but are offset towards slightly higher values. Inset: Variation of the contact angle as a function of the structures' height. Over a height variation of 350 nm, the contact angle changed by only 22% compared to a variation as function of r/R by a factor of 7.

ESI, S3†) exhibiting the evident dependence on the hexagonally packed cone geometry:

$$\cos\theta_r = \frac{\left(\frac{H}{R}\right)\cos\theta - \left[\frac{2\sqrt{3}}{\pi}\left(\frac{R}{r}\right)^2 - 1\right]}{\left(\frac{H}{R}\right)\cos\theta + \left[\frac{2\sqrt{3}}{\pi}\left(\frac{R}{r}\right)^2 - 1\right]} \quad (4)$$

For a hexagonal array of cones (Fig. 4c–e), the area fraction of the solid surface that is in contact with the liquid is given by[4–7]

$$f_s \approx \frac{\pi}{4\sqrt{3}}(r/R)^2 \quad (5)$$

For the surface morphologies shown in Fig. 4a and b, and only considering the top of the nano-hair like surfaces roughness, the theoretical contact angle can be extracted from the eqn (3a), (3b) and (5). Fig. 5 shows the experimental contact angles and hysteresis on the fabricated surfaces as well as the function of morphological geometric parameters. The effects of structure morphologies and dimensions, fabricated *via* the CNT-EHL, on the water contact angle and hysteresis, both experimentally measured and theoretically calculated, are summarised in Table 1.

It can be clearly seen that the wetting behaviour is considerably enhanced by the surface structure and dimensions in comparison to the flat surfaces of the same material. Super apolar behaviour is demonstrated from all the CNT-EHL patterned structures with contact angles exceeding 160° except the cylindrical pillars geometry (Fig. 5c) and the S2L2 exhibiting the most superhydrophobic properties with a contact angle as high as 173°. Nevertheless, while SNH, S1L and S2L2 structures exhibit roll-off superhydrophobicity mimicking the *lotus-leaf* like behaviour (Fig. 5b and c) in the case of CNH and S2L structures, water appears to penetrate a few nanometres into the voids and therefore, facilitates strong adhesive forces combined with the superhydrophobicity, mimicking the *rose-petal* effect (Fig. 5a and c).

Whereas for the hierarchical S2L structures both levels of roughness contribute to the pinning effect, with complete wetting on the larger spikes and the smaller cones which contribute to the second order of roughness with the air trapped within, in the case of the S2L2 surface, where similar morphology is observed, the second order roughness of the small

spikes is considerably lower than the primary cones and therefore, their effect is negligible.[31] According to Cassie-impregnating wetting regime, the liquid wets the larger-scale structure and penetrates the smaller nanoscale valleys and therefore the adhesive force between the water drop and the surface is very high supporting the droplet even when the surface is tilted at an angle or turned upside down (Fig. 5a). In addition defects and artifacts on the mesoscale (micro-to nano) have been shown to yield either the high localised surface energy, possibly penetrating into the static drop increasing the adhesion forces resulting in sticky surfaces on the macroscale.[14,32] The degree of opening angle of the cone structures has been also shown to influence the transition from the slippery to sticky behaviour.[14,33]

It is evident from Fig. 5d that the contact angles as a function of the geometric parameters of the surface roughness of the CNT-EHL patterned surfaces have a linear dependence, indicating that the larger the fractional contact area, the smaller the apparent contact angle (Fig. 5d). As qualitatively extracted from Fig. 5a and b the marked structural height has only a minor influence on the contact angle. This is quantitatively shown in the inset of Fig. 5d, where θ_r changed by only 22% over height variation, despite a relative variation of the water penetration by a factor of 7 indicating a considerably smaller influence of the height on the superhydrophobicity in comparison to the surface roughness factor.

Finally, our results highlight the importance of the ratio of the surface roughness factor and heterogeneity parameters, R_s for tuning the superhydrophobic properties. Typically, the ratio of the roughness factor as well as the fractional area of contact can be calculated by averaging the surface roughness over a given area which is smaller than the liquid droplet. The contact angle hysteresis is influenced by the value of the surface roughness which itself affects the ability of the interface to pin the triple line and therefore, decreasing the R_s relative to the liquid drop size eventually rendering the contact angle hysteresis of a negligible value. For the hexagonally packed cone structures, the dependence of the surface roughness in Fig. 5(c and d) implies that the triple-phase contact length has a linear dependence on the contact angle hysteresis (see ESI, S4†).

In summary, we have demonstrated an innovative, controllable and facile yet scalable method to fabricate a broad range of super apolar surface morphologies with a single or multi-

Table 1 Geometrical effects of the CNT-EHL generated surfaces on the contact angle and hysteresis (Hys). The experimental results in comparison to the theoretical predictions as function of varying surface roughness

Surface	R/nm	r/nm	H/nm	θ_r/°	STDV θ_r	Hys/°	STDV Hys	Property	Calculated θ_r/°
PCTFE film	—	—	100	119	1	—	—	—	—
HP	1750	—	250	155	3	28	7	Wenzel	156
SNH	1.3	1	1250	165	3	8	1	*Lotus*	167
S1L	2500	300	1500	169	5	8	2	*Lotus*	174
S2L2	3000	300	1400	173	1	5	3	*Lotus*	174
CNH	3.5	1.3	1150	167	2	83	2	*Petal*	169
S2L	1000	300	1200	168	1	75	2	*Petal*	170

level hierarchy. Vertically aligned carbon nanotube forests were exploited in an unconventional way to produce a range of robust lithographic electrodes, further exploited in conjunction with electrohydrodynamic patterning. A range of configurations was produced by verifying the top electrode design and the experimental parameters during the CNT-EHL patterning process yielding various hierarchical architectures, mimicking the *lotus-leaf* and *rose-petal* like surface morphologies and properties. The generated hierarchical structures enable enhancing the hydrophobicity *via* different length scales of roughness. When the water can penetrate the larger-scale texture, but cannot enter into the smaller structures, the patterned surface effectively mimics the '*lotus-leaf*' effect. However, when the larger micro- and nanostructures are impregnated by water this gives rise to high solid–water adhesion and therefore high contact angle hysteresis. The tuneable wetting properties can be easily switched between the various behaviours including the sticky or roll-off superhydrophobicity and super-hydrophilic surfaces can also be fabricated upon demand from a simple switch to alternative polymers and morphologies. Furthermore, thin EHL patterned films can be easily floated off the supporting substrates and transferred on different support surfaces and therefore, can be used as advanced superhydrophobic coatings which conformally adhere to underlying substrates with any dimension and morphology. The versatility of the CNT-EHL technique renders it easily extendable for a broad range of more intricate, adjustable geometrical microstructures enabling direct biomimetics of nature's unique wettability. Vertically aligned carbon nanotube forests patterned into predesigned structures can be also utilized for additional applications including for instance, straightforward and cost-effective substrates for high-throughput multiplex detection. Moreover, because vertically oriented CNTs exhibit functionalities such as electrical conductivity and unique adsorption properties, these can be further harnessed in their development as novel chemical and bio-sensing platforms. In this tuneable mode, CNT-EHL is a promising prospect for the robust, straightforward, and low-cost fabrication of sub-micrometer patterned substrates to facilitate a plethora of low energy surfaces for coatings, fabrics and microfluidic device technologies with high mechanical durability and optical transparency.

Experimental

Growth of the vertically aligned carbon nanotube forests

CNT forests were grown on the 5×5 mm^2 silicon wafers, using the cold-wall system of the catalytic chemical vapour deposition (CVD) process.[34] Substrates were sputter-coated with a catalyst layer consisting of Al_2O_3 buffer and iron catalysts. During the growth process, initially 500 sccm of H_2 was heated to 750 °C at 5 min under controlled system pressure of 15 mbar. CNTs growth proceeded at 750 °C with a gas flow of $H_2 : C_2H_2$ (460 : 40 sccm). Upon the completion of the growth,

the substrate was cooled to room temperature under the flow of 500 sccm of hydrogen.

Fabrication of patterned CNT arrays

CNTs arrays were generated using an electron beam lithography combined with CVD growth process, where initially, a layer of photoresist was spin-coated on a silicon wafer which was further annealed at 120 °C for 2 minutes. Consequently, the resist was exposed under the electron beam with (pre)-written dimensions. Finally, it was post-baked at 140 °C for 2 minutes and developed in CD26 for 30 s, and the CNT-based pillar arrays were obtained. These structures were further filled by depositing 10 nm alumina and 1.3 nm of iron through a sputtering process, followed by lifting-off the resist with acetone. CVD process was utilised using a combination of $H_2 : C_2H_2$ (70 : 30 sccm) at 750 °C for 2 minutes. CNTs arrays with desired dimensions and pitches were eventually grown on top of the patterned catalysts.

Fabrication of the inverted CNT forests

Initially, a homogeneous poly(methyl methacrylate) film was spin-cast on a silicon substrate, followed by placing the VACNTs facing the PMMA layer and annealing at 180 °C for 1 minute. The substrate was then cooled down t below the glass-transition temperature of the polymer film, resulting in a solidification of the film while embedding the upper ends of the CVD-grown CNTs forest. The VACNTs were subsequently peeled off the original silicon wafer, exposing well-defined straight tips.

CNT-EHL patterning

The fabricated CNT-based electrodes were coated with a silicon layer (Kurt J. Lesker Si sputtering target 99.999% purity). To ensure the reusability of the CNT-based electrodes, these were rendered hydrophobic by the deposition of a 1,1,1,2*H*-perfluorodecyltrichlorosilane self-assembled monolayer to reduce the adhesion between the mask and the EHL patterned polymer. Alternatively, a non-stick self-assembled monolayer was deposited from liquid octadecyltrichlorosilane phase. Silanization was performed by immersion of the substrate in the freshly prepared silane solution (0.25% OTS in hexadecane).

Highly polished p-doped silicon (Si) wafers, with <100> crystal orientation (Wafernet Gmbh, Eching, Germany) covered by 100 nm thick silicon oxide layer were used as substrates. Initially, the substrates were cleaned in a 'Piranha' solution consisting of $3 : 1$ H_2SO_4 (98%) : H_2O_2 (30%), followed by thorough rinsing with deionised water and dried under N_2. Thereafter, silicon wafers were cleaned using a snow-jet gun immediately before film deposition and capacitor patterning assembly. Transparent indium–tin oxide (ITO) covered glass slides with a resistivity of 80 cm^{-2} were also used as substrates, allowing the *in situ* optical tracking of the pattern formation or replication process. Thin films of PCTFE (Young's modulus 2.7×10^9 Pa, $\varepsilon = 2.6$, $T_g = 103$ °C, density = 1 g mL^{-1} at 25 °C, intrinsic viscosity, $[\eta] = 0.70$) were spin-coated onto a silicon

wafer with typical concentrations of 2–3% polymer by weight. Facing it, a top electrode comprised of the silicon coated VACNT (as-grown and inverted) forests and arrays, was mounted at a specific distance, leaving a thin air gap, d. The silicon wafers were electrically contacted by evaporating a 10 nm chromium layer, followed by a 100 nm gold layer on the unpolished backside. When ITO glass was used as bottom electrodes, these were contacted by scratching the polymer film at two corners before applying the silver paste.

The experiment was initiated by liquefying the spin-cast PCTFE films by annealing above the softening/glass transition temperature (typically to around 130 °C) of the polymer while the voltage (between 40–70 V) was applied to the electrodes and subsequently, cooling sample to RT solidified the polymer before the voltage was removed, terminating the patterning process (typically 20 h). A laterally varying electric field density was introduced to the system by mounting a topographically structured CNT-based master electrode onto the polymer film. Expressed by the ratio between the intrinsic wavelength λ_i and the lateral periodicity (or lateral size of nonperiodic structures) Λ_m of the master structure, three replication cases are described: (i) $\lambda_i < \Lambda_m$ (ii) $\lambda_i \approx \Lambda_m$ and (iii) $\lambda_i > \Lambda_m$. After freezing-in the samples by reducing the temperature to room temperature, the electric field was disconnected and the upper electrode was removed. Pattern replication was monitored and recorded by a microscope and a connected computer throughout the experiment. After removal of the top electrode, the quenched polymer film was further characterized by the atomic force microscopy.

Characterisation

AFM measurements were performed using a Nanoscope IV Dimension 3100 (Veeco Instruments Inc.) microscope operated in tapping mode using the NSG 20 cantilevers with a resonance frequency of 260 kHz and a stiffness of 28 N m^{-1}. Image processing and analysis was carried out with the instrument's software version V612r2 and V530r2. AFM measurements yielded the geometric dimensions of the CNT-EHL structure including, the aspect ratio, the pitch between the generated morphologies, their heights and diameters. Contact angle and hysteresis were measured at 3–5 different areas on each sample using a computer controlled telescopic goniometer (KSV CAM 200) with digital image acquisition. A numerical fitting algorithm was applied to determine the advancing and receding contact angles from the side-view of drops. Static contact angles are measured on drops with a volume between $5\ \mu l < V < 20\ \mu l$. The drop pictures were fitted using the contact angle goniometer software. For static contact angles, the Young–Laplace fitting algorithm was used and a base-line tilt was allowed. Dynamic contact angles were measured by continuously increasing or decreasing the size of a drop on a surface. The increasing and decreasing speed was between $0.5\ \mu l\ s^{-1} < S_{drop} < 2\ \mu l\ s^{-1}$. The images of the advancing and receding drops were analysed using ImageJ (Drop_Analysis Package). The scanning electron microscopy (SEM) measurements were performed using a LEO ULTRA 55 SEM including

a Schottky emitter (ZrO/W cathode) at acceleration voltages of 1–5 kV with a lateral resolution of 2–5 nm. Low-angle backscattered electron imaging mode was used to contrast the non-coated VACNTs and those sputtered with silicon, providing the atomic number contrast.

Acknowledgements

References

1 A. Venkateswara Rao, S. S. Latthe, D. Y. Nadargi, H. Hirashima and V. Ganesan, *J. Colloid Interface Sci.*, 2009, **332**, 484–490.

2 A. V. Rao, S. S. Latthe, S. A. Mahadik and C. Kappenstein, *Appl. Surf. Sci.*, 2011, **257**, 5772–5776.

3 M. A. Sarshar, C. Swarctz, S. Hunter, J. Simpson and C.-H. Choi, *Colloid Polym. Sci.*, 2013, **291**, 427–435.

4 R. N. Wenzel, *Ind. Eng. Chem.*, 1936, **28**, 988–994.

5 A. B. D. Cassie and S. Baxter, *Trans. Faraday Soc.*, 1944, **40**, 546–551.

6 M. Jin, X. Feng, L. Feng, T. Sun, J. Zhai, T. Li and L. Jiang, *Adv. Mater.*, 2005, **17**, 1977–1981.

7 C. Cao, Y. Feng, J. Zang, G. P. López and X. Zhao, *Extreme Mech. Lett.*, 2015, **4**, 18–25.

8 D. Öner and T. J. McCarthy, *Langmuir*, 2000, **16**, 7777–7782.

9 L. Zhu, Y. Xiu, J. Xu, P. A. Tamirisa, D. W. Hess and C.-P. Wong, *Langmuir*, 2005, **21**, 11208–11212.

10 N. M. B. Perney, J. J. Baumberg, M. E. Zoorob, M. D. B. Charlton, S. Mahnkopf and C. M. Netti, *Opt. Express*, 2006, **14**, 847–857.

11 E. Menard, M. A. Meitl, Y. Sun, J.-U. Park, D. J.-L. Shir, Y.-S. Nam, S. Jeon and J. A. Rogers, *Chem. Rev.*, 2007, **107**, 1117–1160.

12 M. Kahl, E. Voges, S. Kostrewa, C. Viets and W. Hill, *Sens. Actuators, B*, 1998, **51**, 285–291.

13 T. N. Krupenkin, J. A. Taylor, T. M. Schneider and S. Yang, *Langmuir*, 2004, **20**, 3824–3827.

14 L. Schneider, M. Laustsen, N. Mandsberg and R. Taboryski, *Sci. Rep.*, 2016, **6**, 21400.

15 S. Y. Chou, P. R. Krauss and P. J. Renstrom, *Science*, 1996, **272**, 85–87.

16 S. Zankovych, T. Hoffmann, J. Seekamp, J. U. Bruch and C. M. S. Torres, *Nanotechnology*, 2001, **12**, 91.

17 L. Feng, S. Li, H. Li, J. Zhai, Y. Song, L. Jiang and D. Zhu, *Angew. Chem., Int. Ed.*, 2002, **41**, 1221–1223.

18 N. J. Shirtcliffe, G. McHale, M. I. Newton, G. Chabrol and C. C. Perry, *Adv. Mater.*, 2004, **16**, 1929–1932.

19 A. Checco, A. Rahman and C. T. Black, *Adv. Mater.*, 2014, **26**, 886–891.

20 B. Balu, J. S. Kim, V. Breedveld and D. W. Hess, *J. Adhes. Sci. Technol.*, 2009, **23**, 361–380.

21 Y. Xiu, L. Zhu, D. W. Hess and C. P. Wong, *Nano Lett.*, 2007, **7**, 3388–3393.

22 P. Goldberg-Oppenheimer, D. Kabra, S. Vignolini, S. Hüttner, M. Sommer, K. Neumann, M. Thelakkat and U. Steiner, *Chem. Mater.*, 2013, **25**, 1063–1070.

23 P. Goldberg-Oppenheimer, P. Kohn, R. M. Langford and U. Steiner, *Small*, 2012, **8**, 2595–2601.

24 J. J. S. Rickard, I. Farrer and P. Goldberg Oppenheimer, *ACS Nano*, 2016, **10**, 3865–3870.

25 P. Goldberg-Oppenheimer and U. Steiner, *Small*, 2010, **6**, 1248–1254.

26 P. G. Oppenheimer, *Electrohydrodynamic Patterning of Functional Materials*, Springer International Publishing, 2013.

27 P. Goldberg Oppenheimer, *Polymer Surfaces in Motion: Unconventional Patterning Methods: Electrohydrodynamic Lithography of Functional Soft Materials for Advanced Applications*, Springer International Publishing, 2015.

28 Y. Zhou, A. Nicolas, K. R. Thomas and U. Steiner, *Soft Matter*, 2012, **8**, 3841–3847.

29 L. Feng, S. Li, Y. Li, H. Li, L. Zhang, J. Zhai, Y. Song, B. Liu, L. Jiang and D. Zhu, *Adv. Mater.*, 2002, **14**, 1857–1860.

30 C. Longquan, X. Zhiyong, C. H. C. Philip and L. Yi-Kuen, *J. Micromech. Microeng.*, 2010, **20**, 105001.

31 B. Bhushan and M. Nosonovsky, *Philos. Trans. R. Soc., A*, 2010, **368**, 4713–4728.

32 S. Tian, L. Li, W. Sun, X. Xia, D. Han, J. Li and C. Gu, *Sci. Rep.*, 2012, **2**, 511.

33 N. Wang, Y. Yuan, Y. Wu, T. Hang and M. Li, *Langmuir*, 2015, **31**, 10807–10812.

34 P. Goldberg-Oppenheimer, T. Hutter, B. Chen, J. Robertson, S. Hofmann and S. Mahajan, *J. Phys. Chem. Lett.*, 2012, **3**, 3486–3492.

List of References

[1]   M.P. Mattson, Superior pattern processing is the essence of the evolved human brain, Front. Neurosci. (2014). doi:10.3389/fnins.2014.00265.

[2]   TIMAEUS, in: Dialogues Plato Transl. into English, with Anal. Introd., Cambridge University Press, (2010) 465–466.

[3]   I. ADLER, A History of the Study of Phyllotaxis, Ann. Bot. 80 (1997) 231–244. doi:10.1006/anbo.1997.0422.

[4]   A. Lindenmayer, Mathematical models for cellular interactions in development II. Simple and branching filaments with two-sided inputs, J. Theor. Biol. 18 (1968) 300–315. doi:10.1016/0022-5193(68)90080-5.

[5]   fractal @ en.oxforddictionaries.com, (n.d.). https://en.oxforddictionaries.com/definition/fractal.

[6]   B. Li, J. Miller, Fractal Cityscape, Int. J. 9 (2010) 7–12.

[7]   3275 @ Cybergeo.Revues.Org, (n.d.). http://cybergeo.revues.org/3275.

[8]   Clifford A. Pickover, The Pattern Book: fractals, art, and nature, World Scientific Publishing Co. Pte. Ltd. (1995).

[9]   S. Vignolini, E. Moyroud, B.J. Glover, U. Steiner, Analysing photonic structures in plants Analysing photonic structures in plants, Jorunal R. Soc. Interface. 10 (2013). doi:10.1098/rsif.2013.0394.

[10]   G.S. Watson, J.A. Watson, S. Hu, C.L. Brown, B. Cribb, S. Myhra, Micro and nanostructures found on insect wings–designs for minimising adhesion and friction, Int. J. Nanomanuf. 5 (2010) 112–128. doi:10.1504/IJNM.2010.029929.

[11]   A.J. Scardino, R. de Nys, Mini review: Biomimetic models and bioinspired

surfaces for fouling control., Biofouling. 27 (2011) 73–86. doi:10.1080/08927014.2010.536837.

[12] B. Bhushan, Y.C. Jung, Natural and biomimetic artificial surfaces for superhydrophobicity, self-cleaning, low adhesion, and drag reduction, Prog. Mater. Sci. 56 (2011) 1–108. doi:10.1016/j.pmatsci.2010.04.003.

[13] G. Zhang, J. Zhang, G. Xie, Z. Liu, H. Shao, Cicada wings: A stamp from nature for nanoimprint lithography, Small. 2 (2006) 1440–1443. doi:10.1002/smll.200600255.

[14] P. Vukusic, J.R. Sambles, Photonic structures in biology., Nature. 424 (2003) 852–5. doi:10.1038/nature01941.

[15] V. Sharma, M. Crne, J.O. Park, M. Srinivasarao, Structural origin of circularly polarized iridescence in jeweled beetles., Science. 325 (2009) 449–51. doi:10.1126/science.1172051.

[16] M. Sitti, R.S. Fearing, Synthetic Gecko Foot-Hair Micro/Nano-Structures as Dry Adhesives, J. Adhes. Sci. Technol. 18 (2003) 1055–1074. doi:10.1163/156856103322113788.

[17] K. Koch, B. Bhushan, W. Barthlott, Multifunctional surface structures of plants: An inspiration for biomimetics, Prog. Mater. Sci. 54 (2009) 137–178. doi:10.1016/j.pmatsci.2008.07.003.

[18] H. Gao, Z. Liu, J. Zhang, G. Zhang, G. Xie, Precise replication of antireflective nanostructures from biotemplates, Appl. Phys. Lett. 90 (2007) 12–15. doi:10.1063/1.2715094.

[19] E. Arzt, S. Gorb, R. Spolenak, From micro to nano contacts in biological attachment devices., Proc. Natl. Acad. Sci. U. S. A. 100 (2003) 10603–6. doi:10.1073/pnas.1534701100.

[20] K. Autumn, M. Sitti, Y.A. Liang, A.M. Peattie, W.R. Hansen, S. Sponberg, T.W. Kenny, R. Fearing, J.N. Israelachvili, R.J. Full, Evidence for van der Waals adhesion in gecko setae, Proc. Natl. Acad. Sci. 99 (2002) 12252–12256. doi:10.1073/pnas.192252799.

[21] W.D. 4 Hamilton, J. Seger, W.D. Hamilton, R.E. Michod, B.R. Levin, 176±193, Sinauer, S. Associates, R. Axelrod, R. Tanese, Adhesive force of a single gecko foot-hair\n, NATUREnature.com J. Theor. Biol. Oikos J. Theor. Biol. Am. Nat. Judson, O. P. Preserv. Genet. Res. Proc. R. Soc. B Evol. 405 (2000) 671–702. doi:10.1038/35015073.

[22] J. Yu, M. Tan, S. Wang, E. Chen, Development of a biomimetic robotic fish and its control algorithm, IEEE Trans. Syst. Man, Cybern. Part B Cybern. 34 (2004) 1798–1810. doi:10.1109/TSMCB.2004.831151.

[23] C. Menon, M. Murphy, M. Sitti, Gecko Inspired Surface Climbing Robots, 2004 IEEE Int. Conf. Robot. Biomimetics. (2004) 431–436. doi:10.1109/ROBIO.2004.1521817.

[24] X.D.X. Deng, L. Schenato, S.S. Sastry, Flapping flight for biomimetic robotic insects: part II-flight control design, IEEE Trans. Robot. 22 (2006) 776–788. doi:10.1109/TRO.2006.875483.

[25] D. Stuart-Fox, A. Moussalli, Selection for social signalling drives the evolution of chameleon colour change, PLoS Biol. 6 (2008) 0022–0029. doi:10.1371/journal.pbio.0060025.

[26] J. Teyssier, S. V. Saenko, D. Van Der Marel, M.C. Milinkovitch, Photonic crystals cause active colour change in chameleons, Nature. (2015) 1–7. doi:10.1038/ncomms7368.

[27] S.R. Schachat, R.L. Brown, Color Pattern on the Forewing of Micropterix

(Lepidoptera: Micropterigidae): Insights into the Evolution of Wing Pattern and Wing Venation in Moths, PLoS One. 10 (2015). doi:10.1371/journal.pone.0139972.

[28] S.S. Hardaker, R. V Gregory, Progress toward Dynamic Color-Responsive "Chameleon" Fiber Systems, MRS Bull. 28 (2003) 564–567. doi:10.1557/mrs2003.166.

[29] S.-W. Chung, D.S. Ginger, M.W. Morales, Z. Zhang, V. Chandrasekhar, M.A. Ratner, C.A. Mirkin, Top-down meets bottom-up: dip-pen nanolithography and DNA-directed assembly of nanoscale electrical circuits., Small. 1 (2005) 64–9. doi:10.1002/smll.200400005.

[30] A. Biswas, I.S. Bayer, A.S. Biris, T. Wang, E. Dervishi, F. Faupel, Advances in top-down and bottom-up surface nanofabrication: Techniques, applications & future prospects, Adv. Colloid Interface Sci. 170 (2012) 2–27. doi:10.1016/j.cis.2011.11.001.

[31] M. Pillers, V. Goss, M. Lieberman, Electron-beam lithography and molecular liftoff for directed attachment of DNA nanostructures on silicon: Top-down meets bottom-up, Acc. Chem. Res. 47 (2014) 1759–1767. doi:10.1021/ar500001e.

[32] S. Verma, R. Gokhale, D.J. Burgess, A comparative study of top-down and bottom-up approaches for the preparation of micro/nanosuspensions, Int. J. Pharm. 380 (2009) 216–222. doi:10.1016/j.ijpharm.2009.07.005.

[33] J.Y. Cheng, C.A. Ross, H.I. Smith, E.L. Thomas, Templated Self-Assembly of Block Copolymers: Top-Down Helps Bottom-Up, Adv. Mater. 18 (2006) 2505–2521. doi:10.1002/adma.200502651.

[34] N.C. Seeman, DNA in a material world, Nature. 421 (2003) 427–431. doi:10.1038/nature01406.

[35] M. Shimomura, T. Sawadaishi, Bottom-up strategy of materials fabrication: a new trend in nanotechnology of soft materials, Curr. Opin. Colloid Interface Sci. 6 (2001) 11–16. doi:10.1016/S1359-0294(00)00081-9.

[36] R. Luttge, Nano- and microfabrication for industrial and biomedical applications, Elsevier (2016). doi:10.1016/B978-0-323-37828-4.00002-9.

[37] R. Luttge, Micro and Nano Technologies, Elsevier (2011). doi:10.1016/B978-0-323-37828-4.00002-9.

[38] S.Y. Chou, Nanoimprint lithography, Woodhead Publishing Limited (1996). doi:10.1116/1.588605.

[39] P. Goldberg-Oppenheimer, D. Eder, U. Steiner, Carbon nanotube alignment via electrohydrodynamic patterning of nanocomposites, Adv. Funct. Mater. 21 (2011) 1895–1901. doi:10.1002/adfm.201002692.

[40] A.M. Urbas, Z. Jacob, L.D. Negro, N. Engheta, A.D. Boardman, P. Egan, A.B. Khanikaev, V. Menon, M. Ferrera, N. Kinsey, C. DeVault, J. Kim, V. Shalaev, A. Boltasseva, J. Valentine, C. Pfeiffer, A. Grbic, E. Narimanov, L. Zhu, S. Fan, A. Alù, E. Poutrina, N.M. Litchinitser, M.A. Noginov, K.F. MacDonald, E. Plum, X. Liu, P.F. Nealey, C.R. Kagan, C.B. Murray, D.A. Pawlak, I.I. Smolyaninov, V.N. Smolyaninova, D. Chanda, Roadmap on optical metamaterials, J. Opt. 18 (2016) 93005. doi:10.1088/2040-8978/18/9/093005.

[41] T. Betancourt, L. Brannon-Peppas, Micro- and nanofabrication methods in nanotechnological medical and pharmaceutical devices, Int. J. Nanomedicine. 1 (2006) 483–495.

[42] A. Biswas, I.S. Bayer, A.S. Biris, T. Wang, E. Dervishi, F. Faupel, Advances in top–down and bottom–up surface nanofabrication: Techniques, applications and future prospects, Adv. Colloid Interface Sci. 170 (2012) 2–27.

doi:10.1016/j.cis.2011.11.001.

[43] B.W. Smith, Optical projection lithography, Woodhead Publishing Limited (2014). doi:10.1533/9780857098757.1.

[44] Gas-assisted focused electron beam and ion beam processing and fabrication, J. Vac. Sci. Technol. B Microelectron. Nanom. Struct. Process. Meas. Phenom. 26 (2008) 1197–1276. doi:10.1116/1.2955728.

[45] H.N.G. King, Electron beam lithography, Woodhead Publishing Limited (1967). doi:10.1016/0042-207X(85)90207-6.

[46] C. Vieu, F. Carcenac, A. Pépin, Y. Chen, M. Mejias, A. Lebib, L. Manin-Ferlazzo, L. Couraud, H. Launois, Electron beam lithography: resolution limits and applications, Appl. Surf. Sci. 164 (2000) 111–117. doi:10.1016/S0169-4332(00)00352-4.

[47] S.W. Chang, J.P. Evans, S.R. Ge, V. V Ginzburg, J.W. Kramer, B. Landes, C. Lee, G. Meyers, D.J. Murray, J. Park, R. Sharma, P. Trefonas, J.D. Weinhold, J.Q. Zhang, P.D. Hustad, New Materials and Processes for Directed Self-Assembly, Altern. Lithogr. Technol. V. 8680 (2013) 1–9. doi:Unsp 86800f\nDoi 10.1117/12.2011604.

[48] Y. Seino, H. Yonemitsu, H. Sato, M. Kanno, H. Kato, K. Kobayashi, A. Kawanishi, T. Azuma, M. Muramatsu, S. Nagahara, T. Kitano, T. Toshima, Contact hole shrink process using graphoepitaxial directed self-assembly lithography, J. Micro/Nanolithography, MEMS, MOEMS. 12 (2013) 33011. doi:10.1117/1.JMM.12.3.033011.

[49] C.T. Black, Polymer Self-Assembly as a Novel Extension to Optical Lithography, ACS Nano. 1 (2007) 147–150. doi:10.1021/nn7002663.

[50] M. Park, C. Harrison, P.M. Chaikin, R.A. Register, D.H. Adamson, Block

Copolymer Lithography: Periodic Arrays of ~1011 Holes in 1 Square Centimeter, Science. 276 (1997) 1401 LP-1404.

[51] M. Ramanathan, Y.-C. Tseng, K. Ariga, S.B. Darling, Emerging trends in metal-containing block copolymers: synthesis, self-assembly, and nanomanufacturing applications, J. Mater. Chem. C. 1 (2013) 2080–2091. doi:10.1039/C3TC00930K.

[52] Liddy Halm, G. Vereinigung für Angewandte Botanik, Q. Deutsche Gesellschaft für Qualitätsforschung, L. Dokoupil, Journal of applied botany and food quality , Angewandte botanik, 2004.

[53] B. Bhushan, Y.C. Jung, Natural and biomimetic artificial surfaces for superhydrophobicity, self-cleaning, low adhesion, and drag reduction, Prog. Mater. Sci. 56 (2011) 1–108. doi:10.1016/j.pmatsci.2010.04.003.

[54] B. Bhushan, Biomimetics inspired surfaces for drag reduction and oleophobicity/philicity, Beilstein J. Nanotechnol. 2 (2011) 66–84. doi:10.3762/bjnano.2.9.

[55] K. Liu, Y. Tian, L. Jiang, Bio-inspired superoleophobic and smart materials: Design, fabrication, and application, Prog. Mater. Sci. 58 (2013) 503–564. doi:10.1016/j.pmatsci.2012.11.001.

[56] Y. Zhang, Y. Chen, L. Shi, J. Li, Z. Guo, Recent progress of double-structural and functional materials with special wettability, J. Mater. Chem. 22 (2012) 799–815. doi:10.1039/c1jm14327a.

[57] R. Ma, M. Hill, Superhydrophobic surfaces, Curr. Opin. Colloid Interface Sci. 11 (2006) 193–202. http://www.sciencedirect.com.ezproxyd.bham.ac.uk/science/book/9780128011096.

[58] H.K. Webb, R.J. Crawford, E.P. Ivanova, Wettability of natural

superhydrophobic surfaces, Adv. Colloid Interface Sci. 210 (2014) 58–64. doi:10.1016/J.CIS.2014.01.020.

[59] B. Luk'yanchuk, N.I. Zheludev, S. a Maier, N.J. Halas, P. Nordlander, H. Giessen, C.T. Chong, The Fano resonance in plasmonic nanostructures and metamaterials., Nat. Mater. 9 (2010) 707–15. doi:10.1038/nmat2810.

[60] T. Renaissance, Emergence of the, 8 (1800) 506–507. doi:10.1038/nphoton.2010.247.

[61] V.M. Shalaev, Optical negative-index metamaterials, Nat. Photonics. 1 (2007) 41–48. doi:10.1038/nphoton.2006.49.

[62] W. Cai, V. Shalaev, Optical metamaterials: Fundamentals and applications, Opt. Metamaterials Fundam. Appl. (2010) 1–200. doi:10.1007/978-1-4419-1151-3.

[63] J.H. Lee, J.P. Singer, E.L. Thomas, Micro-/nanostructured mechanical metamaterials, Adv. Mater. 24 (2012) 4782–4810. doi:10.1002/adma.201201644.

[64] Q. Liu, W.M. Zhu, D.P. Tsai, N.I. Zheludev, Micromachined tunable metamaterials: a review, J. Opt. 14 (2012) 114009. doi:10.1088/2040-8978/14/11/114009.

[65] N. Horiuchi, Strength in diversity, Nat. Photonics. 9 (2015) 714–716. doi:10.1038/nphoton.2015.210.

[66] C.M. Soukoulis, M. Wegener, Past achievements and future challenges in the development of three-dimensional photonic metamaterials, Nat Phot. 5 (2011) 523–530.

[67] A.A. Zharov, I. V Shadrivov, Y.S. Kivshar, Nonlinear Properties of Left-Handed Metamaterials, Phys. Rev. Lett. 91 (2003) 37401. http://link.aps.org/doi/10.1103/PhysRevLett.91.037401.

[68]   I.A. Buriak, V.O. Zhurba, A review of microwave metamaterial structures classifications and applications, 2016 9th Int. Kharkiv Symp. Phys. Eng. Microwaves, Millim. Submillim. Waves. (2016) 1–3. doi:10.1109/MSMW.2016.7538118.

[69]   D.R. Smith, J.B. Pendry, M.C.K. Wiltshire, Metamaterials and Negative Refractive Index, Science. 305 (2004) 788 LP-792.

[70]   F. Bilotti, L. Sevgi, Metamaterials: Definitions, properties, applications, and FDTD-based modeling and simulation, Int. J. RF Microw. Comput. Eng. 22 (2012) 422–438. doi:10.1002/mmce.20634.

[71]   R.S. and M.W. Muamer Kadic1, Tiemo Buckmann, Metamaterials beyond electromagnetism, Rep. Prog. Phys. 76 (2013). http://iopscience.iop.org/article/10.1088/0034-4885/76/12/126501/pdf.

[72]   A.E. Dubinov, A. Mytareva, V.A. Burov, V.B. Voloshinov, K. V Dmitriev, A. V Kildishev, W. Cai, U.K. Chettiar, V. V Shevchenko, A.M. Urbas, Z. Jacob, L. Dal Negro, V.G. Veselago, Transformation optics and metamaterials, Phys.Usp. 54 (2011).

[73]   P. Dastmalchi, A. Haddadpour, G. Veronis, Nanophotonics: devices for manipulating light at the nanoscale, Nanolithography Art Fabr. Nanoelectron. Nanophotonic Devices Syst. (2014) 376–398. doi:10.1533/9780857098757.376.

[74]   Y.-C. Chuang, R. Dudley, M.A. Fiddy, Optimal arrangement of meta-atoms composing metamaterials, in: A. Adibi, S.-Y. Lin, A. Scherer (Eds.), International Society for Optics and Photonics. (2012) 82691D. doi:10.1117/12.906331.

[75]   T. Bückmann, N. Stenger, M. Kadic, J. Kaschke, A. Frölich, T. Kennerknecht, C. Eberl, M. Thiel, M. Wegener, Tailored 3D mechanical metamaterials made by

dip-in direct-laser-writing optical lithography, Adv. Mater. 24 (2012) 2710–2714. doi:10.1002/adma.201200584.

[76] Flexible metasurfaces and metamaterials: A review of materials and fabrication processes at micro- and nano-scales, Appl. Phys. Rev. 2 (2015) 11303. doi:10.1063/1.4913751.

[77] Y. Liu, X. Zhang, Metamaterials: a new frontier of science and technology, Chem. Soc. Rev. 40 (2011) 2494–2507. doi:10.1039/c0cs00184h.

[78] S. Yang, P. Liu, M. Yang, Q. Wang, J. Song, L. Dong, From Flexible and Stretchable Meta-Atom to Metamaterial: A Wearable Microwave Meta-Skin with Tunable Frequency Selective and Cloaking Effects., Sci. Rep. 6 (2016) 21921. doi:10.1038/srep21921.

[79] X. Zhao, Bottom-up fabrication methods of optical metamaterials, J. Mater. Chem. 22 (2012) 9439. doi:10.1039/c2jm15979a.

[80] Y. Zhao, J. Shi, L. Sun, X. Li, A. Al??, Alignment-free three-dimensional optical metamaterials, Adv. Mater. 26 (2014) 1439–1445. doi:10.1002/adma.201304379.

[81] K.A. Arpin, A. Mihi, H.T. Johnson, A.J. Baca, J.A. Rogers, J.A. Lewis, P. V. Braun, Multidimensional architectures for functional optical devices, Adv. Mater. 22 (2010) 1084–1101. doi:10.1002/adma.200904096.

[82] C. Rockstuhl, F. Lederer, C. Etrich, T. Pertsch, T. Scharf, Design of an artificial three-dimensional composite metamaterial with magnetic resonances in the visible range of the electromagnetic spectrum, Phys. Rev. Lett. 99 (2007) 1–4. doi:10.1103/PhysRevLett.99.017401.

[83] K.Q. Le, Q.M. Ngo, T.K. Nguyen, Nanostructured Metal/Insulator/Metal Metamaterials for Refractive Index Biosensing Applications: Design,

Fabrication, and Characterization, IEEE J. Sel. Top. Quantum Electron. 23 (2017) 1–6. doi:10.1109/JSTQE.2016.2615944.

[84]   W. Zhou, D. Zhao, Y.-C. Shuai, H. Yang, S. Chuwongin, A. Chadha, J.-H. Seo, K.X. Wang, V. Liu, Z. Ma, S. Fan, Progress in 2D photonic crystal Fano resonance photonics, Prog. Quantum Electron. 38 (2014) 1–74. doi:http://dx.doi.org/10.1016/j.pquantelec.2014.01.001.

[85]   J. Serbin, A. Ovsianikov, B. Chichkov, Fabrication of woodpile structures by two-photon polymerization and investigation of their optical properties, Opt. Express. 12 (2004) 5221–5228. doi:10.1364/OPEX.12.005221.

[86]   M.S. Rill, C. Plet, M. Thiel, I. Staude, G. von Freymann, S. Linden, M. Wegener, Photonic metamaterials by direct laser writing and silver chemical vapour deposition, Nat Mater. 7 (2008) 543–546.

[87]   W. Xiong, L.J. Jiang, T. Baldacchini, Y.F. Lu, 9 – Laser additive manufacturing using nanofabrication by integrated two-photon polymerization and multiphoton ablation, in: Laser Addit. Manuf. (2017) 237–256. doi:10.1016/B978-0-08-100433-3.00009-9.

[88]   M. Farsari, B.N. Chichkov, Materials processing: Two-photon fabrication, Nat Phot. 3 (2009) 450–452. http://dx.doi.org/10.1038/nphoton.2009.131.

[89]   R.W. Keyes, Miniaturization of electronics and its limits, IBM J. Res. Dev. 32 (1988) 84–88. doi:10.1147/rd.321.0024.

[90]   H.A. Mantooth, M.D. Glover, P. Shepherd, Wide Bandgap Technologies and Their Implications on Miniaturizing Power Electronic Systems, IEEE J. Emerg. Sel. Top. Power Electron. 2 (2014) 374–385. doi:10.1109/JESTPE.2014.2313511.

[91]   E. Ozbay, Plasmonics: Merging Photonics and Electronics at Nanoscale

Dimensions, Science. 311 (2006) 189 LP-193.

[92] E.B. Brousseau, S.S. Dimov, D.T. Pham, Some recent advances in multi-material micro- and nano-manufacturing, Int. J. Adv. Manuf. Technol. 47 (2010) 161–180. doi:10.1007/s00170-009-2214-5.

[93] A.A. Tseng, Nanofabrication Fundamentals and Applications, World Scientific. (2008). doi:10.1142/6276.

[94] D. Mijatovic, J.C.T. Eijkel, A. van den Berg, Technologies for nanofluidic systems: top-down vs. bottom-up-a review, Lab Chip. 5 (2005) 492–500. doi:10.1039/B416951D.

[95] A. Biswas, I.S. Bayer, A.S. Biris, T. Wang, E. Dervishi, F. Faupel, Advances in top–down and bottom–up surface nanofabrication: Techniques, applications & future prospects, Adv. Colloid Interface Sci. 170 (2012) 2–27. doi:10.1016/j.cis.2011.11.001.

[96] J.A. Liddle, G.M. Gallatin, Nanomanufacturing: A Perspective, ACS Nano. 10 (2016) 2995–3014. doi:10.1021/acsnano.5b03299.

[97] Y. Geng, A.C. Pearson, E.P. Gates, B. Uprety, R.C. Davis, J.N. Harb, A.T. Woolley, Electrically conductive gold- and copper-metallized DNA origami nanostructures, Langmuir. 29 (2013) 3482–3490. doi:10.1021/la305155u.

[98] A. Gopinath, E. Miyazono, A. Faraon, P.W.K. Rothemund, Engineering and mapping nanocavity emission via precision placement of DNA origami, Nature. 535 (2016) 401–405. http://dx.doi.org/10.1038/nature18287.

[99] C. Busà, J.J.S. Rickard, E. Chun, Y. Chong, V. Navaratnam, P. Goldberg Oppenheimer, Tunable superapolar Lotus-to-Rose hierarchical nanosurfaces via vertical carbon nanotubes driven electrohydrodynamic lithography, Nanoscale. 9 (2017) 1625–1636. doi:10.1039/C6NR08706J.

[100] P. Goldberg-Oppenheimer, U. Steiner, Rapid electrohydrodynamic lithography using low-viscosity polymers, Small. 6 (2010) 1248–1254. doi:10.1002/smll.201000060.

[101] P.G. Oppenheimer, Patterning of Crystalline Organic Materials via EHL, in: Electrohydrodynamic Patterning Funct. Mater., Springer International Publishing, Heidelberg (2013) 91–105. doi:10.1007/978-3-319-00783-0_7.

[102] S.-M. Lee, T.H. Kwon, Effects of intrinsic hydrophobicity on wettability of polymer replicas of a superhydrophobic lotus leaf, J. Micromechanics Microengineering. 17 (2007) 687–692. doi:10.1088/0960-1317/17/4/003.

[103] Replication of surfaces of natural leaves for enhanced micro-scale tribological property, Mater. Sci. Eng. C. 27 (2007) 875–879. doi:10.1016/J.MSEC.2006.10.007.

[104] R.A. Singh, E.-S. Yoon, H.J. Kim, J. Kim, H.E. Jeong, K.Y. Suh, Replication of surfaces of natural leaves for enhanced micro-scale tribological property, Mater. Sci. Eng. C. 27 (2007) 875–879. doi:10.1016/J.MSEC.2006.10.007.

[105] B.D. Gates, Q. Xu, M. Stewart, D. Ryan, C.G. Willson, G.M. Whitesides, New Approaches to Nanofabrication: Molding, Printing, and Other Techniques, (n.d.). doi:10.1021/cr030076o.

[106] M. Feldman, Nanolithography: the art of fabricating nanoelectronics, nanophotonics and nanobiology devices and systems, Woodhead Publishing Ltd. (2014).

[107] P. Bandelier, A.-L. Charley, A. Lagrange, Photolithography, in: Lithography, John Wiley & Sons, Inc. (2013). 1–40. doi:10.1002/9781118557662.ch1.

[108] F. Xia, L. Jiang, Bio-inspired, smart, multiscale interfacial materials, Adv. Mater. 20 (2008) 2842–2858. doi:10.1002/adma.200800836.

[109] S. Yang, X. Jin, K. Liu, L. Jiang, Nanoparticles assembly-induced special wettability for bio-inspired materials, Particuology. 11 (2013) 361–370. doi:10.1016/j.partic.2013.02.001.

[110] X. Gao, X. Yan, X. Yao, L. Xu, K. Zhang, J. Zhang, B. Yang, L. Jiang, The dry-style antifogging properties of mosquito compound eyes and artificial analogues prepared by soft lithography, Adv. Mater. 19 (2007) 2213–2217. doi:10.1002/adma.200601946.

[111] J. Bowen, D. Cheneler, A.P.G. Robinson, Direct e-beam lithography of PDMS, Microelectron. Eng. 97 (2012) 34–37. doi:10.1016/j.mee.2012.02.049.

[112] B. Teshome, S. Facsko, A. Keller, Topography-controlled alignment of DNA origami nanotubes on nanopatterned surfaces, Nanoscale. 6 (2014) 1790–1796. doi:10.1039/C3NR04627C.

[113] J. Xu, Z. Guo, Biomimetic photonic materials with tunable structural colors, J. Colloid Interface Sci. 406 (2013) 1–17. doi:10.1016/j.jcis.2013.05.028.

[114] H. Hassanin, a. Mohammadkhani, K. Jiang, Fabrication of hybrid nanostructured arrays using a PDMS/PDMS replication process, Lab Chip. 12 (2012) 4160. doi:10.1039/c2lc40512a.

[115] W.-L. Min, B. Jiang, P. Jiang, Bioinspired Self-Cleaning Antireflection Coatings, Adv. Mater. 20 (2008) 3914–3918. doi:10.1002/adma.200800791.

[116] Y. Li, J. Zhang, S. Zhu, H. Dong, F. Jia, Z. Wang, Z. Sun, L. Zhang, Y. Li, H. Li, W. Xu, B. Yang, Biomimetic Surfaces for High-Performance Optics, Adv. Mater. 21 (2009). doi:10.1002/adma.200901335.

[117] J.-Y. Shiu, C.-W. Kuo, P. Chen, C.-Y. Mou, Fabrication of Tunable Superhydrophobic Surfaces by Nanosphere Lithography, Planta Adv. Mater. Angew. Chem., Int. Ed. Chem. Mater. Angew. Chem., Int. Ed. Sci. 79 (1997)

677–894. doi:10.1021/cm034696h.

[118] B. Gorowitz, R.J. Saia, Reactive Ion Etching, VLSI Electron. Microstruct. Sci. 8 (1984) 297–339. doi:10.1016/B978-0-12-234108-3.50015-7.

[119] W.N.G. Hitchon, Plasma Processes for Semiconductor Fabrication, Cambridge University Press (1999). doi:10.1017/CBO9780511529511.005.

[120] R. V Ulijn, Molecular self-assembly: Best of both worlds, Nat. Publ. Gr. 10 (2015). doi:10.1038/nnano.2015.59.

[121] J. 1. H. Ronald P. Andres,* Jeffery D. Bielefeld, C.P.K. David B. Janes, Venkat R. Kolagunta, R.G.O. William J. Mahoney, Self-Assembly of a Two-Dimensional Superlattice of Molecularly Linked Metal Clusters, Sci. 273 (1996) 1690–1693.

[122] Nanofabrication by self-assembly, Mater. Today. 12 (2009) 12–23. doi:10.1016/S1369-7021(09)70156-7.

[123] S. Zhang, Fabrication of novel biomaterials through molecular self-assembly, Nat. Biotechnol. 21 (2003) 1171–1178. doi:10.1038/nbt874.

[124] B.W. Ninham, P. Lo Nostro, Molecular forces and self assembly: in colloid, nano sciences and biology, Cambridge University Press, (2010).

[125] E. Koukharenko, Z. Moktadir, M. Kraft, M.E. Abdelsalam, D.M. Bagnall, C. Vale, M.P.A. Jones, E.A. Hinds, Microfabrication of gold wires for atom guides, Sensors Actuators, A Phys. 115 (2004) 600–607. doi:10.1016/j.sna.2004.03.069.

[126] T. a. Green, M.-J. Liew, S. Roy, Electrodeposition of Gold from a Thiosulfate-Sulfite Bath for Microelectronic Applications, J. Electrochem. Soc. 150 (2003) C104. doi:10.1149/1.1541006.

[127] P.A. Kohl, Electrodeposition of Gold, Mod. Electroplat. Fifth Ed. (2011) 115–130. doi:10.1002/9780470602638.ch4.

[128] I.B.S. Beaman, H. Park, E. Fuad, N. Y, L. James, United States Patent, (1996) 1–4.

[129] C. Mu, J.-P. Zhang, D. Xu, Au nanoparticle arrays with tunable particle gaps by template-assisted electroless deposition for high performance surface-enhanced Raman scattering., Nanotechnology. 21 (2010) 15604. doi:10.1088/0957-4484/21/1/015604.

[130] B.D. Barker, Electroless deposition of metals, Surf. Technol. 12 (1981) 77–88. doi:10.1016/0376-4583(81)90138-2.

[131] L.A. Porter, H.C. Choi, A.E. Ribbe, J.M. Buriak, Controlled Electroless Deposition of Noble Metal Nanoparticle Films on Germanium Surfaces, (2002).

[132] J.W. Haus, A. Sarangan, 5 – Nanofabrication, in: Fundam. Appl. Nanophotonics, (2016) 149–184. doi:10.1016/B978-1-78242-464-2.00005-1.

[133] H.O. Pierson, Handbook of chemical vapor deposition : principles, technology, and applications, Noyes Publications. (1999).

[134] A.C. Jones, M.L. Hitchman, Chemical vapour deposition : precursors, processes and applications, Royal Society of Chemistry. (2009).

[135] C.A. Bishop, Atomic Layer Deposition, Vac. Depos. onto Webs, Film. Foils. (2011) 331–336. doi:10.1016/B978-1-4377-7867-0.00019-2.

[136] P.G. Oppenheimer, Theoretical Background and Physical Principles of EHD Instabilities, Springer. (2013) 11–30. doi:10.1007/978-3-319-00783-0_2.

[137] A. Oron, S.H. Davis, S.G. Bankoff, Long-scale evolution of thin liquid films, Rev. Mod. Phys. 69 (1997) 931–980. doi:10.1103/RevModPhys.69.931.

[138] Lubrication Approximation, in: Incompressible Flow, John Wiley & Sons, Inc. (2013) 650–668. doi:10.1002/9781118713075.ch22.

[139] P.G. Oppenheimer, Electrohydrodynamic Lithography of Functional Soft

Materials for Advanced Applications, in: J. Rodríguez-Hernández, C. Drummond (Eds.), Polym. Surfaces Motion Unconv. Patterning Methods, Springer International Publishing, (2015) 163–182. doi:10.1007/978-3-319-17431-0_7.

[140] Micro and nano-fabrication of biodegradable polymers for drug delivery, Adv. Drug Deliv. Rev. 56 (2004) 1621–1633. doi:10.1016/J.ADDR.2004.05.002.

[141] T. Betancourt, L. Brannon-Peppas, Micro- and nanofabrication methods in nanotechnological medical and pharmaceutical devices., Int. J. Nanomedicine. 1 (2006) 483–95.

[142] Nanofabrication in polymer matrices, Prog. Polym. Sci. 28 (2003) 5–26. doi:10.1016/S0079-6700(02)00077-1.

[143] Y.C. Tseng, S.B. Darling, Block copolymer nanostructures for technology, Polymers (Basel). 2 (2010) 470–489. doi:10.3390/polym2040470.

[144] S. Salvatore, A. Demetriadou, S. Vignolini, S.S. Oh, S. Wuestner, N.A. Yufa, M. Stefik, U. Wiesner, J.J. Baumberg, O. Hess, U. Steiner, Tunable 3D extended self-assembled gold metamaterials with enhanced light transmission, Adv. Mater. 25 (2013) 2713–2716. doi:10.1002/adma.201300193.

[145] N. Hadjichristidis, S. Pispas, G. Floudas, Block Copolymer Applications, in: Block Copolym., John Wiley & Sons, Inc. (2003) 383–408. doi:10.1002/0471269808.ch21.

[146] S. Wang, Q. Yang, Y. Tao, Y. Guo, J. Yang, Y. Liu, L. Zhao, Z. Xie, W. Huang, Fully conjugated block copolymers for single-component solar cells: synthesis, purification, and characterization, New J. Chem. 40 (2016) 1825–1833. doi:10.1039/C5NJ02636A..

[147] M.C. Orilall, U. Wiesner, Block copolymer based composition and morphology control in nanostructured hybrid materials for energy conversion and storage:

solar cells, batteries, and fuel cells, Chem. Soc. Rev. 40 (2011) 520–535. doi:10.1039/C0CS00034E.

[148] S.-J. Jeong, J.Y. Kim, B.H. Kim, H.-S. Moon, S.O. Kim, Directed self-assembly of block copolymers for next generation nanolithography, Mater. Today. 16 (2013) 468–476. doi:http://dx.doi.org/10.1016/j.mattod.2013.11.002.

[149] L. Wan, R. Ruiz, H. Gao, K.C. Patel, T.R. Albrecht, J. Yin, J. Kim, Y. Cao, G. Lin, The Limits of Lamellae-Forming PS-b-PMMA Block Copolymers for Lithography, ACS Nano. 9 (2015) 7506–7514. doi:10.1021/acsnano.5b02613.

[150] Y. Sun, Y. Xia, Triangular Nanoplates of Silver: Synthesis, Characterization, and Use as Sacrificial Templates For Generating Triangular Nanorings of Gold, Adv. Mater. 15 (2003) 695–699. doi:10.1002/adma.200304652.

[151] K. Yu, T. Fan, S. Lou, D. Zhang, Progress in Materials Science Biomimetic optical materials : Integration of nature ' s design for manipulation of light, Prog. Mater. Sci. 58 (2013) 825–873. doi:10.1016/j.pmatsci.2013.03.003.

[152] B. Lindman, P. Alexandridis, Amphiphilic block copolymers : self-assembly and applications, Elsevier, (2000) 435.

[153] S. Ji, L. Wan, C.-C. Liu, P.F. Nealey, Directed self-assembly of block copolymers on chemical patterns: A platform for nanofabrication, Prog. Polym. Sci. 54 (2016) 76–127. doi:10.1016/j.progpolymsci.2015.10.006.

[154] H. Wang, L. Qi, Controlled Synthesis of Ag 2 S, Ag 2 Se, and Ag Nanofibers by Using a General Sacrificial Template and Their Application in Electronic Device Fabrication, Adv. Funct. Mater. 18 (2008) 1249–1256. doi:10.1002/adfm.200700953.

[155] A.M. Hung, C.M. Micheel, L.D. Bozano, L.W. Osterbur, G.M. Wallraff, J.N. Cha, Large-area spatially ordered arrays of gold nanoparticles directed by

lithographically confined DNA origami., Nat. Nanotechnol. 5 (2010) 121–126. doi:10.1038/nnano.2009.450.

[156] S.P. Surwade, F. Zhou, B. Wei, W. Sun, A. Powell, C. O'Donnell, P. Yin, H. Liu, Nanoscale growth and patterning of inorganic oxides using DNA nanostructure templates, J. Am. Chem. Soc. 135 (2013) 6778–6781. doi:10.1021/ja401785h.

[157] S.J. Tan, M.J. Campolongo, D. Luo, W. Cheng, Building plasmonic nanostructures with DNA., Nat. Nanotechnol. 6 (2011) 268–276. doi:10.1038/nnano.2011.49.

[158] H. Noh, A.M. Hung, C. Choi, J.H. Lee, J.-Y. Kim, S. Jin, J.N. Cha, 50 nm DNA Nanoarrays Generated from Uniform Oligonucleotide Films, ACS Nano. 3 (2009) 2376–2382. doi:10.1021/nn900559m.

[159] J.D. Brodin, E. Auyeung, C.A. Mirkin, DNA-mediated engineering of multicomponent enzyme crystals, Proc. Natl. Acad. Sci. 112 (2015) 4564–4569. doi:10.1073/pnas.1503533112.

[160] T. Song, S. Garg, R. Mokhtar, H. Bui, J. Reif, Analog Computation by DNA Strand Displacement Circuits, ACS Synth. Biol. 5 (2016) 898–912. doi:10.1021/acssynbio.6b00144.

[161] E. Boisselier, D. Astruc, Gold nanoparticles in nanomedicine: preparations, imaging, diagnostics, therapies and toxicity, Chem. Soc. Rev. 38 (2009) 1759. doi:10.1039/b806051g.

[162] C.R. Calladine, H. Drew, B. Luisi, A. Travers, Understanding DNA : the molecule and how it works, 3rd ed. Elsevier Academic Press, (2004).

[163] P.W.K. Rothemund, Folding DNA to create nanoscale shapes and patterns., Nature. 440 (2006) 297–302. doi:10.1038/nature04586.

[164] P.W.K. Rothemund, Design of DNA origami, IEEE/ACM Int. Conf. Comput. Des.

Dig. Tech. Pap. ICCAD. 2005 (2005) 470–477. doi:10.1109/ICCAD.2005.1560114.

[165] B. Saccà, C.M. Niemeyer, DNA origami: The art of folding DNA, Angew. Chemie - Int. Ed. 51 (2012) 58–66. doi:10.1002/anie.201105846.

[166] B. Yurke, A.J. Turberfield, A.P. Mills, F.C. Simmel, J.L. Neumann, A DNA-fuelled molecular machine made of DNA, Nature. 406 (2000) 605–608. doi:10.1038/35020524.

[167] N.C. Seeman, The construction of 3-D stick figures from branched DNA , DNA Cell Biol. 10 (1991) 475–486.

[168] A.N. Marchi, I. Saaem, B.N. Vogen, S. Brown, T.H. LaBean, Toward Larger DNA Origami TL - 14, Nano Lett. 14 (2014) 5740–5747. doi:10.1021/nl502626s.

[169] N.C. Seeman, DNA enables nanoscale control of the structure of matter., Q. Rev. Biophys. 38 (2005) 363–371. doi:10.1017/S0033583505004087.

[170] A. Katsnelson, DNA robot could kill cancer cells, Nature. (2012). doi:10.1038/nature.2012.10047.

[171] A.R. Chandrasekaran, O. Levchenko, DNA Nanocages, Chem. Mater. 28 (2016) 5569–5581. doi:10.1021/acs.chemmater.6b02546.

[172] S. Phongtongpasuk, S. Paulus, J. Schnabl, R.K.O. Sigel, B. Spingler, M.J. Hannon, E. Freisinger, Binding of a designed anti-cancer drug to the central cavity of an RNA three-way junction, Angew. Chemie - Int. Ed. 52 (2013) 11513–11516. doi:10.1002/anie.201305079.

[173] J. Liu, Y. Geng, E. Pound, S. Gyawali, J.R. Ashton, J. Hickey, A.T. Woolley, J.N. Harb, Metallization of branched DNA origami for nanoelectronic circuit fabrication, ACS Nano. 5 (2011) 2240–2247. doi:10.1021/nn1035075.

[174] M. Manning, G. Redmond, Formation and characterization of DNA microarrays

at silicon nitride substrates, Langmuir. 21 (2005) 395–402. doi:10.1021/la0480033.

[175] C. Mao, W. Sun, N.C. Seeman, Designed two-dimensional DNA Holliday junction arrays visualized by atomic force microscopy , J. Am. Chem. Soc. . 121 (1999) 5437–5443. http://dx.doi.org/10.1021/ja9900398.

[176] R.J. Kershner, L.D. Bozano, C.M. Micheel, A.M. Hung, A.R. Fornof, J.N. Cha, C.T. Rettner, M. Bersani, J. Frommer, P.W.K. Rothemund, G.M. Wallraff, Placement and orientation of individual DNA shapes on lithographically patterned surfaces., Nat. Nanotechnol. 4 (2009) 557–561. doi:10.1038/nnano.2009.220.

[177] G. Dai, X. Lu, Z. Chen, C. Meng, W. Ni, Q. Wang, DNA origami-directed, discrete three-dimensional plasmonic tetrahedron nanoarchitectures with tailored optical chirality, ACS Appl. Mater. Interfaces. 6 (2014) 5388–5392. doi:10.1021/am501599f.

[178] M.B. Scheible, G. Pardatscher, A. Kuzyk, F.C. Simmel, Single Molecule Characterization of DNA Binding and Strand Displacement Reactions on Lithographic DNA Origami Microarrays, Nano Lett. 14 (2014) 1627–1633. doi:DOI 10.1021/nl500092j.

[179] V. Linko, B. Shen, K. Tapio, J.J. Toppari, M.A. Kostiainen, S. Tuukkanen, One-step large-scale deposition of salt-free DNA origami nanostructures, Sci. Rep. 5 (2015) 15634. doi:10.1038/srep15634.

[180] B. Shen, V. Linko, K. Tapio, M.A. Kostiainen, J.J. Toppari, Custom-shaped metal nanostructures based on DNA origami silhouettes, Nanoscale. (2015) 1–5. doi:10.1039.

[181] D. Han, S. Pal, J. Nangreave, Z. Deng, Y. Liu, H. Yan, DNA Origami with

Complex Curvatures in Three-Dimensional Space, Science. 332 (2011) 342–346. doi:10.1126/science.1202998.

[182] N. Li, A. Tittl, S. Yue, H. Giessen, C. Song, B. Ding, N. Liu, DNA-assembled bimetallic plasmonic nanosensors, Light Sci. Appl. 3 (2014) 226. doi:10.1038/lsa.2014.107.

[183] Introduction to Molecular Genetics, in: Essentials Med. Genomics, John Wiley & Sons, Inc., (n.d.) 1–30. doi:10.1002/9780470336168.ch1.

[184] N.C. Seeman, Single-stranded DNA topology and motif design, Struct. DNA Nanotechnol., Cambridge University Press, (n.d) 44–63. doi:10.1017/CBO9781139015516.005.

[185] J. SantaLucia, A unified view of polymer, dumbbell, and oligonucleotide DNA nearest-neighbor thermodynamics., Proc. Natl. Acad. Sci. U. S. A. 95 (1998) 1460–5. doi:10.1073/pnas.95.4.1460.

[186] T. Tørring, N. V. Voigt, J. Nangreave, H. Yan, K. V. Gothelf, Advances in DNA-based nanotechnology themed issue Guest editors Eugen Stulz , Guido Clever , Mitsuhiko Shionoya and, Chem. Soc. Rev. 40 (2011) 5621–5928.

[187] Y. Lvov, G. Decher, G. Sukhorukov, Assembly of Thin Films by Means of Successive Deposition ofAlternate Layers of DNA and Poly(allylamine), Macromolecules. 26 (1993) 5396–5399. doi:10.1021/ma00072a016.

[188] Y. Yang, D. Han, J. Nangreave, Y. Liu, H. Yan, DNA Origami with Double-Stranded DNA As a Unified Scaffold, (2012) 8209–8215.

[189] N.C. et al. Seeman, Synthesis from DNA of a molecule with the connectivity of a cube, Nature. 354 (1991) 56–58.

[190] H. Kim, S. Surwade, A. Powell, C. O'Donnell, H. Liu, Stability of DNA Origami Nanostructure under Diverse Chemical Environments, Chem. Mater. (2014).

doi:10.1021/cm5019663.

[191] E. Pibiri, P. Holzmeister, B. Lalkens, G.P. Acuna, P. Tinnefeld, Single-molecule positioning in zeromode waveguides by DNA origami nanoadapters, Nano Lett. 14 (2014) 3499–3503. doi:10.1021/nl501064b.

[192] A.E. Gerdon, S.S. Oh, K. Hsieh, Y. Ke, H. Yan, H.T. Soh, Controlled delivery of DNA origami on patterned surfaces, Small. 5 (2009) 1942–1946. doi:10.1002/smll.200900442.

[193] C.M. Erben, R.P. Goodman, A.J. Turberfield, Single-molecule protein encapsulation in a rigid DNA cage, Angew. Chemie - Int. Ed. 45 (2006) 7414–7417. doi:10.1002/anie.200603392.

[194] K.M.M. Carneiro, F.A. Aldaye, H.F. Sleiman, 7. K. Carneiro, H. F. Sleiman, Long-Range Assembly of DNA into Rigid Nanofibers and Highly Ordered Networks Using a Block Copolymer Approach, Nat. Mater. 327 (2010) 4570–4570.

[195] R.P. Goodman, I. a T. Schaap, C.F. Tardin, C.M. Erben, R.M. Berry, C.F. Schmidt, a J. Turberfield, Rapid chiral assembly of rigid DNA building blocks for molecular nanofabrication., Science. 310 (2005) 1661–1665. doi:10.1126/science.1120367.

[196] Y. He, M. Su, P. Fang, C. Zhang, A.E. Ribbe, W. Jiang, C. Mao, On the Chirality of Self-Assembled DNA Octahedra, Angew. Chemie. 122 (2010) 760–763. doi:10.1002/ange.200904513.

[197] Y. He, T. Ye, M. Su, C. Zhang, A.E. Ribbe, W. Jiang, C. Mao, Hierarchical self-assembly of DNA into symmetric supramolecular polyhedra., Nature. 452 (2008) 198–201. doi:10.1038/nature06597.

[198] R.H. Davis, The microbial models of molecular biology : from genes to genomes,

Oxford University Press (2003).

[199] A. Kumar, K.C. Upadhyaya, Chapter 31 – Perspectives on the Human Genome, in: Anim. Biotechnol. (2014) 577–595. doi:10.1016/B978-0-12-416002-6.00031-6.

[200] R.P. Goodman, I. a T. Schaap, C.F. Tardin, C.M. Erben, R.M. Berry, C.F. Schmidt, a J. Turberfield, Rapid chiral assembly of rigid DNA building blocks for molecular nanofabrication., Science. 310 (2005) 1661–1665. doi:10.1126/science.1120367.

[201] R.P. Goodman, NANEV: A program employing evolutionary methods for the design of nucleic acid nanostructures, Biotechniques. 38 (2005) 548–550. doi:10.2144/05384BM06.

[202] C. Zhang, S.H. Ko, M. Su, Y. Leng, A.E. Ribbe, W. Jiang, C. Mao, Symmetry controls the face geometry of DNA polyhedra, J. Am. Chem. Soc. 131 (2009) 1413–1415. doi:10.1021/ja809666h.

[203] C. Zhang, M. Su, Y. He, Y. Leng, A.E. Ribbe, G. Wang, W. Jiang, C. Mao, Exterior modification of a DNA tetrahedron., Chem. Commun. (Camb). 46 (2010) 6792–6794. doi:10.1039/c0cc02363a.

[204] D. Pastré, O. Piétrement, S. Fusil, F. Landousy, J. Jeusset, M.-O. David, L. Hamon, E. Le Cam, A. Zozime, Adsorption of DNA to mica mediated by divalent counterions: a theoretical and experimental study., Biophys. J. 85 (2003) 2507–18. doi:10.1016/S0006-3495(03)74673-6.

[205] Y. Hayashi, Pot economy and one-pot synthesis, Chem. Sci. 0 (2016) 1–15. doi:10.1039/c5sc02913a.

[206] Z. Zhao, Y. Liu, H. Yan, Organizing DNA origami tiles into larger structures using preformed scaffold frames, Nano Lett. 11 (2011) 2997–3002.

doi:10.1021/nl201603a.

[207] D. Han, S. Pal, J. Nangreave, Z. Deng, Y. Liu, H. Yan, DNA Origami with Complex Curvatures in Three-Dimensional Space, Science. 332 (2011).

[208] S. Woo, P.W.K. Rothemund, Programmable molecular recognition based on the geometry of DNA nanostructures., Nat. Chem. 3 (2011) 620–627. doi:10.1038/nchem.1070.

[209] D.R. Smith, S. Schultz, P. Markoš, C.M. Soukoulis, Determination of effective permittivity and permeability of metamaterials from reflection and transmission coefficients, Phys. Rev. B. 65 (2002) 195104. doi:10.1103/PhysRevB.65.195104.

[210] G.B. Sukhorukov, H. Möhwald, G. Decher, Y.M. Lvov, Assembly of polyelectrolyte multilayer films by consecutively alternating adsorption of polynucleotides and polycations, Thin Solid Films. 284–285 (1996) 220–223. doi:10.1016/S0040-6090(95)08309-X.

[211] G. Decher, B. Lehr, K. Lowack, Y. Lvov, J. Schmitt, New nanocomposite films for biosensors: layer-by-layer adsorbed films of polyelectrolytes, proteins or DNA, Biosens. Bioelectron. 9 (1994) 677–684. doi:10.1016/0956-5663(94)80065-0.

[212] L.-P. Lu, S.-Q. Wang, X.-Q. Lin, Fabrication of layer-by-layer deposited multilayer films containing DNA and gold nanoparticle for norepinephrine biosensor, Anal. Chim. Acta. 519 (2004) 161–166. doi:10.1016/j.aca.2004.05.062.

[213] R. Pei, X. Cui, X. Yang, E. Wang, Assembly of alternating polycation and DNA multilayer films by electrostatic layer-by-layer adsorption, Biomacromolecules. 2 (2001) 463–468. doi:10.1021/bm0001289.

[214] G.B. Sukhorukov, H. Möhwald, G. Decher, Y.M. Lvov, Assembly of polyelectrolyte multilayer films by consecutively alternating adsorption of polynucleotides and polycations, Thin Solid Films. 284–285 (1996) 220–223. doi:10.1016/S0040-6090(95)08309-X.

[215] C.S. Peyratout, L. Dähne, Tailor-Made Polyelectrolyte Microcapsules: From Multilayers to Smart Containers, Angew. Chemie Int. Ed. 43 (2004) 3762–3783. doi:10.1002/anie.200300568.

[216] Renjun Pei, Xiaoqiang Cui, * and Xiurong Yang, † Erkang Wang*, Assembly of Alternating Polycation and DNA Multilayer Films by Electrostatic Layer-by-Layer Adsorption, (2001). doi:10.1021/BM0001289.

[217] C. Cortez, E. Tomaskovic-Crook, A.P.R. Johnston, B. Radt, S.H. Cody, A.M. Scott, E.C. Nice, J.K. Heath, F. Caruso, Targeting and Uptake of Multilayered Particles to Colorectal Cancer Cells, Adv. Mater. 18 (2006) 1998–2003. doi:10.1002/adma.200600564.

[218] B. Liu, J. Liu, DNA Adsorption by Indium Tin Oxide Nanoparticles, (2015). doi:10.1021/la503917j.

[219] T.G. Drummond, M.G. Hill, J.K. Barton, Electrochemical DNA sensors, Nat Biotech. 21 (2003) 1192–1199. http://dx.doi.org/10.1038/nbt873.

[220] J. Xu, J.-J. Zhu, Q. Huang, H.-Y. Chen, A novel DNA-modified indium tin oxide electrode, Electrochem. Commun. 3 (2001) 665–669. doi:10.1016/S1388-2481(01)00245-4.

[221] B. Gao, K. Sarveswaran, G.H. Bernstein, M. Lieberman, Guided deposition of individual DNA nanostructures on silicon substrates, Langmuir. 26 (2010) 12680–12683. doi:10.1021/la101343k.

[222] W. Kern, J.E. Soc, The Evolution of Silicon Wafer Cleaning Technology, J.

Electrochem. Soc. 137 (1990) 1887–1892. doi:10.1149/1.2086825.

[223] R. Sherman, Carbon Dioxide Snow Cleaning, in: Dev. Surf. Contam. Clean., Elsevier. (2016) 695–716. doi:10.1016/B978-0-323-29960-2.00016-2.

[224] N. Wang, J.D. Zimmerman, X. Tong, X. Xiao, J. Yu, S.R. Forrest, Snow cleaning of substrates increases yield of large-area organic photovoltaics, Appl. Phys. Lett. 101 (2012). doi:10.1063/1.4754690.

[225] D. Gupta, M. Katiyar, Deepak, T. Hazra, A. Verma, S.S. Manoharan, A. Biswas, Energy transfer and morphology study of a new iridium based cyclometalated phosphorescent complex, Opt. Mater. (Amst). 28 (2006) 1355–1361. doi:10.1016/j.optmat.2005.08.007.

[226] G. Wypych, G. Wypych, Handbook of Polymers, ChemTec Pub. (2012).

[227] D. Tordera, J.J. Serrano-Pérez, A. Pertegás, E. Ortí, H.J. Bolink, E. Baranoff, M.K. Nazeeruddin, J. Frey, Correlating the lifetime and fluorine content of iridium(III) emitters in green light-emitting electrochemical cells, Chem. Mater. 25 (2013) 3391–3397. doi:10.1021/cm402473j.

[228] F. Monti, F. Kessler, M. Delgado, J. Frey, F. Bazzanini, G. Accorsi, N. Armaroli, H.J. Bolink, E. Ortí, R. Scopelliti, M.K. Nazeeruddin, E. Baranoff, Charged bis-cyclometalated iridium(III) complexes with carbene-based ancillary ligands, Inorg. Chem. 52 (2013) 10292–10305. doi:10.1021/ic400600d.

[229] K.-H. Cho, L.-J. Chen, Fabrication of sticky and slippery superhydrophobic surfaces via spin-coating silica nanoparticles onto flat/patterned substrates, Nanotechnology. 22 (2011) 445706. doi:10.1088/0957-4484/22/44/445706.

[230] D.W. Hess, K.A. Reinhard, 6 – Plasma Stripping, Cleaning, and Surface Conditioning, in: Handb. Silicon Wafer Clean. Technol. (2008) 355–427. doi:10.1016/B978-081551554-8.50009-4.

[231] J.L. Keddie, R. a L. Jones, R. a Cory, Temperature in Thin Polymer Films, Faraday Discuss. 98 (1994) 219–230.

[232] P. Goldberg-Oppenheimer, T. Hutter, B. Chen, J. Robertson, S. Hofmann, S. Mahajan, Optimized Vertical Carbon Nanotube Forests for Multiplex Surface-Enhanced Raman Scattering Detection, J. Phys. Chem. Lett. 3 (2012) 3486–3492. doi:10.1021/jz301333r.

[233] P. Goldberg-Oppenheimer, U. Steiner, Rapid electrohydrodynamic lithography using low-viscosity polymers., Small. 6 (2010) 1248–54. doi:10.1002/smll.201000060.

[234] I. Severcan, C. Geary, A. Chworos, N. Voss, E. Jacovetty, L. Jaeger, A polyhedron made of tRNAs., Nat. Chem. 2 (2010) 772–779. doi:10.1038/nchem.733.

[235] B. Wei, M. Dai, P. Yin, Complex shapes self-assembled from single-stranded DNA tiles, Nature. 485 (2012) 623–626. doi:10.1038/nature11075.

[236] C. Zhang, Y. He, M. Su, S.H. Ko, T. Ye, Y. Leng, X. Sun, A.E. Ribbe, W. Jiang, C. Mao, DNA self-assembly: from 2D to 3D, Faraday Discuss. 143 (2009) 221. doi:10.1039/b905313c.

[237] C. Rivetti, M. Guthold, C. Bustamante, Scanning force microscopy of DNA deposited onto mica: equilibration versus kinetic trapping studied by statistical polymer chain analysis., J. Mol. Biol. 264 (1996) 919–932. doi:10.1006/jmbi.1996.0687.

[238] Z. Xiao, M. Xu, T. Ohgi, K. Sagisaka, D. Fujita, Controlled assembly of DNA nanostructures on silanized silicon and mica surfaces for future molecular devices, Superlattices Microstruct. 32 (2002) 215–220. doi:10.1016/S0749-6036(03)00021-1.

[239] R.M. Pasternack, S.R. Amy, Y.J. Chaba, Attachment of 3- Aminopropyl triethoxysilane on Silicon Oxide Surfaces: Dependence on Solution Temperature, Langmuir. 24 (2008) 12963–12971.

[240] P.N. Bartlett, J.J. Baumberg, S. Coyle, M.E. Abdelsalam, Optical properties of nanostructured metal films., Faraday Discuss. 125 (2004) 117-32-219. doi:10.1039/b304116f.

[241] S. Vignolini, N.A. Yufa, P.S. Cunha, S. Guldin, I. Rushkin, M. Stefik, K. Hur, U. Wiesner, J.J. Baumberg, U. Steiner, A 3D Optical Metamaterial Made by Self-Assembly, Adv. Mater. 24 (2012) OP23-OP27. doi:10.1002/adma.201103610.

[242] M.S. Chandrasekar, M. Pushpavanam, Pulse and pulse reverse plating-Conceptual, advantages and applications, Electrochim. Acta. 53 (2008) 3313–3322. doi:10.1016/j.electacta.2007.11.054.

[243] J. Horkans, L.T. Romankiw, Pulsed Potentiostatic Deposition of Gold from Solutions of the Au(I) Sulfite Complex, J. Electrochem. Soc. 124 (1977) 1499–1505. doi:10.1149/1.2133100.

[244] O. Yevtushenko, H. Natter, R. Hempelmann, Grain-growth kinetics of nanostructured gold, Thin Solid Films. 515 (2006) 353–356. doi:10.1016/j.tsf.2005.12.098.

[245] E. Deposition, O.F. Gold, Electroless deposition of gold, US Pat. 4154877. (2010) 483–498. doi:10.1002/9780470602638.ch21.

[246] Z. Zhao, E.L. Jacovetty, Y. Liu, H. Yan, Encapsulation of gold nanoparticles in a DNA origami cage, Angew. Chemie - Int. Ed. 50 (2011) 2041–2044. doi:10.1002/anie.201006818.

[247] M. Merano, A. Aiello, M.P. van Exter, J.P. Woerdman, Observing angular deviations in the specular reflection of a light beam, Nat. Photonics. 3 (2009)

337–340. doi:10.1038/nphoton.2009.75.

[248] D. Tasis, N. Tagmatarchis, A. Bianco, M. Prato, Chemistry of Carbon Nanotubes, Chem. Rev. 106 (2006) 1105–1136. doi:10.1021/cr050569o.

[249] S. Kumar, T.D. Dang, F.E. Arnold, A.R. Bhattacharyya, B.G. Min, X. Zhang, R.A. Vaia, C. Park, W.W. Adams, R.H. Hauge, R.E. Smalley, S. Ramesh, P.A. Willis, Synthesis, Structure, and Properties of PBO/SWNT Composites &, Macromolecules. 35 (2002) 9039–9043. doi:10.1021/ma0205055.

[250] R.H. Baughman, A.A. Zakhidov, W.A. de Heer, Carbon Nanotubes--the Route Toward Applications, Science. 297 (2002) 787.

[251] P. Goldberg-Oppenheimer, D. Kabra, S. Vignolini, S. Hüttner, M. Sommer, K. Neumann, M. Thelakkat, U. Steiner, Hierarchical Orientation of Crystallinity by Block-Copolymer Patterning and Alignment in an Electric Field, Chem. Mater. 25 (2013) 1063–1070. doi:10.1021/cm3038075.

[252] J.J.S. Rickard, I. Farrer, P. Goldberg Oppenheimer, Tunable Nanopatterning of Conductive Polymers via Electrohydrodynamic Lithography, ACS Nano. 10 (2016) 3865–3870. doi:10.1021/acsnano.6b01246.

[253] S.I. Rapoport, Osmotic Opening of the Blood--Brain Barrier: Principles, Mechanism, and Therapeutic Applications, Cell. Mol. Neurobiol. 20 (2000) 217–230. doi:10.1023/A:1007049806660.

[254] C. Maurel, Aquaporins and Water Permeability of Plant Membranes, Annu. Rev. Plant Physiol. Plant Mol. Biol. 48 (1997) 399–429. doi:10.1146/annurev.arplant.48.1.399.

[255] Z. Guo, W. Liu, B.-L. Su, Superhydrophobic surfaces: From natural to biomimetic to functional, J. Colloid Interface Sci. 353 (2011) 335–355. doi:10.1016/j.jcis.2010.08.047.

[256] Z. Han, J. Fu, Z. Wang, Y. Wang, B. Li, Z. Mu, J. Zhang, S. Niu, Long-term durability of superhydrophobic properties of butterfly wing scales after continuous contact with water, Colloids Surfaces A Physicochem. Eng. Asp. 518 (2017) 139–144. doi:10.1016/j.colsurfa.2017.01.030.

[257] K.-Y. Law, Definitions for Hydrophilicity, Hydrophobicity, and Superhydrophobicity: Getting the Basics Right, J. Phys. Chem. Lett. 5 (2014) 686–688. doi:10.1021/jz402762h.

[258] C.R. Crick, I.P. Parkin, Water droplet bouncing-a definition for superhydrophobic surfaces, Chem. Commun. 47 (2011) 12059–12061. doi:10.1039/C1CC14749H.

[259] B.S. Wang, L. Jiang, Definition of Superhydrophobic States, (2007) 3423–3424. doi:10.1002/adma.200700934.

[260] R.J. Vrancken, H. Kusumaatmaja, K. Hermans, A.M. Prenen, O. Pierre-Louis, C.W.M. Bastiaansen, D.J. Broer, Fully reversible transition from wenzel to cassie-baxter states on corrugated superhydrophobic surfaces, Langmuir. 26 (2010) 3335–3341. doi:10.1021/la903091s.

[261] B. Wang, Y. Zhang, L. Shi, J. Li, Z. Guo, Advances in the theory of superhydrophobic surfaces, J. Mater. Chem. 22 (2012) 20112. doi:10.1039/c2jm32780e.

[262] B. Bhushan, M. Nosonovsky, The rose petal effect and the modes of superhydrophobicity., Philos. Trans. A. Math. Phys. Eng. Sci. 368 (2010) 4713–4728. doi:10.1098/rsta.2010.0203.

[263] M. Callies, D. Quere, On water repellency, Soft Matter. 1 (2005) 55–61. doi:10.1039/B501657F.

[264] E.Y. Bormashenko, Wetting of Real Surfaces, DeGruyter, (2013).

doi:10.1515/9783110258790.

[265] K.L. Johnson, K. Kendall, A.D. Roberts, Surface Energy and the Contact of Elastic Solids, Proc. R. Soc. London. A. Math. Phys. Sci. 324 (1971) 301 LP-313.

[266] E.N. Hartmann, R. White, A. Leh, A. Baksi, R. Tadmor, Fundamental Understanding of Drops Wettability Behavior Theoretically and Experimentally, (2017) 87–96. doi:10.1002/9781118795620.ch5.

[267] D. Bonn, J. Eggers, J. Indekeu, J. Meunier, Wetting and spreading, Rev. Mod. Phys. 81 (2009) 739–805. doi:10.1103/RevModPhys.81.739.

[268] G. Bracco, B. Holst, Surface science techniques, Springer. (2013).

[269] D. Quéré, Wetting and Roughness, Annu. Rev. Mater. Res. 38 (2008) 71–99. doi:doi:10.1146/annurev.matsci.38.060407.132434.

[270] L. Feng, Y. Zhang, J. Xi, Y. Zhu, N. Wang, F. Xia, L. Jiang, Petal Effect: A Superhydrophobic State with High Adhesive Force, Langmuir. 24 (2008) 4114–4119. doi:10.1021/la703821h.

[271] L. Gao, T.J. McCarthy, "Artificial Lotus Leaf" Prepared Using a 1945 Patent and a Commercial Textile, Langmuir. 22 (2006) 5998–6000. doi:10.1021/la061237x.

[272] L. Jiang, Y. Zhao, J. Zhai, A lotus-leaf-like superhydrophobic surface: A porous microsphere/nanofiber composite film prepared by electrohydrodynamics, Angew. Chemie - Int. Ed. 43 (2004) 4338–4341. doi:10.1002/anie.200460333.

[273] P. Roach, N.J. Shirtcliffe, M.I. Newton, Progess in superhydrophobic surface development, Soft Matter. 4 (2008) 224–240. doi:10.1039/B712575P.

[274] S. Sethi, L. Ge, L. Ci, P.M. Ajayan, A. Dhinojwala, Gecko-Inspired Carbon Nanotube-Based Self-Cleaning Adhesives, (2007) 6–9.

[275] C.L. Pint, Y.-Q. Xu, S. Moghazy, T. Cherukuri, N.T. Alvarez, E.H. Haroz, S.

Mahzooni, S.K. Doorn, J. Kono, M. Pasquali, R.H. Hauge, Dry Contact Transfer Printing of Aligned Carbon Nanotube Patterns and, ACS Nano. 4 (2010) 1131–1145.

[276] J. Ou, W. Hu, C. Li, Y. Wang, M. Xue, F. Wang, W. Li, Tunable Water Adhesion on Titanium Oxide Surfaces with Different Surface Structures, (2012).

[277] A. Giacomello, S. Meloni, M. Chinappi, C.M. Casciola, D. Fisica, R. La, P.A. Moro, Cassie − Baxter and Wenzel States on a Nanostructured Surface: Phase Diagram, Metastabilities, and Transition Mechanism by Atomistic Free Energy Calculations, (2012).

[278] R.N. Wenzel, Resistance of Solid Surfaces, Ind. Eng. Chem. 28 (1936) 988–994. doi:10.1021/ie50320a024.

[279] C. Dorrer, J. Rühe, Drops on Microstructured Surfaces Coated with Hydrophilic Polymers: Wenzel's Model and Beyond, Langmuir. 24 (2008) 1959–1964. doi:10.1021/la7029938.

[280] Z. Cheng, M. Du, H. Lai, N. Zhang, K. Sun, From petal effect to lotus effect: a facile solution immersion process for the fabrication of super-hydrophobic surfaces with controlled adhesion., Nanoscale. 5 (2013) 2776–83. doi:10.1039/c3nr34256e.

[281] R.A. Singh, E.S. Yoon, H.J. Kim, J. Kim, H.E. Jeong, K.Y. Suh, Replication of surfaces of natural leaves for enhanced micro-scale tribological property, Mater. Sci. Eng. C. 27 (2007) 875–879. doi:10.1016/j.msec.2006.10.007.

[282] A.J. Schulte, D.M. Droste, K. Koch, W. Barthlott, Hierarchically structured superhydrophobic flowers with low hysteresis of the wild pansy (Viola tricolor) - new design principles for biomimetic materials, Beilstein J. Nanotechnol. 2 (2011) 228–236. doi:10.3762/bjnano.2.27.

[283] A.M. Peters, C. Pirat, M. Sbragaglia, B.M. Borkent, M. Wessling, D. Lohse, R.G.H. Lammertink, Cassie-Baxter to Wenzel state wetting transition: Scaling of the front velocity, Eur. Phys. J. E. 29 (2009) 391–397. doi:10.1140/epje/i2009-10489-3.

[284] E. Bormashenko, Wetting of Flat and Rough Curved Surfaces, J. Phys. Chem. C. 113 (2009) 17275–17277. doi:10.1021/jp905237v..

[285] A.B.D. Cassie, S. Baxter, Wettability of porous surfaces, Trans. Faraday Soc. 40 (1944) 546–551. doi:10.1039/TF9444000546.

[286] W. Wu, X. Wang, D. Wang, M. Chen, F. Zhou, W. Liu, Q. Xue, Alumina nanowire forests via unconventional anodization and super-repellency plus low adhesion to diverse liquids, Chem. Commun. (2009) 1043–1045. doi:10.1039/B818633B.

[287] R. Fallica, R. Kirchner, H. Schift, Y. Ekinci, High-resolution grayscale patterning using extreme ultraviolet interference lithography, Microelectron. Eng. 177 (2017) 1–5. doi:10.1016/j.mee.2017.01.007.

[288] C. Busà, J.J.S. Rickard, E. Chun, Y. Chong, V. Navaratnam, P. Goldberg Oppenheimer, Tunable superapolar Lotus-to-Rose hierarchical nanosurfaces via vertical carbon nanotubes driven electrohydrodynamic lithography, Nanoscale. 9 (2017) 1625–1636. doi:10.1039/C6NR08706J.

[289] X. Dai, B.B. Stogin, S. Yang, T.-S. Wong, Slippery Wenzel State, ACS Nano. 9 (2015) 9260–9267. doi:10.1021/acsnano.5b04151.

[290] G. Wolansky, A. Marmur, Apparent contact angles on rough surfaces: the Wenzel equation revisited, Colloids Surfaces A Physicochem. Eng. Asp. 156 (1999) 381–388. doi:10.1016/S0927-7757(99)00098-9.

[291] R.J. Crawford, E.P. Ivanova, R.J. Crawford, E.P. Ivanova, Chapter One – Superhydrophobicity – An Introductory Review, in: Superhydrophobic Surfaces,

2015: pp. 1–6. doi:10.1016/B978-0-12-801109-6.00001-X.

[292] J. Bico, U. Thiele, D. Quéré, Wetting of textured surfaces, Colloids Surfaces A Physicochem. Eng. Asp. 206 (2002) 41–46. doi:10.1016/S0927-7757(02)00061-4.

[293] C. Ishino, K. Okumura, D. Quéré, Wetting transitions on rough surfaces, Europhys. Lett. 68 (2004) 419–425. doi:10.1209/epl/i2004-10206-6.

[294] T. Koishi, K. Yasuoka, S. Fujikawa, T. Ebisuzaki, X.C. Zeng, Coexistence and transition between Cassie and Wenzel state on pillared hydrophobic surface, Proc. Natl. Acad. Sci. U. S. A. 106 (2009) 8435–40. doi:10.1073/pnas.0902027106.

[295] J.B. Lee, H.R. Gwon, S.H. Lee, M. Cho, Wetting Transition Characteristics on Microstructured Hydrophobic Surfaces, Mater. Trans. 51 (2010) 1709–1711. doi:10.2320/matertrans.M2010118.

[296] N. Wang, Y. Yuan, Y. Wu, T. Hang, M. Li, Wetting transition of the caterpillar-like superhydrophobic Cu/Ni-Co hierarchical structure by heat treatment., Langmuir. 31 (2015) 10807–12. doi:10.1021/acs.langmuir.5b02535.

[297] L. Feng, S. Li, Y. Li, H. Li, L. Zhang, J. Zhai, Y. Song, B. Liu, L. Jiang, D. Zhu, Super-Hydrophobic Surfaces: From Natural to Artificial, Adv. Mater. 14 (2002) 1857–1860. doi:10.1002/adma.200290020.

[298] C.N. W. Barthlott, Purity of the sacred lotus, or escape from contamination in biological surfaces, Planta. 202 (1997) 1–8.

[299] C. Neinhuis, Characterization and Distribution of Water-repellent, Self-cleaning Plant Surfaces, Ann. Bot. 79 (1997) 667–677. doi:10.1006/anbo.1997.0400.

[300] S. Iijima, Helical microtubules of graphitic carbon, Nature. 354 (1991) 56–58. http://dx.doi.org/10.1038/354056a0.

[301] V. Choudhary, A. Gupta, Polymer/Carbon Nanotube Nanocomposites, in: Carbon Nanotub. - Polym. Nanocomposites, InTech, (2011). doi:10.5772/18423.

[302] T. Sun, G. Wang, H. Liu, L. Feng, L. Jiang, D. Zhu, Control over the Wettability of an Aligned Carbon Nanotube Film, J. AM. CHEM. SOC. 125 (2003) 14996–14997. doi:10.1021/ja038026o.

[303] D. Öner, T.J. McCarthy, Ultrahydrophobic Surfaces. Effects of Topography Length Scales on Wettability, Langmuir. 16 (2000) 7777–7782. doi:10.1021/la000598o.

[304] N.M.B. Perney, J.J. Baumberg, M.E. Zoorob, M.D.B. Charlton, S. Mahnkopf, C.M. Netti, Tuning localized plasmons in nanostructured substrates for surface-enhanced Raman scattering, Opt. Express. 14 (2006) 847–857. doi:10.1364/OPEX.14.000847.

[305] T.N. Krupenkin, J.A. Taylor, T.M. Schneider, S. Yang, From Rolling Ball to Complete Wetting: The Dynamic Tuning of Liquids on Nanostructured Surfaces, Langmuir. 20 (2004) 3824–3827. doi:10.1021/la036093q.

[306] L. Schneider, M. Laustsen, N. Mandsberg, R. Taboryski, The Influence of Structure Heights and Opening Angles of Micro- and Nanocones on the Macroscopic Surface Wetting Properties, Sci. Rep. 6 (2016) 21400. doi:10.1038/srep21400.

[307] S. Tian, L. Li, W. Sun, X. Xia, D. Han, J. Li, C. Gu, Robust adhesion of flower-like few-layer graphene nanoclusters, Sci. Rep. 2 (2012) 511. doi:10.1038/srep00511.

[308] W. Cai, U.K. Chettiar, A. V. Kildishev, V.M. Shalaev, Optical cloaking with metamaterials, Nat. Photonics. 1 (2007) 224–227.

doi:10.1038/nphoton.2007.28.

[309] J. Valentine, J. Li, T. Zentgraf, G. Bartal, X. Zhang, An optical cloak made of dielectrics, Nat. Mater. 8 (2009) 568–571. doi:10.1038/nmat2461.

[310] N. Landy, J. Hunt, D.R. Smith, Homogenization analysis of complementary waveguide metamaterials, Photonics Nanostructures - Fundam. Appl. 11 (2013) 453–467. doi:10.1016/j.photonics.2013.07.004.

[311] M. Ghasemi, P.K. Choudhury, Nanostructured concentric gold ring resonator-based metasurface filter device, Opt. - Int. J. Light Electron Opt. 127 (2016) 9932–9936. doi:10.1016/j.ijleo.2016.07.048.

[312] H. Butt, Q. Dai, N.N. Lal, T.D. Wilkinson, J.J. Baumberg, G.A.J. Amaratunga, Metamaterial filter for the near-visible spectrum, (2012). doi:10.1063/1.4747323.

[313] X. Zhang, W. Adams, M. Sadatgol, D.Ö. Güney, Enhancing the resolution of hyperlens by the compensation of losses without gain media, (2016). http://arxiv.org/abs/1607.07466 (accessed April 19, 2017).

[314] F. Ballout, E. Bründermann, D.A. Schmidt, M. Havenith, Design of a plasmonic near-field tip for super-resolution IR-imaging, (2016). http://arxiv.org/abs/1605.04169 (accessed April 19, 2017).

[315] S. Foteinopoulou, Photonic crystals as metamaterials, Phys. B Condens. Matter. 407 (2012) 4056–4061. doi:10.1016/j.physb.2012.01.092.

[316] C. Zhang, M. Su, Y. He, X. Zhao, P. Fang, A.E. Ribbe, W. Jiang, C. Mao, Conformational flexibility facilitates self-assembly of complex DNA nanostructures., Proc. Natl. Acad. Sci. U. S. A. 105 (2008) 10665–10669. doi:10.1073/pnas.0803841105.

[317] A.T. Winzer, C. Kraft, S. Bhushan, V. Stepanenko, I. Tessmer, Correcting for AFM tip induced topography convolutions in protein-DNA samples,

Ultramicroscopy. 121 (2012) 8–15. doi:10.1016/j.ultramic.2012.07.002.

[318] P. Markiewicz, M.C. Goh, Atomic force microscopy probe tip visualization and improvement of images using a simple deconvolution procedure, Langmuir. 10 (1994) 5–7. doi:10.1021/la00013a002.

[319] K. a. Ramirez-Aguilar, K.L. Rowlen, Tip Characterization from AFM Images of Nanometric Spherical Particles, Langmuir. 14 (1998) 2562–2566. doi:10.1021/la971277o.

[320] P. Ares, M.E. Fuentes-Perez, E. Herrero-Galan, J.M. Valpuesta, A. Gil, J. Gomez-Herrero, F. Moreno-Herrero, High resolution atomic force microscopy of double-stranded RNA, Nanoscale. 8 (2016) 11818–11826. doi:10.1039/c5nr07445b.

[321] D. Tranchida, S. Piccarolo, R. a C. Deblieck, Some experimental issues of AFM tip blind estimation: the effect of noise and resolution, Meas. Sci. Technol. 17 (2006) 2630–2636. doi:10.1088/0957-0233/17/10/014.

[322] J. Canet-Ferrer, E. Coronado, A. Forment-Aliaga, E. Pinilla-Cienfuegos, Correction of the tip convolution effects in the imaging of nanostructures studied through scanning force microscopy., Nanotechnology. 25 (2014) 395703. doi:10.1088/0957-4484/25/39/395703.

[323] I. Review, Letters 28, Quantum. 75 (1995) 1687–1691. doi:10.1103/PhysRevLett.60.1314.

[324] D. Keller, Reconstruction of STM and AFM images distorted by finite-size tips, Surf. Sci. 253 (1991) 353–364. doi:10.1016/0039-6028(91)90606-S.

[325] J. Gao, M.B. Chan-Park, Adhesive behavior of DNA molecules on silicon wafers treated by argon and oxygen plasma, Surf. Coatings Technol. 194 (2005) 244–250. doi:10.1016/j.surfcoat.2004.08.189.

[326] J. Bath, A.J. Turberfield., DNA nanomachines, Nature. Nanotech. 2 (2007) 275–284. http://dx.doi.org/10.1038/nnano.2007.104.

[327] D. Felbacq, G. Bouchitté, Negative refraction in periodic and random photonic crystals, New J. Phys. 7 (2005) 159–159. doi:10.1088/1367-2630/7/1/159.

[328] D.A. Pawlak, S. Turczynski, M. Gajc, K. Kolodziejak, R. Diduszko, K. Rozniatowski, J. Smalc, I. Vendik, How Far Are We from Making Metamaterials by Self-Organization? The Microstructure of Highly Anisotropic Particles with an SRR-Like Geometry, Adv. Funct. Mater. 20 (2010) 1116–1124. doi:10.1002/adfm.200901875.

[329] M. Rupin, F. Lemoult, G. Lerosey, P. Roux, Experimental Demonstration of Ordered and Disordered Multiresonant Metamaterials for Lamb Waves, Phys. Rev. Lett. 112 (2014) 234301. doi:10.1103/PhysRevLett.112.234301.

[330] S.S. Mallajosyula, S.K. Pati, Toward DNA Conductivity: A Theoretical Perspective, J. Phys. Chem. Lett. 1 (2010) 1881–1894. doi:10.1021/jz1003654.

[331] full-text, (n.d.).

[332] P.J. De Pablo, F. Moreno-Herrero, J. Colchero, J. Gómez Herrero, P. Herrero, A.M. Baró, P. Ordejón, J.M. Soler, E. Artacho, Absence of dc-Conductivity in l-DNA, 871514 (2000).

[333] M. Matlosz, Electrochemical Society (United States). Electrodeposition Division., Fundamental aspects of electrochemical deposition and dissolution : proceedings of the international symposium, Electrochemical Society, (2000) .

[334] L.A. Porter, H.C. Choi, A.E. Ribbe, J.M. Buriak, Controlled Electroless Deposition of Noble Metal Nanoparticle Films on Germanium Surfaces, (n.d.). doi:10.1021/nl025677u.

[335] Z. Deng, C. Mao, Molecular lithography with DNA nanostructures, Angew.

Chemie - Int. Ed. 43 (2004) 4068–4070. doi:10.1002/anie.200460257.

[336] J.E.G.J. Wijnhoven, S.J.M. Zevenhuizen, M.A. Hendriks, D.È. Vanmaekelbergh, J.J. Kelly, W.L. Vos, Electrochemical Assembly of Ordered Macropores in Gold**, Adv. Mater. 12 (2000).

[337] R.S. Sundaram, M. Steiner, H.-Y. Chiu, M. Engel, A.A. Bol, R. Krupke, M. Burghard, K. Kern, P. Avouris, The GrapheneÀGold Interface and Its Implications for Nanoelectronics, (2011). doi:10.1021/nl201907u.

[338] K.H.J. Buschow, Encyclopedia of materials : science and technology, Elsevier, (2001).

[339] G. Yang, L. Li, J. Jiang, Y. Yang, Direct electrodeposition of gold nanotube arrays of rough and porous wall by cyclic voltammetry and its applications of simultaneous determination of ascorbic acid and uric acid, Mater. Sci. Eng. C. 32 (2012) 1323–1330. doi:10.1016/j.msec.2012.04.004.

[340] N. Kanani, N. Kanani, Processes for the Deposition of Metallic Coatings, in: Electroplating, Elsevier, (2004) 87–140. doi:10.1016/B978-185617451-0/50004-X.

[341] N. Kanani, N. Kanani, Electrodeposition Considered at the Atomistic Level, in: Electroplating, Elsevier, (2004) 141–177. doi:10.1016/B978-185617451-0/50005-1.

[342] S.A. Denisov, Y. Cudré, P. Verwilst, G. Jonusauskas, M. Marín-Suárez, J.F. Fernández-Sánche, E. Baranoff, N.D. McClenaghan, Direct observation of reversible electronic energy transfer involving an iridium center, Inorg. Chem. 53 (2014) 2677–2682. doi:10.1021/ic4030712.